EISSN 1305-3612

DIR

Diagnostic and Interventional Radiology

TSR 1924
TURKISH SOCIETY OF RADIOLOGY

dirjournal.org

VOLUME 29
ISSUE 4
JULY 2023

Diagnostic and Interventional Radiology

Official Journal of the Turkish Society of Radiology

E-ISSN: 1305-3612
www.dirjournal.org

Editor in Chief

Mehmet Ruhi Onur, MD
Department of Radiology, Hacettepe University Faculty of Medicine, Ankara, Turkey
ORCID ID: 0000-0003-1732-7862

Section Editors and Scientific Editorial Board

Abdominal Imaging

İlkay S. İdilman, MD
Department of Radiology, Hacettepe University Faculty of Medicine, Ankara, Turkey
ORCID ID: 0000-0002-1913-2404

Sonay Aydın, MD
Department of Radiology, Erzincan Binali Yıldırım University Faculty of Medicine, Erzincan, Turkey
ORCID ID: 0000-0002-3812-6333

Artificial Intelligence and Informatics

Burak Koçak, MD
Department of Radiology, University of Health Sciences, Başakşehir Çam and Sakura City Hospital, İstanbul, Turkey
ORCID ID: 0000-0002-7307-396X

Breast Imaging

Füsun Taşkın, MD
Department of Radiology, Acıbadem University Faculty of Medicine, İstanbul, Turkey
ORCID ID: 0000-0001-7985-3660

Chest and Cardiovascular Imaging

Furkan Ufuk, MD
Department of Radiology, Pamukkale University Faculty of Medicine, Denizli, Turkey
ORCID ID: 0000-0002-8614-5387

Hybrid Imaging and Nuclear Medicine

Evrim Bengi Türkbey, MD
Radiology and Imaging Sciences, Clinical Center, National Institutes of Health Bethesda, Maryland, United States
ORCID ID: 0000-0002-5216-3528

Interventional Radiology

Barbaros Çil, MD, FCIRSE
Department of Radiology, Koç University School of Medicine, İstanbul, Turkey
ORCID ID: 0000-0003-1079-0088

Bahri Üstünsöz, MD
Department of Radiology, LSUHSC (Louisiana State University Health Science Center) School of Medicine, New Orleans, United States
ORCID ID: 0000-0003-4308-6708

James Milburn, MD
Department of Radiology, Ochsner Medical System, New Orleans, Louisiana, USA
ORCID ID: 0000-0003-3403-2628

Musculoskeletal Imaging

Zeynep Maraş Özdemir, MD
Department of Radiology, İnönü University Faculty of Medicine, Malatya, Turkey
ORCID ID: 0000-0003-1085-8978

Neuroradiology

Gülgün Yılmaz Ovalı, MD
Department of Radiology, Celal Bayar University Faculty of Medicine, Manisa, Turkey
ORCID ID: 0000-0001-8433-5622

Erkan Gökçe, MD
Department of Radiology, Tokat Gaziosmanpaşa University Faculty of Medicine, Tokat, Turkey
ORCID ID: 0000-0003-3947-2972

Pediatric Radiology

Meltem Ceyhan Bilgici, MD
Department of Radiology, 19 Mayıs University Faculty of Medicine, Samsun, Turkey
ORCID ID: 0000-0002-0133-0234

Evrim Özmen, MD
Department of Radiology, Koç University Hospital, İstanbul, Turkey
ORCID ID: 0000-0003-3100-4197

Publication Coordinator

Şükrü Mehmet Ertürk, MD
Department of Radiology, İstanbul University, İstanbul Faculty of Medicine, İstanbul, Turkey
ORCID ID: 0000-0003-4086-675X

Biostatistical Consultant

İlker Ercan, PhD
Department of Biostatistics, Uludağ University School of Medicine, Bursa, Turkey
ORCID ID: 0000-0002-2382-290X

Publication Services

Galenos Publishing, İstanbul, TR

Past Editors

Editors in Chief

Mustafa Seçil, MD (2016-2022)
Nevzat Karabulut, MD (2011-2016)
Üstün Aydıngöz, MD (2010-2011)
Okan Akhan, MD (2001-2010)
Ferhun Balkancı, MD (1999-2001)
Aytekin Besim, MD (1994-1999)*

** Dr. Aytekin Besim actually served as the General Coordinator. His work in this capacity, however, was in effect that of an Editor in Chief.*

Editors

Ayşenur Cila, MD (2001-2002)
Suat Kemal Aytaç, MD (1997-2001)
Erhan Ilgıt, MD (1994-2001)
Okan Akhan, MD (1994-2001)
Ferhun Balkancı, MD (1994-2000)
Serdar Akyar, MD (1994-1997)

Section Editors

Section Editorship was established in 2002 at the tenure of Dr Okan Akhan, Editor in Chief.

Abdominal Imaging

Bengi Gürses, MD (2020-2023)
Mehmet Ruhi Onur, MD (2016-2022)
Barış Türkbey, MD (2014-2020)
Mustafa N. Özmen, MD (2012-2018)
Murat Acar, MD (2015-2016)
Mustafa Seçil, MD (2011-2016)
Ahmet Tuncay Turgut, MD (2011)
Deniz Akata, MD (2007-2011)
Ayşe Erden, MD (2002-2011)
Okan Akhan, MD (2002-2010)
Hakan Özdemir, MD (2002-2010)

Diagnostic and Interventional Radiology

Official Journal of the Turkish Society of Radiology

E-ISSN: 1305-3612
www.dirjournal.org

Artificial Intelligence and Informatics
Barış Türkbey, MD (2020-2023)

Breast Imaging
Mustafa Erkin Arıbal, MD (2016-2023)
Sibel Kul (2015-2018)
Ayşenur Oktay, MD (2009-2014)
Ayşegül Özdemir, MD (2004-2009)

Cardiovascular Imaging
Uğur Bozlar, MD (2016-2023)
Muşturay Karçaaltıncaba, MD (2007-2010)
Mecit Kantarcı (2010-2016)

Chest Imaging
Nevzat Karabulut, MD (2010-2014)
Çetin Atasoy, MD (2007-2010)
Macit Arıyürek, MD (2002-2007)
Figen Demirkazık, MD, (2014-2018)

General Radiology
Ersin Öztürk, MD (2014-2017)
Utku Şenol, MD (2010-2013)
Oğuz Dicle, MD (2007-2010)

Interventional Radiology
Cüneyt Aytekin, MD (2016-2023)
Bora Peynircioğlu, MD (2012-2015)
Levent Oğuzkurt, MD (2011-2014)
Fatih Boyvat, MD (2007-2010)
İsmail Oran, MD (2015-2019)

Musculoskeletal Imaging
Hatice Tuba Sanal, MD (2016-2023)
Fatih Kantarcı, MD (2014-2016)
Ayşenur Oktay, MD (2011-2013)
Üstün Aydıngöz, MD (2002-2011)
Berna Dirim Mete (2016-2017)

Neuroradiology and Head & Neck Imaging
Kubilay Aydın, MD (2016-2023)
Nafi Aygün, MD (2016-2023)
Kader Karlı Oğuz, MD (2011-2015)
Süleyman Men, MD (2007-2013)
Muhteşem Ağıldere, MD (2002-2011)

Nuclear Medicine
A. Cahid Civelek, MD (2016-2023)
Oktay Sarı, MD (2015)
Akın Yıldız, MD (2011-2014)

Pediatric Radiology
Korgün Koral, MD (2016-2023)
Murat Kocaoğlu, MD (2016-2023)
Ensar Yekeler, MD (2014-2016)
Suat Fitöz, MD (2007-2013)

Diagnostic and Interventional Radiology (Diagn Interv Radiol) is a bimonthly periodical of the Turkish Society of Radiology and the content of the journal is available at https://www.dirjournal.org/. It is peer-reviewed and adheres to the highest ethical and editorial standards. The editors of the journal endorse the Editorial Policy Statements Approved by the Council of Science Editors Board of Directors (www.councilscienceeditors.org/services/draft_approved.cfm). The journal is in compliance with the Recommendations for the Conduct, Reporting, Editing and Publication of Scholarly Work in Medical Journals published by the International Committee of Medical Journal Editors (updated May 2022, www.icmje.org).

First ten volumes of Diagnostic and Interventional Radiology have been published in Turkish under the name of Tanısal ve Girişimsel Radyoloji (Index Medicus® abbreviation: Tani Girisim Radyol), the current title's exact Turkish translation.

Diagnostic and Interventional Radiology is an open access publication, and the journal's publication model is based on Budapest Open Access Initiative (BOAI) declaration. All published content is available online, free of charge at https://www.dirjournal.org/. Authors retain the copyright of their published work in Diagnostic and Interventional Radiology. The journal's content is licensed under a Creative Commons Attribution-NonCommercial (CC BY-NC) 4.0 International License which permits third parties to share and adapt the content for non-commercial purposes by giving the appropriate credit to the original work.

Diagnostic and Interventional Radiology is indexed in **Pubmed/Medline, Pubmed Central, Web of Science, TUBITAK ULAKBIM TR Index, HINARI, EMBASE, CINAHL, Scopus, Gale** and **CNKI**.

Contact Information

Diagnostic and Interventional Radiology Turkish Society of Radiology
Hoşdere Cad., Güzelkent Sok., Çankaya Evleri, F/2, 06540
Ankara, Turkey
E-mail: info@dirjournal.org
Phone: +90 (312) 442 36 53 **Fax:** +90 (312) 442 36 54

Publisher Contact

Address: Molla Gürani Mah. Kaçamak Sk.
No: 21/1 34093 İstanbul, Turkey
Phone: +90 (530) 177 30 97
E-mail: info@galenos.com.tr/yayin@galenos.com.tr
Web: www.galenos.com.tr **Publisher Certificate Number:** 14521

Online Publication Date: July 2023

EISSN 1305-3612

International scientific journal published bimonthly.

Turkish Society of Radiology is one of the foremost medical specialty organizations in Turkey. It was formed by the merger of the two main radiology societies of Turkey, one of which was founded in 1924. The Society is based in Ankara, Turkey.

TSR 1924 TURKISH SOCIETY OF RADIOLOGY

Diagnostic and Interventional Radiology

Instructions to Authors

Diagnostic and Interventional Radiology (Diagn Interv Radiol) is a medium for disseminating scientific information based on research, clinical experience, and observations pertaining to diagnostic and interventional radiology. The journal is the double-blind peer-reviewed, bimonthly, open-access publication organ of the Turkish Society of Radiology and its publication language is English. Diagnostic and Interventional Radiology is currently indexed by Science Citation Index Expanded, PubMed MEDLINE, PubMed Central, TUBITAK ULAKBIM TR Index, HINARI, EMBASE, CINAHL, Scopus, Gale and CNKI.

The journal is a medium for original articles, reviews, pictorial essays, technical notes related to all fields of diagnostic and interventional radiology.

The editorial and publication process of the Diagnostic and Interventional Radiology are shaped in accordance with the guidelines of the International Committee of Medical Journal Editors (ICMJE), World Association of Medical Editors (WAME), Council of Science Editors (CSE), Committee on Publication Ethics (COPE), European Association of Science Editors (EASE), and National Information Standards Organization (NISO). The journal is in conformity with the Principles of Transparency and Best Practice in Scholarly Publishing.

Authorship

Each individual listed as an author should fulfill the authorship criteria recommended by the International Committee of Medical Journal Editors (ICMJE - www.icmje.org). To be listed as an author, an individual should have made substantial contributions to all four categories established by the ICMJE: (a) conception and design, or acquisition of data, or analysis and interpretation of data, (b) drafting the article or revising it critically for important intellectual content, (c) final approval of the version to be published, and (d) agreement to be accountable for all aspects of the work in ensuring that questions related to the accuracy or integrity of any part of the work are appropriately investigated and resolved. Individuals who contributed to the preparation of the manuscript but do not fulfill the authorship criteria should be acknowledged in an acknowledgements section, which should be included in the title page of the manuscript. If the editorial board suspects a case of "gift authorship", the submission will be rejected without further review.

Ethical standards

For studies involving human or animal participants, the authors should indicate whether the procedures followed were in accordance with the ethical standards of the responsible committee on human and animal experimentation (institutional or regional) and with the Helsinki Declaration). Application or approval number/year of the study should also be provided. The editorial board will act in accordance with COPE guidelines if an ethical misconduct is suspected.

It is the authors' responsibility to carefully protect the patients' anonymity and to verify that any experimental investigation with human subjects reported in the submission was performed with informed consent and following all the guidelines for experimental investigation with human subjects required by the institution(s) with which all the authors are affiliated with. For photographs that may reveal the identity of the patients, signed releases of the patient or of his/her legal representative should be enclosed.

Prospective human studies require both an ethics committee approval and informed consent by participants. Retrospective studies require an ethics committee approval with waiver of informed consent. Authors may be required to document such approval.

All submissions are screened by a similarity detection software (iThenticate by CrossCheck). Manuscripts with an overall similarity index of greater than 20%, or duplication rate at or higher than 5% with a single source are returned back to authors without further evaluation along with the similarity report.

In the event of alleged or suspected research misconduct, e.g., plagiarism, citation manipulation, and data falsification/fabrication, the Editorial Board will follow and act in accordance with COPE guidelines.

Withdrawal Policy

Articles may be withdrawn under certain circumstances.

The article will be withdrawn if it;

- violates professional ethical codes,
- is subject to a legal dispute,
- has multiple submissions,
- includes fake claims of authorship, plagiarism, misleading data, and false data that may pose a severe health risk.

The editorial board will follow the principles set by COPE (Committee on Publication Ethics) in case of an article withdrawal.

Manuscript Preparation

The manuscripts should be prepared in accordance with ICMJE-Recommendations for the Conduct, Reporting, Editing, and Publication of Scholarly Work in Medical Journals (updated in May 2022 - https://www.icmje.org/recommendations/).

Original Investigations and Reviews should be presented in accordance with the following guidelines: randomized study – CONSORT, observational study – STROBE, study on diagnostic accuracy – STARD, systematic reviews and meta-analysis PRISMA, nonrandomized behavioral and public health intervention studies – TREND.

Diagnostic and Interventional Radiology will only evaluate manuscripts submitted via the journal's self-explanatory online manuscript submission and evaluation system available at mc04.manuscriptcentral.com/dir. Evaluation process of submitted manuscripts takes 4 weeks on average.

Manuscripts are evaluated and published on the understanding that they are original contributions, and do not contain data that have been published elsewhere or are under consideration by another journal. Authors are required to make a full statement at the time of submission about all prior reports and submissions that might be considered duplicate or redundant publication, and mention any previously published abstracts for meeting presentations that contain partial or similar material in the cover letter. They must reference any similar previous publications in the manuscript.

Authors must obtain written permission from the copyright owner to reproduce previously published figures, tables, or any other material in both print and electronic formats and present it during submission. The original source should be cited within the references and below the reprinted material.

Cover letter: A cover letter must be provided with all manuscripts. This letter may be used to emphasize the importance of the study. The authors should briefly state the existing knowledge relevant to the study and the contributions their study make to the existing knowledge. The correspondent author should also include a statement in the cover letter declaring that he/she accepts to undertake all the responsibility for authorship during the submission and review stages of the manuscript.

Diagnostic and Interventional Radiology

Instructions to Authors

Title page: A separate title page should be submitted with all manuscripts and should include the title of the manuscript, name(s), affiliation(s), and major degree(s) of the author(s). The name, address, telephone (including the mobile phone number) and fax numbers and e-mail address of the corresponding author should be clearly listed. Grant information and other sources of support should also be included. Individuals who contributed to the preparation of the manuscript but do not fulfill the authorship criteria should also be acknowledged in the title page. Manuscripts should not be signed by more than 6 authors unless they are multicenter or multidisciplinary studies.

Main document

Abstract: All submissions (except for Letters to the Editor) should be accompanied by an abstract limited to 400 words. A structured abstract is only required with original articles and it should include the following subheadings: PURPOSE, METHODS, RESULTS, CONCLUSION.

Main points: Each submission should be accompanied by 3 to 5 "main points", which should emphasize the most striking results of the study and highlight the message that is intended to be conveyed to the readers. As these main points would be targeting radiology residents, experts and residents of other fields of medicine, as well as radiology experts, they should be kept as plain and simple as possible. These points should be constructed in a way that provides the readers with a general overview of the article and enables them to have a general idea about the article.

The main points should be listed at the end of the main text, above the reference list.

Example: Liu S, Xu X, Cheng Q, et al. Simple quantitative measurement based on DWI to objectively judge DWI-FLAIR mismatch in a canine stroke model. Diagn Interv Radiol 2015; 21:348–354.

• The relative diffusion-weighted imaging signal intensity (rDWI) of ischemic lesions might be helpful to identify the status of fluid attenuated inversion recovery (FLAIR) imaging in acute ischemic stroke.

• The relative apparent diffusion coefficient (rADC) value appears not useful to identify the status of FLAIR imaging in the acute period.

• Based on our embolic canine model, rDWI increased gradually in the acute period, while the rADC kept stable, which might explain why rDWI is helpful to identify the status of FLAIR imaging, while rADC is not.

Main text

Original Articles

Original articles should provide new information based on original research. The main text should be structured with Introduction, Methods, Results, and Discussion subheadings. The number of cited references should not exceed 50 and the main text should be limited to 4500 words. Number of tables included in an original article should be limited to 4 and the number of figures should be limited to 7 (or a total of 15 figure parts).

Introduction

State briefly the nature and purpose of the work, quoting the relevant literature.

Methods

Include the details of clinical and technical procedures.

Research ethics standards compliance

All manuscripts dealing with human subjects must contain a statement indicating that the study was approved by the Institutional Review Board or a comparable formal research ethics review committee. If none is present at your institution, there should be a statement that the research was performed according to the Declaration of Helsinki principles (www.wma.net/e/policy/b3.htm). There should also be a statement about whether informed consent was obtained from research subjects.

Results

Present these clearly, concisely, and without comment. Statistical analysis results should also be provided in this section to support conclusions when available.

Discussion

Explain your results and relate them to those of other authors; define their significance for clinical practice. Limitations, drawbacks, or shortcomings of the study should also be stated in the discussion section before the conclusion paragraph. In the last paragraph, a strong conclusion should be written.

Review Articles

Review articles are scientific analyses of recent developments on a specific topic as reported in the literature. No new information is described, and no opinions or personal experiences are expressed. Reviews include only the highlights on a subject. Main text should be limited to 4000 words and the number of cited references should not exceed 75. Number of tables included in a review article should be limited to 4 and the number of figures should be limited to 15 (or a total of 30 figure parts).

Pictorial Essay

This is a continuing medical education exercise with the teaching message in the figures and their legends. Text should include a brief abstract; there may be as many as 30 figure parts. No new information is included. The value of the paper turns on the quality of the illustrations. Authors can submit dynamic images (e.g. video files) or include supplemental image files for online presentation that further illustrate the educational purpose of the essay. Maximums: Pages of text – 4 (1,500 words); References – 20; Figures – 15 or total of 30 images; No table Main text should be limited to 1500 words and the number of cited references should not exceed 15.

Technical Notes

Technical note is a brief description of a specific technique, procedure, modification of a technique, or new equipment of interest to radiologists. It should include a brief introduction followed by Technique section for case reports or Methods section for case series, and Discussion is limited to the specific message, including the uses of the technique, equipment, or software. Literature reviews and lengthy descriptions of cases are not appropriate.

Main text should be limited to 1500 words and the number of cited references should not exceed 8. Number of tables included in a technical note should be limited to 4 and the number of figures should be limited to 3 (or a total of 6 figure parts).

Diagnostic and Interventional Radiology

Instructions to Authors

Letter to the Editor and Reply

Letters to the Editor and Replies should offer objective and constructive criticism of published articles within last 6 months. Letters may also discuss matters of general interest to radiologists and may include images. Material being submitted or published elsewhere should not be duplicated in letters.

Main text should be limited to 500 words and the number of cited references should not exceed 6. No tables should be included and the number of figures should be limited to 2 (or a total of 4 figure parts).

Recommendations for Manuscripts:

Type of manuscript	Word limit	Abstract word limit	Reference limit	Author limit	Table limit	Figure limit
Original Article	4500	400 (Structured)	50	6*	4	7 or total of 15 images
Review Article	4000	200	75	5	4	15 or total of 24 images
Pictorial Essay	1500	400	20	5	1	15 figures or total of 30 figure parts
Technical Note	1500	200	8	5	2	3 figures or total of 6 figure parts
Letter	500	N/A	6	4	No tables	2 figures or total of 4 figure parts

*Manuscripts should not be signed by more than 6 authors unless they are multicenter or multidisciplinary studies.
**Considering the specific condition of the manuscript, minor flexibilites may be applied for the recommendations upon the decision of Editor-in-Chief or the Section Editors.

References

Both in-text citations and the references must be prepared according to the AMA Manual of style.

While citing publications, preference should be given to the latest, most up-to-date publications. Authors are responsible for the accuracy of references If an ahead-of-print publication is cited, the DOI number should be provided. Journal titles should be abbreviated in accordance with the journal abbreviations in Index Medicus/MEDLINE/PubMed. When there are six or fewer authors, all authors should be listed. If there are seven or more authors, the first three authors should be listed followed by "et al." In the main text of the manuscript, references should be cited in superscript after punctuation. The reference styles for different types of publications are presented in the following examples.

Journal Article: Economopoulos KJ, Brockmeier SF. Rotator cuff tears in overhead athletes. Clin Sports Med. 2012;31(4):675-692.

Book Section: Fikremariam D, Serafini M. Multidisciplinary approach to pain management. In: Vadivelu N, Urman RD, Hines RL, eds. Essentials of Pain Management. New York, NY: Springer New York; 2011:17-28.

Books with a Single Author: Patterson JW. Weedon's Skin Pahology. 4th ed. Churchill Livingstone; 2016.

Editor(s) as Author: Etzel RA, Balk SJ, eds. Pediatric Environmental Health. American Academy of Pediatrics; 2011.

Conference Proceedings: Morales M, Zhou X. Health practices of immigrant women: indigenous knowledge in an urban environment. Paper presented at: 78th Association for Information Science and Technology Annual Meeting; November 6-10; 2015; St Louis, MO. Accessed March 15, 2016. https://www.asist.org/files/meetings/am15/proceedings/openpage15.html

Thesis: Maiti N. Association Between Behaviours, Health Charactetistics and Injuries Among Adolescents in the United States. Dissertation. Palo Alto University; 2010.

Online Journal Articles: Tamburini S, Shen N, Chih Wu H, Clemente KC. The microbiome in early life: implications for health outcometes. Nat Med. Published online July 7, 2016. doi:10.1038/nm4142

Epub Ahead of Print Articles: Websites: International Society for Infectious Diseases. ProMed-mail. Accessed February 10, 2016. http://www.promedmail.org

Tables

Tables should be included in the main document and should be presented after the reference list. Tables should be numbered consecutively in the order they are referred to within the main text. A descriptive title should be provided for all tables and the titles should be placed above the tables. Abbreviations used in the tables should be defined below by footnotes (even if they are defined within the main text). Tables should be created using the "insert table" command of the word processing software and they should be arranged clearly to provide an easy reading. Data presented in the tables should not be a repetition of the data presented within the main text but should be supporting the main text.

Figures and figure legends

Figures, graphics, and photographs should be submitted as separate files (in TIFF or JPEG format) through the submission system. The files should not be embedded in a Word document or the main document. When there are figure subunits, the subunits should not be merged to form a single image. Each subunit should be submitted separately through the submission system. Images should not be labelled (a, b, c, etc.) to indicate figure subunits. Thick and thin arrows, arrowheads, stars, asterisks, abbreviations and similar marks can be used on the images to support figure legends. Like the rest of the submission, the figures too should be blind. Any information within the images that may indicate the institution or the patient should be removed.

Figure legends should be listed at the end of the main document.

General

All acronyms and abbreviations used in the manuscript should be defined at first use, both in the abstract and in the main text. The abbreviation should be provided in parenthesis following the definition.

Statistical analysis should be performed in accordance with guidelines on reporting statistics in medical journals (Altman DG, Gore SM, Gardner MJ, Pocock SJ. Statistical guidelines for contributors to medical journals. Br Med J 1983: 7; 1489–1493.). Information on the statistical analysis process of the study should be provided within the main text.

When a drug, product, hardware, or software mentioned within the main text product information, the name and producer of the product should be provided in parenthesis in the following format: "Discovery St PET/CT scanner (GE Healthcare)."

All references, tables, and figures should be referred to within the main text and they should be numbered consecutively in the order they are referred to within the main text.

Initial evaluation and Peer review process

Manuscripts submitted to Diagnostic and Interventional Radiology will first go through a technical evaluation process where the editorial office staff will ensure that the manuscript is prepared and submitted in accordance with the journal's guidelines. Submissions that do not conform the journal's guidelines will be returned to the submitting author with technical correction requests.

All submissions are screened by a similarity detection software (iThenticate by CrossCheck), and those with an overall similarity index of greater than 20%, or duplication rate at or higher than 5% with a single source are returned back to authors without further evaluation along with the similarity report.

Manuscripts meeting the requirements mentioned in journal's guideline will go under the review process. The initial review will be performed by Editor-in-Chief and the Section Editor, which include the evaluation of the manuscript for its originality, importance of the findings, scientific merit, interest to readers and compliance with the policy of the journal in force. Manuscripts with insufficient priority for publication are not sent out for further review and rejected promptly at this level to allow the authors to submit their work elsewhere without delay.

Manuscripts that pass through the initial review are sent to peer review, which is performed in a blinded manner by least two external and independent reviewers. During the review process, all original articles are evaluated by at least one senior consultant of statistics for proper handling and consistency of data, and use of correct statistical method. The Section Editor and / or Editor-n-Chief are the final authority in the decision-making process for all submissions.

Revisions

When submitting a revised version of a paper, the author must submit a detailed "Response to reviewers" that states point by point how each issue raised by the reviewers has been covered and where it can be found (each reviewer's comment followed by the author's reply and line numbers where the changes have been made) as well as an annotated copy, and a clear copy of the main document.

Revised manuscripts must be submitted within 30 days from the date of the decision letter. If the revised version of the manuscript is not submitted within the allocated time, the revision option will be automatically cancelled by the submission system. If the submitting author(s) believe that additional time is required, they should request an extension before the initial 30-day period is over.

Proofs and DOI Number

Accepted manuscripts are copy-edited for grammar, punctuation, and format by professional language editors. Following the copyediting process, the authors will be asked to review and approve the changes made during the process. Authors will be contacted for a second time after the layout process and will be asked to review and approve the PDF proof of their article for publication. Once the production process of a manuscript is completed it is published online on the journal's webpage as an ahead-of-print publication before it is included in its scheduled issue.

Publication Fee Policy

Diagnostic and Interventional Radiology (DIR) applies an Article Processing Charge (APCs) for only accepted articles. No fees are requested from the authors during submission and evaluation process. All manuscripts must be submitted via Manuscript Manager.

An APC fee of and local taxes will be applied depending on the article type (see Table 1)

Review	$ 1250
Original Article	$ 1000
Pictorial Essay	$ 750
Technical Note	

Table 1. Article Types and Fees

The APCs will be accepted through the link that will be sent to the corresponding author of each article via the online article system. In the next step, the authors will be receiving a receipt of their payment.

*Please note that the Article Processing Charge (APC) will not affect neither the editorial and peer-review process nor the priority of the manuscripts by no means. All submissions will be evaluated by the Editorial Board and the external reviewers in terms of scientific quality and ethical standards.

Refund Policy:

Returning the article to the author; Diagnostic and Interventional Radiology (DIR) will refund the submission fees with a coupon code if the article is returned to the author. Using this code, authors can use the submission fees of different articles without making a new payment.

Article Retraction:

Infringements of publication/research ethics, such as multiple submissions, bogus claims of authorship, plagiarism, and fraudulent use of data could lead to article retraction.

A retraction statement titled "Retraction: [article title]" must be signed by the authors and/or the editor. The original article is marked as retracted but a PDF version remains available to readers, and the retraction statement is linked to the original published paper.

Diagnostic and Interventional Radiology

Volume 29 • Issue 4

July 2023

www.dirjournal.org

Contents

Full text of these articles can be accessed online at www.dirjournal.org or through PubMed (https://www.ncbi.nlm.nih.gov/pmc/journals/2754/).

Diagn Interv Radiol 2023; DOI: 10.4274/dir.2022.221730

ABDOMINAL IMAGING

ORIGINAL ARTICLE

Copyright@Author(s) - Available online at dirjournal.org.
Content of this journal is licensed under a Creative Commons Attribution-NonCommercial 4.0 International License.

Relationship between hepatic and pancreatic steatosis and the COVID-19 pneumonia total severity score and prognosis with an emphasis on prognostic strength

Hakan Doğan
Evren Uzer
Ömer Tarık Esengür
Hür Hassoy
Serkan Güneyli

PURPOSE

To investigate the relationship between hepatic steatosis (HS), pancreatic steatosis (PS), coexisting HS and PS and the Coronavirus disease-2019 (COVID-19) pneumonia total severity score (TSS) and prognosis, assessed through computed tomography (CT), and to evaluate the degree of effectiveness of the three steatosis conditions on TSS and prognosis.

METHODS

This retrospective study involved 461 patients (255 male and 206 female, median age of 53 years) with COVID-19 who underwent unenhanced chest CT. HS, PS, and coexisting HS and PS, assessed through CT, were compared with patient demographics, comorbidities, TSS, hospitalization and intubation requirements, and mortality rates. The parameters were compared using Mann–Whitney U and chi-square tests. The parameters of three groups of patients with only HS, only PS, and both HS and PS were compared using the Kruskal–Wallis test.

RESULTS

Results revealed that TSS ($P < 0.001$ for all) and hospitalization rates ($P < 0.001$ for all except for HS [$P = 0.004$]) were higher in patients with HS, PS, and both than in those without. Intubation ($P = 0.003$) and mortality rates ($P = 0.018$) were significantly higher solely in patients with PS. However, TSS, hospitalization, and diabetes mellitus were significantly higher than in age-standardized analyses for PS. In a comparison between only HS, only PS, and coexisting HS and PS in 210 patients, the highest TSS was in the coexistence group ($P < 0.001$).

CONCLUSION

The TSS and hospitalization rates correlate with HS, PS, and coexisting HS and PS, whereas intubation and mortality rates only correlate with PS. However, TSS correlates with coexisting HS and PS at the highest rate.

KEYWORDS

Computed tomography, COVID-19, hepatic, pancreas, steatosis

From the Department of Radiology (H.D., E.U.), Koç University Faculty of Medicine, İstanbul, Turkey; Medical Student (Ö.T.E.), Koç University Faculty of Medicine, İstanbul, Turkey; Department of Public Health (H.H.), Ege University Faculty of Medicine, İzmir, Turkey; Department of Radiology (S.G. ✉ drserkanguneyli@gmail.com), İzmir Bakırçay University Faculty of Medicine, İzmir, Turkey.

Received 04 July 2022; revision requested 27 September 2022; last revision received 29 October 2022; accepted 08 November 2022.

Ebup: 21.12.2022

Publication date: 21.07.2023

DOI: 10.4274/dir.2022.221730

In the last few years, Coronavirus disease-2019 (COVID-19) has become a public health concern and crisis, with a total of approximately 540 million cases and 6.3 million deaths as of June 2022.[1] Caused by severe acute respiratory syndrome-coronavirus-2 (SARS-CoV-2), the disease has similar clinical features to many other viral diseases originating in the respiratory system, such as cough, fever, and fatigue. However, it can also lead to more severe complications, resulting in hospitalization, intubation, and death.

Although it is primarily a respiratory system disease, COVID-19 can also be related to other organ systems, especially the gastrointestinal (GI) tract. Evidence suggests that SARS-CoV-2 infection can intensify pre-existing GI conditions.[2] Furthermore, GI pathologies, such as

You may cite this article as: Doğan H, Uzer E, Esengür ÖT, Hassoy H, Güneyli S. Relationship between hepatic and pancreatic steatosis and the COVID-19 pneumonia total severity score and prognosis with an emphasis on prognostic strength. *Diagn Interv Radiol.* 2023;29(4):563-570.

pre-existing liver diseases or GI cancers, have been demonstrated to be correlated with COVID-19 prognosis.[2-12] This prognosis is also related to the COVID-19 pneumonia total severity score (TSS) because it is a comprehensive and systematic structure that gathers common findings from COVID-19 chest computed tomography (CT) within one scoring system.[13,14] The hepatobiliary system also plays an essential role in determining the outcome of COVID-19, as demonstrated by studies that have analyzed the effects of hepatic steatosis (HS) on COVID-19 prognosis.[2-5,7-10,12] In addition, assessing HS during the management of COVID-19 is feasible because HS can easily be identified in unenhanced chest CT. Similarly, evaluating the pancreas can help clarify a COVID-19 prognosis because this organ can be observed in a chest CT. In a recent study by Guneyli et al.[15], correlations between pancreatic steatosis (PS) and the clinical severity of COVID-19 pneumonia in 396 patients and the prognosis in 201 hospitalized patients were reported. However, to our knowledge, no studies until now have focused on the relationship between the radiological severity of COVID-19 pneumonia and prognosis and the three following parameters in a single study: HS, PS, and the coexistence of HS and PS in a single patient.

Main points

- Hepatic steatosis (HS), pancreatic steatosis (PS), and coexisting HS and PS, which are components of metabolic syndrome, can be used for the assessment of Coronavirus disease-2019 (COVID-19) prognosis with the help of unenhanced chest computed tomography (CT).
- Of 461 patients, male sex was found to be correlated with HS, and older age showed an association with PS and coexisting HS and PS. Comorbidities such as diabetes mellitus, hypertension (HT), and coronary artery disease showed a strong association with only PS.
- HS, PS, and coexisting HS and PS were all strongly correlated with the disease severity demonstrated by the COVID-19 pneumonia total severity score (TSS) and higher rates of hospitalization, and of the three, PS was also correlated with rates of intubation and mortality.
- When only HS, only PS, and both HS and PS were compared with each other, patients with only PS were older and had higher rates of HT than those in the other two groups.
- The TSS medians in the three groups with only HS, only PS, and both HS and PS were ranked as 5 (HS), 6 (PS), and 7 (both HS and PS), of which the latter had significant correlation.

Therefore, we hypothesize that HS, PS, and their coexistence correlate with the COVID-19 pneumonia TSS, hospitalization and intubation requirements, and COVID-19 mortality rates. This study aims to understand the relationship between HS and PS, both individually and, in one case, coexisting, and COVID-19 TSS and prognosis with the assistance of chest CT and to investigate which of these parameters have a more effective role in COVID-19 pneumonia prognosis by comparing them.

Methods

Study population

The Institutional Review Board authorized the waiver of informed consent for this retrospective investigation (decision number of the ethics committee approval: 2021.468. IRB1.135). We searched the data of 724 individuals who had received a positive SARS-CoV-2 reverse transcription-polymerase chain reaction test result and had undergone a chest CT using a 64-slice CT scanner between March 2020 and March 2021 at a single institution. Patients under the age of 18 (n = 9), those with a pancreatic or liver mass (n = 6) or diffuse liver disease (n = 2) or splenectomy (n = 1), those who had a contrast-enhanced chest CT (n = 26), those whose CT scans did not cover the pancreas (n = 206), and those with significant artifacts (n =13) were all excluded, leaving 461 patients (255 male and 206 female) with a median age of 53 (minimum 18, maximum 91) years. No patient with hemochromatosis or amiodarone use, both of which may change the density measurements, was included.

Throughout the research procedure, patient demographics and associated chronic conditions, including diabetes mellitus (DM), hypertension (HT), coronary artery disease (CAD), and cerebrovascular disease (CVD), were recorded. In addition, hospitalization and intubation requirements and mortality rates were documented.

CT image acquisition

All CT scans were performed without contrast material using a 64-slice scanner (Siemens, Somatom Definition Flash, Erlangen, Germany). The patients were placed in a supine position, and the images were taken while they held their breaths. The upper abdomen and the whole thoracic cavity were scanned. The CT technique was as follows: helical scanning mode; tube voltage, 120 kV; tube current-time product, 50–350 mAs; pitch, 1.2 and 1.375; matrix, 512x512; reconstructed in lung and soft tissue windows; reconstructed slice thickness, 1.00 mm.

Assessment of PS and HS

The Hounsfield unit (HU) of fat tissue ranges from –150 to –30 HU on unenhanced CT.[16] Two radiologists with expertise in thoracic and abdominal radiology (E.U. with 9 years and H.D. with 3 years of clinical expertise), blinded to patient information, reviewed the CT scans using a dedicated workstation; their decisions were based on consensus. Four regions of interest (ROIs), each separated by the hepatic veins, were drawn using a circular ROI of 1 cm^2 from four distinct places on both lobes (Figure 1a), and the top, middle, and lower sections of the spleen were marked with three ROIs.[16,17] To assess the HU values more accurately, ROIs were generated while avoiding vessels and parenchymal calcifications. The average attenuation values of both organs pointing to the final hepatic and splenic attenuation values were obtained. The liver-to-spleen (L/S) attenuation ratio was then calculated by dividing the liver's attenuation value by that of the spleen. If the L/S attenuation ratio was less than 0.9, HS was assumed to be present in the patient.[9]

The uncinate process, head, neck, body, and tail of the pancreas were marked with five ROIs (Figure 1b, c). After calculating the average attenuation value of the pancreas, the pancreas-to-spleen (P/S) attenuation ratio was calculated by dividing the pancreatic attenuation value by the spleen attenuation value. If the P/S attenuation ratio was less than 0.70, a patient was classified as having PS.[18]

Assessment of TSS

Two radiologists (E.U. with 9 years and H.D. with 3 years of clinical expertise) assessed all images while blinded to patient information, and agreement was reached on the patients with varied scores. The amount of lobar involvement in each of the five lung lobes was measured and categorized as none (0%), minimal (1–25%), mild (26–50%), moderate (51–75%), or severe (76–100%), with reference scores ranging from 0 to 4 (Figure 2). After adding all the scores from the five lobes, a total TSS ranging from 0 to 20 was calculated.[13]

Statistical analysis

For the data analysis, SPSS version 17.0 software (IBM, Chicago, IL, USA) was used. The Kolmogorov–Smirnov test was used to determine if there was a normal distribution.

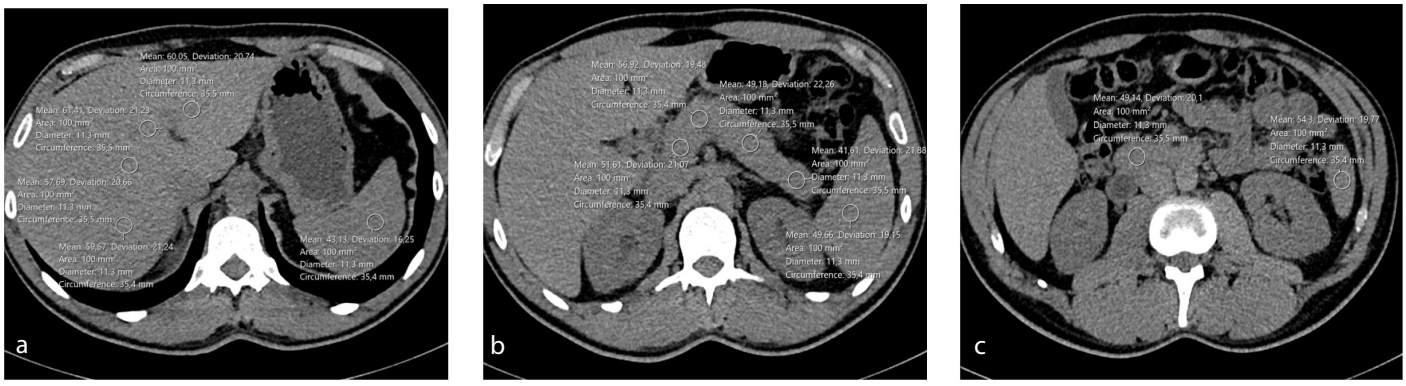

Figure 1. Axial computed tomography images at three levels: **(a)** upper part of the liver and spleen; **(b)** head, neck, body, and tail of the pancreas and the middle part of the spleen; **(c)** uncinate process of the pancreas and lower part of the spleen. The average attenuation value of the four regions of interest (ROIs) in the liver, five ROIs in the pancreas, and three ROIs in the spleen were 59.56, 49.69, and 49.03 Hounsfield units, respectively. The liver-to-spleen attenuation ratio of 1.21 confirmed "liver without steatosis," and the pancreas-to-spleen attenuation ratio of 1.01 confirmed "pancreas without steatosis."

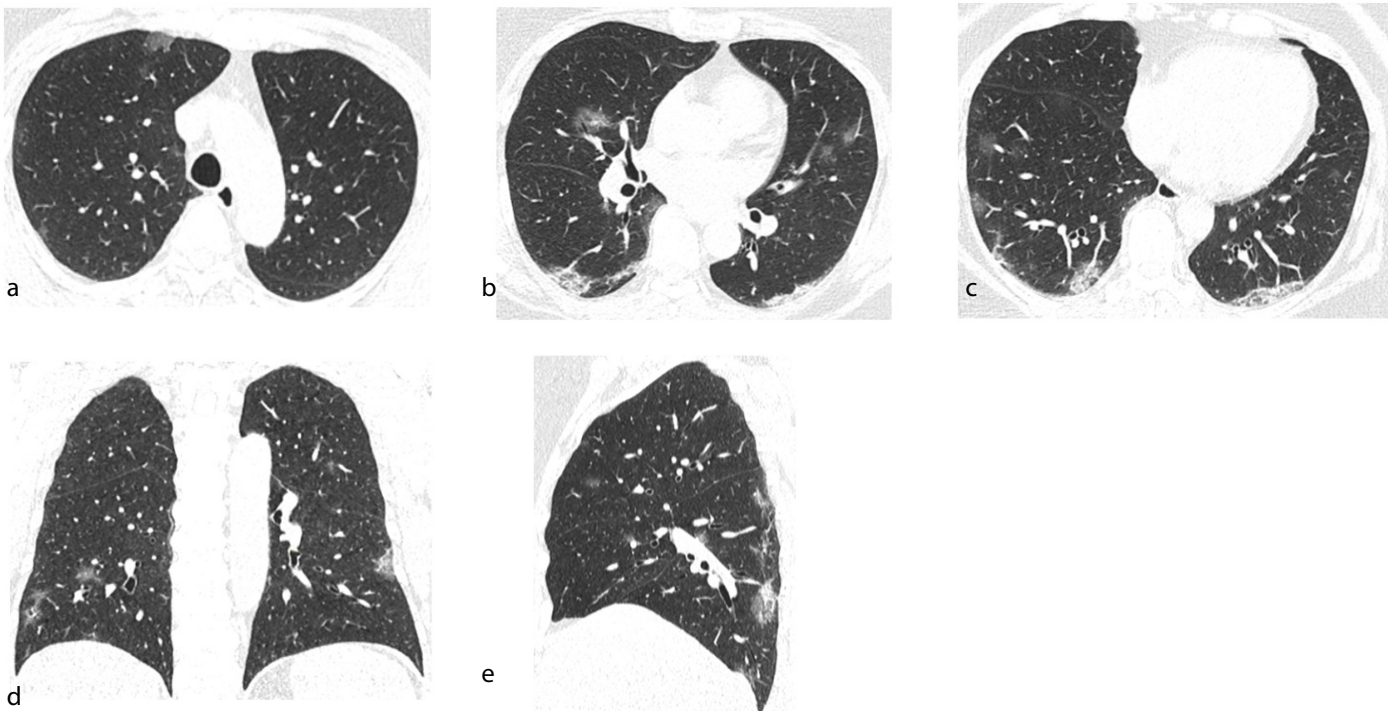

Figure 2. Axial computed tomography images at three levels and the other two planes: **(a)** axial image at the level of the upper lung lobes; **(b)** axial image at the level of the right middle lung lobe; **(c)** axial image at the level of the lower lung lobes; **(d)** coronal image; **(e)** sagittal image. Multifocal, mild involvement of bilateral lungs was revealed, and the COVID-19 pneumonia total severity score was 6. COVID-19, coronavirus disease-2019.

The chi-square test was used to compare HS, PS, and coexisting HS and PS with sex, comorbidities, hospitalization and intubation requirements, and mortality rates, and the Mann–Whitney U test was used to compare HS, PS, and coexisting HS and PS with age and TSS. Age-standardized analyses for PS based on comorbidities, hospitalization, intubation, and mortality rates were investigated using logistic regression, and the unstandardized B value for PS based on TSS was evaluated using linear regression. The parameters were then compared using the Kruskal–Wallis test across the three groups of patients with only HS, only PS, or both. The Mann–Whitney U test was performed for double comparisons. The medians of age and TSS were calculated. Fisher's exact test and Fisher–Freeman–Halton test were also used when required. Statistical significance was defined as a *P* value less than 0.05.

Results

From a total of 461 patients, HS (n = 104, 22.55%), PS (n = 151, 32.75%), and coexisting HS and PS (n = 45, 9.76%) rates were determined. The comparisons of the patients with and without HS, PS, or both according to age, sex, and comorbidities are presented in Table 1.

Age was positively correlated with PS ($P < 0.001$) and coexisting PS and HS ($P = 0.014$), and HS ($P = 0.001$) was higher in male than in female patients (Figure 3). Regarding comorbidities, DM ($P < 0.001$), HT ($P < 0.001$), and CAD ($P < 0.001$) showed a significant correlation with PS, whereas CVD ($P = 0.105$) did not show any significant correlation with this group. Of the four comorbidities, HS and co-

Table 1. Comparisons of patients with and without HS, PS, and both HS and PS according to age, sex, and comorbidities from a total of 461 patients

	Age (years)	Sex (male)	Sex (female)	DM +	DM –	HT +	HT –	CAD +	CAD –	CVD +	CVD –
HS + (n = 104)	54 (26–85)	72 (69.2%)	32 (30.8%)	35 (33.7%)	69 (66.3%)	40 (38.5%)	64 (61.5%)	12 (11.5%)	92 (88.5%)	0 (0%)	104 (100%)
HS – (n = 357)	52 (18–91)	183 (51.3%)	174 (48.7%)	58 (16.2%)	299 (83.8%)	113 (31.7%)	244 (68.3%)	34 (9.5%)	323 (90.5%)	4 (1.1%)	353 (98.9%)
P	0.300	**0.001***		**<0.001***		0.194		0.546		0.579‡	
PS + (n = 151)	63 (31–91)	84 (55.6%)	67 (44.4%)	53 (35.1%)	98 (64.9%)	85 (56.3%)	66 (43.7%)	31 (20.5%)	120 (79.5%)	3 (2%)	148 (98.0%)
PS – (n = 310)	46 (18–87)	171 (55.2%)	139 (44.8%)	40 (12.9%)	270 (87.1%)	68 (21.9%)	242 (78.1%)	15 (4.8%)	295 (95.2%)	1 (0.3%)	309 (99.7%)
P	**<0.001***	0.924		**<0.001***		**<0.001***		**<0.001***		0.105‡	
Coexistence of HS and PS + (n = 45)	57 (35–85)	28 (62.2%)	17 (37.8%)	18 (40.0%)	27 (60.0%)	19 (42.2%)	26 (57.8%)	6 (13.3%)	39 (86.7%)	0 (0%)	45 (100%)
Coexistence of HS and PS – (n = 416)	52 (18–91)	227 (54.6%)	189 (45.4%)	75 (18.0%)	341 (82.0%)	134 (32.2%)	282 (67.8%)	40 (9.6%)	376 (90.4%)	4 (1%)	412 (99.0%)
P	**0.014***	0.327		**<0.001***		0.176		0.431‡		1.000‡	

*Statistically significant values ($P < 0.05$ was used as the significance level). Numeric parameters are expressed as medians. ‡Fisher's exact test was used. CAD, coronary artery disease; CVD, cerebrovascular disease; DM, diabetes mellitus; HS, hepatic steatosis; HT, hypertension; PS, pancreatic steatosis.

existing HS and PS correlated only with DM ($P < 0.001$).

The comparisons of the patients with and without HS, PS, or both according to the TSS, hospitalization and intubation requirements, and mortality rates are presented in Table 2.

Higher TSSs were determined in patients with HS ($P < 0.001$), PS ($P < 0.001$), and both ($P < 0.001$), and higher hospitalization rates were identified in patients with HS ($P = 0.004$), PS ($P < 0.001$), and both ($P < 0.001$) than in patients without (Figure 4). Intubation ($P = 0.003$) and mortality rates ($P = 0.018$) were significant only in patients with PS. The requirement for intubation in patients with and without PS were 9.3% and 2.9%, respectively, whereas mortality rates were 6% and 1.6%, respectively.

The age-standardized odds ratios for PS according to the comorbidities, hospitalization, intubation, mortality rates, and unstandardized B value for PS according to the TSS are presented in Table 3. When the effect of age on the results was eliminated, the presence of DM was 1.8 times greater, hospitalization was 1.7 times greater, and TSS was higher in the patients with PS than in those without PS.

Following these comparisons, three novel groups of interest were formed: Patients with only HS, patients with only PS, and finally, patients with both HS and PS that do not co-

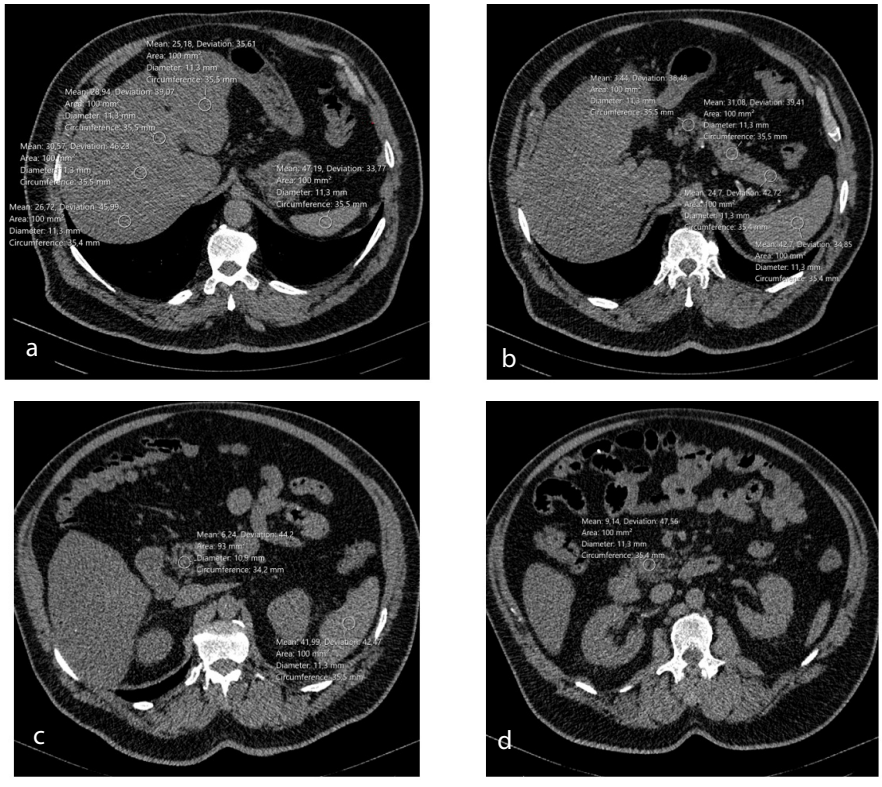

Figure 3. Axial computed tomography images at three levels: **(a)** upper part of the liver and the spleen; **(b)** neck, body, and tail of the pancreas and the middle part of the spleen; **(c)** head of the pancreas and lower part of the spleen; **(d)** uncinate process of the pancreas. The average attenuation value of four regions of interest (ROIs) in the liver, five ROIs in the pancreas, and three ROIs in the spleen were 27.85, 14.92, and 43.96 Hounsfield unit, respectively. The liver-to-spleen attenuation ratio of 0.63 (<0.9) confirmed hepatic steatosis, and the pancreas-to-spleen attenuation ratio of 0.33 (<0.7) confirmed pancreatic steatosis.

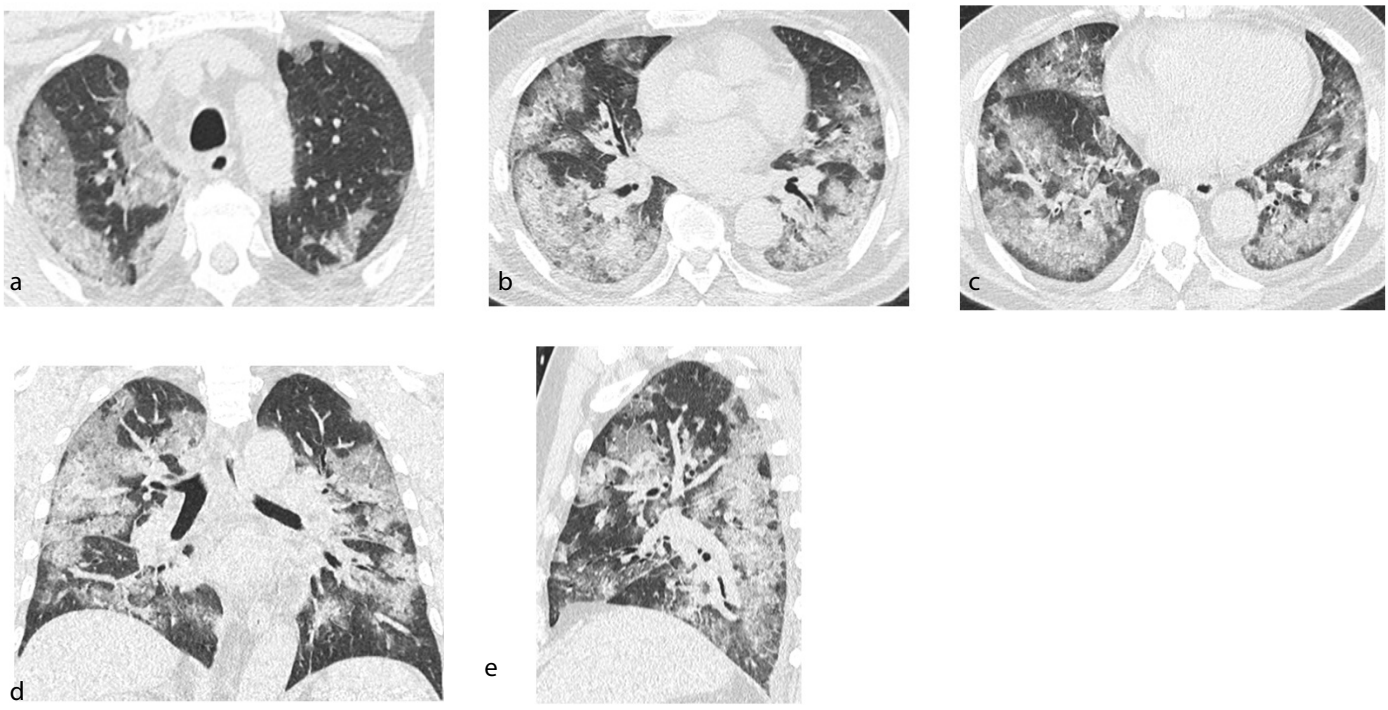

Figure 4. Axial computed tomography images at three levels and the other two planes: **(a)** axial image at the level of the upper lung lobes; **(b)** axial image at the level of the right middle lung lobe; **(c)** Axial image at the level of the lower lung lobes; **(d)** coronal image; **(e)** sagittal image. Severe involvement of bilateral lungs was revealed, and the COVID-19 pneumonia total severity score was 17. COVID-19, coronavirus disease-2019.

Table 2. Comparisons of patients with and without HS, PS, and both HS and PS according to TSS, hospitalization, intubation, and mortality rates from a total of 461 patients

	TSS	Hospitalization +	Hospitalization –	Intubation +	Intubation –	Mortality +	Mortality –
HS + (n = 104)	5 (0–17)	59 (56.7%)	45 (43.3%)	6 (5.8%)	98 (94.2%)	4 (3.8%)	100 (96.2%)
HS – (n = 357)	5 (0–17)	146 (40.9%)	211 (59.1%)	17 (4.8%)	340 (95.2%)	10 (2.8%)	347 (97.2%)
P	**<0.001***	**0.004***		0.678		0.529‡	
PS + (n = 151)	6 (0–17)	98 (64.9%)	53 (35.1%)	14 (9.3%)	137 (90.7%)	9 (6.0%)	142 (94.0%)
PS – (n = 310)	4 (0–17)	107 (34.5%)	203 (65.5%)	9 (2.9%)	301 (97.1%)	5 (1.6%)	305 (98.4%)
P	**<0.001***	**<0.001***		**0.003***		**0.018*‡**	
Coexisting HS and PS + (n = 45)	7 (0–15)	33 (73.3%)	12 (26.7%)	3 (6.7%)	42 (93.3%)	2 (4.4%)	43 (95.6%)
Coexisting of HS and PS – (n = 416)	5 (0–17)	172 (41.3%)	244 (58.7%)	20 (4.8%)	396 (95.2%)	12 (2.9%)	404 (97.1%)
P	**<0.001***	**<0.001***		0.482‡		0.637‡	

Numeric parameters are expressed as medians. *Statistically significant values ($P < 0.05$ was used as the significance level). ‡Fisher's exact test was used. HS, hepatic steatosis; PS, pancreatic steatosis; TSS, total severity score.

incide with the first two groups. Of the 210 patients with HS, PS, or both, 59 (28.09%) had only HS, 106 (50.47%) had only PS, and 45 (21.42%) had both. The comparisons of the three groups of patients with only HS, only PS, and both according to the parameters in patients with HS and/or PS are presented in Tables 4, 5. In this study, the median age was found to be 65.5 years in patients with only PS, which was higher than the median ages (53 and 57 years) determined in the other groups ($P < 0.001$). The rate of HT was also demonstrated as 62.3% in patients with PS, which was higher than the rates (42.4% and 42.2%) determined in the other groups ($P = 0.015$). The TSS medians were 5, 6, and 7 in the patients with only HS, only PS, and both, revealing the TSS of the group with coexisting HS and PS to be significantly higher than those of the other two groups ($P < 0.001$). The other parameters were not significant between the groups.

Discussion

This research determines that HS, PS, and coexisting HS and PS are related to TSS and

Table 3. Age-standardized odds ratios for PS according to comorbidities, hospitalization, intubation, mortality rates, and unstandardized B value for PS according to TSS

	Odds ratio (95% CI) and *P* value
DM	**1.81 (1.06–3.10), *P* = 0.029***
HT	1.53 (0.92–2.55), *P* = 0.097
CAD	1.81 (0.86–3.79), *P* = 0.115
CVD	3.95 (0.31–50.17), *P* = 289
TSS‡	**1.04 (0.43–1.66), *P* = 0.001***
Hospitalization	**1.70 (1.07–2.72), *P* = 0.024***
Intubation	1.01 (0.37–2.73), *P* = 979
Mortality	0.62 (0.16–2.34), *P* = 0.486

*Statistically significant values (*P* < 0.05 was used as the significance level). ‡Unstandardized B value is expressed for TSS. CAD, coronary artery disease; CVD, cerebrovascular disease; DM, diabetes mellitus; HT, hypertension; PS, pancreatic steatosis; CI, confidence interval; TSS, total severity score.

Table 4. Comparisons of the three groups of patients with only HS, only PS, and both according to age, sex, and comorbidities from a total of 210 patients with HS and/or PS

	Age (years)	Sex (male)	Sex (female)	DM +	DM –	HT +	HT –	CAH +	CAH –	CVD +	CVD –
HS + (n = 59)	53 (23–87)	33 (55.9%)	26 (44.1%)	16 (27.1%)	43 (72.9%)	25 (42.4%)	34 (57.6%)	9 (15.3%)	50 (84.7%)	1 (1.7%)	58 (98.3%)
PS + (n = 106)	**65.5 (31–91)**	56 (52.8%)	50 (47.2%)	35 (33.0%)	71 (67.0%)	**66 (62.3%)**	40 (37.7%)	25 (23.6%)	81 (76.4%)	3 (2.8%)	103 (97.2%)
Coexisting HS and PS + (n = 45)	57 (35–85)	28 (62.2%)	17 (37.8%)	18 (40.0%)	27 (60.0%)	19 (42.2%)	26 (57.8%)	6 (13.3%)	39 (86.7%)	0 (0%)	45 (100%)
P	**<0.001***	0.568		0.382		**0.015***		0.232		0.812‡	

Numeric parameters are expressed as medians. *Statistically significant values (*P* < 0.05 was used as the significance level). ‡Fisher–Freeman–Halton test was used. CAD, coronary artery disease; CVD, cerebrovascular disease; DM, diabetes mellitus; HS, hepatic steatosis; HT, hypertension; PS, pancreatic steatosis.

Table 5. Comparisons of the three groups of patients with only HS, only PS, and both according to TSS, hospitalization, intubation, and mortality rates from a total of 210 patients with HS and/or PS

	TSS	Hospitalization +	Hospitalization –	Intubation +	Intubation –	Mortality +	Mortality –
HS + (n = 59)	5 (0–16)	32 (54.2%)	27 (45.8%)	6 (10.2%)	53 (89.8%)	3 (5.1%)	56 (4.9%)
PS + (n = 106)	6 (0–17)	65 (61.3%)	41 (38.7%)	11 (10.4%)	95 (89.6%)	7 (6.6%)	99 (93.4%)
Coexisting HS and PS + (n = 45)	**7 (0–15)**	33 (73.3%)	12 (26.7%)	3 (6.7%)	42 (93.3%)	2 (4.4%)	43 (95.6%)
P	**<0.001***	0.137		0.762		0.929‡	

Numeric parameters are expressed as medians. *Statistically significant values (*P* < 0.05 was used as the significance level). ‡Fisher–Freeman–Halton test was used. HS, hepatic steatosis; PS, pancreatic steatosis; TSS, total severity score.

the requirement for hospitalization. However, PS alone was correlated with the requirement for intubation and mortality rates in patients with COVID-19. In addition, TSS, hospitalization, and DM were significant in patients with PS when age-standardized analyses were conducted for PS. Furthermore, the contrast between patients with only HS, only PS, and both using an analysis of variance revealed that patients that only had PS had a higher age and level of HT, whereas patients with both PS and HS had a higher TSS.

Visceral steatosis can affect the overall outcome of diseases. For instance, in hemochromatosis and hepatitis C virus infections, having HS influences the progression of the fibrotic changes in the liver.[19,20] Moreover, infections in organs other than those where the steatosis originated can be affected. For example, research indicates that non-alcoholic fatty liver disease is associated with increased mortality in patients with community-acquired pneumonia.[21] In the present study, we hypothesized that steatosis of the GI organs could aggravate COVID-19 outcomes, considering its effects on human metabolism and its concomitant nature with obesity. There is a gap in the literature in this respect in relation to some of the GI organs. Although previous research has revealed that HS is a factor that worsens the outcomes of patients with COVID-19,[3,4,7,9] the gap is more evident in the research on PS and COVID-19. Furthermore, PS does not need to be a single steatotic entity but can co-occur with HS. Hence, we chose the three main groups of focus to be patients with COVID-19 with HS, PS, and both in our study.

The prevalence of HS and PS in patients with COVID-19 was 22.5% and 32.7%, respectively. In line with our study, previous studies have reported the rates of HS in patients with COVID-19 as 25.6–30%, and the global prevalence of HS has been stated as 25.4%.[7,8] In a case–control study,[16] PS assessed through CT was found in 71.9% and 45.3% of the prediagnostic pancreatic ductal adenocarcinoma cases and controls, respectively, identifying a relatively high rate of PS even in the healthy control participants. Although a limited number of studies have been conducted, we believe that the prevalence of PS may be higher than the prevalence of HS.

In a study by Guneyli et al.[15], PS accounted for approximately one third of patients with COVID-19 pneumonia. They also reported that PS correlated with clinical severity and hospitalization in all patients with COVID-19 pneumonia.[15] In the present study, we found that patients with PS presented with higher TSS and hospitalization rates, and intubation and mortality rates were significant in patients with PS in all 461 patients. In comparison, PS did not correlate with intubation and mortality in the 201 hospitalized patients with COVID-19 included in the study by Guneyli et al.[15], possibly because of the small number of intubations and low death rates.

Initially, we investigated the three groups according to their relationships with epidemiologic data. Older age exhibited a substantial correlation in patients with PS and with coexisting HS and PS. Although those with HS lacked this connection with age, this group correlated with the male sex. It was also crucial to compare the essential manifestations of the metabolic syndrome among the patients in this study, as these comorbidities have previously proven to worsen the COVID-19 diagnosis.[12] In this study, PS became more prominent because its existence in a patient with COVID-19 was correlated with DM, HT, and CAD. A correlation between DM and having HS and both PS and HS was also noted. However, CVD was not associated with any of the three groups. Previously, Singh and Khan[11] conducted an extensive multicentered study of 250 patients with COVID-19, and liver disease predominantly comprised of HS. They demonstrated that pre-existing liver disease was associated with older age and comorbidities such as HT and DM. Among the other studies focusing on HS, Çoraplı et al.[7] noted that HS did not correlate with older age or sex. In contrast with our study, Chen et al.[3] demonstrated that although younger age was correlated with HS, sex, HT, and DM had no association with this condition. Additionally, Forlano et al.[8] found that the median age was higher in patients with COVID-19 without HS than in those with HS. However, sex and comorbidities were not correlated with HS in the same study.

To clarify the relationship between these three groups of steatosis and COVID-19 prognosis, we used four parameters for comparison: TSS and the presence of hospitalization, intubation, and mortality. TSS was notably detected in direct proportion to all three groups of steatoses, thus supporting the hypothesis that PS, HS, and coexisting PS and HS are factors that exacerbate COVID-19 severity. This correlation also existed for the presence of hospitalization in all three groups. Subsequently, intubation was correlated with only the presence of PS. However, no correlation was uncovered between intubation and HS or the coexistence of the two steatoses. Finally, mortality rates followed a similar pattern; mortality exhibited a significant change of 4.4% only with PS. The significant correlation between intubation and mortality with only PS may be because PS is a more specific prognostic factor in patients with COVID-19 than HS or coexisting HS and PS. Furthermore, the concept of PS being a more specific prognostic factor can also be affiliated with the presence of metabolic syndrome. Singh and Khan[11] demonstrated higher hospitalization and mortality rates among patients with pre-existing liver disease (predominantly HS) and COVID-19. Among the studies focusing more specifically on HS and COVID-19, Parlak et al.[10] had similar results to ours in terms of severity after investigating CT findings indicating that severity, such as upper lobar involvement and paving pattern lung lesions, was more common in patients with a fatty liver. Compared with this and other similar studies, our research uses an even more tangible severity indicator, TSS.[13,14] Çoraplı et al.[7], who also focused only on HS, found that HS was notably correlated with TSS and hospitalization rates. Furthermore, Chen et al.[3] demonstrated that HS was correlated with intubation rates, whereas mortality rates were inversely correlated with HS. Furthermore, Forlano et al.[8] revealed that higher mortality was not associated with patients with COVID-19 having fatty liver disease.

When the effect of age was eliminated following the initial comparisons, hospitalization was 1.7 times greater, and TSS was higher in the patients with PS than in those without PS. This validates the view that severe disease is more commonly demonstrated in patients with PS. Although intubation and mortality rates did not correlate with PS in these analyses, a significant correlation of PS with hospitalization and TSS would potentially contribute to the management of patients with COVID-19 pneumonia. Among the comorbidities, only the presence of DM was more commonly seen in patients with PS, which can be expected during DM.

Several studies have reported that increased age, cardiometabolic risk factors, and comorbidities lead to a poor prognosis in patients with COVID-19, and HS is considered part of metabolic syndrome.[3,4,7-12] Although the underlying mechanisms of HS indicate that patients with HS are more susceptible to severe COVID-19 than those without HS, some factors are considered contributing factors to the severity of the disease. First, HS can accompany DM, increasing the risk and severity of infection. Second, the prevalence of cardiovascular and pulmonary diseases, in which an impaired patient response tends to occur, is higher among patients with HS than among those without HS. Finally, the cytokine storm appears to be the main culprit behind severe disease and high mortality rates in these patients.[8] Forlano et al.[8] reported that patients with HS presented with higher levels of C-reactive protein than those without HS. They also demonstrated that in patients with HS, the survival rates were lower in those who presented with higher inflammatory markers (ferritin, prothrombin time, and lactate dehydrogenase) than in those with lower inflammatory markers. Interleukin-6 levels and the production of proinflammatory cytokines, such as tumor necrosis factor-alpha from Kupffer cells that have negative impacts on infectious diseases, were also found to be increased in patients with COVID-19 with HS.[7] PS, also known to be a risk factor for metabolic syndrome, is thought to allow mechanisms similar to HS to occur, resulting in a poor prognosis.[17]

The groups with HS and/or PS were also compared to fully understand their role in the disease. To this end, the number of patients corresponding to the earlier parameters was analyzed again in each group. However, this time, the groups did not overlap, meaning that each patient with one of the types of steatoses was not included in the coexisting group. Age was the only substantial parameter for the epidemiological parameters, as patients with only PS were significantly older than those in the other two groups. Similarly, for the comorbidities, patients with only PS exhibited higher percentages of HT than those with only HS or both.

Moreover, TSS was the only parameter that demonstrated a significant difference in terms of severity factors, as patients with coexisting HS and PS had a higher TSS than the other two groups. This finding must be emphasized because a higher TSS has been observed previously in patients with and without HS, PS, or both. The fact that a higher TSS is the only severity factor that exceeds the number of patients with coexisting HS and PS demonstrates that this coexistence is a potentially helpful prognostic parameter for COVID-19. In this study, the lack of substantial correlations between the three groups and the prognostic parameters except TSS can be attributed to the low numbers of patients, especially for those who were deceased or intubated. As the literature lacks extensive research on this matter, we could not compare these final findings with existing data.

This study has several limitations. First, the study was retrospective and conducted in a single center. Second, the baseline chest CT findings for the patients were not considered in our study; some might have overlapped with the chest CT findings attributed to COVID-19 pneumonia. Third, the disease course at the time of CT varied among patients, and CT images with the highest TSS were considered for patients who underwent multiple CT examinations. However, this affected only six patients, making the possible effect of this issue minimal in the study. Some of the routine chest CTs we reviewed did not cover the entire pancreas in several patients, making the sample size smaller, and coverage may lead to increased radiation doses. In addition, HS can be visually evaluated in most patients on CT, whereas density measurements are required in nearly all patients during the evaluation of PS through CT, which may not be routinely feasible in all patients in busy radiology departments. Additionally, the degree of HS was not considered in our study. As another limitation, the HU values of the pancreas were obtained with the consensus of two radiologists. Finally, HS can have a geographical appearance that can affect density measurements, and the assessment of HS and PS based on histopathologic specimens can be more accurate than that assessed on CT. However, using ≥4 ROIs in the liver and pancreas rendered more accurate assessments.

In conclusion, the unenhanced chest CT imaging of COVID-19 patients allows the assessment of HS and PS without difficulty. These two conditions, both separately and together, are vital tools for understanding the severity of COVID-19. The presence of HS, PS, and their coexistence have been demonstrated to play a role in TSS and hospitalization rates. Furthermore, PS is correlated with intubation and mortality rates among patients with COVID-19. Age-standardized analyses for PS revealed that TSS, hospitalization, and DM were statistically meaningful in individuals with PS. Patients with only HS, only PS, or HS and PS together were compared, with the TSS being the greater among patients with coexisting HS and PS, making this coexistence a possible prognostic factor. Future investigations with larger sample sizes may reveal any probable links by comparing other prognostic features of COVID-19 with HS, PS, or both.

Conflict of interest disclosure

The authors declare no conflicts of interest.

References

1. WHO Coronavirus (COVID-19) Dashboard. World Health Organization. Updated 20 June 2022. Accessed 26 June 2022. [CrossRef]
2. Sarin SK, Choudhury A, Lau GK, et al. Pre-existing liver disease is associated with poor outcome in patients with SARS CoV2 infection; The APCOLIS Study (APASL COVID-19 Liver Injury Spectrum Study). *Hepatol Int*. 2020;14(5):690-700. [CrossRef]
3. Chen VL, Hawa F, Berinstein JA, et al. Hepatic steatosis is associated with increased disease severity and liver injury in coronavirus disease-19. *Dig Dis Sci*. 2021;66(9):3192-3198. [CrossRef]
4. Mahamid M, Nseir W, Khoury T, et al. Nonalcoholic fatty liver disease is associated with COVID-19 severity independently of metabolic syndrome: a retrospective case-control study. *Eur J Gastroenterol Hepatol*. 2021;33(12):1578-1581. [CrossRef]
5. Cichoż-Lach H, Michalak A. Liver injury in the era of COVID-19. *World J Gastroenterol*. 2021;27(5):377-390. [CrossRef]
6. Chen F, Dai Z, Huang C, Chen H, Wang X, Li X. Gastrointestinal disease and COVID-19: a review of current evidence. *Dig Dis*. 2022;40(4)506-514. [CrossRef]
7. Çoraplı M, Çil E, Oktay C, Kaçmaz H, Çoraplı G, Bulut HT. Role of hepatosteatosis in the prognosis of COVID 19 disease. *Clin Imaging*. 2021;80:1-5. [CrossRef]
8. Forlano R, Mullish BH, Mukherjee SK, et al. In-hospital mortality is associated with inflammatory response in NAFLD patients admitted for COVID-19. *PLoS One*. 2020;15(10):e0240400. [CrossRef]
9. Palomar-Lever A, Barraza G, Galicia-Alba J, et al. Hepatic steatosis as an independent risk factor for severe disease in patients with COVID-19: A computed tomography study. *JGH Open*. 2020;4(6):1102-1107. [CrossRef]
10. Parlak S, Çıvgın E, Beşler MS, Kayıpmaz AE. The effect of hepatic steatosis on COVID-19 severity: chest computed tomography findings. *Saudi J Gastroenterol*. 2021;27(2):105-110. [CrossRef]
11. Singh S, Khan A. Clinical characteristics and outcomes of coronavirus disease 2019 among patients with preexisting liver disease in the united states: a multicenter research network study. *Gastroenterology*. 2020;159(2):768-771.e3. [CrossRef]
12. Zheng KI, Gao F, Wang XB, et al. Letter to the Editor: Obesity as a risk factor for greater severity of COVID-19 in patients with metabolic associated fatty liver disease. *Metabolism*. 2020;108:154244. [CrossRef]
13. Li K, Fang Y, Li W, et al. CT image visual quantitative evaluation and clinical classification of coronavirus disease (COVID-19). *Eur Radiol*. 2020;30(8):4407-4416. [CrossRef]
14. Yang R, Li X, Liu H, et al. Chest CT severity score: an imaging tool for assessing severe COVID-19. *Radiology Cardiothoracic Imaging*. 2020;2(2):e200047. [CrossRef]
15. Guneyli S, Dogan H, Esengur OT, Hassoy H. Computed tomography evaluation of pancreatic steatosis: correlation with COVID-19 prognosis. *Future Virol*. 2022;17(4):231-237. [CrossRef]
16. Hoogenboom SA, Bolan CW, Chuprin A, et al. Pancreatic steatosis on computed tomography is an early imaging feature of pre-diagnostic pancreatic cancer: a preliminary study in overweight patients. *Pancreatology*. 2021;21(2):428-433. [CrossRef]
17. Lee JS, Kim SH, Jun DW, et al. Clinical implications of fatty pancreas: correlations between fatty pancreas and metabolic syndrome. *World J Gastroenterol*. 2009;15(15):1869-1875. [CrossRef]
18. Fukuda Y, Yamada D, Eguchi H, et al. CT density in the pancreas is a promising imaging predictor for pancreatic ductal adenocarcinoma. *Ann Surg Oncol*. 2017;24(9):2762-2769. [CrossRef]
19. Westin J, Nordlinder H, Lagging M, Norkrans G, Wejstål R. Steatosis accelerates fibrosis development over time in hepatitis C virus genotype 3 infected patients. *J Hepatol*. 2002;37(6):837-842. [CrossRef]
20. Cross TJ, Quaglia A, Hughes S, Joshi D, Harrison PM. The impact of hepatic steatosis on the natural history of chronic hepatitis C infection. *J Viral Hepat*. 2009;16(7):492-499. [CrossRef]
21. Nseir WB, Mograbi JM, Amara AE, Abu Elheja OH, Mahamid MN. Non-alcoholic fatty liver disease and 30-day all-cause mortality in adult patients with community-acquired pneumonia. *Qjm*. 2019;112(2):95-99. [CrossRef]

Diagn Interv Radiol 2023; DOI: 10.4274/dir.2023.232299

ABDOMINAL IMAGING

ORIGINAL ARTICLE

Copyright@Author(s) - Available online at dirjournal.org.
Content of this journal is licensed under a Creative Commons Attribution-NonCommercial 4.0 International License.

Chemotherapy-associated liver morphological changes in hepatic metastases (CALMCHeM)

Matthew C. Pope
Michael C. Olson
Kristina T. Flicek
Neema J. Patel
Candice W. Bolan
Christine O. Menias
Zhen Wang
Sudhakar K. Venkatesh

PURPOSE

To review imaging findings in chemotherapy-associated liver morphological changes in hepatic metastases (CALMCHeM) on computed tomography (CT)/magnetic resonance imaging (MRI) and its association with tumor burden.

METHODS

We performed a retrospective chart review to identify patients with hepatic metastases who received chemotherapy and subsequent follow-up imaging where CT or MRI showed morphological changes in the liver. The morphological changes searched for were nodularity, capsular retraction, hypodense fibrotic bands, lobulated outline, atrophy or hypertrophy of segments or lobes, widened fissures, and one or more features of portal hypertension (splenomegaly/venous collaterals/ascites). The inclusion criteria were as follows: a) no known chronic liver disease; b) availability of CT or MRI images before chemotherapy that showed no morphological signs of chronic liver disease; c) at least one follow-up CT or MRI image demonstrating CALMCHeM after chemotherapy. Two radiologists in consensus graded the initial hepatic metastases tumor burden according to number (≤10 and >10), lobe distribution (single or both lobes), and liver parenchyma volume affected (<50%, or ≥50%). Imaging features after treatment were graded according to a pre-defined qualitative assessment scale of "normal," "mild," "moderate," or "severe." Descriptive statistics were performed with binary groups based on the number, lobar distribution, type, and volume of the liver affected. Chi-square and t-tests were used for comparative statistics. The Cox proportional hazard model was used to determine the association between severe CALMCHeM changes and age, sex, tumor burden, and primary carcinoma type.

RESULTS

A total of 219 patients met the inclusion criteria. The most common primaries were from breast (58.4%), colorectal (14.2%), and neuroendocrine (11.0%) carcinomas. Hepatic metastases were discrete in 54.8% of cases, confluent in 38.8%, and diffuse in 6.4%. The number of metastases was >10 in 64.4% of patients. The volume of liver involved was <50% in 79.8% and ≥50% in 20.2% of cases. The severity of CALMCHeM at the first imaging follow-up was associated with a larger number of metastases ($P = 0.002$) and volume of the liver affected ($P = 0.015$). The severity of CALMCHeM had progressed to moderate to severe changes in 85.9% of patients, and 72.5% of patients had one or more features of portal hypertension at the last follow-up. The most common features at the final follow-up were nodularity (95.0%), capsular retraction (93.4%), atrophy (66.2%), and ascites (65.7%). The Cox proportional hazard model showed metastases affected ≥50% of the liver ($P = 0.033$), and the female gender ($P = 0.004$) was independently associated with severe CALMCHeM.

CONCLUSION

CALMCHeM can be observed with a wide variety of malignancies, is progressive in severity, and the severity correlates with the initial metastatic liver disease burden.

KEYWORDS

Liver metastases, pseudocirrhosis, liver tumor burden

From the Department of Radiology, Division of Abdominal Imaging (M.C.P., M.C.O., K.T.F., S.K.V. ✉venkatesh. sudhakar@mayo.edu), Mayo Clinic, Minnesota, USA; Department of Radiology, Division of Abdominal Imaging (N.J.P., C.W.B.), Mayo Clinic, Florida, USA; Department of Radiology, Division of Abdominal Imaging (C.O.M.), Mayo Clinic, Arizona, USA; Department of Biostatistics (Z.W.), Mayo Clinic, Minnesota, USA.

Received 09 May 2023; revision requested 16 May 2023; accepted 30 May 2023.

Epub: 13.06.2023

Publication date: 21.07.2023

DOI: 10.4274/dir.2023.232299

You may cite this article as: Pope MC, Olson MC, Flicek KT, et al. Chemotherapy-associated liver morphological changes in hepatic metastases (CALMCHeM). *Diagn Interv Radiol.* 2023;29(4):571-578.

In recent decades, the number of chemotherapeutic and biological agents employed to treat hepatic metastatic disease has increased exponentially and has resulted in prolonged survival, particularly in metastatic breast cancers.[1] Many of these cytotoxic medications are metabolized in the liver, and systemic chemotherapy-induced hepatotoxicity is a well-recognized complication of treatment, with a spectrum ranging from an asymptomatic elevation of liver enzymes to acute hepatitis.[2,3] The pathological modes of systemic chemotherapy-associated liver injury can be steatosis, chemotherapy-associated steatohepatitis (CASH), and sinusoidal obstruction syndrome (SOS), and these specific changes are related to metabolic byproducts of the agents used.[4]

A specific form of hepatic injury occurs only in the presence of hepatic metastatic disease and in association with systemic chemotherapy.[5-9] This injury possibly results from a desmoplastic reaction surrounding the chemotherapy-treated tumors, repeated tumor shrinkage and enlargement, and reactive nodular parenchymal regeneration following treatment.[10] When progressive, it leads to a scarred and contracted liver that simulates cirrhosis and may be complicated by portal hypertension and ascites.[6] This unique condition was first described as hepatic lobatum carcinomatosum in 1987 by Honma[11] in a case of scirrhous breast carcinoma. Subsequently, this entity was described in several case reports and case series as pseudocirrhosis,[5,7,9,12,13] and the term was applied to describe a constellation of liver findings: fine, diffuse nodularity of the liver surface, multifocal retraction of the hepatic capsule, and caudate lobe enlargement. However, in histopathological specimens, there was a characteristic absence of regenerating nodules and bridging fibrosis, which is typically found in cirrhosis from chronic liver disease.[5,7,9,12,13]

For lack of a better term, non-specific "pseudocirrhosis" continues to be used to describe not only this unique injury but also many other pathologic processes that occur in the liver, such as untreated diffuse hepatic metastases, granulomatous diseases like sarcoidosis and tertiary syphilis, chronic Budd–Chiari syndrome, chronic portal vein thrombosis, schistosomiasis, non-cirrhotic portal hypertension, and nodular regenerative hyperplasia.[13-15] Emerging evidence suggests that pseudocirrhosis may be a misnomer, as many of these patients develop sequelae of portal hypertension, including splenomegaly, formation of portosystemic collaterals, and ascites.

While the imaging and clinical picture may be similar to cirrhosis, the pathologic changes that only occur in post-chemotherapy hepatic metastatic disease could be more properly termed chemotherapy-associated liver parenchymal changes in hepatic metastases (CALMCHeM). CALMCHeM characteristically has normal liver parenchyma between fibrotic bands and no known association with chronic liver disease etiologies. Normal liver function is maintained until late or severe changes occur.

CALMCHeM has mostly been described in breast carcinoma metastatic disease, with few case reports on other primaries.[16-19] Previous studies have described the incidence, prevalence, risk factors, and natural history progression of CALMCHeM and mostly focused on breast carcinoma.[7,9,20] The purpose of our study was to characterize the baseline tumor burden and imaging appearances of CALMCHeM among a broader spectrum of malignancies and evaluate its temporal progression of severity.

Main points

- Chemotherapy-associated liver morphological changes in hepatic metastases (CALMCHeM) can be observed in a wide variety of malignancies.
- CALMCHeM occurs only in the presence of hepatic metastases and following systemic chemotherapy.
- CALMCHeM severity correlates with the metastatic liver disease burden.
- Metastatic liver disease burden is associated with the development of portal hypertension.
- CALMCHeM severity progresses over time and requires follow-up for detection of the development of complications.

Methods

Study cohort

In this Health Insurance Portability and Accountability-compliant, single-institute, multisite retrospective study, we conducted a systematic search of electronic medical records to identify patients with potential imaging features of CALMCHeM. The Institution of Mayo Clinic's Review Board approved the retrospective study (reference: IRB 12-009433) with the waiver of informed consent for its retrospective nature. A proprietary search engine was used to analyze radiology reports from 1995 to 2020. The search matrix included various combinations of the terms "pseudocirrhosis," "metastases," "liver/hepatic," "cirrhosis," "fibrosis," and "nodular contour/nodularity." The more general descriptors in the search were included due to the relatively inconsistent use of "pseudocirrhosis" in clinical notes to describe features of CALMCHeM.

The inclusion criteria were as follows: a) no known chronic liver disease; b) the presence of hepatic metastases on imaging; c) the availability of a contrast-enhanced computed tomography (CT) or magnetic resonance imaging (MRI) image before chemotherapy that showed no morphological signs of chronic liver disease; d) at least one follow-up CT or MRI image demonstrating CALMCHeM after chemotherapy.

The exclusion criteria included adjunctive chemotherapy associated with surgical resection and/or ablation therapy, percutaneous ablation therapy, chemoembolization, and directed radiation therapy due to the potential for confounding morphologic changes that could occur following these treatments. Patients with known chronic liver disease were excluded, as fibrotic or cirrhotic changes can coexist.

Data collection and analysis

Before the radiologists responsible for analyzing the images began data collection, they participated in an online training session to familiarize themselves with the definitions and grading systems used in the study. Following the training session, imaging studies (CT and/or MRI) were reviewed by two radiologists in consensus at all three sites. The burden of hepatic metastases in each case was quantified according to a predetermined grading system (Table 1) that included the number of metastatic lesions (1–5, 6–10, >10), and the estimated volume of the liver affected (0%–25%, >25%–50%, and ≥50%). The qualitative parameters, such as the distribution of lesions [single lobe (right or left) and both lobes] and lesion morphological characteristics (discrete, diffuse, or confluent) were also recorded (Table 1). Follow-up CT and MRI scans performed after treatment initiations were then evaluated sequentially.

Imaging features were graded according to a qualitative assessment scale including "minimal," "mild," "moderate," or "severe" CALMCHeM changes (Table 2), relative to the baseline study (Figure 1). Assessed features included capsular retraction, nodularity, lobulations parenchymal atrophy or hyper-

trophy, widened fissures, splenomegaly, portosystemic collaterals, and ascites. Patients were considered to manifest mild, moderate, or severe changes when one or more features listed in Table 2 were present. Capsular retraction was defined as the focal indentation of the hepatic capsule below the adjacent normal contour of the liver. All follow-up CT/MRI studies were evaluated. The time interval between studies that demonstrated new changes and resulted in the upgrading of the severity score was recorded for a maximum of four follow-up examinations. Therefore, the time intervals for CALMCHeM changes from minimal to mild, mild to moderate, and moderate to severe were recorded. Patient demographics, primary malignancy type, chemotherapeutic agents, and the time interval between changes in CALMCHeM severity were recorded for each case.

Statistical analysis

Descriptive statistics were performed to characterize patient demographics, primary cancer types, and general CALMCHeM feature frequencies. The baseline metastases characteristics into binary groups for each of the following characteristics: number (≤10 and >10), lobar distribution (single or both lobes), type (discrete vs. diffuse or confluent), and volume of the liver affected (<50% vs. ≥50%). Chi-square and t-tests were used for comparative statistics of imaging features at various time points. After the initial analysis of all tumor types, only the four most common primaries were considered for regression analysis, as there were few representative cases in other primaries. Similarly, chemotherapeutic agents were not included in the regression analysis, as different agents and different combinations were used for patients in the study group. The Cox proportional hazard model was used to determine the association between severe CALMCHeM changes and age, sex, tumor burden, and primary carcinoma type. Schoenfeld residuals tests found no violation of the proportional hazard assumption for the Cox model. All statistical analyses were performed using Stata/SE version 16.1 (StataCorp LLC, College Station, TX).

Table 1. Hepatic metastases characteristics at baseline CT or MRI

Characteristic	Classification
Number of metastases	1–5 6–10 >10
Lobar distribution	Right lobe Left lobe Both lobes
Liver volume affected	0%–25% >25%–50% ≥50%
Morphology	• Discrete-with intervening normal liver parenchyma • Confluent-multiple coalescing or fusing without intervening liver parenchyma between the metastasis nodules at one or more locations • Diffuse-multiple tiny nodules with barely visible intervening liver parenchyma

CT, computed tomography; MRI, magnetic resonance imaging.

Table 2. Severity grading of CALMCHeM

Grade	Description
Minimal	Perfusion changes around the metastases
Mild	Mild retraction of capsule Hypodense bands around or replacing metastases No volume loss
Moderate	Retraction of capsule Hypodense bands Nodularity of surface Lobulated liver Mild volume loss (atrophy) compared to prior or baseline study
Severe	Nodularity and lobulated outline of the liver Loss of liver volume Atrophy of segments or lobes Compensatory hypertrophy Widened fissures

CALMCHeM, chemotherapy-associated liver morphological changes in hepatic metastases.

Results

Study cohort

The search results yielded 1,288 patients who met the initial eligibility requirements. The final number of unique patients meeting the inclusion criteria was 219. There were 62 (28.3%) males and 157 (71.7%) females in the cohort, with a mean ± standard deviation (SD) age of 61.4 ± 11.4 years. The most common primary malignancy included breast carcinoma (58.4%), colorectal carcinoma (14.2%), neuroendocrine carcinoma (11.0%), pancreatic adenocarcinoma (3.7%), and cholangiocarcinoma (3.2%). The complete list of primary malignancies is shown in Table 3. The chemotherapeutic agents are summarized in Supplementary Table 1. The mean ± SD duration of follow-up was 695 ± 608.5 days. The most common baseline imaging modality was CT in 213/219 (95.9%) cases, with only six patients having MRI as the baseline imaging modality. CT was also the most common follow-up imaging modality, with only one patient having MRI for three follow-up studies and four patients having only one MRI study during their follow-up.

Baseline imaging findings prior to chemotherapy initiation

Hepatic metastases were discrete in 120/219 cases (54.8%), confluent in 85/219 cases (38.8%), and diffuse in 14/219 cases (6.4%). The metastases were present in both liver lobes in 179/219 cases (81.7%), the right hepatic lobe only in 26/219 cases (11.9%), and in the left hepatic lobe only in 14/219 cases (6.4%). The number of hepatic metastases was >10 in 141/219 cases (64.4%), 6–10 in 23/219 cases (10.5%), and 1–5 in 55/219 cases (25.1%). The volume of the liver affected by metastases was <25% in 115/219 cases (52.5%), >25% to 50% in 59/219 cases (26.9%), and ≥50% in 45/219 cases (20.5%).

CALMCHeM findings

At the first CT or MRI follow-ups where all cases showed CALMCHeM, minimal changes were seen in 16%, mild changes in 58%, moderate changes in 19.2%, and severe changes in only 6.8%. However, at the final follow-up, severe changes were seen in 54.8% of patients, moderate changes in 31.1%, mild changes in 11.9%, and minimal changes in only 2.3%. CALMCHeM at final follow-up included a nodular surface contour in 209/219 (95.4%), focal capsular retraction in 206/219 (94.1%), parenchymal atrophy for 146/219 (66.7%), ascites in 144/219 (65.8%),

widened fissures for 98/219 (44.7%), portosystemic collaterals in 91/219 (41.6%), caudate lobe hypertrophy for 81/219 (37%), and splenomegaly in 56/219 (25.6%). Severe CALMCHeM significantly correlated with collaterals ($P = 0.001$), splenomegaly ($P = 0.014$), and ascites ($P = 0.001$).

Temporal progression in CALMCHeM

There was a progression in the severity of CALMCHeM over time, and this correlated with baseline metastatic disease burden (Figure 2). At the first follow-up, only 6.8% had severe CALMCHeM, which increased to 54.8% at the final follow-up. Among the patients who developed severe CALMCHeM, those with ≥50% liver volume metastatic disease did so earlier than those with <50% volume of the liver affected (370 days vs. 592 days, $P = 0.012$). Similarly, those with confluent or diffuse metastases reached severe CALMCHeM changes significantly earlier than those with discrete metastases (403 days vs. 713 days, $P = 0.013$). Although patients with >10 metastases (430 days vs. 676 days, $P = 0.322$) and bilobar distribution (460 days vs. 584 days, $P = 0.847$) showed a trend to early severe changes, the differences were not statistically significant.

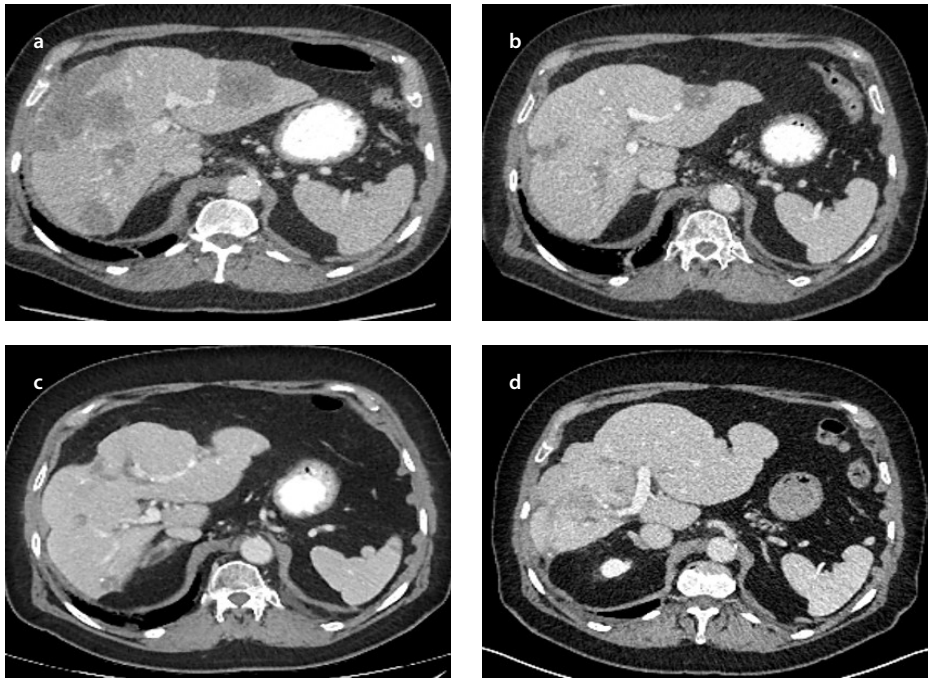

Figure 1. Temporal progression of CALMCHeM in a 72-year-old male with rectal carcinoma and multiple liver metastases. Contrast-enhanced CT images **(a)** before chemotherapy, **(b)** at 3 months, **(c)** at 8 months, and **(d)** at 10 months following systemic chemotherapy (including FOLFOX and bevacizumab). The hepatic metastases were >10 in number, involved both liver lobes, and affected ≥50% of the liver parenchyma. The CALMCHeM changes are mild at 3 months, with retraction of the capsule and some nodularity that progresses to moderate changes at 8 months with a lobulated outline and some atrophy of the right lobe. At 10 months, the changes are severe with significant atrophy of the right lobe and compensatory hypertrophy of the left lobe. CALMCHeM, chemotherapy-associated liver morphological changes in hepatic metastases; CT, computed tomography; FOLFOX, folinic acid, fluorouracil, and oxaliplatin.

Table 3. Primary malignancies in the study group (n = 219)

Primary malignancy	Number	%
Breast carcinoma	128	58.4
Colorectal carcinoma	31	14.2
Neuroendocrine	24	11.0
Pancreatic adenocarcinoma	8	3.7
Cholangiocarcinoma	7	3.2
Gastroesophageal carcinoma	4	1.8
Prostate carcinoma	4	1.8
Lung carcinoma	3	1.4
Leiomyosarcoma	2	1.0
Melanoma	2	1.0
Renal cell carcinoma	2	1.0
Urothelial carcinoma	1	0.5
Thyroid carcinoma	1	0.5
Unknown adenocarcinoma	1	0.5
Parotid carcinoma	1	0.5

Association of tumor burden at baseline with CALMCHeM severity

The proportion of severe changes at the final follow-up was significantly associated with >10 metastases ($P = 0.009$), bilobar distribution ($P = 0.001$), and ≥50% volume of the liver affected ($P = 0.001$). There was no significant association with the morphologic type of metastases. We further evaluated the associations with the four largest metastatic disease types in the study group. This group comprised four main primary carcinomas (breast, colorectal, neuroendocrine, and pancreatic) and a total of 183 cases. Severe changes at the final follow-up were significantly associated with bilobar distribution ($P = 0.006$) and the volume of the liver affected ($P = 0.011$), but not significantly associated with the number or morphologic types of metastases (Table 4, Figure 3). Cox regression analysis was performed in this group and showed that the proportion of cases with severe changes at the final follow-up was significantly associated with the female sex (hazard ratio: 0.46, $P = 0.004$) and volume of the liver affected prior to chemotherapy (hazard ratio: 1.88, $P = 0.033$) (Table 5).

Association of baseline findings with specific CALMCHeM features

Patients with a higher tumor volume at initial presentation had a significantly higher proportion of developed collaterals and splenomegaly. Patients with a ≥50% liver tumor volume, compared to patients with a <50% liver tumor volume, developed more collaterals (64% vs. 37%, $P = 0.001$) and splenomegaly (41% vs. 21%, $P = 0.007$), but there was no difference in ascites (68% vs. 65%, $P = 0.619$). Similarly, patients with >10 metastases, when compared to those with <10 metastases, developed more collaterals (48% vs. 31%, $P = 0.017$) and splenomegaly (30% vs. 16%, $P = 0.017$) but not ascites (66.2% vs. 65%, $P = 0.815$). Patients with bilobar metastases, compared to unilobar metastases,

developed more collaterals (45% vs. 28%, $P = 0.040$) and splenomegaly (28% vs. 13%, $P = 0.042$) but not ascites (67% vs. 63%, $P = 0.632$). Comparing patients with discrete metastases and those with confluent or diffuse metastases, there were no differences in the development of collaterals (40% vs. 44%, $P = 0.5$), splenomegaly (29% vs. 22%, $P = 0.196$), or ascites (64% vs. 68%, $P = 0.586$).

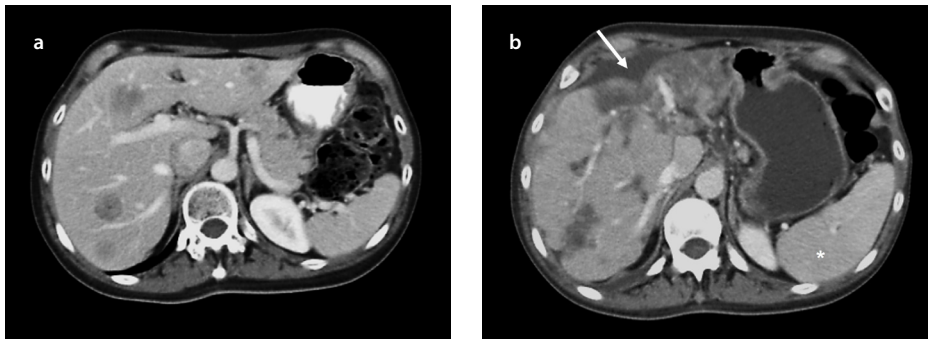

Figure 2. Severe CALMCHeM with portal hypertension. Metastatic infiltrative breast carcinoma in a 52-year-old female with multiple liver metastases. Contrast-enhanced CT images **(a)** before chemotherapy and **(b)** at 23 months following multiple chemotherapy sessions. Severe CALMCHeM changes at 23 months with the development of ascites (white arrow) and splenomegaly (*), consistent with portal hypertension due to CALMCHeM. CALMCHeM, chemotherapy-associated liver morphological changes in hepatic metastases; CT, computed tomography.

Further analyses of the four main cancer types showed similar results. The volume of the liver affected was significantly associated with collaterals ($P = 0.001$) and splenomegaly ($P = 0.032$) but not ascites ($P = 0.652$). Bilobar distribution also showed an association with collaterals ($P = 0.037$) but not splenomegaly ($P = 0.078$) or ascites ($P = 0.294$).

Chemotherapeutic agents and CALMCHeM at the final follow-up

Among the several chemotherapeutic agents used, only the following were significantly associated with severe changes at final follow-up: bevacizumab ($P = 0.038$), cyclophosphamide ($P = 0.022$), docetaxel ($P = 0.019$), doxorubicin ($P = 0.002$), gemcitabine ($P = 0.007$), paclitaxel ($P = 0.027$), and zoledronic acid ($P = 0.046$). When analyzed by the four most common primary malignancy types as a group, significant associations with severe changes were observed

Table 4. Patient characteristics, baseline tumor burden features, and CALMCHeM features at final follow-up in all patients and the four most common primaries

Primary tumor	All (n = 219)	Breast (n = 128)	Colorectal (n = 31)	NET (n = 24)	PDAC (n = 8)
Mean age ± SD (years)	61.4 ± 11.4	61.5 ± 11.8	60.2 ± 11.7	63.3 ± 9.8	63.1 ± 9.4
Male:female	62:157	0:128	21:10	19:5	3:5
Number of metastases					
<10	78 (35.6%)	46 (36%)	8 (25.8%)	3 (12.5%)	4 (50%)
>10	141 (64.4%)	82 (64%)	23 (74.2%)	21 (87.5%)	4 (50%)
Lobar distribution					
Single lobe	179 (81.7%)	25 (19.5%)	2 (6.5%)	0 (0%)	3 (37.5%)
Both lobes	40 (18.3%)	103 (80.5%)	29 (93.5%)	24 (100%)	5 (62.5%)
Volume of the liver affected					
<50%	174 (79.5%)	105 (82%)	20 (64.5%)	18 (75%)	7 (87.5%)
≥50%	45 (20.5%)	23 (18%)	11 (35.5%)	6 (25%)	1 (12.5%)
Type of metastases					
Discrete	120 (54.8%)	74 (57.8%)	14 (45.2%)	13 (54.2%)	6 (75%)
Diffuse/confluent	99 (45.2%)	54 (42.2%)	17 (54.8%)	11 (45.8%)	2 (25%)
Median time to first CALMCHeM (days)	537	155	187	223	214
Median time to severe CALMCHeM (days)	673	493	869	439	430
Capsular retraction	205 (93.6%)	122 (95.3%)	29 (93.5%)	22 (91.7%)	8 (100%)
Surface nodularity/lobulations	208 (95%)	125 (97.7%)	26 (83.9%)	24 (100%)	8 (100%)
Atrophy	145 (66.2%)	91 (71.1%)	15 (48.4%)	20 (83.3%)	7 (87.5%)
Widened fissures	98 (44.75)	66 (51.6%)	10 (32.3%)	12 (50%)	5 (62.5%)
Compensatory hypertrophy	80 (36.5%)	50 (39.1%)	10 (32.3%)	10 (41.7%)	3 (37.5%)
Splenomegaly	55 (25.1%)	28 (21.9%)	13 (41.9%)	4 (16.7%)	1 (12.5%)
Portosystemic collaterals	92 (42%)	50 (39.1%)	13 (41.9%)	11 (45.8%)	5 (62.5%)
Ascites	144 (65.8%)	85 (66.4%)	23 (74.2%)	10 (41.7%)	5 (62.5%)
PHTN	159 (72.6%)	92 (71.8)	26 (83.9%)	13 (54.2%)	6 (75%)
CALMCHeM grade at final follow-up					
Minimal	5 (2.3%)	1 (0.8%)	1 (3.2%)	0 (0%)	0 (0%)
Mild	26 (11.9%)	11 (8.6%)	6 (19.4%)	2 (8.3%)	1 (12.5%)
Moderate	68 (31.1%)	39 (30.5%)	12 (38.7%)	6 (25%)	2 (25%)
Severe	120 (54.8%)	76 (59.4%)	12 (38.7%)	16 (66.7%)	5 (62.5%)

CALMCHeM, chemotherapy-associated liver morphological changes in hepatic metastases; NET, neuroendocrine tumor; PDAC, pancreatic ductal adenocarcinoma; PHTN, portal hypertension, SD, Standard deviation.

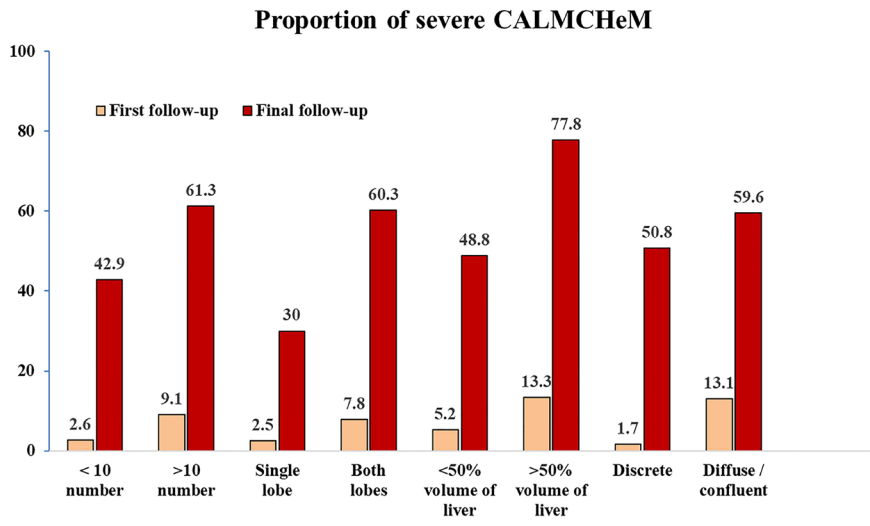

Figure 3. Bar graph showing the proportion of severe CALMCHeM at first and final follow-up imaging vs. the number of metastases, lobe involvement, the volume of the liver affected, and the type of metastases. CALMCHeM, chemotherapy-associated liver morphological changes in hepatic metastases.

Table 5. The hazard ratio for severe CALMCHeM changes in 183 patients (four largest groups of primaries: breast, colorectal, neuroendocrine, and pancreatic)

Characteristic	Hazard ratio	95% CI	*P* value
Female sex	0.46	0.28–0.78	0.004
The volume of the liver affected	1.88	1.05–3.01	0.03

CALMCHeM, chemotherapy-associated liver morphological changes in hepatic metastases; CI, confidence interval

with docetaxel (P = 0.022), doxorubicin (P = 0.001), gemcitabine (P = 0.002), paclitaxel (P = 0.014), and zoledronic acid (P = 0.031). Chemotherapeutic agents were not included in the regression analysis, as different agents and combinations were used in different patients.

Discussion

In this study, we showed that CALMCHeM occurred in metastatic liver disease from a variety of primary malignancies and that the severity of CALMCHeM correlated with tumor burden, primarily the volume of the liver affected. We also showed that these changes were progressive, and the progression to severe changes was also related to the tumor burden. Regression analysis showed a significant association between the female sex and a higher initial volume of hepatic disease with disease severity.

Breast carcinoma was the most common tumor associated with severe CALMCHeM. Several of the previous case reports and case series reported breast carcinoma as the most common cause of CALMCHeM.[5,7,9,21] Possible reasons for CALMCHeM reports with breast carcinoma include the longer survival of the patients with breast carcinoma metastases and the fact that, usually, hormone receptor-positive breast cancer patients are on systemic therapy for longer periods, which may allow for the CALMCHeM to manifest during follow up.[22,23] However, our study confirmed that these changes could also occur in hepatic metastatic disease from other primaries, and we postulate that, in the future, it may be seen more commonly in other metastatic diseases, given the advances in the chemotherapy regimens and, accordingly, the prolonged survival of patients.

Our study analysis shows that tumor burden is the most important factor for predicting the severity of CALMCHeM. A larger tumor burden was observed in cases comprising >10 metastases, bilobar distribution, and a larger volume of the liver parenchyma affected by the metastases. We hypothesize that it is possibly due to the large volume of the liver parenchyma affected by the desmoplastic changes around the metastases, resulting in scarring with accompanied vascular changes that overwhelm the regenerative capacity of the liver parenchyma, and subsequently portal hypertension. The influence of other coexistent liver diseases, particularly fatty liver, diabetes, hypertension, and excessive alcohol intake on the development of CALMCHeM, is not well known. In one study on breast carcinoma metastases by Huppert et al.[22], the study population had a very low incidence of fatty liver or other risk factors, and the researchers concluded that the presence of other risk factors may not be a significant driver of CALMCHeM. Other risk factors may modify CALMCHeM manifestation, as patients with reduced hepatic function reserve are less likely to be candidates for hepatotoxic chemotherapeutic agents and multiple chemotherapy drug regimens.

Although a common finding, ascites was not significantly associated with severe CALMCHeM, which may be explained by the fact that lymphatics and the hepatic functional reserve are preserved in most of the patients, even those with severe CALMCHeM. There may be other reasons for ascites, such as chemotherapy and the presence of peritoneal metastases. Ascites in patients with cirrhosis from chronic liver disease is usually a sign of hepatocellular failure and signifies the progression of the disease. However, the literature shows that ascites is a common finding in patients developing CALMCHeM, but preserved liver function until late stages, similar to our experience. Additionally, there is a very low incidence of hepatic encephalopathy in this population.[21] It is also possible that an increased report of ascites is due to the detection of free fluid in these patients on imaging. Interestingly, in a series by Huppert et al.[22] studying breast carcinoma patients, ascites was associated with a worse median overall survival rate from the time of diagnosis of the metastatic disease. More prospective studies are required to validate this finding.

In our study, patients with a tumor burden ≥50% liver volume and those with diffuse or confluent metastases developed severe CALMCHeM significantly earlier than those who had a smaller liver volume affected or had discrete metastases. This may be explained by the involvement of a larger volume of metastases resulting in the exposure of a larger volume of liver parenchyma to chemotherapy-induced changes which, in turn, cause a larger response of nodular regenerative hyperplasia[5] and perilesional fibrosis, resulting in the faster development of severe changes. Similarly, diffuse confluent metastases are likely to be infiltrative and, accordingly, result in more desmoplastic reaction.[8,24]

Portal hypertension is seen in a significant number of patients with CALMCHeM. In our study population, 73% developed portal hypertension, similar to a recent meta-analysis that showed 80% of patients developed

portal hypertension.[21] In this meta-analysis, there was no further analysis regarding tumor burden parameters. However, in our study, we showed that portal hypertension (splenomegaly and venous collaterals) was related to tumor burden.

Furthermore, we found an association between some chemotherapeutic agents such as docetaxel, doxorubicin, and paclitaxel, with severe CALMCHeM. Although the precise reasons are not clear, doxorubicin and paclitaxel are known to be associated with nodular regenerative hyperplasia.[21,25-27] Several patients received multiple drugs, and some of the association may be due to their concomitant use with chemotherapeutic agents that are known to cause nodular regenerative hyperplasia.

This study has limitations. First, we searched for our cases using radiology reports, and cases with mild CALMCHeM may have been missed or underreported and, hence, excluded from the search. However, CALMCHeM is mainly a radiological diagnosis, which is why we used this approach. Pathological proof of metastases and CALMCHeM in the liver was not available in all the patients, and it was not clinically necessary to perform a liver biopsy for confirmation in these patients. Although we have postulated that the changes occurred due to perilesional fibrosis, histological proof was not available in all patients, and it was impractical or clinically indicated that a liver biopsy was necessary for confirmation in these patients. However, existing studies have implicated perilesional fibrosis as a potential cause of these changes.[5,7,9,11,12] The imaging interval for the heterogeneous group of patients varied, as this was a retrospective study with scans completed per clinical indication and as needed. The time interval for the development of severe CALMCHeM may thus have been affected by the scanning intervals. We did not compare our study cohort with those who did not have hepatic metastases; however, Oliai et al. demonstrated CALMCHeM changes do not occur in the absence of hepatic metastases.[9]

It is difficult to determine the outcome of CALMCHeM in our study, as the population was heterogeneous in terms of primary disease, the chemotherapy regimen received, and the presence of metastatic disease elsewhere in the body. Patients with CALMCHeM rarely develop the complication of liver failure, as they usually do not have chronic liver disease, or chemotherapy is not administered if the liver functions are abnormal. We did not evaluate patients with known chronic liver disease, as doing so would confound with the morphological features evaluated. Studies have shown that CALMCHeM changes in patients could result in portal hypertension and its associated complications.[9] Furthermore, studies have also indicated that survival is shorter in patients with CALMCHeM who develop ascites.[21,22] However, this needs to be confirmed in future studies and possibly with a prospective subject population.

Some of the changes may have been caused by CASH and SOS, particularly in patients with long-term follow-ups. We could not confirm the presence of hepatic steatosis or SOS with imaging, as most patients only received a single portal venous phase scan. The presence of these changes alongside CALMCHEM could not be completely excluded, and their contribution to the severe changes could not be separately assessed.

In conclusion, our study highlights that CALMCHeM changes occur in all malignancies, are progressive in many, and are associated with the development of portal hypertension. The temporal progression and severity of CALMCHeM are associated with the initial burden of liver metastatic disease. Early recognition of CALMCHeM by radiologists can help alert clinicians to possible progression, which may be useful information for clinical decision making about systemic chemotherapy. CALMCHeM is possibly a more appropriate term to use in patients with hepatic metastatic disease, as the appearance of pseudocirrhosis can be caused by several other etiologies. Furthermore, many patients with CALMCHeM develop portal hypertension with preserved hepatic function.

Conflict of interest disclosure

The authors declared no conflicts of interest.

References

1. Chia SK, Speers CH, D'yachkova Y, et al. The impact of new chemotherapeutic and hormone agents on survival in a population-based cohort of women with metastatic breast cancer. *Cancer*. 2007;110:973-979. [CrossRef]
2. Sharma A, Houshyar R, Bhosale P, Choi JI, Gulati R, Lall C. Chemotherapy induced liver abnormalities: an imaging perspective. *Clin Mol Hepatol*. 2014;20:317-326. [CrossRef]
3. Grigorian A, O'Brien CB. Hepatotoxicity secondary to chemotherapy. *J Clin Transl Hepatol*. 2014;2:95-102. [CrossRef]
4. Vernuccio F, Dioguardi Burgio M, Barbiera F, et al. CT and MR imaging of chemotherapy-induced hepatopathy. *Abdom Radiol (NY)*. 2019;44(10):3312-3324. [CrossRef]
5. Young ST, Paulson EK, Washington K, Gulliver DJ, Vredenburgh JJ, Baker ME. CT of the liver in patients with metastatic breast carcinoma treated by chemotherapy: findings simulating cirrhosis. *AJR Am J Roentgenol*. 1994;163(6):1385-1388. [CrossRef]
6. Sass DA, Clark K, Grzybicki D, Rabinovitz M, Shaw-Stiffel TA. Diffuse desmoplastic metastatic breast cancer simulating cirrhosis with severe portal hypertension: a case of "pseudocirrhosis". *Dig Dis Sci*. 2007;52(3):749-752. [CrossRef]
7. Qayyum A, Lee GK, Yeh BM, Allen JN, Venook AP, Coakley FV. Frequency of hepatic contour abnormalities and signs of portal hypertension at CT in patients receiving chemotherapy for breast cancer metastatic to the liver. *Clin Imaging*. 2007;31(1):6-10. [CrossRef]
8. Lee SL, Chang ED, Na SJ, et al. Pseudocirrhosis of breast cancer metastases to the liver treated by chemotherapy. *Cancer Res Treat*. 2014;46(1):98-103. [CrossRef]
9. Oliai C, Douek ML, Rhoane C, et al. Clinical features of pseudocirrhosis in metastatic breast cancer. Breast *Cancer Res Treat*. 2019;177(2):409-417. [CrossRef]
10. Calistri L, Rastrelli V, Nardi C, et al. Imaging of the chemotherapy-induced hepatic damage: yellow liver, blue liver, and pseudocirrhosis. *World J Gastroenterol*. 2021;27(46):7866-7893. [CrossRef]
11. Honma K. Hepar lobatum carcinomatosum due to metastatic breast carcinoma. *Virchows Arch A Pathol Anat Histopathol*. 1987;410(6):465-469. [CrossRef]
12. Schreiner SA, Gorman B, Stephens DH. Chemotherapy-related hepatotoxicity causing imaging findings resembling cirrhosis. *Mayo Clin Proc*. 1998;73(8):780-783. [CrossRef]
13. Jha P, Poder L, Wang ZJ, Westphalen AC, Yeh BM, Coakley FV. Radiologic mimics of cirrhosis. *AJR Am J Roentgenol*. 2010;194(4):993-999. [CrossRef]
14. Elbaz T, Esmat G. Hepatic and intestinal schistosomiasis: review. *J Adv Res*. 2013;4(5):445-452. [CrossRef]
15. Navin PJ, Hilscher MB, Welle CL, et al. The utility of MR elastography to differentiate nodular regenerative hyperplasia from cirrhosis. *Hepatology*. 2019;69(1):452-454. [CrossRef]
16. Kang SP, Taddei T, McLennan B, Lacy J. Pseudocirrhosis in a pancreatic cancer patient with liver metastases: a case report of complete resolution of pseudocirrhosis with an early recognition and management. *World J Gastroenterol*. 2008;14(10):1622-1624. [CrossRef]

17. Teke Z, Nessar G, Kiremitci S, Aksoy E, Elbir OH. Hepar lobatum carcinomatosum associated with metastatic rectal carcinoma: an unusual cause of liver dysmorphy. *Med Princ Pract*. 2011;20(1):93-96. [CrossRef]
18. Harry BL, Smith ML, Burton JR, Dasari A, Eckhardt SG, Diamond JR. Medullary thyroid cancer and pseudocirrhosis: case report and literature review. *Curr Oncol*. 2012;19(1):e36-41. [CrossRef]
19. Battisti S, Guida FM, Pagliara E, Tonini G, Zobel BB, Santini D. Pseudocirrhosis after anti-EGFR-based neoadjuvant therapy for hepatic metastasis from colon cancer: a different point of view. *Clin Colorectal Cancer*. 2014;13(3):e13-15. [CrossRef]
20. Fennessy FM, Mortele KJ, Kluckert T, et al. Hepatic capsular retraction in metastatic carcinoma of the breast occurring with increase or decrease in size of subjacent metastasis. *AJR Am J Roentgenol*. 2004;182(3):651-655. [CrossRef]
21. Villani R, Di Cosimo F, Sangineto M, Romano AD, Serviddio G. Pseudocirrhosis and portal hypertension in patients with metastatic cancers: a systematic review and meta-analysis. *Sci Rep*. 2022;12(1):19865. [CrossRef]
22. Huppert LA, Walker Z, Li M, et al. Clinical characteristics and outcomes in patients with metastatic breast cancer and pseudocirrhosis: a single center retrospective cohort study. *Breast Cancer Res Treat*. 2023;197(1):137-148. [CrossRef]
23. Ozaki K, Higuchi S, Kimura H, Gabata T. Liver metastases: correlation between imaging features and pathomolecular environments. *Radiographics*. 2022;42(7):1994-2013. [CrossRef]
24. Nascimento AB, Mitchell DG, Rubin R, Weaver E. Diffuse desmoplastic breast carcinoma metastases to the liver simulating cirrhosis at MR imaging: report of two cases. *Radiology*. 2001;221(1):117-121. [CrossRef]
25. Jeong WK, Choi SY, Kim J. Pseudocirrhosis as a complication after chemotherapy for hepatic metastasis from breast cancer. *Clin Mol Hepatol*. 2013;19(2):190-194. [CrossRef]
26. Wicherts DA, de Haas RJ, Sebagh M, et al. Regenerative nodular hyperplasia of the liver related to chemotherapy: impact on outcome of liver surgery for colorectal metastases. *Ann Surg Oncol*. 2011;18(3):659-669. [CrossRef]
27. Bissonnette J, Généreux A, Côté J, et al. Hepatic hemodynamics in 24 patients with nodular regenerative hyperplasia and symptomatic portal hypertension. *J Gastroenterol Hepatol*. 2012;27(8):1336-1340. [CrossRef]

Supplementary Table 1.
Chemotherapeutic agents

Agent used	Number of subjects
Paclitaxel	95
Capecitabine	83
Gemcitabine	58
Fulvestrant	56
5-fluorouracil	55
Oxaliplatin	49
Folinic acid	47
Carboplatin	41
Bevacizumab	40
Cyclophosphamide	37
Doxorubicin	36
Letrozole	33
Palbociclib	33
Irinotecan	32
Docetaxel	31
Exemestane	29
Anastrozole	28
Zoledronic acid	26
Everolimus	23
Trastuzumab	23
Tamoxifen	20
Denosumab	18
Cisplatin	17
Eribulin	15
Vinorelbine	15
Pertuzumab	14
Panitumumab	11
Goserelin	9
Temozolomide	9
Ixabepilone	8
Cetuximab	7
Etoposide	7
Octreotide	6
Sandostatin	6
Abemaciclib	5
Lapatinib	5
Sunitinib	5
TAS	5
Endoxifen	4
Erlotinib	4
Leuprorelin	4
Methotrexate	4
Alisertib	3
Dacarbazine	3
Megestrol acetate	3
Pazopanib	3
Pemetrexed	3
Ramucirumab	3
Regorafenib	3
Ribociclib	3
Atezolizumab	2
Bicalutamide	2
Lanreotide	2
Pembrolizumab	2
Sirolimus	2
Streptozotocin	2
Telotristat	2
Temsirolimus	2
Vincristine	2
Afatinib	1
Albociclib	1
Anthracycline	1
Bortezomib	1
Brostallicin	1
Cabazitaxel	1
Cabozantinib	1
Cixutumumab	1
Durvalumab	1
Enzalutamide	1
Epirubicin	1
Estradiol	1
Evofosfamide	1
Falsodex	1
Fluoxymesterone	1
Ikpilimumab	1
Interleukin-2	1
Ipilimumab	1
Leuprolide	1
Levatinib	1
Mitoxantrone	1
Nivolumab	1
p38 MAP kinase inhibitor	1
Pamidronic acid	1
Phenylalanine mustard	1
Pixantrone	1
Poziotinib	1
Quarfloxin	1
Rovalpituzumab	1
Silmitasertib	1
Tanespimycin	1
Trabectedin	1
Tremelimumab	1
Triapine	1
Vandetanib	1
Varililumab	1
VEGF	1
Venlavaxine	1
Vismodegib	1

Diagn Interv Radiol 2023; DOI: 10.4274/dir.2022.221790

BREAST IMAGING

ORIGINAL ARTICLE

Copyright@Author(s) - Available online at dirjournal.org.
Content of this journal is licensed under a Creative Commons Attribution-NonCommercial 4.0 International License.

Outcomes of high-risk breast lesions diagnosed using image-guided core needle biopsy: results from a multicenter retrospective study

Ayşenur Oktay, Özge Aslan, Füsun Taşkın, Nermin Tunçbilek, Selma Gül Esen İçten, Pınar Balcı, Mustafa Erkin Arıbal, Levent Çelik, İhsan Şebnem Örgüç, Figen Başaran Demirkazık, Serap Gültekin, Ayşe Murat Aydın, Emel Durmaz, Sibel Kul, Figen Binokay, Meltem Çetin, Ganime Dilek Emlik, Meltem Gülsün Akpınar, Sadiye Nuray Kadıoğlu Voyvoda, Ahmet Veysel Polat, Işıl Başara Akın, Şeyma Yıldız, Necdet Poyraz, Arzu Özsoy, Pelin Seher Öztekin, Eda Elverici, İlkay Koray Bayrak, Türkan İkizceli, Funda Dinç, Gülten Sezgin, Gökçe Gülşen, Işıl Tunçbilek, Sabiha Rabia Yalçın, Gül Çolakoğlu, Serpil Ağlamış, Ravza Yılmaz, Günay Rona, Gamze Durhan, Davut Can Güner, Fatma Çelik Yabul, Leman Günbey Karabekmez, Burçin Tutar, Muhammet Göktaş, Onur Buğdaycı, Aslı Suner, Necmettin Özdemir

From the Department of Radiology (A.O. ✉ oktay.aysenur@gmail.com, Ö.A.), Ege University Faculty of Medicine, İzmir, Turkey; Department of Radiology (F.T.), Acıbadem MAA University Faculty of Medicine; Acıbadem MAA University Senology Research Institute, Acıbadem Atakent Hospital, İstanbul, Turkey; Department of Radiology (N.T.), Trakya University Faculty of Medicine, Edirne, Turkey; Department of Radiology (S.G.E.İ.), Acıbadem MAA University Faculty of Medicine; Acıbadem MAA University Senology Research Institute, İstanbul, Turkey; Department of Radiology (P.B., I.B.A.), Dokuz Eylül University Faculty of Medicine, İzmir, Turkey; Department of Radiology (M.E.A.), Acıbadem MAA University Faculty of Medicine, İstanbul, Turkey; Department of Radiology (L.Ç., D.C.G.), Maltepe University Faculty of Medicine; İstanbul, Turkey; Department of Radiology (İ.Ş.Ö.), Manisa Celal Bayar University Faculty of Medicine, Manisa, Turkey; Department of Radiology (F.B.D., M.G.A., G.D.), Hacettepe University Faculty of Medicine, Ankara, Turkey; Department of Radiology (S.G.), Gazi University Faculty of Medicine, Ankara, Turkey; Department of Radiology (A.M.A., S.A.), Fırat University Faculty of Medicine, Elazığ, Turkey; Department of Radiology (E.D.), Akdeniz University Faculty of Medicine, Antalya, Turkey; Department of Radiology (S.K.), Karadeniz Techinal University Faculty of Medicine, Trabzon, Turkey; Department of Radiology (F.B.), Çukurova University Faculty of Medicine, Adana, Turkey; Department of Radiology (M.Ç.), Süleyman Demirel University Faculty of Medicine, Isparta, Turkey; Department of Radiology (G.D.E., N.P.), Necmettin Erbakan University Meram Faculty of Medicine, Konya, Turkey; Department of Radiology (S.N.K.V., G.R.), University of Health Sciences Turkey, Kartal Dr. Lütfi Kırdar City Hospital, İstanbul, Turkey; Department of Radiology (A.V.P., İ.K.B.), Ondokuz Mayıs University Faculty of Medicine, Samsun, Turkey; Department of Radiology (Ş.Y., F.Ç.Y.), Bezmialem Vakıf University Faculty of Medicine, İstanbul, Turkey; Department of Radiology (A.Ö., E.E.), University of Health Sciences Turkey, Ankara City Hospital, Ankara, Turkey; Department of Radiology (P.S.Ö.), Ankara Training and Research Hospital, Ankara, Turkey; Department of Radiology (T.İ., G.G.), University of Health Sciences Turkey, İstanbul Haseki Training and Research Hospital, İstanbul, Turkey; Department of Radiology (F.D.), Muğla Sıtkı Koman University Faculty of Medicine, Muğla Turkey; Department of Radiology (G.S.), İzmir Katip Çelebi University, Atatürk Training and Research Hospital, İzmir, Turkey; Department of Radiology (I.T., S.R.Y.), Medsentez Private Clinic, Ankara, Turkey; Department of Radiology (G.Ç.), University of Health Sciences Turkey, İzmir Tepecik Training and Research Hospital, İzmir, Turkey; Department of Radiology (R.Y.), İstanbul University, İstanbul Faculty of Medicine, İstanbul, Turkey; Department of Radiology (L.G.K), Ankara Yıldırım Beyazıt University Faculty of Medicine, Ankara, Turkey; Department of Radiology (B.T.), Acıbadem Maslak Hospital, İstanbul, Turkey; Department of Radiology (M.G.), Ministry of Health Çerkezköy State Hospital, İstanbul, Turkey; Department of Radiology (O.B.), Marmara University Faculty of Medicine, İstanbul, Turkey; Department of Biostatistics and Medical Informatics (A.S.), Ege University Faculty of Medicine, İzmir, Turkey; Department of Medical Pathology (N.Ö.), Ege University Faculty of Medicine, İzmir, Turkey.

Received 25 July 2022; revision requested 05 August 2022; accepted 27 August 2022.

Epub: 09.01.2023

Publication date: 21.07.2023

DOI: 10.4274/dir.2022.221790

You may cite this article as: Oktay A, Aslan Ö, Taşkın F, et al. Outcomes of high-risk breast lesions diagnosed using image-guided core needle biopsy: results from a multicenter retrospective study. *Diagn Interv Radiol.* 2023;29(4):579-587.

PURPOSE

The clinical management of high-risk lesions using image-guided biopsy is challenging. This study aimed to evaluate the rates at which such lesions were upgraded to malignancy and identify possible predictive factors for upgrading high-risk lesions.

METHODS

This retrospective multicenter analysis included 1.343 patients diagnosed with high-risk lesions using an image-guided core needle or vacuum-assisted biopsy (VAB). Only patients managed using an excisional biopsy or with at least one year of documented radiological follow-up were included. For each, the Breast Imaging Reporting and Data System (BI-RADS) category, number of samples, needle thickness, and lesion size were correlated with malignancy upgrade rates in different histologic subtypes. Pearson's chi-squared test, the Fisher–Freeman–Halton test, and Fisher's exact test were used for the statistical analyses.

RESULTS

The overall upgrade rate was 20.6%, with the highest rates in the subtypes of intraductal papilloma (IP) with atypia (44.7%; 55/123), followed by atypical ductal hyperplasia (ADH) (38.4%; 144/375), lobular neoplasia (LN) (12.7%; 7/55), papilloma without atypia (9.4%; 58/611), flat epithelial atypia (FEA) (8.7%; 10/114), and radial scars (RSs) (4.6%; 3/65). There was a significant relationship between the upgrade rate and BI-RADS category, number of samples, and lesion size Lesion size was the most predictive factor for an upgrade in all subtypes.

CONCLUSION

ADH and atypical IP showed considerable upgrade rates to malignancy, requiring surgical excision. The LN, IP without atypia, pure FEA, and RS subtypes showed lower malignancy rates when the BI-RADS category was lower and in smaller lesions that had been adequately sampled using VAB. After being discussed in a multidisciplinary meeting, these cases could be managed with follow-up instead of excision.

KEYWORDS

Core needle biopsy, B3 lesions, breast cancer, image guided breast biopsy, vacuum assisted biopsy

High-risk breast lesions comprise a heterogeneous group of proliferative lesions that are precursors of breast carcinogenesis and are associated with a higher risk of future breast cancer development.[1,2] These lesions include atypical ductal hyperplasia (ADH), lobular neoplasia (LN) (a term encompassing both atypical lobular hyperplasia [(ALH) and lobular carcinoma in situ (LCIS)], intraductal papilloma (IP) with/without atypia, flat epithelial atypia (FEA), and radial scars (RSs)/complex sclerosing lesions.[3,4] Other terms used in the literature to describe these entities are "lesions of the breast with uncertain malignant potential", "borderline lesions", or "B3 lesions". High-risk lesions are commonly detected due to the increased use of core or vacuum biopsy techniques for screen-detected lesions. High-risk lesions are found in about 3%–9% of cases of percutaneous image-guided breast biopsies performed following a suspicious imaging finding.[5,6]

Percutaneous image-guided needle biopsy has become a standard approach for the tissue diagnosis of suspicious breast lesions. It is performed using either the core needle biopsy (CNB) or vacuum-assisted biopsy (VAB) technique. CNBs are usually performed under ultrasound (US) guidance, while stereotactic system or magnetic resonance imaging (MRI) guidance is used for VABs. When the CNB/VAB detects a high-risk lesion, the possibility of missing the malignant component of the lesion exists; ductal carcinoma in situ (DCIS) and invasive carcinoma can only be detected when surgical excision is performed. The positive predictive value (PPV) for malignancy for CNB/VAB is about 10%–30%.[5,7,8]

The appropriate management of a high-risk lesion following diagnosis using image-guided biopsy is controversial, and recommendations, including surgical excision and follow-up, vary for different lesions.[9] Surgical excision has been used as a general approach to avoid missing an underlying malignancy.[10] However, in recent studies, risk parameters have been identified to upgrade a lesion to suspected malignancy, allowing more conservative approaches in selected cases. To achieve consensus about managing high-risk lesions, the International Consensus Conference was held in Zurich, Switzerland, in 2016 and 2019. This conference introduced second-line VAB as an alternative to open surgical excision in most lesions, and several guidelines were introduced for managing these lesions.[11]

This multicenter study aimed to document the excisional biopsy or follow-up results of high-risk lesions diagnosed on image-guided CNB/VAB and evaluate the clinical, imaging, and histologic features for associated malignancy risk. The possibility of an upgrade related to histologic subtype, tissue sampling, and other variables was also evaluated.

Methods

This retrospective multicenter study included 1.343 patients from 30 centers diagnosed with a high-risk lesion on image-guided CNB or VAB. The ethics committee of the Ege University Faculty of Medicine approved the study (approval number: 20-6T/41; date of approval: June 10, 2020). The study reviewed existing data, so patient consent was not required.

Patients

Radiology records for the 12 years between 2008 and 2020 were reviewed for all image-guided biopsies and pathology reports. Patients diagnosed with ADH, LN (ALH/LCIS), papilloma (with or without atypia), RSs, or FEA on image-guided CNB/VAB were included. The needle biopsy could be performed using either US or stereotactic guidance and tru-cut or vacuum biopsy needles. In addition, patients managed with an excisional biopsy or those with at least one year of documented radiological follow-up after diagnosis with one of the above-mentioned high-risk lesions were included in the study. FEA, seen in conjunction with LN or ADH, was categorized under either LN or ADH as appropriate. Pleomorphic LCIS, fibroepithelial lesions, and mucocele-like tumors were excluded. Further, lesions associated with *in situ* or invasive carcinoma on CNB were excluded.

All patients were discussed at a multidisciplinary meeting, and decisions were made based on biopsy and radiology findings. Histopathologic diagnoses were made according to the current guidelines.[12]

Data analysis

The images used in this study were retrieved from the Picture Archiving and Communication System digital archive, and the results of mammograms, US images, and MRI scans were re-evaluated. The findings were categorized by imaging method, as follows: microcalcifications, a mass/nodular opacity, or suspicious non-mass findings (i.e., architectural distortion and asymmetry) on a mammogram; a mass/nodular lesion or non-mass lesion (i.e., distortion or echogenicity changes) on a US examination; and a mass or non-mass contrast-enhancing lesion on an MRI scan. The patients without imaging findings were also noted. In each case, the lesion's largest diameter was recorded and categorized into two groups: under and above 15 mm. The final Breast Imaging Reporting and Data System (BI-RADS) category on the imaging reports was also documented.

Other data collected from the records included the needle biopsy type and biopsy sampling method. The imaging-guidance modality was chosen based on the findings and visibility of the lesion on imaging. Stereotactic guidance was usually preferred for microcalcifications, while US was used for lesions that were visible on the US. Stereotactically guided biopsies were performed in 182/1.343 (13.6%) patients on a prone table or an add-on unit using a 9 to 12 G directional vacuum-assisted needle. US-guided biopsies were performed in 1.161/1.343 (86.4%) patients with an automated tru-cut system using 14 to 16 G needles with a 2-cm cutting surface. The number of cores used was another analysis point, and this information was categorized as n <4 and n ≥4.

The final pathology reports of the patients who had surgical excision or were stable for at least one year of follow-up were documented. The follow-up period varied between 12 and 180 months (median: 30 months). In total, 929 patients underwent surgical excisional biopsy, and 414 were followed up with at six-month intervals. Recommendations for excision or surveillance were made in a multidisciplinary meeting. The pathological results of excisional biopsies were recorded as either no change in the primary diagnosis by needle biopsy or upgraded to indicate malignancy. The presence of DCIS or invasive carcinoma on histologic examination after an excisional biopsy was regarded as necessitating an upgrade of the high-risk lesion. In follow-up patients, the diagnosis on needle biopsy was considered a compatible result if there was no change in the findings; however, a biopsy was recommended if any suspicious change was observed on follow-up.

Main points

- High-risk breast lesions are a heterogeneous group of proliferative lesions that are precursors to breast carcinogenesis and are associated with a higher risk of future breast cancer.
- Clinical management of high-risk lesions using image-guided biopsy is challenging.
- High-risk breast lesions should be managed in a case-based manner after discussion among a multidisciplinary team.

The diagnosis on CNB/VAB and the outcomes were compared, and the upgrade rate and PPV for malignancy [i.e., (number of malignant cases/total number of participants) × 100] were calculated. The association between the parameters described above and the upgrade rate or PPV for malignancy were evaluated.

Statistical analysis

All patient information was anonymously submitted to a medium in an anonymized manner via software from all included centers. Patient characteristics were reported as frequencies and percentages (%) for categorical variables, and descriptive statistics (mean, median, minimum, and maximum values) were calculated for continuous variables. If the variables had a normal distribution, the mean and standard deviation (SD) were given; otherwise, the median and range were given. Pearson's chi-squared test, the Fisher–Freeman–Halton test, and Fisher's exact test were used to analyze the categorical variables in groups. A value of $P < 0.05$ was considered statistically significant. The data were analyzed using the IBM SPSS Statistics version 25.0 statistical software package.

Results

In total, 1.343 patients met our criteria, of which 375 (27.9%) had ADH, 55 (4.1%) had LN (ALH/LCIS), 611 (45.5%) had IP without atypia, 123 (9.2%) had IP with atypia, 114 (8.5%) had FEA, and 65 (4.8%) had RSs. The patients were between 17 and 86 years of age, with a mean age of 47.45 years (SD: 0.459).

In all cases, the upgrade rate to malignancy was 20.6% (Table 1). Of these, 52% (144/277) were cases of ADH. Almost half (47.2%) of all upgrades were to invasive cancer. Upgrades to low-grade DCIS were more common than upgrades to high-grade DCIS (32.9% vs. 19.9%, respectively). According to the pathologic subtypes, IP with atypia was the most common type, with an upgrade rate of 44.7% (55 of 123 cases), followed by ADH (38.4%, 144 of 375 patients). The upgrade rate was 12.7% in LN, 8.7% in FEA, 9.4% in IP without atypia, and 4.6% in RSs. The pathological subtype had a statistically significant relationship with malignant vs. benign diagnosis $P < 0.001$).

In about half the cases (49%), the lesions were categorized as BI-RADS 4A lesions, followed by BI-RADS 4B (26.7%), BI-RADS 4C (13.1%), and BI-RADS 5 (3.3%). These categories were most common in the subtypes ADH and IP with atypia. A biopsy was still recommended in 7.9% of patients, although the lesions were categorized as BI-RADS 3. The malignancy upgrade rate had a statistically significant relationship with the BI-RADS category ($P < 0.05$). In the imaging findings, microcalcifications on mammograms were common in the LN, FEA, and ADH subtypes (70.3%, 64%, and 54.8%, respectively). The mass lesions detected on mammography, US, or MRI were most frequently IPs with or without atypia. Lesions presenting as non-mass lesions on mammography, US, or MRI were seen in all subtypes. There was no statistically significant relationship between the imaging findings and upgrade rates.

Table 2 summarizes the outcomes of biopsy or follow-up and malignancy upgrade rate according to the BI-RADS category, needle size, number of samples, and lesion size. There was no statistically significant relationship between malignancy upgrade rate and needle size ($P > 0.05$). However, the relationship between the malignancy upgrade rate and the number of samples and lesion size was statistically significant ($P = 0.008$ and $P < 0.001$, respectively). Lesion sizes were between 4 and 135 mm (mean: 13.8; median: 10), which was the most predictive factor for an upgrade when all the patients were analyzed together.

The results varied among the lesion subtypes. In the ADH group, a statistically significant change in the upgrade rate was recorded according to BI-RADS category, needle thickness, number of samples, and lesion diameter (Table 3). The malignancy rate was higher in the BI-RADS 4C and 5-category le-

Table 1. Upgrade to malignancy related to subtypes of high-risk lesions

Pathology subtype n (%)	Benign n (%)	Malignant n (%)				Total (n)	*P*
		Low-grade DCIS n (%)	High-grade DCIS n (%)	Invasive carcinoma n (%)	Total n (%)		
ADH	231 (61.6)	42 (11.2)	37 (9.8)	65 (17.3)	144 (38.4)	375	
LN	48 (87.3)	1 (1.8)	2 (3.6)	4 (7.3)	7 (12.7)	55	
RS	62 (95.4)	0 (0)	2 (3.1)	1 (1.5)	3 (4.6)	65	
IP with atypia	68 (55.3)	19 (15.4)	7 (5.7)	29 (23.6)	55 (44.7)	123	<0.001*
FEA	104 (91.2)	4 (3.6)	3 (2.6)	3 (2.6)	10 (8.8)	114	
IP without atypia	553 (90.5)	25 (4.1)	4 (0.6)	29 (4.8)	58 (9.5)	611	
Total	1.066 (79.4)	91 (6.8)	55 (4.1)	131 (9.7)	277 (20.6)	1.343	

Benign, benign and stable on follow-up; *$P < 0.05$. ADH, atypical ductal hyperplasia; LN, lobular neoplasia; RS, radial scar; IP, intraductal papilloma; FEA, flat epithelial atypia; DCIS, ductal carcinoma in situ.

Table 2. Distribution of malignancy upgrade according to BI-RADS category, needle size, number of samples, and lesion size

		Benign n (%)	Malignant n (%)	Total n	*P*
BI-RADS category	BI-RADS 3–4A–B	949 (84.5)	174 (15.5)	1,123	<0.001*
	BI-RADS 4C–5	117 (53.2)	103 (46.8)	220	
Needle thickness	9–12 gauge	152 (84.0)	29 (16.0)	181	0.100
	14–16 gauge	914 (78.7)	248 (21.3)	1.162	
Number of samples	<4	309 (75.0)	103 (25.0)	412	0.008*
	≥4	757 (81.3)	174 (18.7)	931	
Diameter of lesion	≤15 mm	753 (86.0)	123 (14.0)	876	<0.001*
	>15 mm	313 (67.0)	154 (33.0)	467	

Benign, benign and stable on follow-up; *$P < 0.05$. BI-RADS, Breast Imaging Reporting and Data System.

sions. The upgrade rate varied according to needle type, 41% vs. 28% for tru-cut vs. vacuum biopsies. The number of samples and lesion size correlated with upgrade rates, being 49.0% when there were fewer than four samples vs. 34.3% when there were four samples or more, and 29.1% vs. 51.6% for lesions ≤15 mm and >15 mm, respectively. In the multivariate analysis, the lesion diameter and needle size were the most predictive of a lower upgrade rate (20% when 9 to 12 G needles were used for lesions ≤15 mm in size) (Table 4).

The only statistically significant variable in the LN subtype was the BI-RADS category. There was no statistically significant correlation between the needle thickness, number of samples, lesion size, and upgrade at the final diagnosis. In the multivariate analysis, the results did not predict malignancy when larger needle sizes were used in lesions ≤15 mm (Table 4).

In the IP without atypia and FEA subtypes, the upgrade rate changed with the lesion diameter and BI-RADS category (Table 3). In the multivariate analysis, the patients who had IP without atypia, diagnosed using a 9 to 12 G needle and a lesion ≤15 mm, were all in the benign group (n = 34; Table 4). In IP without atypia, the upgrade rate was 6% in patients with lesions ≤15 mm, in whom 14 to 16 G needles were used for sampling, vs. 18% in patients with lesions >15 mm, in whom samples were taken using the same needle size. The difference between these results was statistically significant. The percentage of upgrade to malignancy did not change even when 9 to 12 G needles were used in lesions >15 mm (18%). In the FEA subtype, there was no malignancy at final diagnosis when 14 to 16 G needles were used to sample lesions ≤15 mm in 44 patients; however, the upgrade rate was 20% with the same needle size when the lesion size was >15 mm. The upgrade rate also varied with lesion size when 9 to 12 G needles were used (4% for lesions ≤15 mm, and 17% for lesions >15 mm) ($P = 0.002$; Table 4).

In patients with atypical IP, a statistically significant difference was found between lesion size and an upgrade to malignancy (Table 3). Of the 123 atypical IP lesions, 121 were sampled with 14 to 16 G needles, and the malignancy rate was 38% for lesions ≤15 mm in size and 57% for those >15 mm, which was statistically significant ($P = 0.043$; Table 4).

In the RS subtype, a statistically significant difference was found between needle size and upgrade to malignancy ($P = 0.038$; Table 3). Fourteen to 16 G needles were used for all these lesions, and the 42 lesions that were ≤15 mm in size were all benign at the final diagnosis. The other predictive factor for the upgrade was lesion size, with only one malignant of the 46 RS lesions ≤15 mm (Table 4).

Discussion

This multicenter study reviewed the outcomes of surgical biopsies and long-term follow-up visits of high-risk lesions (B3 lesions) diagnosed using a CNB. More than two-thirds of the patients (n = 929) underwent a surgical biopsy, and 20.6% were found to have a breast malignancy. At final diagnosis, more than half of all malignancies were DCIS (52.8%), and low-grade DCIS was more common than high-grade DCIS (32.9% vs. 19.9%, respectively). In the literature, the PPVs ranged from 9.9% to 35.1% when all subtypes of B3 lesions were included.[7,13,14] Bianchi et al.[7] reviewed 3.107 cases and re-

ported a 21.2% upgrade rate, similar to this study's results. In addition, the number of DCIS cases was higher than that of invasive cancers in studies by Houssami et al.[14] and Strachan et al.[15]

Several variables should be considered when deciding what the next steps should be following a diagnosis of a high-risk lesion of the breast through an image-guided needle biopsy. In this study, upgrades to malignancy were associated with the BI-RADS category, the number of samples taken, and the lesion size. The lesion size was the most predictive factor for an upgrade, the rate being 14% vs. 33% for tumors that were ≤15 mm vs. those that were >15 mm in size, respectively. The underestimation rate was reduced with more sampling, 18.7% for four samples or more and 25% for fewer than four samples. In all lesions, 16.4% were categorized as BI-RADS 4C or 5, and the malignancy rate in this group was 47.2% vs. 15.5% for BI-RADS 3 or 4A–B lesions. These results show the importance of the BI-RADS classification and the radiologic–pathologic concordance of the lesions. There was no statistically significant relationship between radiologic findings (i.e., calcification and mass or non-mass lesion) and upgrade rate.

In managing high-risk lesions, surveys have shown significant variation in the recommendations of radiologists, pathologists, and surgeons.[9,16,17] Surgical excision has traditionally been performed as a safe option to exclude any associated adjacent malignancy that could have been missed when performing a CNB on high-risk lesions. However, high-risk breast lesions comprise a variety of lesion subtypes, showing different radiologic and histologic features and levels of malignancy risk.[11] Malignancy diagnosed at surgical excision is more frequent in lesions with atypia than in those without. In the present study, an associated DCIS or invasive cancer malignancy was most commonly seen in cases of atypical IP (upgrade rate of 44.7%), followed by ADH (38.4%). Accordingly, this study's results indicate that the surgical excision of these two categories of lesions is warranted. Strachan et al.[15], Rakha et al.[18], and de Beça et al.[19] also reported that the underestimation of malignancy is much higher in lesions with atypia than in those without atypia. Moreover, distinguishing ADH from a low-grade DCIS through a pathology review can be difficult. As such, the management of these two lesion types was consistent, with excision still being recommended in the guidelines for both. However, alternatives such as further sampling or surveillance can be considered for lesions without atypia.[11,20]

The reported rates of underlying co-existing malignancy for ADH diagnosed by needle biopsy varied between 4% and 54%, with a pooled median diagnosis upgrade rate of 25%.[1,21] There have been efforts to identify indicators of ADH lesions with a low risk of being upgraded to malignancy. Several histopathologic criteria, including the extent of the ADH and percentage of lesion removal, were found to be predictive factors of the upgrade rate.[22-24] While the present study did not evaluate any histopathologic parameters, the variables of biopsy type, needle size, number of samples, lesion size, and BI-RADS category of the lesion all showed a statistically significant correlation with the upgrade rate. ADH lesions ≤15 mm sampled with larger core needle sizes had a lower upgrade rate. However, this rate was too high to avoid excisional biopsy, which was done in 11 of 56 cases. Schiaffino et al.[25] proposed the conservative management of ADH only in a highly selective group of patients diagnosed using a stereotactic VAB for a single group of microcalcifications, without residual findings, and without a high percentage of hyperplasia at histological assessment.

In the current study, the upgrade rate within the subtype of LN was 12.7%. Pleomorphic types and variants of LCIS were excluded from this study, as there is already a consensus that excision is necessary for such types to ensure no underlying cancer is missed.[26] The BI-RADS score, lesion size, and needle type predicted an upgrade to LN carcinoma. Lesions measuring ≤15 mm and sampled with 9 to 12 G VAB needles were benign at surgical excision; however, the upgrade rate was 10% when 14 to 16 G needles were used for the same lesion sizes. The malignancy rate for lesions >15 mm also changed depending on the needle type, 40% for vacuum and 20% for core biopsy needles. Although the upgrade rate in LN has been reported to range between 0% and 50% in the literature.[4,27-29] Recent studies have shown that the upgrade rates decrease significantly when the BI-RADS score and pathologic results are concordant.[30-33] Mooney et al.[6] reported a 5% upgrade rate upon excision for LN diagnosed incidentally vs. a 39% upgrade rate for targeted lesions. Therefore, routine excision is no longer required in all ALH or LCIS cases.[34]

In the current study, the upgrade rate for IP with atypia was 44.7%, and for IP without atypia, 9.4%. A meta-analysis demonstrated a 15.7% pooled underestimation for non-malignant papillary breast lesions, with higher rates among atypical lesions (i.e., 36.9% for atypical lesions vs. 7% for benign IPs).[35] Therefore, there is no debate that surgical excision should be done after diagnosing atypical papillary breast lesions on core biopsy. However, there is no consensus on how best to manage benign IPs. In the current study, the lesion diameter and BI-RADS score correlated with an upgrade to malignancy in IPs without atypia. No malignancy was found in lesions ≤15 mm, sampled with larger needle sizes. When sampling lesions of the same size with 14 to 16 G needles, the upgrade rate was 6.1%. It has previously been demonstrated that lesions >15 mm in a peripheral location, with image-pathology discordance, are associated with a significant risk of upgrade to malignancy.[36]

Recent studies have suggested that imaging follow-up may be reasonable in selected cases, including radiologically concordant or incidentally detected benign IPs of ≤15 mm diagnosed using large-gauge core biopsy needles.[37-39] Pareja et al.[40] found an upgrade rate of 2.3% in their evaluation of 171 radiologic–pathologic concordant IPs without atypia. In a study by Menes et al.[41], upgrades to cancer occurred in 2% of asymptomatic women diagnosed with a benign papillary lesion using a needle biopsy following a mammogram showing a lesion classified as BI-RADS 4. From these results, imaging follow-up seems reasonable for benign papillomas found to be small upon core biopsy, adequately sampled, and radiologically concordant.

For the pure FEA subtype, the reported malignancy upgrade rates vary widely; most published studies have recommended excision. However, in several recent studies, imaging follow-up has been proposed for patients without residual calcifications.[42,43] In the present study, these upgrade rates were statistically significantly correlated with lesion diameter and BI-RADS score. The rate was 1.5% for lesions ≤15 mm. In relation to needle sizes, the upgrade rate was 0% (0/44 cases) for 14 to 16 G and 4% (1/23 cases) for 9 to 12 G needle sizes. A sampling error may have caused the only positive case in this study. In a recent systematic review and meta-analysis including 2.482 cases across 42 studies, this rate was 5%; however, when more than 90% of the calcifications were removed, no cancer was found at excision, and close imaging follow-up was recommended for such patients.[44] Schiaffino et al.[45] found a malignancy rate of less than 2% in patients

Table 3. Distribution of malignancy upgrade in different subtypes of high-risk lesions according to various variables

		ADH (n = 375)			IP without atypia (n = 611)			RS (n = 65)		
		Malignant n (%)	Benign n (%)	*P*	Malignant n (%)	Benign n (%)	*P*	Malignant n (%)	Benign n (%)	*P*
Mammography finding	**Microcalcification**	57 (40.4)	84 (59.6)	0.473	11 (15.7)	59 (84.3)	0.784	1 (11.1)	8 (88.9)	1.000
	Mass	31 (48.4)	33 (51.6)		18 (12.5)	126 (87.5)		0 (0)	5 (100)	
	Non mass	20 (38.5)	32 (61.5)		7 (12.3)	50 (87.7)		1 (5.9)	16 (94.1)	
Microcalcification morphology	**Amorphous**	14 (37.8)	23 (62,2)	0.330	4 (12.5)	28 (87.5)	0.782	1 (14.3)	6(85,7)	1.000
	Coarse heterogeneous	7 (41.2)	10 (58.8)		2 (20.0)	8 (80.0)		0 (0)	1 (100)	
	Newly identified suspect	3 (21.4)	11 (78.6)		0 (0)	2 (100)		0 (0)	0 (0)	
	Fine linear	10 (58.8)	7 (41.2)		1 (25.0)	3 (75.0)		0 (0)	0 (0)	
	Fine pleomorphic	23 (41.1)	33 (58.9)		4 (18.2)	18 (81.8)		0 (0)	1 (100)	
Ultrasonography finding	**Mass**	72 (39.3)	111 (60.7)	0.290	49 (9.7)	457 (90.3)	<0.001*	0 (0)	29 (100)	0.493
	Non mass	55 (45.5)	66 (54.5)		88 (10.1)	71 (89.9)		2 (6.3)	30 (93.8)	
MRI finding	**Mass**	29 (36,7)	50 (63.3)	0.368	27 (13.0)	180 (87.0)	<0.001*	0 (0)	14 (100)	0.224
	Non mass	48 (44.0)	61 (56.0)		31 (32.6)	64 (67.4)		3(20.0)	12 (80.0)	
Lesion diameter	**≤1.5 cm**	64 (29.1)	156 (70.9)	<0.001*	24 (5.6)	403 (94.4)	<0.001*	1 (2.2)	45 (97.8)	0.202
	>1.5 cm	80 (51.6)	75 (48.4)		34 (18.5)	150(81,5)		2 (10.5)	17 (89.5)	
BI-RADS	**3, 4A, 4B**	82 (31.1)	182 (68.9)	<0.001*	43 (7.7)	519 (92.3)	<0.001*	2 (3.4)	56 (96.6)	0.294
	4C–5	62 (55.9)	49 (44.1)		15 (30.6)	34 (69.4)		1 (14.3)	6 (85.7)	
Needle thickness	**9–12 G**	20 (27.8)	52 (72.2)	0.039*	2 (4.4)	43 (95.6)	0.298	2 (25.0)	6 (75.0)	0.038*
	14–16 G	124 (40.9)	179 (59.1)		56 (9.9)	510 (90.1)		1 (1.8)	56 (98.2)	
Number of samples	**<4**	51 (49.0)	53 (51.0)	0.009*	26 (12.3)	186 (87.7)	0.088	1 (5.9)	16 (94.1)	1.000
	≥4	93 (34.3)	178 (65.7)		32 (8.0)	367 (92.0)		2 (4.2)	46 (95.8)	

Benign, benign and stable on follow-up; *$P < 0.05$. ADH, atypical ductal hyperplasia; LN, lobular neoplasia; RS, radial scar; IP, intraductal papilloma; FEA, flat epithelial atypia.
MRI, magnetic resonance imaging; BI-RADS, Breast Imaging Reporting and Data System.

diagnosed using VAB with no residual microcalcifications in concordant findings. The World Health Organization Working Group proposed observation as an acceptable management strategy for radiological–pathological correlated pure FEA.[46]

The upgrade rate was 4.6% for RSs in this study. When the lesion was ≤15 mm, the rate of associated malignancy at surgical excision was 2.2% (1/46 cases). There are variable results in the literature, ranging between 0% and 40%.[47] In a meta-analysis of 49 studies, including 3.163 RS cases with surgical outcomes, the pooled upgrade rate was 7%; yet in the subtype assessed with an 8 to 11 G VAB needle and lacking atypia, this rate was 1%.[48] Li et al.[49] and Conlon et al.[50] found 0.9% and 2% upgrade rates in patients without atypia. Accordingly, imaging surveillance seems to be a reasonable option for selected patients.

The large sample size of high-risk lesions in each subtype and the multicenter design are major strengths of the current study. This makes the statistical analysis more valuable. However, this study has several limitations, including its retrospective design, which could have resulted in missing data, and the potential differences in the clinical practices used for selecting and managing patients in different centers. Last, this study did not look at long-term follow-up results for the participants.

In conclusion, high-risk lesions identified by needle biopsy do not follow similar

Table 3. Continued

		FEA (n = 114)			LN (n = 35)			IP with atypia (n = 123)		
		Malignant n (%)	Benign n (%)	*P*	Malignant n (%)	Benign n (%)	*P*	Malignant n (%)	Benign n (%)	*P*
Mammography finding	**Microcalcification**	8	40 (83.3)	0.230	2 (10.5)	17 (89.5)	1.000	6 (66.7)	3 (33.3)	0.245
	Mass	1	12 (92.3)		0 (0)	2 (100)		21 (47.7)	23 (52.3)	
	Non mass	0(0)	14(100)		1 (16.7)	5 (83.3)		13 (68.4)	6 (31.6)	
Microcalcification morphology	**Amorphous**	3 (10.7)	25 (89.3)	0.269	1 (12.5)	7 (87.5)	1.000	2 (50.0)	2 (50.0)	0.600
	Coarse heterogeneous	1 (33.3)	2 (66.7)		0 (0)	0 (0)		2 (100)	0 (0)	
	Newly identified suspect	0 (0)	4 (100)		1 (20.0)	4 (80.0)		0 (0)	0 (0)	
	Fine linear	1 (33.3)	2 (66.7)		0 (0)	1 (100)		1 (100)	0 (0)	
	Fine pleomorphic	3 (30.0)	7 (70.0)		0 (0)	5 (100)		1 (33.3)	2 (66.7)	
Ultrasonography finding	**Mass**	0 (0)	44 (100)	0.003*	4 (19.0)	17 (81.0)	0.355	48 (42.9)	64 (57. 1)	0.077
	Non mass	7 (18.4)	31 (81.6)		1 (5.9)	16 (94.1)		7 (77.8)	2 (22.2)	
MRI finding	**Mass**	0 (0)	25 (100)	0.030*	2 (22.2)	7 (77.8)	1.000	15 (37.5)	25 (62.5)	0.084
	Non mass	6 (18.8)	26 (81.3)		4 (19.0)	17 (81.0)		7 (70.0)	3 (30.0)	
Lesion diameter	**≤1.5 cm**	1 (1.5)	67 (98.5)	0.001*	2 (5.7)	33 (94.3)	0.086	31 (38.3)	50 (61.7)	0.046*
	>1.5 cm	9 (19.6)	37 (80.4)		5 (25.0)	15 (75.0)		24 (57.1)	18 (42.9)	
BI-RADS	**3, 4A, 4B**	1 (1.1)	93 (98.9)	<0.001*	3 (6.4)	44 (93.6)	0.006*	43 (43.9)	55 (56.1)	0.711
	4C–5	9 (45.0)	11 (55.0)		4 (50.0)	4 (50.0)		12 (48.0)	13 (52.0)	
Needle thickness	**9–12 G**	3 (8.6)	32 (91.4)	1.000	2 (10.0)	18 (90.0)	1.000	1 (50.0)	1 (50.0)	1.000
	14–16 G	7 (8.9)	72 (91.1)		5 (14.3)	30 (85.7)		54 (44.6)	67 (55.4)	
Number of samples	**<4**	4 (16.0)	21 (84.0)	0.222	2 (18.2)	9 (81.8)	0.617	19 (44.2)	24 (55.8)	0.931
	≥4	6 (6.7)	83 (93.3)		5 (11.4)	39 (88.6)		36 (45.0)	44 (55.0)	

patterns; routine excision is unnecessary for every lesion. This study's upgrade rates to malignancy were related to the subtype, presence of atypia, and other variables, such as the BI-RADS score, lesion size, biopsy method used, and sampling adequacy. Because of these variables, there cannot be a general recommendation for all high-risk lesions of the breast. Clinical, radiologic, and pathologic features should all be reviewed before deciding whether surgical excision or close follow-up is most appropriate for a lesion. For ADH, although current guidelines recommend surveillance for small-volume lesions that are entirely removed through core biopsy, the recommendation remains typical management of surgical excision. IP with atypia also requires excision following CNB/VAB because of the high rate of associated malignancy. For LN, IP without atypia, pure FEA and RSs, underestimation rates were related to the BI-RADS score and, therefore, to radiology–pathology concordance, sampling adequacy, and lesion size. The upgrade rates increased with higher BI-RADS scores and lesion size in conjunction with insufficient tissue sampling. Boateng et al.[10] reported lower rates when large core needles (i.e., 9 to 11 G) were used and higher rates when 14 G needles were used. Therefore, all cases should be managed case-wise after a multidisciplinary team discussion.

Table 4. Multivariate analysis of malignancy upgrade in different subtypes of high-risk lesions according to needle thickness and lesion diameter

Pathologic subtype	Needle thickness	Lesion diameter	Benign n (%)	Malignant n (%)	Total n	*P*
ADH (n = 375)	9–12 G	≤15 mm	45 (80)	11 (20)	56	0.009*
		>15 mm	7 (44)	9 (56)	16	
	14–16 G	≤15 mm	111 (68)	53 (32)	164	0.001*
		>15 mm	68 (49)	71 (51)	139	
IP without atypia (n = 611)	9–12 G	≤15 mm	34 (100)	0 (0)	34	0.056
		>15 mm	9 (82)	2 (18)	11	
	14–16 G	≤15 mm	369 (94)	24 (6)	393	<0.001*
		>15 mm	141 (82)	32 (18)	173	
Lobular neoplasia (n = 35)	9–12 G	≤15 mm	15 (100)	0 (0)	15	0.053
		>15 mm	3 (60)	2 (40)	5	
	14–16 G	≤15 mm	18 (90)	2 (10)	20	0.631
		>15 mm	12 (80)	3 (20)	15	
Radial scar (n = 65)	9–12 G	≤15 mm	3 (75)	1 (25)	4	1.000
		>15 mm	3 (100)	0 (0)	3	
	14–16 G	≤15 mm	42 (100)	0 (0)	42	
		>15 mm	14 (87)	2 (13)	16	0.073
FEA (n = 79)	9–12 G	≤15 mm	22 (96)	1 (4)	23	0.266
		>15 mm	10 (83)	2 (17)	12	
	14–16 G	≤15 mm	44 (100)	0 (0)	44	0.002*
		>15 mm	28 (80)	7 (20)	35	
Atypical IP (n = 123)	9–12 G	≤15 mm	1(50)	1 (50)	2	-
		>15 mm	0 (0)	0 (0)	-	
	14–16 G	≤15 mm	49 (62)	30 (38)	79	0.043*
		>15 mm	18 (43)	24 (57)	42	

Benign, benign and stable on follow-up; *$P < 0.05$. ADH, atypical ductal hyperplasia; IP, intraductal papilloma; FEA, flat epithelial atypia.

Conflict of interest disclosure

The authors declared no conflicts of interest.

References

1. Falomo E, Adejumo C, Carson KA, Harvey S, Mullen L, Myers K. Variability in the management recommendations given for high-risk breast lesions detected on image-guided core needle biopsy at U.S. Academic Institutions. *Curr Probl Diagn Radiol.* 2019;48(5):462-466. [CrossRef]
2. Thomas PS. Diagnosis and management of high-risk breast lesions. *J Natl Compr Canc Netw.* 2018;16(11):1391-1396. [CrossRef]
3. Gulla S, Lancaster R, De Los Santos J. High-risk breast lesions and current management. *Semin Roentgenol.* 2018;53(4):252-260. [CrossRef]
4. Nakhlis F. How do we approach benign proliferative lesions? *Curr Oncol Rep.* 2018;20(4):34. [CrossRef]
5. Bick U, Trimboli RM, Athanasiou A, et al. Image-guided breast biopsy and localisation: recommendations for information to women and referring physicians by the European Society of Breast Imaging. *Insights Imaging.* 2020;11(1):12. [CrossRef]
6. Mooney KL, Bassett LW, Apple SK. Upgrade rates of high-risk breast lesions diagnosed on core needle biopsy: a single-institution experience and literature review. *Mod Pathol.* 2016;29(12):1471-1484. [CrossRef]
7. Bianchi S, Caini S, Renne G, et al. Positive predictive value for malignancy on surgical excision of breast lesions of uncertain malignant potential (B3) diagnosed by stereotactic vacuum-assisted needle core biopsy (VANCB): a large multi-institutional study in Italy. *Breast.* 2011;20(3):264-270. [CrossRef]
8. Lucioni M, Rossi C, Lomoro P, et al. Positive predictive value for malignancy of uncertain malignant potential (B3) breast lesions diagnosed on vacuum-assisted biopsy (VAB): is surgical excision still recommended? *Eur Radiol.* 2021;31(2):920-927. [CrossRef]
9. Nizri E, Schneebaum S, Klausner JM, Menes TS. Current management practice of breast borderline lesions-need for further research and guidelines. *Am J Surg.* 2012;203(6):721-725. [CrossRef]
10. Boateng S, Tirada N, Khorjekar G, Richards S, Ioffe O. Excision or observation: the dilemma of managing high-risk breast lesions. *Curr Probl Diagn Radiol.* 2020;49(2):124-132. [CrossRef]
11. Pinder SE, Shaaban A, Deb R, et al. NHS breast screening multidisciplinary working group guidelines for the diagnosis and management of breast lesions of uncertain malignant potential on core biopsy (B3 lesions). *Clin Radiol.* 2018;73(8):682-692. [CrossRef]
12. Wells CAAI, Apostolikas N, Bellocq JP. Quality assurance guidelines for pathology. In: Perry NMBM, de Wolf C, editors. EC working group on breast screening pathology: Quality assurance guidelines for pathology in mammography screening – open biopsy and resection specimens European guidelines for quality assurance in mammography screening. 4th ed. Luxembourg: Office for Official Publications of the European Communities; 2006:219-256. [CrossRef]
13. Shaaban AM, Sharma N. Management of B3 lesions-practical issues. *Current Breast Cancer Reports.* 2019;11(2):83-88. [CrossRef]
14. Houssami N, Ciatto S, Bilous M, Vezzosi V, Bianchi S. Borderline breast core needle histology: predictive values for malignancy in lesions of uncertain malignant potential (B3). *Br J Cancer.* 2007;96(8):1253-1257. [CrossRef]
15. Strachan C, Horgan K, Millican-Slater RA, Shaaban AM, Sharma N. Outcome of a new patient pathway for managing B3 breast lesions by vacuum-assisted biopsy: time to

change current UK practice? *J Clin Pathol.* 2016;69(3):248-254. [CrossRef]

16. Georgian-Smith D, Lawton TJ. Variations in physician recommendations for surgery after diagnosis of a high-risk lesion on breast core needle biopsy. *AJR Am J Roentgenol.* 2012;198(2):256-263. [CrossRef]
17. Lawton TJ, Georgian-Smith D. Excision of high-risk breast lesions on needle biopsy: is there a standard of core? *AJR Am J Roentgenol.* 2009;192(5):W268. [CrossRef]
18. Rakha EA, Lee AH, Jenkins JA, Murphy AE, Hamilton LJ, Ellis IO. Characterization and outcome of breast needle core biopsy diagnoses of lesions of uncertain malignant potential (B3) in abnormalities detected by mammographic screening. *Int J Cancer.* 2011;129(6):1417-1424. [CrossRef]
19. de Beça FF, Rasteiro C, Correia A, Costa S, Amendoeira I. Improved malignancy prediction by B3 breast lesions subclassification. *Ann Diagn Pathol.* 2013;17(5):434-436. [CrossRef]
20. Falomo E, Adejumo C, Carson KA, Harvey S, Mullen L, Myers K. Variability in the management recommendations given for high-risk breast lesions detected on image-guided core needle biopsy at U.S. Academic Institutions. *Curr Probl Diagn Radiol.* 2019;48(5):462-466. [CrossRef]
21. Co M, Kwong A, Shek T. Factors affecting the under-diagnosis of atypical ductal hyperplasia diagnosed by core needle biopsies - A 10-year retrospective study and review of the literature. *Int J Surg.* 2018;49:27-31. [CrossRef]
22. Nguyen CV, Albarracin CT, Whitman GJ, Lopez A, Sneige N. Atypical ductal hyperplasia in directional vacuum-assisted biopsy of breast microcalcifications: considerations for surgical excision. *Ann Surg Oncol.* 2011;18(3):752-761. [CrossRef]
23. Peña A, Shah SS, Fazzio RT, et al. Multivariate model to identify women at low risk of cancer upgrade after a core needle biopsy diagnosis of atypical ductal hyperplasia. *Breast Cancer Res Treat.* 2017;164(2):295-304. [CrossRef]
24. Caplain A, Drouet Y, Peyron M, et al. Management of patients diagnosed with atypical ductal hyperplasia by vacuum-assisted core biopsy: a prospective assessment of the guidelines used at our institution. *Am J Surg.* 2014;208(2):260-267. [CrossRef]
25. Schiaffino S, Massone E, Gristina L, et al. Vacuum assisted breast biopsy (VaB) excision of subcentimeter microcalcifications as an alternative to open biopsy for atypical ductal hyperplasia. *Br J Radiol.* 2018;91(1085):20180003. [CrossRef]
26. Krishnamurthy S, Bevers T, Kuerer H, Yang WT. Multidisciplinary considerations in the management of high-disk breast lesions. *AJR Am J Roentgenol.* 2012;198(2):W132-W140. [CrossRef]
27. Brem RF, Lechner MC, Jackman RJ, et al. Lobular neoplasia at percutaneous breast biopsy: variables associated with carcinoma at surgical excision. *AJR Am J Roentgenol.* 2008;190(3):637-641. [CrossRef]
28. Cohen MA. Cancer upgrades at excisional biopsy after diagnosis of atypical lobular hyperplasia or lobular carcinoma in situ at core needle biopsy: some reasons why. *Radiology.* 2004;231(3):617-621. [CrossRef]
29. Hussain M, Cunnick GH. Management of lobular carcinoma in-situ and atypical lobular hyperplasia of the breast--a review. *Eur J Surg Oncol.* 2011;37(4):279-289. [CrossRef]
30. Chaudhary S, Lawrence L, McGinty G, Kostroff K, Bhuiya T. Classic lobular neoplasia on core biopsy: a clinical and radio-pathologic correlation study with follow-up excision biopsy. *Mod Pathol.* 2013;26(6):762-771. [CrossRef]
31. Murray MP, Luedtke C, Liberman L, Nehhozina T, Akram M, Brogi E. Classic lobular carcinoma in situ and atypical lobular hyperplasia at percutaneous breast core biopsy: outcomes of prospective excision. *Cancer.* 2013;119(5):1073-1079. [CrossRef]
32. Nakhlis F, Gilmore L, Gelman R, et al. Incidence of adjacent synchronous invasive carcinoma and/or ductal carcinoma in-situ in patients with lobular neoplasia on core biopsy: results from a prospective multi-institutional registry (TBCRC 020). *Ann Surg Oncol.* 2016;23(3):722-728. [CrossRef]
33. Hwang H, Barke LD, Mendelson EB, Susnik B. Atypical lobular hyperplasia and classic lobular carcinoma in situ in core biopsy specimens: routine excision is not necessary. *Mod Pathol.* 2008;21(10):1208-1216. [CrossRef]
34. Morrow M, Schnitt SJ, Norton L. Current management of lesions associated with an increased risk of breast cancer. *Nat Rev Clin Oncol.* 2015;12(4):227-238. [CrossRef]
35. Wen X, Cheng W. Nonmalignant breast papillary lesions at core-needle biopsy: a meta-analysis of underestimation and influencing factors. *Ann Surg Oncol.* 2013;20(1):94-101. [CrossRef]
36. Ahn Sk, Han W, Moon HG, et al. Management of benign papilloma without atypia diagnosed at ultrasound guided core needle biopsy: Scoring system for predicting malignancy. *Eur J Surg.* 2018;44(1):53-58. [CrossRef]
37. Zaleskia M, Chenb YA, Chetlenc AL, et al. Should we excise? Are there any clinical or histologic features that predict upgrade in papillomas, incidental or non-incidental? *Ann Diagn Pathol.* 2018;35:62-68. [CrossRef]
38. Mosier AD, Keylock J, Smith DV. Benign papillomas diagnosed on large gauge vacuum assisted core needle biopsy which span <1.5 cm do not need surgical excision. *Breast J.* 2013;19(6);611-617. [CrossRef]
39. Ko D, Kang E, Park SY, et al. The management strategy of benign solitary intraductal papilloma on breast core biopsy. *Clin Breast Cancer.* 2017;17(5):367-372. [CrossRef]
40. Pareja F, Corben A, Brennan S, et al. Breast intraductal papillomas without atypia in radiologic-pathologic concordant core needle biopsies: Rate of upgrade to carcinoma at excision. *Cancer.* 2016;122(18):2819-2827. [CrossRef]
41. Menes TS, Rosenberg R, Balch S, Jaffer S, Kerlikowske K, Miglioretti DL. Upgrade of high-risk breast lesions detected on mammography in the Breast Cancer Surveillance Consortium. *Am J Surg.* 2014;207(1):24-31. [CrossRef]
42. Piubello Q, Parisi A, Eccher A, Barbazeni G, Franchini Z, Iannucci A. Flat epithelial atypia on core needle biopsy: which is the right management? *Am J Surg Pathol.* 2009;33(7): 1078-1084. [CrossRef]
43. Villa A, Chiesa F, Massa T, et al. Flat epithelial atypia: comparison between 9-gauge and 11-gauge devices. *Clin Breast Cancer.* 2013;13(6):450-454. [CrossRef]
44. Wahab RA, Lee SJ, Mulligan ME, Zhang B, Mahoney MC. Upgrade rate of pure flat epithelial atypia diagnosed at core needle biopsy: a systematic review and meta-analysis. *Radiol Imaging Cancer.* 2021;3(1):e200116. [CrossRef]
45. Schiaffino S, Gristina L, Villa A, et al. Flat epithelial atypia: conservative management of patients without residual microcalcifications post-vacuum-assisted breast biopsy. *Br J Radiol.* 2018;91(1081):20170484. [CrossRef]
46. Verschuur-Maes AH, van Deurzen CH, Monninkhof EM, van Diest PJ. Columnar cell lesions on breast needle biopsies: is surgical excision necessary? A systematic review. *Ann Surg.* 2012;255(2):259-265. [CrossRef]
47. Linda A, Zuiani C, Furlan A, et al. Radial scars without atypia diagnosed at imaging-guided needle biopsy: How often Is associated malignancy found at subsequent surgical excision, and do mammography and sonography predict which lesions are malignant? *AJR Am J Roentgenol.* 2010;194(4):1146-1151. [CrossRef]
48. Farshid G, Buckley E. Meta-analysis of upgrade rates in 3163 radial scars excised after needle core biopsy diagnosis. *Breast Cancer Res Treat.* 2019;174(1):165-177. [CrossRef]
49. Li Z, Ranade A, Zhao C. Pathologic findings of follow-up surgical excision for radial scar on breast core needle biopsy. *Hum Pathol.* 2016;48;76-80. [CrossRef]
50. Conlon N, D'Arcy C, Kaplan JB, et al. Radial scar at image-guided needle biopsy: is excision necessary? *Am J Surg Pathol.* 2015;39(6):779-785. [CrossRef]

Diagn Interv Radiol 2023; DOI: 10.4274/dir.2022.22826

BREAST IMAGING

ORIGINAL ARTICLE

Copyright@Author(s) - Available online at dirjournal.org.
Content of this journal is licensed under a Creative Commons Attribution-NonCommercial 4.0 International License.

Improved breast lesion detection in mammogram images using a deep neural network

Wen Zhou
Xiaodong Zhang
Jia Ding
Lingbo Deng
Guanxun Cheng
Xiaoying Wang

PURPOSE

This study aimed to investigate the effect of using a deep neural network (DNN) in breast cancer (BC) detection.

METHODS

In this retrospective study, a DNN-based model was constructed from a total of 880 mammograms that 220 patients underwent between April and June 2020. The mammograms were reviewed by two senior and two junior radiologists with and without the aid of the DNN model. The performance of the network was assessed by comparing the area under the curve (AUC) and receiver operating characteristic curves for the detection of four features of malignancy (masses, calcifications, asymmetries, and architectural distortions), with and without the aid of the DNN model and by the senior and junior radiologists. Additionally, the effect of utilizing the DNN on diagnosis time for both the senior and junior radiologists was evaluated.

RESULTS

The AUCs of the model for the detection of mass and calcification were 0.877 and 0.937, respectively. In the senior radiologist group, the AUC values for evaluation of mass, calcification, and asymmetric compaction were significantly higher with the DNN model than those obtained without the model. Similar effects were observed in the junior radiologist group, but the increase in the AUC values was even more dramatic. The median mammogram assessment time of the junior and senior radiologists was 572 (357–951) s, and 273.5 (129–469) s, respectively, with the DNN model, and the corresponding assessment time without the model, was 739 (445–1003) s and 321 (195–491) s, respectively.

CONCLUSION

The DNN model exhibited high accuracy in detecting the four named features of BC and effectively shortened the review time by both senior and junior radiologists.

KEYWORDS

Breast cancer, deep neural network, mammography

From the Department of Radiology (W.Z., X.Z., X.W. ✉ wangxiaoying@bjmu.edu.cn), Peking University First Hospital, Beijing, China; Department of Radiology (W.Z., L.D., G.C. ✉ chengguanxun@outlook.com) Peking University Shenzhen Hospital, Shenzhen, China; (J.D.), Beijing Yizhun Medical AI Co., Ltd, Beijing, China.

Received 02 September 2021; revision requested 05 March 2022; last revision received 22 July 2022; accepted 27 August 2022.

Epub: 20.03.2023

Publication date: 21.07.2023

DOI: 10.4274/dir.2022.22826

Breast cancer (BC) is the most common cancer and the second leading cause of cancer deaths in women worldwide,[1] but there is a large difference in the survival rate of BC patients who live in different countries. In particular, the five-year survival rate of BC patients in China is much lower than that in developed countries, such as the United States.[2] One of the main reasons for this discrepancy is the low early diagnosis rate in China.[3] Therefore, the accurate and early diagnosis of BC is critical for early treatment options and for reducing BC mortality in China.

Mammography is the most effective screening method for BC and has been shown to increase the detection rate and reduce the mortality rate of BC.[4-6] Mammography images can clearly show the tissues and glands of the breast as well as the surrounding areas through non-invasive methods. Such images facilitate the identification of lumps, burrs, slight calci-

You may cite this article as: Zhou W, Zhang X, Ding J, Deng L, Cheng G, Wang X. Improved breast lesion detection in mammogram images using a deep neural network. *Diagn Interv Radiol.* 2023;29(4):588-595.

fications, and cancer spread and metastasis in the breast. Notably, mammography approaches have advantages over similar imaging techniques, such as ultrasound, in detecting microcalcifications.[7] However, it is very difficult to locate and characterize a lesion, and the consistency of doing so across doctors is very poor.[8,9] Lehman et al.[10] reported that the average sensitivity and specificity of reviewing mammography images were 86.9% and 88.9%, respectively. In addition, the false positive and false negative rates of mammography assessment are approximately 7%–12% and 4%–34%, respectively.[11,12] Nevertheless, mammography remains the gold standard for the detection of malignancy, with its high resolution enabling the detection of masses, microcalcifications, asymmetries, and architectural distortions. For the detection of microcalcifications, in particular, mammography has distinct advantages over ultrasound. To detect malignancy, radiologists have to review a large number of images, particularly with digital breast tomosynthesis, which impacts interpretation time. Additionally, because the detection of malignancy depends on factors such as breast density, identifying and accurately localizing a lesion can differ from one physician to another.

Several machine learning algorithms have been applied to the research of mammography data in recent years. In 2014, Wang et al.[13] proposed a breast tumor detection algorithm based on the extreme learning machine, which performs breast tumor edge segmentation for the microscopic detection of a tumor. Similarly, Agrawal et al.[14] used a support vector machine to perform feature extraction on the segmented region in the mammogram X-ray image and then target detection, which effectively segmented the tumor mass region within the normal chest parenchyma. Deep learning approaches used in medical imaging fields leverage the use of more sophisticated algorithms and image processing technology to assess samples with a more refined decomposition of tissue properties. The continuing maturity of deep learning technology can help doctors perform more accurate localization and diagnosis of pathological tissues. These algorithms were found to decrease interpretation time, which facilitates more rapid treatment.

Main points

- The use of a deep neural network (DNN) improved breast cancer detection.
- With the help of the DNN, radiologists could more accurately detect tumor mass, calcification, and asymmetric compaction.
- An auxiliary effect of the deep learning model on doctors of different seniority was that it increased the detection accuracy of inexperienced doctors.
- The deep learning model shortened the average mammogram assessment time for both junior and senior radiologists.

In recent years, many scholars have applied deep learning algorithms to medical image recognition problems.[15,16] Bayramoglu et al.[17] proposed two different architectures based on a convolutional neural network to predict malignant breast tumors. Zhang et al.[18] constructed a two-layer deep learning architecture to automatically extract imaging features for classification, and their model performed well in terms of classification accuracy, sensitivity, and specificity. Mohamed et al.[19] built and trained a convolutional neural network model based on mammography images to accurately and rapidly classify breast density to clarify the risk of BC, and the area under the curve (AUC) of the model classification reached 0.992.

However, current deep learning approaches in BC research are mostly based on pathological images or algorithm optimization techniques that aim to better segment images. Therefore, it is necessary to establish a reliable model for assessing BC in mammography images that is comparable to a radiologist's assessment. This study investigates the effect of a deep neural network (DNN) on BC detection in clinical practice.

Methods

Study design

The study was approved by the research ethics review board of Peking University (approval number: 2020-011), and informed consent was waived because it was a retrospective study. Mammography images acquired consecutively between April 2020 and June 2020 at a single institution were analyzed, and all of them were anonymized. The exclusion criteria included cases with prior benign and malignant breast surgery, breast reduction, breast augmentation, chemotherapy, radiation therapy, or unknown results from prior biopsies. All mammography analyses were performed by two radiologists experienced in assessing breast mammography images. The lesions were divided into four categories according to the corresponding mammograms, magnetic resonance imaging (MRI), and pathological results. True-positive/negative and false-positive/negative cases were identified by a positive/negative result of the radiologist assessment and confirmation or negation based on MRI and/or pathological evaluation, respectively. Four mammogram images were acquired for each patient and included two images in a mediolateral oblique projection (MLO) and two images in a cranial-caudal projection (CC).

Development of a DNN model

Faster R-CNN was employed as the deep learning framework for model detection, and ResNet50 was used for feature extraction. The feature pyramid network was used to construct new features based on data augmentation techniques. Features were fused in different convolutional layers of the ResNet, ensuring that the model incorporated multi-scale information to improve the ability to detect small lesions. The lesion detection network is shown in Figure 1.

Image resizing for uniform resolution: The size of the input image was converted to a pixel size of 0.15 mm x 0.15 mm. Random cropping was used for data expansion at a rate of 0.8-1.2 times the size of the original image. Images were also randomly flipped horizontally. The model training used four NVIDIA TITAN RTX P8 graphics cards with a configuration of 28 GB video memory and a batch size of four images.

Algorithm optimization: The momentum stochastic gradient descent learning rate was 0.005. The learning rate was adjusted according to the number of iterations using the learning rate scheduler method for learning rate decay. The L2-norm regularization parameter weight decay was 0.0001. The maximum number of iterations was set to 25,000, and the number of warm-start iterations was 500. In the test phase, horizontal and vertical flips were used to expand the data.

Image gray-level normalization: If the original gray value was not compatible with the algorithm for subsequent prediction, the grayscale of the image was normalized to ensure consistency in the gray value range across different images. The grayscale of the segmented region was recorded, and the gray level was linearly mapped according to the statistical results. This procedure was performed so that 90% of the gray value pixels were in the range of 0–1, 5% of the gray value pixels were <0, and 5% of the gray value pixels were >1.

Breast segmentation: The background of the breast mammogram images was re-

moved, and only the breast was retained. The grayscale distribution histogram of the image was recorded, and the threshold value was obtained using the triangle method. The image pixels with a gray level higher than the threshold were segmented as the breast. The minimum rectangular range that contained the breast was then taken as the input of the subsequent module.

Quadrant and depth analysis of the lesion: The relationship between the images in the MLO and CC position was judged according to multiple features. After the detection stage, the location, size, type, and probability of a lesion(s) were obtained. Then, more features of the lesion were analyzed to match lesions more accurately. These features included the quadrant of the lesion and the distance between the lesion and the nipple.

Lesion quadrant division: A mask was used to indicate the location of the lesions, and the classification network was used to classify the MLO lesions. The lesions in the MLO position were divided into five regions: upper, middle, lower, axillary tail, and areola. The lesions in the CC position were divided into four quadrants: outer, middle, inner, and areola.

Lesion depth regression: The whole mammogram image and the mask of the target lesion on the image were spliced together as two channels of the image. The distance from the lesion to the nipple was obtained using the regression network. Distance 0 represented the nipple, and distance 1 represented the pectoralis major muscle.

Focus matching: The lesion features in the CC and MLO positions were combined to predict the probability of two lesions being the same lesion using the GBTD method. To construct a matching probability matrix, each element on the matrix represented the matching probability of the two lesions. The matching relationship between MLO and CC lesions was obtained according to a greedy algorithm. The remaining lesions without matching or with a matching probability that was too small were considered as a single lesion, and no matching relationship was given.

The classification of benign and malignant lesions: Multi-task learning was used to predict benign and malignant lesions as well as their morphological distribution at the same time. The two tasks promote and complement each other and make the overall performance more accurate than conducting one task alone. The data from 14,811 cases were used for training, comprising 7,519 cases of labeled data and 7,292 cases of unlabeled data. Among the labeled data, the labeled regions of interest included 10,480 masses, 6,358 calcifications, 1,713 asymmetries, and 311 architectural distortions. For each lesion, the category of the lesion, such as mass or calcification, was marked, and the outline of the lesion was drawn. The backbone network of the detection model used transfer learning, and the network was trained with a large amount of ImageNet data that was transferred to the breast detection model. This has been shown to significantly improve the detection performance of the model. The percentages of the training set and the test set were 80% and 20%, respectively.

For robustness, we trained the DNN algorithm in three random 80% partitions of the training set. After the detection of lesions, multi-task learning was used to analyze the shape, edges, and other attributes of the lesions and to predict their benign or malignant nature.

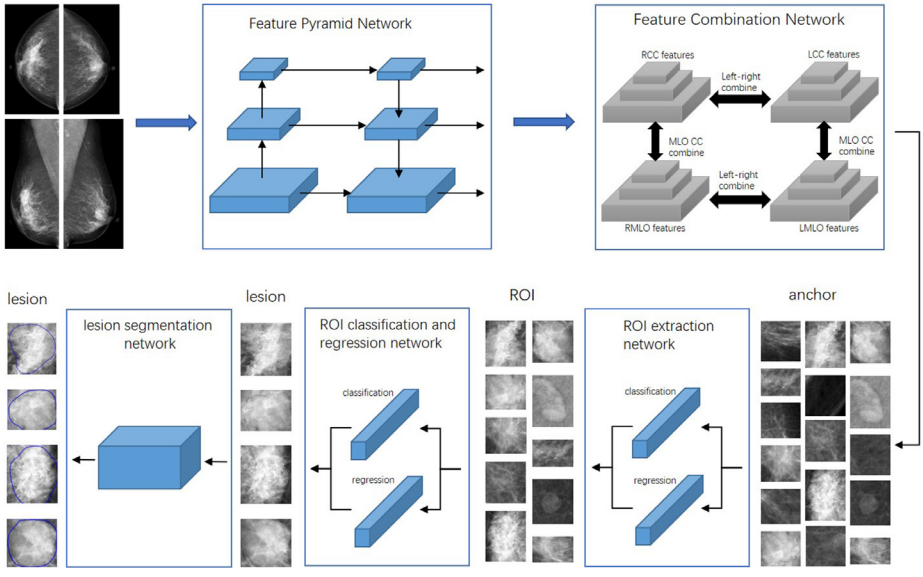

Figure 1. Lesion Detection Network. The input mammograms include two cranial-caudal projection (CC) images and two mediolateral oblique projection (MLO) images, the features of which were extracted using ResNet50. The features were then fused using a Feature Combination Network comprised of right and left MLO and CC images. New features were also constructed with multi-scale information to improve the ability to detect small lesions. Feature pyramid network: Features of the input images were extracted, and several layers of features from fine to abstract were obtained. Feature fusion network: the information from four molybdenum palladium images of the same patient was used to improve the quality of the features and improve lesion detection. This framework included a left and right feature fusion network and MLO/CC feature fusion network. Key area extraction network: a series of anchors were set with different positions, sizes, and aspect ratios using a sliding window. The key area extraction network classified and regressed each anchor to predict whether the anchor was the key area and where the key area was located. ROI, region of interest.

The reading time and breast imaging reporting and data system (BI-RADS) score of senior and junior radiologists with and without the help of a DNN model

A total of 880 images from 220 patients were used to test the impact of the DNN model on radiologist assessment. Two senior radiologists (with 16 and 18 years of mammogram reading experience) and two junior ones (with 1 and 2 years of mammogram reading experience) reviewed all four mammogram images from each study in random order, both with and without the aid of the DNN. The second reading was performed three weeks later. For both readings, the order of images was randomized on an individual assessor basis. All the radiologists were blinded to the patient information. For each patient, the radiologists provided a BI-RADS score according to the following scale: 1 = negative; 2 = benign; 3 = probably benign; 4 = suspicious abnormality (a possibility of malignancy or cancer); and 5 = highly likely to be malignant. Reading times were measured from the opening of a new case to the validation of the lesions and the BI-RADS score. Both the reading time and BI-RADS score were recorded for later analysis.

Statistical analysis

All statistical analyses were performed using IBM SPSS 20.0 (SPSS Inc, Chicago, IL, USA) and MedCalc statistical software (ver-

sion 20.026, MedCalc Software). Descriptive statistics of the data are presented with n (%) and are shown as median (min–max) for non-normalized variables. The normality test was determined using the Shapiro–Wilk test. Comparisons between the two groups were performed using the Wilcoxon signed-rank test for variables with a non-normal distribution. Receiver operating characteristic (ROC) curves and the AUC were used to evaluate the performance of the DNN model as well as the senior and junior radiologists, with and without the help of artificial intelligence (AI). The sensitivity, specificity, and Youden index of the ROC curves were calculated, and the highest Youden index was used to determine the cut-off value. Comparisons of the ROC curves were evaluated using a Delong test. The inter-rater agreement of the senior and junior radiologists in terms of the location and BI-RADS assessment was evaluated using a kappa coefficient. The kappa coefficient for the strength of the agreement was categorized as follows: −1, none; 0, poor; 0.0–0.20, slight; 0.21–0.40, fair; 0.41–0.60, moderate; 0.61–0.80, substantial; and 0.81–1: almost perfect.[20] A *P* value <0.05 was considered statistically significant.

Results

The ROC curves of the models for the four distinct lesion features are shown in Figure 2. The AUCs of the model for mass, calcification, asymmetric compaction, and structural distortion were 0.877 [95% confidence interval (CI), 0.843–0.906], 0.937 (95% CI, 0.910–0.958), 0.697 (95% CI, 0.652–0.740), and 0.624 (95% CI, 0.577–0.669), respectively. The sensitivity values for the detection of the same features were 76.71%, 89.73%, 73.68%, and 99.77%, respectively. Similarly, the specificity values for these four features were 98.66%, 97.68%, 65.76%, and 25.00%, respectively (Table 1).

Figure 3 displays the ROC curves of the senior and junior radiologist assessments with and without the help of the model. The corresponding AUC, specificity, and sensitivity values are listed in Table 1. For senior radiologists, the AUC values of the ROC curves for assessments based on mass with and without the help of the model were 0.926 and 0.909, respectively. Similarly, for junior radiologists, the ROC curves were 0.879 and 0.803 with and without the help of the model, respectively. Regarding calcification, the AUC values of the ROC curves for the senior radiologists were 0.955 and 0.946 with and without the aid of the model, respectively. In addition, the AUC values of the calcification ROC curves for the junior radiologists were 0.932 and 0.898 with and without the aid of the model, respectively. The AUCs between the radiologists with and without the aid of the model were compared using a Delong test (Table 2). In general, the AUCs of the junior radiologists for mass and calcification were significantly larger with the DNN model than those without the model (both *P* < 0.001), but there were no significant differ-

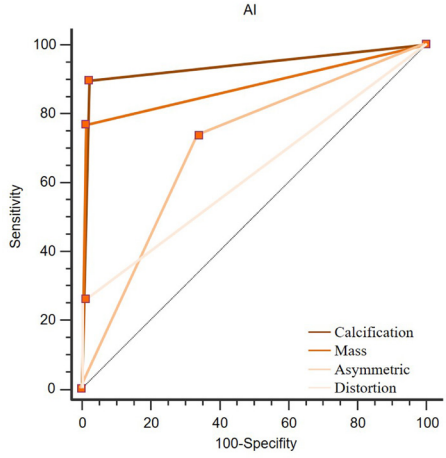

Figure 2. Receiver operating characteristic curve of the model for the detection of mass, calcification, asymmetry, and distortion. AI, artificial intelligence.

Table 1. AUC values and related parameters for the detection of the four lesion features of mass, calcification, asymmetry, and distortion by senior and junior radiologists with and without the assistance of the deep neural network model

Features		AUC	SE	*P* value	Sensitivity	Specificity	Cut-off
	AI	0.877 (0.843 – 0.906)	0.018	<0.001	76.71	98.66	0.754
	J_noAI	0.803 (0.775 – 0.829)	0.014	<0.001	61.3	99.33	0.606
Mass	**J_AI**	0.879 (0.856 – 0.900)	0.013	<0.001	77.74	98.15	0.759
	S_noAI	0.909 (0.888 – 0.927)	0.011	<0.001	82.53	99.33	0.819
	S_AI	0.926 (0.906 – 0.942)	0.010	<0.001	85.62	99.5	0.851
	AI	0.937 (0.910 – 0.958)	0.012	<0.001	89.73	97.68	0.874
	J_noAI	0.898 (0.877– 0.918)	0.011	<0.001	80.27	99.42	0.797
Calcification	**J_AI**	0.932 (0.913 – 0.947)	0.009	<0.001	87.3	99.03	0.863
	S_noAI	0.946 (0.929 – 0.960)	0.008	<0.001	89.73	99.42	0.892
	S_AI	0.955 (0.939 – 0.968)	0.007	<0.001	91.62	99.42	0.910
	AI	0.697 (0.652 – 0.740)	0.038	<0.001	73.68	65.76	0.395
	J_noAI	0.626 (0.593 – 0.658)	0.028	<0.001	34.21	91.01	0.252
Asymmetric	**J_AI**	0.661 (0.628 – 0.692)	0.030	<0.001	51.32	80.79	0.321
	S_noAI	0.782 (0.753 – 0.808)	0.028	<0.001	61.84	94.46	0.563
	S_AI	0.801 (0.774 – 0.827)	0.026	<0.001	72.37	87.93	0.603
	AI	0.624 (0.577 – 0.669)	0.065	0.058	25	99.77	0.248
	J_noAI	0.516 (0.482 – 0.549)	0.021	0.516	4.17	98.96	0.031
Distortion	**J_AI**	0.539 (0.505 – 0.572)	0.029	0.179	8.33	99.42	0.078
	S_noAI	0.679 (0.647 – 0.709)	0.051	0.000	37.5	98.26	0.358
	S_AI	0.644 (0.611 – 0.675)	0.047	0.003	29.17	99.54	0.287

AUC, area under the curve; SE, standard error; J_noAI, junior radiologists unaided; J_AI, junior radiologists aided; S_noAI, senior radiologists unaided; S_AI, senior radiologists aided. AI, artificial intelligence.

ences for the senior radiologists ($P = 0.081$ for mass and $P = 0.061$ for calcification). However, the AUCs for asymmetric compaction and structural distortion showed no difference between the radiologists with or without the aid of the model (for asymmetric compaction, $P = 0.244$ for junior radiologists and $P = 0.475$ for senior radiologists; for structural distortion, $P = 0.527$ for junior radiologists and $P = 0.554$ for senior radiologists). On the other hand, the AUCs of the senior radiologist assessments for mass, calcification, asymmetry, and distortion were significantly larger than those of the junior radiologist assessments with ($P < 0.001$, $P = 0.003$, $P < 0.001$, and $P = 0.044$) and without the aid of the model (all $P < 0.001$) (Table 2).

The review times of the radiologists in the aided and unaided scenarios were compared using a Wilcoxon signed-rank test (Table 3). The median reading times of the senior and junior radiologists unaided were 321 (195–491) s and 739 (445–1003) s, respectively. With the help of the model, the median reading times of the senior and junior radiologists fell to 273.5 (129–469) s and 572 (357–951) s, respectively, representing a reduction of 41.9 s (13.6%) for the senior radiologists and 153.5 s (20.5%) for the junior radiologists. The median review times of the senior and junior radiologists were both significantly shorter with the DNN model than those without the model (both $P < 0.001$) (Table 3). Figure 4 shows an example of using AI to help detect linear pleomorphic calcifications in the upper left outer quadrant, which suggests a BI-RADS score of 4C. 4C means high suspicion for malignancy (>50% to <95% likelihood of malignancy).

The inter-rater agreement of the senior and junior radiologists in terms of tumor mass, calcification, asymmetry, and distortion assessment was evaluated using the kappa coefficient. As shown in Table 4, for junior radiologists, the kappa coefficients of mass assessment were 0.836 and 0.676 with and without the help of DNN, respectively, and those of calcification assessment were 0.913 and 0.839 with and without the help of DNN, respectively. These values indicate that the reliability of the junior radiologist assessments regarding mass and calcification can be improved with the help of the DNN model.

Discussion

In the current study, a DNN model was built and found to be helpful in the detection of masses, calcifications, asymmetries, and architectural distortions representing BC. The model was able to significantly shorten the review time of mammogram images by both senior and junior radiologists. Typically, radiologists analyze multiple mammographic images of the same patient, which is time- and energy-consuming. The DNN model proposed in the current work is very promising for clinical application and may be used to help radiologists more efficiently review mammography images, enhancing the accuracy of their diagnosis with the ultimate goal of improving the prognosis of BC. These advantages of the model were further exemplified by the fact that mammogram reading time decreased for both senior and junior radiologists when using AI.

Previous research has used different deep-learning methods to detect BC and has demonstrated a gradual performance improvement.[21-23] The Dialogue for Reverse Engineering Assessments and Methods challenge has tested a large number of mammograms and obtained an AUC of 0.87 with a sensitivity and specificity of 0.81 and 0.8, respectively.[24] Another study focused on categories of breast lesions according to BI-RADS scores using a deep convolutional neural network to analyze mammograms.[25] The sensitivity of this model for the detection of mass, calcification, asymmetry, and compaction was higher than 74% for each feature and is comparable with the Breast Cancer

Table 2. AUC values for the detection of the four lesion features of mass, calcification, asymmetry, and distortion by senior and junior radiologists with and without the assistance of the deep neural network model

Features	J_noAI vs. J_AI	S_AI vs. J_AI	S_noAI vs. J_noAI	S_noAI vs. S_AI
Mass	$P < 0.001$	$P < 0.001$	$P < 0.001$	$P = 0.081$
Calcification	$P < 0.001$	$P = 0.003$	$P < 0.001$	$P = 0.061$
Asymmetry	$P = 0.244$	$P < 0.001$	$P < 0.001$	$P = 0.475$
Distortion	$P = 0.527$	$P = 0.044$	$P < 0.001$	$P = 0.554$

AUC, area under the curve; J_noAI, junior radiologists unaided; J_AI, junior radiologists aided; S_noAI, senior radiologists unaided; S_AI, senior radiologists aided.

Table 3. Junior and senior radiologist review times for unaided and artificial intelligence-aided cases using the Wilcoxon signed-rank test

		Review time (seconds)		
Group		Unaided	Aided	*P* value
Junior radiologists	Median (min–max)	739 (445–1003)	572 (357–951)	<0.001
Senior radiologists	Median (min–max)	321 (195–491)	273.5 (129–469)	<0.001

Table 4. The consistency between senior and junior radiologists in recognizing mass, calcification, asymmetry, and distortion using the kappa coefficient

	Senior (without AI)		Senior (with AI)		Junior (without AI)		Junior (with AI)	
	Kappa	*P* value	Kappa	*P* value	Kappa	*P* value	Kappa	*P* value
Mass	0.861	<0.001	0.900	<0.001	0.676	<0.001	0.836	<0.001
Calcification	0.938	<0.001	0.981	<0.001	0.839	<0.001	0.913	<0.001
Asymmetric	0.495	<0.001	0.343	<0.001	0.298	<0.001	0.303	<0.001
Distortion	0.383	<0.001	0.156	0.001	-0.011	0.814	0.244	<0.001

AI, artificial intelligence.

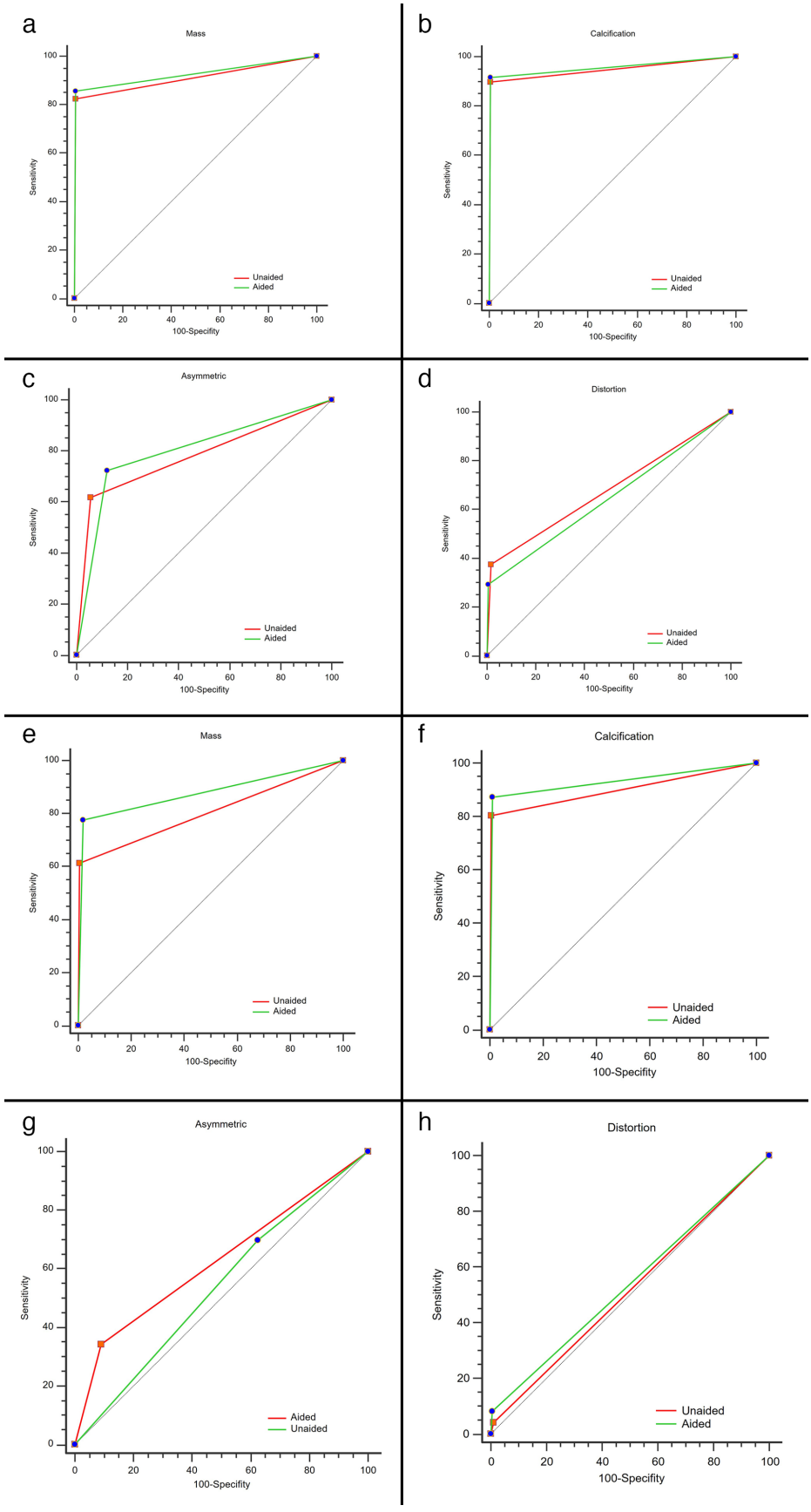

Figure 3. (a-h) Receiver operating characteristic curves of the diagnosis based on mass **(a, e)**, calcification **(b, f)**, asymmetry **(c, g)**, and structural distortion **(d, h)** by senior and junior radiologists, with or without the help of artificial intelligence.

Surveillance Consortium benchmark used in another study that exhibited a sensitivity of 75%.[10]

In this study, with the assistance of the DNN model, the radiologists were able to recognize features such as mass, calcification, asymmetry, and distortion with high sensitivity and specificity. Akselrod-Ballin et al.[26] reported that a deep learning model was able to detect 48% of the false-negative findings missed by radiologists and confirmed by surgical pathology with a sensitivity of 87%. According to the results from the present study, the time that senior and junior radiologists spent on diagnosis was significantly reduced with the use of the model, especially for junior radiologists. Therefore, it was established that a deep learning algorithm trained by experts in the field was able to better assist less experienced radiologists who are at particular risk of making diagnostic errors.

The analysis described in this paper showed that the proposed model can be used to assist junior radiologists and help improve their performance in identifying lesions when reviewing mammograms. Additionally, this study showed that when junior radiologists were provided with the assistance of the trained model, their ability to detect breast lesions significantly improved, thus diminishing diagnostic errors and improving efficiency.

There are several limitations to this study that should be noted. First, the DNN model used in the current work was verified in a dataset acquired from the same mammography vendor and manufacturer. Furthermore, the patients from whom the data were collected were all from the Peking University Shenzhen Hospital. Therefore, the results presented here must be validated using images from different vendors and populations. Second, only mammograms were analyzed in this study to improve lesion detection, and clinical information was not utilized. In clinical practice, radiologists usually review a patient's clinical history and symptoms before making a diagnosis based on mammographic data. Therefore, it would be useful to analyze whether the use of clinical information and imaging data together could help radiologists make even more accurate diagnoses. In addition, the number of patients in this study with asymmetry and structural distortion was small, which may have affected the results to a certain extent.

In conclusion, a DNN model was developed and validated using a dataset of mam-

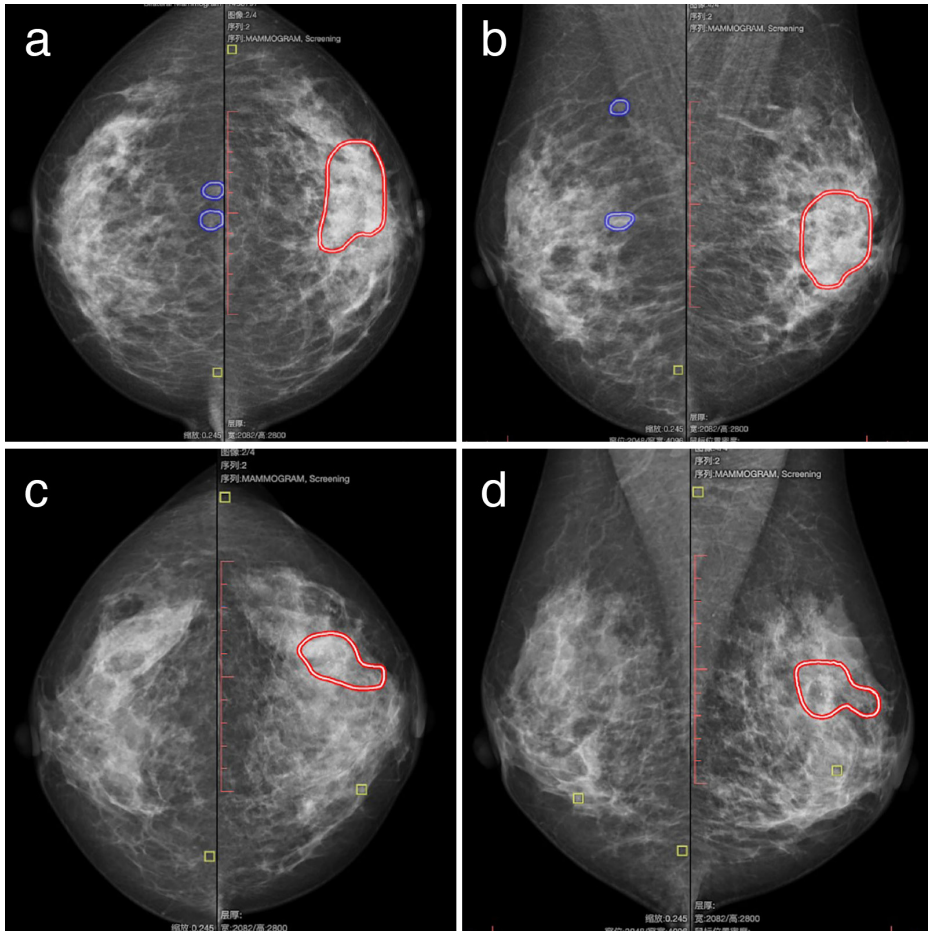

Figure 4. (a-d) Panels **(a, b)** show mammograms of a 48-year-old patient. The top-left panel **(a)** shows the craniocaudal view, and the top-right panel **(b)** shows the mediolateral oblique view of the breast lesions. An irregular high-density mass with calcification is seen in the upper outer quadrant of the left breast with a cluster of pleomorphic calcifications, and the assessment using artificial intelligence (AI) analysis is a breast imaging reporting and data system (BI-RADS) 5 (red circle). Panels **(c, d)** show mammograms of a 51-year-old patient. The bottom-left panel **(c)** shows the craniocaudal view, and the bottom-right panel **(d)** shows the mediolateral oblique view of the breast lesions. Fine linear pleomorphic calcification can be seen in the upper outer quadrant of the left breast, and the assessment using AI analysis is a BI-RADS 4C (red circle).

mograms to improve the detection of BC by radiologists. The model was especially successful at detecting the mass, calcification, asymmetric compaction, and structural distortion of BC lesions. With the assistance of the model, both senior and junior radiologists were able to recognize a lesion within a shorter review time.

Conflict of interest disclosure

The authors declared no conflicts of interest.

References

1. Bray F, Ferlay J, Soerjomataram I, Siegel RL, Torre LA, Jemal A. Global cancer statistics 2018: GLOBOCAN estimates of incidence and mortality worldwide for 36 cancers in 185 countries. *CA Cancer J Clin.* 2018;68(6):394-424. **[CrossRef]**
2. Feuer EJ, Rabin BA, Zou Z, et al. The surveillance, epidemiology, and end results cancer survival calculator SEER*CSC: validation in a managed care setting. *J Natl Cancer Inst Monogr.* 2014;2014(49):265-274. [CrossRef]
3. Feng RM, Zong YN, Cao SM, Xu RH. Current cancer situation in China: good or bad news from the 2018 Global Cancer Statistics? *Cancer Commun (Lond).* 2019;39(1):22. [CrossRef]
4. Hersch J, Jansen J, McCaffery K. Decision-making about mammographic screening: pursuing informed choice. *Climacteric.* 2018;21(3):209-213. [CrossRef]
5. Duffy SW, Vulkan D, Cuckle H, et al. Effect of mammographic screening from age 40 years on breast cancer mortality (UK Age trial): final results of a randomised, controlled trial. *Lancet Oncol.* 2020;21(9):1165-1172. [CrossRef]
6. Carles M, Martínez-Alonso M, Pons A, et al. The effect of information about the benefits and harms of mammography on women's decision-making: study protocol for a randomized controlled trial. *Trials.* 2017;18(1):426. [CrossRef]
7. Zhang K, Lu Q, Hua J, Xu J, Wu G. Positive predictive value of mammographic lymphography in the evaluation of patients with breast cancer: a preliminary study. *Acad Radiol.* 2016;23(10):1278-1282. [CrossRef]
8. Elmore JG, Wells CK, Lee CH, Howard DH, Feinstein AR. Variability in radiologists' interpretations of mammograms. *N Engl J Med.* 1994;331(229):1493-1499. [CrossRef]
9. Svahn TM, Macaskill P, Houssami N. Radiologists' interpretive efficiency and variability in true- and false-positive detection when screen-reading with tomosynthesis (3D-mammography) relative to standard mammography in population screening. *Breast.* 2015;24(6):687-693. [CrossRef]
10. Lehman CD, Arao RF, Sprague BL, et al. National performance benchmarks for modern screening digital mammography: update from the breast cancer surveillance consortium. *Radiology.* 2017;283(1):49-58. [CrossRef]
11. Nelson HD, Fu R, Cantor A, Pappas M, Daeges M, Humphrey L. Effectiveness of breast cancer screening: systematic review and meta-analysis to update the 2009 U.S. preventive services task force recommendation. *Ann Intern Med.* 2016;164:244-255. [CrossRef]
12. Huynh PT, Jarolimek AM, Daye S. The false-negative mammogram. *Radiographics.* 1998;18:1137-1154. [CrossRef]
13. Wang Z, Yu G, Kang Y, Zhao Y, Qu Q. Breast tumor detection in digital mammography based on extreme learning machine. *Neurocomputing.* 2014;128:175-184. [CrossRef]
14. Agrawal P, Vatsa M, Singh R. Saliency based mass detection from screening mammograms. *Signal Processing.* 2014;99:29-27. [CrossRef]
15. McBee MP, Awan OA, Colucci AT, et al. Deep Learning in radiology. *Acad Radiol.* 2018; 25:1472-1480. [CrossRef]
16. Ueda D, Shimazaki A, Miki Y. Technical and clinical overview of deep learning in radiology. *Jpn J Radiol.* 2019;37(1):15-33. [CrossRef]
17. Bayramoglu N, Kannala J, Heikkila J. Deep learning for magnification independent breast cancer histopathology image classification. 2016 23rd ed. International Conference on *Pattern Recognition (ICPR);* 2016. [CrossRef]
18. Zhang Q, Xiao Y, Dai W, et al. Deep learning based classification of breast tumors with shear-wave elastography. *Ultrasonics.* 2016;72:150-157. [CrossRef]
19. Mohamed AA, Berg WA, Peng H, Luo Y, Jankowitz RC, Wu S. A deep learning method for classifying mammographic breast density categories. *Med Phys.* 2018;45:314-321. [CrossRef]

20. Viera AJ, Garrett JM. Understanding interobserver agreement: the kappa statistic. *Fam Med*. 2005;37:360-363. [CrossRef]
21. Kooi T, Litjens G, van Ginneken B, et al. Large scale deep learning for computer aided detection of mammographic lesions. *Med Image Anal*. 2017;35:303-312. [CrossRef]
22. Arevalo J, González FA, Ramos-Pollán R, Oliveira JL, Guevara Lopez MA. Representation learning for mammography mass lesion classification with convolutional neural networks. *Comput Methods Programs Biomed*. 2016;127:248-257. [CrossRef]
23. Becker AS, Marcon M, Ghafoor S, Wurnig MC, Frauenfelder T, Boss A. Deep learning in mammography: diagnostic accuracy of a multipurpose image analysis software in the detection of breast cancer. *Invest Radiol*. 2017;52:434-440. [CrossRef]
24. D.R.E.A.M. The Digital Mammography DREAM Challenge. https://www.synapse.org/#!Synapse:syn4224222/wiki/401743
25. Geras KJ, Wolfson S, Shen Y, et al. High-resolution breast cancer screening with multi-view deep convolutional neural networks. 2017.
26. Akselrod-Ballin A, Chorev M, Shoshan Y, et al. Predicting breast cancer by applying deep learning to linked health records and mammograms. *Radiology*. 2019;292:331-342. [CrossRef]

Diagn Interv Radiol 2023; DOI: 10.4274/dir.2023.232097

GENERAL RADIOLOGY

ORIGINAL ARTICLE

Copyright@Author(s) - Available online at dirjournal.org.
Content of this journal is licensed under a Creative Commons Attribution-NonCommercial 4.0 International License.

Prognostic value of low muscle mass at the 12th thoracic vertebral level in multiple myeloma treated with transplantation: CAREMM-2101 study

Sung-Soo Park*
Daehun Kwag*
Jung Yeon Lee
Young-Woo Jeon
Seung-Ah Yahng
Seung-Hwan Shin
Seo Yeon Youn#
Chang-Ki Min#

***Contributed equally to this work as the first authors.**

#Contributed equally to this work as corresponding authors.

From the Department of Hematology (S-S.P., D.K., J.Y.L., C-K.M. ✉ ckmin@catholic.ac.kr), Seoul St. Mary's Hospital, College of Medicine, The Catholic University of Korea, Seoul, Republic of Korea; Department of Hematology (Y-W.J.), Yeoido St. Mary's Hospital, College of Medicine, The Catholic University of Korea, Seoul, Korea; Department of Hematology (S-A.Y.), Incheon St. Mary's Hospital, College of Medicine, The Catholic University of Korea, Incheon, Korea; Department of Hematology (S-H.S.), Eunpyeong St. Mary's Hospital, College of Medicine, The Catholic University of Korea, Seoul, Republic of Korea; Department of Radiology (S.Y.Y. ✉ imseoyeon@gmail.com), Seoul National University Hospital and Seoul National University College of Medicine; Seoul, Republic of Korea.

Received 10 January 2023; revision requested 06 February 2023; last revision received 10 April 2023; accepted 14 May 2023.

Epub: 14.06.2023

Publication date: 21.07.2023

DOI: 10.4274/dir.2023.232097

PURPOSE

Autologous hematopoietic stem cell transplantation (ASCT) has been introduced as a standard treatment for newly diagnosed multiple myeloma (NDMM) following novel agent-based induction chemotherapy. This study investigated whether pre-ASCT low muscle mass evaluated using the paraspinal muscle index (PMI) at the 12th thoracic vertebra (T12) level is a reliable prognostic marker in NDMM after chemotherapy.

METHODS

A multi-center registry database was retrospectively analyzed. Between 2009 and 2020, 190 patients with chest computed tomography images underwent frontline ASCT following induction therapy. The PMI was defined as the value of the paraspinal muscle area at the T12 level divided by the square of the patient's height. The cut-off value indicating a low muscle mass was sex-specific, using the lowest quintiles.

RESULTS

Of the 190 patients, 38 (20%) were in the low muscle mass group. The low muscle mass group had a lower 4-year overall survival (OS) rate than the non-low muscle mass group (68.5% vs. 81.2%; $P = 0.074$). The median progression-free survival (PFS) in the low muscle mass group was significantly shorter compared with the non-low muscle mass group (23.3 months vs. 29.2 months; $P = 0.029$). The cumulative incidence of transplant-related mortality (TRM) was significantly higher in the low muscle mass group than in the non-low muscle mass group (4-year probability of TRM incidence, 10.6% vs. 0.7%; $P < 0.001$). In contrast, no significant difference in the cumulative incidence of disease progression was found between the two groups. Multivariate analysis revealed that low muscle mass was associated with significant negative outcomes for OS [(hazard ratio (HR): 2.14; $P = 0.047$], PFS (HR: 1.78; $P = 0.012$), and TRM (HR: 12.05; $P = 0.025$).

CONCLUSION

Paraspinal muscle mass may have a prognostic role in NDMM patients who undergo ASCT. Patients with low paraspinal muscle mass have lower survival outcomes compared to non-low muscle mass group.

KEYWORDS

Sarcopenia, myeloma, autologous, transplantation, computed tomography, thoracic

Multiple myeloma (MM) is a hematologic malignancy characterized by the clonal proliferation of malignant plasma cells.[1] The outcomes of MM have improved dramatically in the past two decades owing to the introduction of novel agents, such as immunomodulatory drugs, proteasome inhibitors, and targeted monoclonal antibodies.[2,3] High-dose chemotherapy with autologous hematopoietic stem cell transplantation (ASCT) following upfront induction therapy using a novel agent is considered the standard of care for transplant-eligible and newly diagnosed MM (NDMM).[4] Patient-related prognostic factors, such as age or comorbidities, can limit the eligibility for ASCT.[5] Several prognostic tools based on multidisciplinary evaluation have been used to assess patient fitness for ASCT.[5-8] Howev-

You may cite this article as: Park SS, Kwag D, Lee JY, et al. Prognostic value of low muscle mass at the 12th thoracic vertebral level in multiple myeloma treated with transplantation: CAREMM-2101 study. *Diagn Interv Radiol.* 2023;29(4):596-608.

er, these tools rely on patients self-reporting their comorbidities and are prone to reporting bias. Therefore, tools that can facilitate the standardization of individualized risk factors for MM need to be developed.

Sarcopenia has recently been defined by the European Working Group on Sarcopenia in Older People 2 as the combination of low muscle mass and poor muscle function.[9] Furthermore, sarcopenia has been highlighted as an independent disorder based on individual cancer-related prognostic biomarkers in various malignancies.[10,11] However, published studies reporting patients with MM and sarcopenia and survival outcomes have been unsatisfactory to date due to their retrospective designs and small sample sizes. Williams et al.[12] measured psoas muscle mass at the third lumbar vertebra (L3) using computed tomography (CT) in 142 patients with MM treated with ASCT. They showed that low muscle mass was related to a higher incidence of post-ASCT cardiac complications but was not associated with survival outcomes. Takeoka et al.[13] demonstrated that a low muscle mass at the L3 level did not result in a significant survival difference between 56 patients with NDMM. Although muscle mass at L3, commonly used for CT measurements, was not related to survival outcomes in patients with MM, the prognostic role of muscle mass measured at other sites and sex-specific approaches is yet to be elucidated.[14] Previous studies have revealed that sarcopenia assessment using skeletal muscle measurements at the 12th thoracic vertebra (T12) level is a reliable biomarker for chest CT.[15,16] In addition, the cut-off for low muscle mass should be determined differently based on sex because it is directly related to the total muscle mass.[13,17,18] Therefore, further MM cohort studies are required to determine whether muscle mass is a useful prognostic indicator.

Main points

- Low muscle mass was defined based on a sex-specific cut-off using low-dose chest computed tomography before autologous hematopoietic stem cell transplantation (ASCT).
- Post-ASCT outcomes were significantly associated with low muscle mass in patients with multiple myeloma.
- NDMM patients undergoing ASCT with low paraspinal muscle mass have shorter progression-free survival, higher incidence of transplant-related mortality, and higher significant negative outcomes for overall survival.

This study measured the paraspinal muscle mass area (PSMA) at T12 (12th-PSMA, the area corresponding to the iliocostalis thoracis, longissimus thoracis, spinalis thoracis, rotator thoracis, multifidus, and semispinalis thoracis muscles) on chest CT scans. Low muscle mass was defined as a lower paraspinal muscle index (PMI) (12th-PSMA divided by the height^2) than the sex-specific cut-off. Further, the study explored the prognostic impact of low muscle mass on survival outcomes in patients with NDMM who underwent an ASCT.

Methods

Patient selection and data acquisition

The current study was a multi-center retrospective analysis of patient data from three centers. For patient with MM to be eligible for enrollment in the study, the following criteria had to be met: ND with symptomatic MM, treated with frontline ASCT after induction chemotherapy, aged 20 years or older, and having undergone chest CT within 60 days before the ASCT procedure. First, data from 1511 consecutive patients ND with plasma cell disorders between 2009 and 2020 were analyzed. Then, 264 patients diagnosed with plasma cell disorders other than symptomatic MM were excluded. Of the remaining 1,247 patients with symptomatic NDMM, 414 were transplant-eligible cases. The low-dose chest CT (LDCT) findings of selected patients with a history of pneumonia or airway disease were evaluated between 2009 and 2014. Since 2015, LDCT has been routinely performed to screen for malignancies involving the lungs and mediastinum, subclinical pneumonia, and airway diseases. Two hundred nine patients who lacked a LDCT image before ASCT and 15 patients who received ASCT as a salvage treatment following the failure of induction therapy were excluded. The final cohort included 190 patients with intention-to-treat NDMM who underwent frontline ASCT after induction chemotherapy (Figure 1). Since all centers participating in this study have used thalidomide- or bortezomib-based induction chemotherapy, alone or in combination, since 2009, all patients enrolled in the final cohort received novel agent-based induction therapy. Patient data were collected from August 2021 onward. This study was approved by the Institutional Review Board of Catholic Medical Center (IRB no. KC21RASI0352) and complied with the Declaration of Helsinki. Written informed consent was obtained from all patients.

Computed tomography image acquisition

The CT examinations were performed using multidetector CT scanners with 64 or more channels, either a SOMATOM Definition AS+ (Siemens Healthineers, Erlangen, Germany) or a Discovery CT750 HD (GE Healthcare, Milwaukee, WI, USA). All scans were obtained during a single breath-hold from

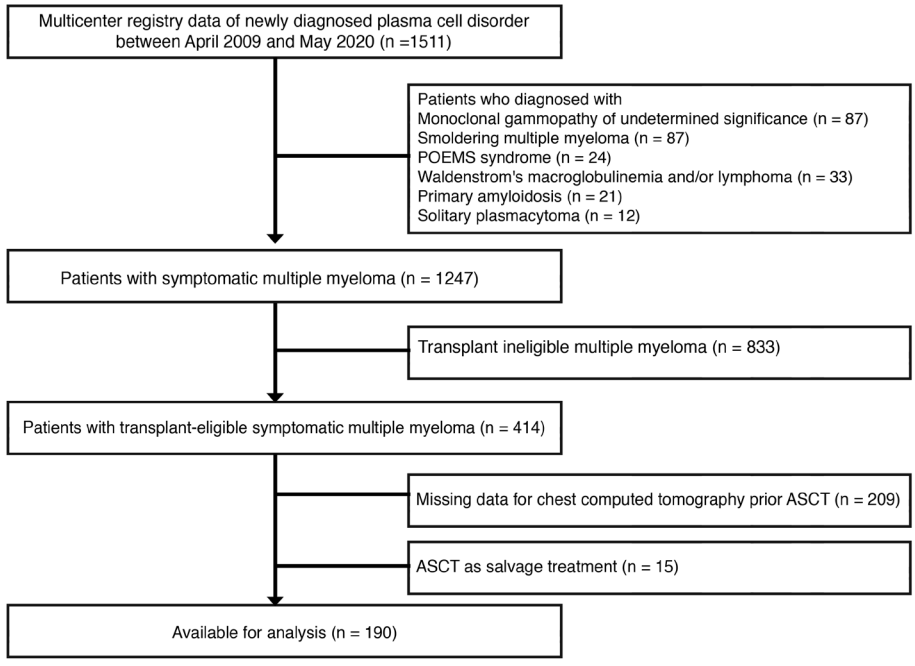

Figure 1. Flow diagram outlining the selection of the study cohort. The final cohort of this study included 190 cases of newly diagnosed multiple myeloma patients who received frontline autologous stem cell transplantation following induction chemotherapy.

the levels of the lower neck to the adrenal glands. The acquisition parameters were as follows: tube voltage 120 kV, tube current 35 mAs for the low-dose scan, automatic exposure control with 130 quality reference value mAs for the standard-dose scan (SOMATOM Definition AS+), a pitch of 1.1–1.2, rotation time of 0.5 s, detector collimation of 64 × 0.6 mm (SOMATOM Definition AS+), or 64 × 0.625 mm (Discovery CT750 HD).

Measurement of the paraspinal muscle at the 12th thoracic vertebra

The patients' 12th-PSMA was evaluated using LDCT within two months before the date of the ASCT according to the strategies used at the participating centers. The LDCT was primarily performed to confirm ASCT eligibility after completing the scheduled induction chemotherapy. A board-certified radiologist with nine years of experience, who was blinded to the clinical information, drew the region of interest using a semi-automated contouring tool available in a non-commercial prototype software (RADIOMICS, Siemens Healthineers, Erlangen, Germany) for all three centers' cases. An axial CT image at the level of T12 was obtained for each patient. The contours of the erector spinae muscles (iliocostalis thoracis, longissimus thoracis, and spinalis thoracis) and transversospinales muscles (rotator thoracis, multifidus, and semispinalis thoracis) were drawn. The 12th-PSMA (mm^2) was obtained from the contours (Figure 2). The mean densities (Hounsfield unit) of these muscles were also determined. Then, the patient's individual PMI was calculated by dividing the 12th-PSMA by the square of the patient's height (mm^2/m^2). The cut-off for low muscle mass was based on sex-specific PMI values using the lowest quintile in each subgroup of males and females.[12]

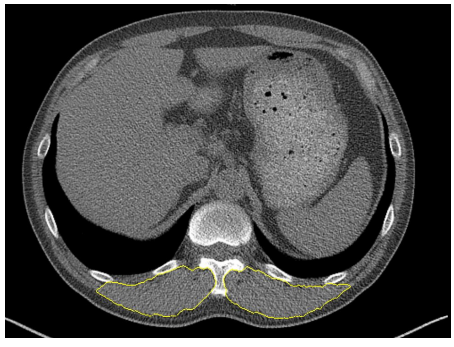

Figure 2. Measurement of paraspinal muscle area using axial computed tomography at the 12th thoracic vertebra level. An axial computed tomography image was selected at the level of the 12th thoracic vertebra's spinous process. The boundaries of the paraspinal muscles (iliocostalis thoracis, longissimus thoracis, spinalis thoracis, rotator thoracis, multifidus, and semispinalis thoracis) were drawn as the region of interest (yellow line). The area of these muscles was obtained to measure muscle mass.

Treatments and transplantation procedures

All patients received an induction treatment consisting of dexamethasone (or prednisolone) together with bortezomib or thalidomide, individually or a combination, in chronological order of approval by the National Health Insurance Service. After the induction chemotherapy, the collected stem cells were mobilized with subcutaneous granulocyte colony stimulation factor (10 μg/kg/day) for five days with or without prior cyclophosphamide therapy (1.5 g/m^2) for two days, etoposide (375 mg/m^2) for one day, or plerixafor (0.24 mg/kg) for one to two days. According to the conditioning strategies implemented by the three centers, a conditioning regimen consisting of high-dose melphalan (70 or 100 mg/m^2/day for two days) was commonly used. Occasionally, busulfan (3.2 mg/kg/day for three days), melphalan (70 mg/m^2/day for two days), busulfan (3.2 mg/kg/day for three days), melphalan (100 mg/day)-thiotepa (150 mg/m^2/day for one day), and busulfan (3.2 mg/kg/day for three days)-thiotepa (150 mg/m^2/day for one day) were used when melphalan was unavailable, as described in a previous report.[19] Some patients received an experimental regimen of bortezomib, busulfan, and melphalan in phase II clinical trials.[20] Other supportive care, including prophylactic antibiotics, prophylaxis for hepatic sinusoidal obstruction syndrome, granulocyte colony stimulation factor, and bisphosphonates, was administered concurrently across the three centers, as described in a previous report.[21,22] A maintenance therapy strategy was designed using thalidomide for 12 months;[23] however, a few individuals rejected this strategy due to insufficient insurance coverage.[19]

Definitions

The patient's MM stage was classified using the MM International Staging System,[1] and the response to treatment was assessed according to the International Myeloma Working Group response criteria.[24] High-risk cytogenetic abnormalities were defined as the presence of one or more of the following aberrations detected by fluorescent *in situ* hybridization: del(17p), t(4;14), or t(14;16).[25]

The PMI cut-off was based on sex-specific PMI values using the lowest quintile in each subgroup of males and females.[12] The low muscle mass group was defined as patients with a lower PMI than the sex-specific cut-off. The overall survival (OS) was defined as the time from transplantation to death from any cause or the date of the last follow-up, and events for progression-free survival (PFS) included disease progression or death from any cause. The transplant-related mortality (TRM) probability and the progression rate were computed by estimating the cumulative incidence based on competing risks, including progression and TRM.

Statistical analysis

Categorical variables were presented as frequencies and percentages, and comparisons used the chi-squared or Fisher's exact tests, as appropriate. Continuous variables were analyzed using the Kolmogorov–Smirnov test to evaluate the null hypothesis of a normal distribution. Normally distributed continuous variables were presented as the mean ± standard deviation and compared using the Student's t-test. Non-normally distributed continuous variables were expressed as medians with interquartile ranges and were compared using the Mann–Whitney U test. Pearson's correlation coefficients determined the statistical correlation between the continuous variables and the PMI. Multiple linear regression analyses were used to confirm the parameters related to the PMI. Regarding linear regression analysis, parameters with $P < 0.050$ on the Student's t-test or Pearson correlation test were included as covariants.

The reverse Kaplan–Meier estimator was used to assess the median duration of the interval. The Kaplan–Meier survival curves were determined, and log-rank tests were performed to analyze time-to-event endpoints, such as the OS and PFS. Univariate survival analyses were performed using Kaplan–Meier estimates and log-rank tests. Cumulative incidence estimates and the Gray's test were used to analyze the data, including competing risks. Variables with $P < 0.150$, according to the univariate analyses, were included in the multivariate models of OS, PFS, and TRM. The Cox proportional hazards model and the Fine–Gray regression model, both with backward stepwise selection, were generated with hazard ratios (HRs) and 95% confidence intervals (CIs) for multivariate analysis. All statistical analyses were performed using R software (ver. 3.6.1, Jul. 07, 2019; R Foundation for Statistical Computing, Vienna, Austria. https://cran.r-project.org/bin/windows/base/old/3.6.1/). A *P* value

of <0.050 was considered statistically significant.

Results

Patient characteristics and outcomes

The final study cohort included 190 of the initial 1,511 consecutive patients, 104 (55.3%) males and 86 (45.3%) females, with a mean age of 55.9 ± 7.0. The mean interval between the LDCD assessment date and the date of the ASCT was 28 ± 16.1 days. As expected, the 12th-PSMA (3206 ± 648 mm^2 for males vs. 2358.9 ± 538.8 mm^2 for females; P < 0.001) and the PMI (1117.3 ± 232.8 mm^2/m^2 for males vs. 973.7 ± 220.2 mm^2/m^2 for females; P < 0.001) were significantly higher in males than in females (Figure 3a). Among the variables considered in the decision-making for ASCT, non-extramedullary plasmacytoma and lower levels of albumin at diagnosis related to lower PMI values (Supplementary Table 1). Supplementary Table 2 shows the results of multiple regression analysis for the PMI, where the dependent parameter was sex. Accordingly, the cut-offs for the 12th-PSMA were defined as 916.9 mm^2/m^2 for males and 807.2 mm^2/m^2 for females. The mean PMI of the low muscle (n = 38) and non-low muscle (n = 152) mass groups were 760.9 ± 103.2 and 1125.1 ± 203.4, respectively. The comparative data of the two groups based on the definition of low muscle mass are presented in Table 1. These characteristics were relatively similar between the two groups.

The median follow-up of the total cohort was 40.7 months (95% CI; 38.1–44.9 months). Among the 36 deaths in the entire cohort, 86.1% (n = 31) were progression-dependent, and 13.9% (n = 5) died of TRM. The TRM-related causes of death included three cases of sepsis, one of hepatic sinusoidal obstruction syndrome, and one of sudden death following fatal arrhythmia.

Survival outcomes of the low and non-low muscle mass groups

The estimated OS rate was poor in the low muscle compared with the non-low muscle mass group [4-year OS rate, 68.5% (95% CI; 49.9%–81.3%) vs. 81.2% (95% CI; 71.7%–87.8%); P = 0.074] (Figure 4a). The median PFS in the low muscle mass group was significantly poorer than in the non-low muscle mass group (23.3 months (95% CI, 14.5–31.4 months) vs. 29.2 months (95% CI, 24.3–38.7 months); P = 0.029) (Figure 4b). The cumulative incidence of TRM was significantly higher in the low muscle than in the non-low muscle mass group [4-year probability of incidence of TRM, 10.6% (95% CI, 3.3%–22.9%) vs. 0.7% (95% CI, 0.1%–3.3%); P < 0.001] (Figure 4c). No statistically significant cumulative incidence of progression was found between the two groups (P = 0.301) (Figure 4d).

Analyses of the factors affecting overall and progression-free survival, and transplant-related mortality

In the univariate analysis (Supplementary Table 3), some variables were identified as potentially related to OS, PFS, and TRM. Eight variables were potentially associated with OS, including low muscle mass, age (≥60 years), lambda chain type MM, high β2-microglobulin at diagnosis (≥5.5 mg/L), low albumin at diagnosis (<3.5 g/dL), mobilization of peripheral blood mononuclear cells using cyclophosphamide, low glomerular filtration rate at baseline (<60 mL/min/1.73 m^2), and conditioning, except for melphalan plus busulfan. Seven variables were found to be potentially related to PFS, including low muscle mass and density, lambda chain type MM, high β2-microglobulin at diagnosis (≥5.5 mg/L), low albumin at diagnosis (<3.5 g/dL), poor response status at baseline, and low platelet at baseline (<150/mm^3). Six variables were found to be potentially related to TRM, including low muscle mass, lambda chain type MM, high β2-microglobulin at diagnosis (≥5.5 mg/L), low albumin at diagnosis (<3.5 g/dL), high lactate dehydrogenase (> upper limit of normal), and low glomerular filtration rate at baseline (<60 mL/min/1.73 m^2). The multivariate analysis (Table 2) showed that low muscle mass resulted in a significantly negative association with OS (HR of 2.14; 95% CI of 1.01–4.87; P = 0.047), PFS (HR of 1.78; 95% CI of 1.14–2.78; P = 0.012), and TRM (HR of 12.05; 95% CI of 1.36–104.93; P = 0.025), even after adjustment for other potential factors.

Discussion

This study evaluated the prognostic role of the PMI using the 12th-PSMA derived from LDCT images and height. Low muscle mass was defined as the sex-specific lowest quintile of the PMI. Low muscle mass was significantly associated with survival outcomes, even after adjusting for confounding factors; this suggests that the lower survival outcomes in the low muscle mass group resulted from a higher incidence of TRM.

Quantitative body composition measurements, including skeletal muscle and visceral and subcutaneous adipose tissue volumes, at various anatomical sites have been extensively performed to identify their role in predicting the outcomes and survival of cancer patients.[14] Studies exploring the association between body composition at the L3 level and clinical outcomes are the most common in cancer cohorts, including MM cohort studies. Previous studies[12,13,26] that applied low muscle mass at the L3 level in patients with MM showed that a low muscle index did not affect survival outcomes, contrary to the conclusion of this study. However, evidence associating low muscle mass at the L3 level with survival has been disputed in cohort studies of patients with MM. For example, Williams et al.[12] and Takeoka et al.[13] did not apply sex-specific cut-offs for the L3 low muscle index. Surov et al.[26] used the sex-specific cut-off values suggested by Prado et al.[27], which were derived for solid tumors of the respiratory or gastrointestinal tract rather than for MM. Although three previous studies on low muscle mass measured at the lumbar vertebral level were not linked to OS in a cohort

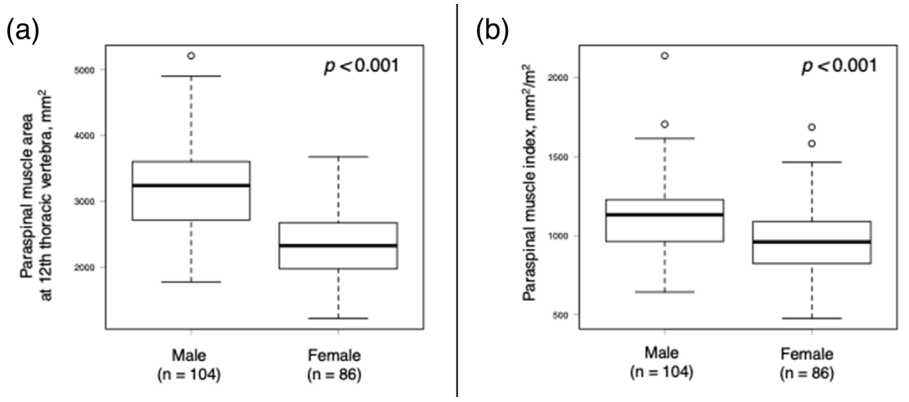

Figure 3. Comparison of **(a)** paraspinal muscle area at the 12th thoracic vertebra (mm^2) and **(b)** paraspinal muscle index (PMI, mm^2/m^2) based on sex using the Student's t-test. The mean of paraspinal muscle area at the 12th thoracic vertebra was 3206 ± 648 mm^2 for males vs. 2358.9 ± 538.8 mm^2 for females. The mean of the PMI was 1117.3 ± 232.8 mm^2/m^2 for males vs. 973.7 ± 220.2 mm^2/m^2 for females. Boxes, 5–95% percentiles; horizontal bars, median; vertical brackets, ranges. PMI, paraspinal muscle index.

Table 1. Comparisons of characteristics between the low and non-low muscle mass groups

Variables	Low muscle mass, (n = 38)	Non-low muscle mass, (n = 152)	*P* value
Paraspinal muscle index, mm^2/m^2, mean ± SD	760.9 ± 103.2	1125.1 ± 203.4	<0.001
Time to ASCT from the assessing date of LDCT scan, days, mean ± SD	27.9 ± 18.9	28.0 ± 15.4	0.975
Age at transplant, years, mean ± SD	54.1 ± 6.3	56.3 ± 7.1	0.071
Sex, number (%)			0.999
Male	21 (55.3)	83 (54.6)	
Female	17 (44.7)	69 (45.4)	
Type of myeloma, number (%)			0.851
IgG	23 (60.5)	80 (52.6)	
IgA	6 (15.8)	27 (17.8)	
IgM or IgD	3 (7.9)	15 (9.9)	
Light chain disease	6 (15.8)	30 (19.7)	
Presence of extramedullary disease at diagnosis, number (%)			0.160
None	34 (89.5)	118 (77.6)	
Present	4 (10.5)	34 (22.4)	
Lactate dehydrogenase at diagnosis, number (%) (missing n = 8)			0.475
> Upper limit of normal	26 (68.4)	116 (76.3)	
Normal	10 (26.3)	30 (19.7)	
β2-microglobulin at diagnosis, mg/L, median (Q1–Q3) (missing n = 5)	3.82 (2.52–6.89)	3.17 (2.32–4.97)	0.103
Albumin at diagnosis, g/dL, mean ± SD (missing n = 5)	3.5 ± 0.7	3.7 ± 0.7	0.267
Cytogenetic risk, number (%) (missing n = 60)			0.426
Standard	20 (52.6)	73 (48.0)	
High	5 (13.2)	32 (21.1)	
Time to ASCT from diagnosis, months, mean ± SD	6.2 ± 1.5	6.5 ± 1.3	0.203
Induction treatment, number (%)			0.182
Bortezomib-thalidomide-dexamethasone	32 (84.2)	141 (92.8)	
Others[a]	6 (15.8)	11 (7.2)	
Lactate dehydrogenase at time prior ASCT, number (%)			0.381
> Upper limit of normal	16 (42.1)	50 (32.9)	
Normal	22 (57.9)	102 (67.1)	
Response status at time prior ASCT, number (%)			0.384
Complete response	15 (39.5)	62 (40.8)	
Very good partial response	21 (55.3)	71 (46.7)	
Partial response or stable disease	2 (5.3)	19 (12.5)	
Mobilization of peripheral blood mononuclear cell			0.679
G-CSF only	9 (23.7)	27 (17.8)	
G-CSF plus cyclophosphamide	14 (36.8)	53 (34.9)	
G-CSF plus etoposide	14 (36.8)	70 (46.1)	
G-CSF plus plerixafor	1 (2.6)	2 (1.3)	
Absolute neutrophil count before ASCT, $/mm^3$, median (Q1–Q3)	2.81 (2.2–3.98)	2.93 (1.93–3.72)	0.364
Platelet count before ASCT, $/mm^3$	236 ± 81.6	226 ± 58.4	0.434
Glomerular filtration rate before ASCT, mL/min/1.73 m^2	87.4 ± 35.0	91.1 ± 25.9	0.468
Conditioning regimen, number (%)			0.278
High dose melphalan	30 (78.9)	92 (60.5)	
Melphalan plus busulfan	2 (5.3)	21 (13.8)	
Melphalan, busulfan, plus thiotepa	4 (10.5)	28 (18.4)	
Busulfan plus thiotepa	0 (0)	2 (1.3)	
Bortezomib, busulfan, plus melphalan	2 (5.3)	9 (5.9)	
Infused CD34+ × 10^6 cells/kg, median (Q1–Q3)	5.22 (4.04–8.56)	5.55 (4.36–6.79)	0.999
Maintenance therapy after ASCT			0.253
Yes	23 (60.5)	109 (71.7)	
No	15 (39.5)	43 (28.3)	

[a]Others included four of bortezomib-dexamethasone, four of bortezomib-melphalan-prednisolone, nine of thalidomide-dexamethasone; ASCT, autologous hematopoietic stem cell transplantation; Ig, immunoglobulin; LDCT, low-dose chest computed tomography; G-CSF, granulocyte-colony stimulation factor; SD, standard deviation; Q, quantile.

of patients with MM,[12,13,26] Umit et al.[28] reported that low femoral muscle mass was significantly associated with poor OS, whereas measuring muscle mass in the lumbar area was not. Therefore, this study hypothesized that muscle volume measurements at different sites from the L3 level and the modality of abdominal CT were worthwhile to explore the prognostic impact in patients with MM.

First, pilot investigations were performed to identify which single muscle area could correspond to the entire muscle volume shown in the cross-sectional image at the T12 level. It was determined that measurements at one site of the paraspinal muscle could be a surrogate marker for the entire muscle volume shown at the T12 level (Supplementary Figure 1). In line with this study's results, pectoralis muscle attenuation and low muscle mass evaluated at the T12 level were negatively associated with clinical outcomes, such as severe airflow obstruction in patients with chronic obstructive pulmonary disease and survival in patients who underwent lung transplantation.[29,30] Furthermore, in several studies, LDCT image muscle mass measurements at the T12 level showed a prognostic role in clinical outcomes.[31,32] Although understanding the pathogenic mechanism of sarcopenia according to the measured site on the clinical outcomes is still lacking, it is suggested that low muscle mass measured at sites other than L3 are valuable prognostic markers, even in patients with MM.

To the researchers' knowledge, the current study is the first to investigate the association between low muscle mass at the T12 level and the survival of patients with MM. As LDCT is routinely performed before ASCT, an additional abdominal CT for muscle mass assessment at the lumbar level may be limited. Although it has been suggested that measuring one muscle area could assess the patient's generalized muscle mass status,[33] such an approach is inevitably linked to increased laboriousness, particularly when measuring larger areas in clinical practice. Furthermore, T12 level evaluation via LDCT is associated with the significant benefit of contrast-free assessment and minimization of radiation exposure compared with conventional abdominal CT of the lumbar region.[34,35]

Although the definition of low muscle mass is yet to be established,[36] it is generally indicated by different cut-off levels based on sex and is closely related to body size. Furthermore, the revised European Working Group on Sarcopenia in Older People 2 guidelines state that sex-specific threshold values for sarcopenia diagnosis improve the prediction of outcomes.[9] It is well known that the body composition index measured

Table 2. Multivariable analysis of overall survival, progression-free survival, and treatment-related mortality

	Overall survival			Progression-free survival			Cumulative incidence of TRM		
Variables	Hazard ratio	95% CI	*P* value	Hazard ratio	95% CI	*P* value	Hazard ratio	95% CI	*P* value
Paraspinal muscle index, $mm^2/m^{2*\dagger\ddagger}$			0.047			0.012			0.025
Low muscle mass vs. non-low muscle mass	2.14	1.01–4.54		1.78	1.14–2.78		12.05	1.36–104.93	
Muscle density, Hounsfield density			NA			0.011			NA
Low density vs. high density	NA	NA		1.73	1.13–2.65		NA	NA	
Age at transplant			0.014			NA			NA
≥60 vs. <60	2.42	1.2–4.89		NA	NA		NA	NA	
Light chain type*†‡			0.139			0.084			0.500
Kappa vs. Lambda	1.66	0.85–3.27		1.39	0.96–2.01		2.35	0.2–27.81	
β2-microglobulin at diagnosis, mg/L*†‡			0.011			0.003			0.430
<5.5 vs. ≥5.5	2.44	1.23–4.83		1.89	1.25–2.85		2.02	0.36–11.29	
Albumin at diagnosis, g/dL*†‡			0.273			0.185			<0.001
≥3.5 vs. <3.5	0.68	0.34–1.36		1.28	0.88–1.86		13.7	3.42–54.9	
Lactate dehydrogenase at time prior ASCT‡			NA			NA			0.790
> Upper limit of normal vs. normal	NA	NA		NA	NA		1.57	0.06–41.63	
Mobilization of peripheral blood mononuclear cell*			0.019			NA			NA
G-CSF plus cyclophosphamide vs. others	2.31	1.15–4.65		NA	NA		NA	NA	
Response status at time prior ASCT†			NA			0.043			NA
SD, PR, vs. VGPR vs. CR or better	NA	NA		1.35	1.01–1.81		NA	NA	
Conditioning regimen			0.170			NA			NA
High dose melphalan vs. melphalan plus busulfan vs. others[1]*	1.33	0.89–1.98		NA	NA		NA	NA	
Platelet count at time prior ASCT, $/mm^{3\dagger}$			NA			0.167			NA
≥150 vs. <150	NA	NA		1.57	0.83–2.97		NA	NA	
Glomerular filtration rate at time prior ASCT, $mL/min/1.73m^{2*\ddagger}$			0.605			NA			0.002
≥60 vs. <60	1.36	0.42–4.39		NA	NA		18.4	3.04–111.7	

*Eight variables were selected by univariate analysis for overall survival with *P* values less than 0.15; †seven variables were selected by univariate analysis for progression-free survival with *P* values less than 0.15; ‡six variables were selected by univariate analysis for cumulative incidence of TRM with *P* values less than 0.15; [1]others include 32 of melphalan, busulfan plus thiotepa, 2 of busulfan plus thiotepa, and 11 of bortezomib, busulfan plus melphalan. ASCT, autologous hematopoietic stem cell transplantation; CI, confidence interval; CR, complete response; G-CSF, granulocyte-colony stimulation factor; NA, not available; PR, partial response; TRM, transplantation-related mortality; SD, stable disease; VGPR, very good partial response.

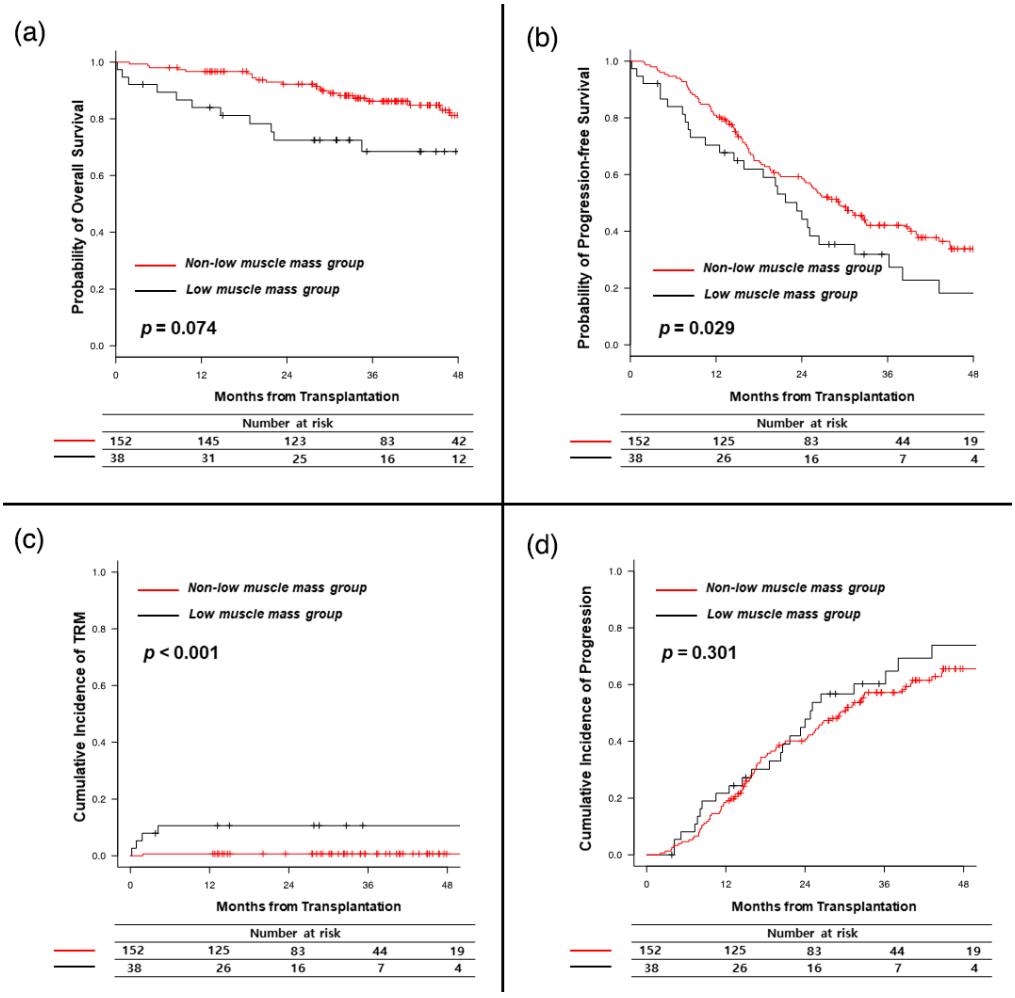

Figure 4. Comparison of survival outcomes between the low (black line) and non-low (red line) muscle mass groups. **(a)** Overall survival. **(b)** Progression-free survival. **(c)** Cumulative incidence of transplant-related mortality (TRM). **(d)** Cumulative incidence of disease progression. The estimated overall survival rate and median progression-free survival were poor in the low muscle mass group compared with the non-low muscle mass group ($P = 0.074$ and 0.029 for the overall survival rate and median progression-free survival, respectively). The cumulative incidence of TRM in the low muscle mass group was significantly higher than in the non-low muscle mass group ($P < 0.001$). No statistical significance in the cumulative incidence of disease progression was found between the two groups ($P = 0.301$).

at the L3 level varies significantly depending on sex.[17] Accordingly, most previous studies defined sex-specific cut-offs to investigate the associations between low muscle mass at the L3 level and the clinical outcomes of several cancers.[37] However, most previous MM cohort studies defined low muscle mass with sex-specific cut-off values.[12,13] Based on previous studies' findings, the researchers believe this methodology is a decisive factor related to the lack of significant association with survival outcomes in this study's MM cohort. Unfortunately, because of the lack of correlation between low muscle mass and survival of patients with MM in previous studies, CT muscle mass measurements have not received substantial attention in MM cohort studies.

No clinical impact of sex-non-specific muscle mass on clinical outcomes was observed in this MM cohort (data not shown). However, this study's results showed that low muscle mass at the T12 level, defined by a sex-specific methodology, was negatively associated with comprehensive survival outcomes, including OS, PFS, and TRM, in patients with MM who received ASCT. The results of this study highlight the need for future studies to establish a reliable sex-specific approach for lowering the muscle mass in patients with MM undergoing ASCT.

Prognostic marker-based treatments are essential to improve the survival of patients with MM. Relevant prognostic parameters for each patient were divided into the patient-, disease-, and treatment-related factors.[38] Patient-related factors, such as age, performance status, MM-specific comorbidity index of the revised myeloma comorbidity index,[8] or the International Myeloma Working Group frailty scale,[5] can predict individual tolerance to anti-MM treatment. It was hypothesized that the PMI using the 12th-PSMA in this study might be a patient-related parameter facilitating pretreatment decisions including its regimen and intensity. Further, the current study demonstrated that low muscle mass significantly contributed to high TRM and poor PFS and OS. The study cohort consisted of intention-to-treat patients with MM with frontline ASCT following the achievement of an overall response to induction chemotherapy. It is critical to avoid TRM after ASCT. Since no optimal conditioning regimen has been developed for ASCT in patients with MM, clinicians should adopt a weak conditioning regimen for individuals with low muscle mass. Evidence from cancer cohorts supports this study's finding that muscle mass status is directly related to critical chemotherapeutic toxicity.[12,37] Above all, MM appears to be strongly linked to low muscle mass because of multidimensional factors, such as epidemiologically old-age onset;[39,40] therefore, patients with MM may face disability related to devastating bone

destruction, including vertebral compression fractures[41] or heavy exposure to high-dose steroids as part of anti-MM treatment.[42] It is known that comprehensive rehabilitation with nutritional support and exercise programs treats and prevents low muscle mass.[43] Moreover, nutritional therapy, including protein of approximately 1.2–1.5 g/kg/day and fat within 20%–30% of total energy content, and exercise therapy, such as resistance training, are recommended for patients with MM.[43,44] Therefore, further studies are needed to investigate the potential clinical benefits of intensive rehabilitation programs for preventing or treating sarcopenia following the diagnosis of MM or before the initiation of induction treatment; this may provide a more comprehensive understanding of the effectiveness of such interventions in managing sarcopenia and enhancing patient outcomes.

This study was limited by its retrospective design and lack of prospective validation using another cohort. Potential selection bias exists as some patients without LDCT images before the ASCT were excluded from the initial cohort. The study's population was also limited by confounding factors, such as heterogeneous induction treatment and the ASCT's conditioning regimen. Further, as some data associated with cytogenetic risk were missing, statistical bias could exist in the association between the cytogenetic risk and clinical outcomes. Although the study's results indicated a prognostic impact of low muscle mass at the T12 level, the optimal sites for computing muscle mass were not confirmed. Therefore, further studies are needed to identify the optimal site among the candidate muscle sites, such as the pectoralis or paraspinal muscles, at other thoracic levels. Nevertheless, the researchers believe the T12 level approach is preferable because it is simpler to measure muscle mass than at other sites. Further studies are warranted to validate the role of the PMI using the 12th-PSMA on outcomes in a larger cohort of transplant-eligible patients with NDMM based on the results of this study.

In conclusion, sex-specific low muscle mass evaluated at the T12 level could be related to the prognosis of patients with MM receiving ASCT. For patients with NDMM preparing for ASCT, an inspection of muscle mass using LDCT may contribute to developing individualized management, including conditioning intensity, rehabilitation, and nutrition.

Conflict of interest disclosure

The authors declared no conflicts of interest.

Funding

This study was supported by the National R&D Program for Cancer Control through the National Cancer Center, funded by the Ministry of Health & Welfare, Republic of Korea (HA21C0013). The authors wish to acknowledge the financial support of the Catholic Medical Center Research Foundation made in 2021.

References

1. Greipp PR, San Miguel J, Durie BG, et al. International staging system for multiple myeloma. *J Clin Oncol*. 2005;23(15):3412-3420. Erratum in: *J Clin Oncol*. 2005;23(25):6281. [CrossRef]
2. Engelhardt M, Terpos E, Kleber M, et al. European Myeloma Network recommendations on the evaluation and treatment of newly diagnosed patients with multiple myeloma. *Haematologica*. 2014;99(2):232-242. [CrossRef]
3. Lee JH, Kim SH. Treatment of relapsed and refractory multiple myeloma. *Blood Res*. 2020;55(S1):S43-S53. [CrossRef]
4. Parrondo RD, Ailawadhi S, Sher T, Chanan-Khan AA, Roy V. Autologous stem-cell transplantation for multiple myeloma in the era of novel therapies. *JCO Oncol Pract*. 2020;16(2):56-66. [CrossRef]
5. Palumbo A, Bringhen S, Mateos MV, et al. Geriatric assessment predicts survival and toxicities in elderly myeloma patients: an International Myeloma Working Group report. *Blood*. 2015;125(13):2068-2074. [CrossRef]
6. Sorror ML, Maris MB, Storb R, et al. Hematopoietic cell transplantation (HCT)-specific comorbidity index: a new tool for risk assessment before allogeneic HCT. *Blood*. 2005;106(8):2912-2919. [CrossRef]
7. Kleber M, Ihorst G, Terhorst M, et al. Comorbidity as a prognostic variable in multiple myeloma: comparative evaluation of common comorbidity scores and use of a novel MM-comorbidity score. *Blood Cancer J*. 2011;1(9):e35. [CrossRef]
8. Engelhardt M, Domm AS, Dold SM, et al. A concise revised myeloma comorbidity index as a valid prognostic instrument in a large cohort of 801 multiple myeloma patients. *Haematologica*. 2017;102(5):910-921. [CrossRef]
9. Cruz-Jentoft AJ, Bahat G, Bauer J, et al. Sarcopenia: revised European consensus on definition and diagnosis. *Age Ageing*. 2019;48(1):16-31. Erratum in: *Age Ageing*. 2019;48(4):601. [CrossRef]
10. Catikkas NM, Bahat Z, Oren MM, Bahat G. Older cancer patients receiving radiotherapy: a systematic review for the role of sarcopenia in treatment outcomes. *Aging Clin Exp Res*. 2022;34(8):1747-1759. [CrossRef]
11. Surov A, Wienke A. Sarcopenia predicts overall survival in patients with malignant hematological diseases: a meta-analysis. *Clin Nutr*. 2021;40(3):1155-1160. [CrossRef]
12. Williams A, Baruah D, Patel J, et al. Prevalence and significance of sarcopenia in multiple myeloma patients undergoing autologous hematopoietic cell transplantation. *Bone Marrow Transplant*. 2021;56(1):225-231. [CrossRef]
13. Takeoka Y, Sakatoku K, Miura A, et al. Prognostic effect of low subcutaneous adipose tissue on survival outcome in patients with multiple myeloma. *Clin Lymphoma Myeloma Leuk*. 2016;16(8):434-441. [CrossRef]
14. Hemke R, Buckless C, Torriani M. Quantitative imaging of body composition. *Semin Musculoskelet Radiol*. 2020;24(4):375-385. [CrossRef]
15. Nemec U, Heidinger B, Sokas C, Chu L, Eisenberg RL. Diagnosing sarcopenia on thoracic computed tomography: quantitative assessment of skeletal muscle mass in patients undergoing transcatheter aortic valve replacement. *Acad Radiol*. 2017;24(9):1154-1161. [CrossRef]
16. Kim JW, Yoon JS, Kim EJ, et al. Prognostic implication of baseline sarcopenia for length of hospital stay and survival in patients with coronavirus disease 2019. *J Gerontol A Biol Sci Med Sci*. 2021;76(8):e110-e116. [CrossRef]
17. Martin L, Birdsell L, Macdonald N, et al. Cancer cachexia in the age of obesity: skeletal muscle depletion is a powerful prognostic factor, independent of body mass index. *J Clin Oncol*. 2013;31(12):1539-1547. [CrossRef]
18. Xia L, Zhao R, Wan Q, et al. Sarcopenia and adverse health-related outcomes: an umbrella review of meta-analyses of observational studies. *Cancer Med*. 2020;9(21):7964-7978. [CrossRef]
19. Park SS, Lim JY, Kim TW, et al. Predictive impact of circulating microRNA-193a-5p on early relapse after autologous stem cell transplantation in patients with multiple myeloma. *Br J Haematol*. 2020;189(3):518-523. [CrossRef]
20. Park SS, Kim K, Kim SJ, et al. A Phase I/II, open-label, prospective, multicenter study to evaluate the efficacy and safety of lower doses of bortezomib plus busulfan and melphalan as a conditioning regimen in patients with multiple myeloma undergoing autologous peripheral blood stem cell transplantation: the KMM103 study. *Biol Blood Marrow Transplant*. 2019;25(7):1312-1319. [CrossRef]
21. Lee SE, Yahng SA, Cho BS, et al. Lymphocyte subset analysis for the assessment of treatment-related complications after

autologous stem cell transplantation in multiple myeloma. *Cytotherapy*. 2012;14(4):505-512. [CrossRef]

22. Kim Y, Park SS, Jeon YW, et al. Response and dynamics of renal function in transplantation-eligible multiple myeloma patients treated with a novel agent: the CAREMM-2201 study. *Transplant Cell Ther*. 2023;29(1):55.e1-55.e9. [CrossRef]
23. Lee HS, Min CK, Lee JJ, et al. The clinical impact of thalidomide maintenance after autologous stem cell transplantation in patients with newly diagnosed multiple myeloma in real clinical practice of Korea. *Ann Hematol*. 2016;95(6):911-919. [CrossRef]
24. Rajkumar SV, Harousseau JL, Durie B, et al. Consensus recommendations for the uniform reporting of clinical trials: report of the International Myeloma Workshop Consensus Panel 1. *Blood*. 2011;117(18):4691-4695. [CrossRef]
25. Palumbo A, Avet-Loiseau H, Oliva S, et al. Revised international staging system for multiple myeloma: a report from International Myeloma Working Group. *J Clin Oncol*. 2015;33(26):2863-2869. [CrossRef]
26. Surov A, Benkert F, Pönisch W, Meyer HJ. CT-defined body composition as a prognostic factor in multiple myeloma. *Hematology*. 2023;28(1):2191075. [CrossRef]
27. Prado CM, Lieffers JR, McCargar LJ, et al. Prevalence and clinical implications of sarcopenic obesity in patients with solid tumours of the respiratory and gastrointestinal tracts: a population-based study. *Lancet Oncol*. 2008;9(7):629-635. [CrossRef]
28. Umit EG, Korkmaz U, Baysal M, et al. Evaluation of sarcopenia with F-18 FDG PET/CT and relation with disease outcomes in patients with multiple myeloma. *Eur J Cancer Care (Engl)*. 2020;29(6):e13318. [CrossRef]
29. Cho YH, Do KH, Chae EJ, et al. Association of Chest CT-based quantitative measures of muscle and fat with post-lung transplant survival and morbidity: a single institutional retrospective cohort study in Korean population. *Korean J Radiol*. 2019;20(3):522-530. [CrossRef]
30. Bak SH, Kwon SO, Han SS, Kim WJ. Computed tomography-derived area and density of pectoralis muscle associated disease severity and longitudinal changes in chronic obstructive pulmonary disease: a case control study. *Respir Res*. 2019;20(1):226. [CrossRef]
31. Panthofer AM, Olson SL, Harris DG, Matsumura JS. Derivation and validation of thoracic sarcopenia assessment in patients undergoing thoracic endovascular aortic repair. *J Vasc Surg*. 2019;69(5):1379-1386. [CrossRef]
32. Tan L, Ji G, Bao T, Fu H, Yang L, Yang M. Diagnosing sarcopenia and myosteatosis based on chest computed tomography images in healthy Chinese adults. *Insights Imaging*. 2021;12(1):163. [CrossRef]
33. Baracos VE. Psoas as a sentinel muscle for sarcopenia: a flawed premise. *J Cachexia Sarcopenia Muscle*. 2017;8(4):527-528. [CrossRef]
34. Smith-Bindman R, Lipson J, Marcus R, et al. Radiation dose associated with common computed tomography examinations and the associated lifetime attributable risk of cancer. *Arch Intern Med*. 2009;169(22):2078-2086. [CrossRef]
35. Larke FJ, Kruger RL, Cagnon CH, et al. Estimated radiation dose associated with low-dose chest CT of average-size participants in the National Lung Screening Trial. *AJR Am J Roentgenol*. 2011;197(5):1165-1169. [CrossRef]
36. Tanaka S, Imataki O, Kitaoka A, et al. Clinical impact of sarcopenia and relevance of nutritional intake in patients before and after allogeneic hematopoietic stem cell transplantation. *J Cancer Res Clin Oncol*. 2017;143(6):1083-1092. [CrossRef]
37. Hopkins JJ, Sawyer MB. Interactions of lean soft-tissue and chemotherapy toxicities in patients receiving anti-cancer treatments. *Cancer Chemother Pharmacol*. 2018;82(1):1-29. [CrossRef]
38. Gengenbach L, Graziani G, Reinhardt H, et al. Choosing the right therapy for patients with relapsed/refractory multiple myeloma (RRMM) in consideration of patient-, disease- and treatment-related factors. *Cancers (Basel)*. 2021;13(17):4320. [CrossRef]
39. Tang CH, Liu HY, Hou HA, et al. Epidemiology of multiple myeloma in Taiwan, a population based study. *Cancer Epidemiol*. 2018;55:136-141. [CrossRef]
40. Hong J, Lee JH. Recent advances in multiple myeloma: a Korean perspective. *Korean J Intern Med*. 2016;31(5):820-834. [CrossRef]
41. Terpos E, Morgan G, Dimopoulos MA, et al. International Myeloma Working Group recommendations for the treatment of multiple myeloma-related bone disease. *J Clin Oncol*. 2013;31(18):2347-2357. [CrossRef]
42. Sharma S, Lichtenstein A. Dexamethasone-induced apoptotic mechanisms in myeloma cells investigated by analysis of mutant glucocorticoid receptors. *Blood*. 2008;112(4):1338-1345. [CrossRef]
43. Kakehi S, Wakabayashi H, Inuma H, et al. Rehabilitation nutrition and exercise therapy for sarcopenia. *World J Mens Health*. 2022;40(1):1-10. [CrossRef]
44. Burtin C, Clerckx B, Robbeets C, et al. Early exercise in critically ill patients enhances short-term functional recovery. *Crit Care Med*. 2009;37(9):2499-2505. [CrossRef]

Supplementary Table 1. Analysis to identify factors associated with paraspinal muscle index

Characteristics	Paraspinal muscle index, mm^2/m^2		
	Correlation coefficient (95% CI)	Mean ± SD (or median with interquartile)	*P* value
Muscle density (Hounsfield unit)	0.045 (-0.099 ~ 0.188)	NA	0.541
Age years at transplant	-0.029 (-0.171 ~ 0.114)	NA	0.692[a]
Sex			<0.001[b]
Male	-	1117.2 ± 232.8	
Female	-	973.7 ± 220.2	
Type of myeloma			0.121[c]
IgG	-	1036.5 ± 248.7	
IgA	-	1034.7 ± 203.9	
IgM or IgD	-	1179.5 ± 289.8	
Light chain disease	-	1049.8 ± 191.0	
Light chain type			0.084[b]
Kappa	-	1024.3 ± 233.6	
Lambda	-	1084.0 ± 239.5	
Presence of extramedullary plasmacytoma			0.009[b]
None	-	1029.8 ± 225.8	
Present	-	1142.1 ± 264.9	
Lactate dehydrogenase at diagnosis			0.699[b]
> Upper limit of normal	-	1039.3 ± 255.3	
β2-microglobulin at diagnosis	-0.033 (-0.112 ~ 0.177)	-	0.654[a]
Albumin at diagnosis, g/dL	0.15 (0.007 ~ 0.288)	-	0.04[a]
ISS stage at diagnosis			0.355[c]
I, n (%)	-	1089.5 ± 206.2	
II, n (%)	-	1045.4 ± 258.0	
III, n (%)	-	1024.9 ± 241.7	
Cytogenetic status at diagnosis			0.23[b]
Standard risk	-	1030.5 ± 246.5	
High risk	-	1085.8 ± 206.9	
Time to transplantation from diagnosis	0.063 (-0.08 ~ 0.204)	NA	0.387[a]
Induction treatment			0.115[c]
Bortezomib-thalidomide-dexamethasone	-	1062.7 ± 239.4	
Bortezomib-dexamethasone	-	831.9 ± 236	
Thalidomide-dexamethasone	-	1078.4 ± 249.3	
Bortezomib-melphalan-prednisolone	-	937.8 ± 126.9	
Lactate dehydrogenase at time prior ASCT			0.323[b]
> Upper limit of normal	-	1028.9 ± 229.4	
Normal	-	1064.7 ± 242.9	
Response status at time prior ASCT			0.246[c]
Complete response	-	1081.0 ± 248.7	
Very good partial response	-	1022.5 ± 213.5	
Partial response or stable disease	-	1077.6 ± 288.5	
Mobilization			0.341[c]
G-CSF	-	996.1 ± 241.8	
G-CSF plus cyclophosphamide	-	1058.4 ± 210.9	
G-CSF plus etoposide	-	1075.0 ± 256.6	
G-CSF plus plerixafor	-	951.7 ± 136.3	
Absolute neutrophil count at time prior ASCT	-0.117 (-0.255 ~ 0.025)	-	0.107[a]
Platelet count at time prior ASCT	0.054 (-0.195 ~ 0.089)	-	0.457[a]
Glomerular filtration rate at time prior ASCT	-0.025 (-0.167 ~ 0.118)	-	0.734[a]
Collected CD34+ cells	-0.02 (-0.162 ~ 0.123)	-	0.786[a]

[a]Correlations between paraspinal muscle index and continuous variables were evaluated using Pearson correlation coefficients; [b]paraspinal muscle index by numerical variable were compared by the Student's t-test; [c]paraspinal muscle index by 3 or more multiple numerical variables were compared by the One-Way ANOVA test. CI, confidence interval; SD, standard deviation; ISS, International Staging System; ASCT, autologous hematopoietic stem cell transplantation; G-CSF, granulocyte-colony stimulation factor; Ig, immunoglobulin.

Supplementary Table 2. The multilinear regression analysis with paraspinal muscle index to independent parameter

Parameters	Paraspinal muscle index, mm^2/m^2	
	Regression coefficient ± SD	*P* value
Sex; male, female	-143.6 ± 53.4	<0.001
Type of myeloma; IgG, IgA, IgM or D, and light chain disease	12.1 ± 17.4	0.489
Light chain type; kappa, lambda	47.9 ± 34.3	0.165
Presence of extramedullary plasmacytoma; none, present	-80.3 ± 43.0	0.063
Albumin at diagnosis, g/dL	-36.9 ± 23.0	0.11
Induction treatment; bortezomib-thalidomide-dexamethasone, bortezomib-dexamethasone, thalidomide-dexamethasone, and bortezomib-melphalan-prednisolone	-44.5 ± 26.3	0.093
Absolute neutrophil count at time prior ASCT	-0.17 ± 0.1	0.089

ASCT, autologous hematopoietic stem cell transplantation; Ig, immunoglobulin; SD, standard deviation.

Supplementary Table 3. Univariable analysis to identify factors associated with survival outcomes

		Overall survival			Progression-free survival			Cumulative incidences of TRM		
Variables	Number	Median	95% CI	*P* value	Median	95% CI	*P* value	% at 4 years	95% CI	*P* value
Paraspinal muscle index, mm^2/m^2				0.074			0.029			<0.001
Low muscle mass	38	NA	34.5–NA		23.3	14.5–31.4		10.6	3.3–22.9	
Non-low muscle mass	152	NA	NA–NA		29.2	24.3–38.7		0.7	0.1–3.3	
Muscle density, Hounsfield unit[1]				0.19			0.01			0.276
Low muscle density	38	NA	45.5–NA		27.2	22.6–38.0		5.3	0.9–15.7	
High muscle density	152	NA	NA–NA		35.8	32.2–49.0		2.0	0.6–5.4	
Time to ASCT from the assessing date of LDCT scan, days				0.984			0.487			0.534
≥ Mean value (28 days)	88	NA	58.2–NA		27.8	20.0–33.0		3.4	0.9–8.8	
< Mean value (28 days)	102	NA	NA–NA		26.4	20.3–38.1		2.0	0.4–6.3	
Age at transplant, years				0.101			0.215			0.483
≥60	66	58.2	52.4–NA		25.2	16.1–32.4		1.5	0.1–7.2	
<60	124	NA	NA–NA		29	21.7–36.2		3.2	1.1–7.5	
Sex				0.217			0.324			0.502
Male	104	NA	54.9–NA		25.4	18.8–31.1		1.9	0.4–6.2	
Female	86	NA	NA–NA		29.3	21.7–43.2		3.5	0.9–9.0	
Type of myeloma				0.192			0.309			0.596
IgG	103	NA	NA–NA		25.4	19.5–30.1		1.9	0.4–6.2	
IgA	33	NA	52.4–NA		43.2	14.5–NA		3.0	0.2–13.6	
IgM or IgD	18	48.5	33.3–NA		18.6	9.6–36.2		0.0	0.0	
Light chain disease	36	NA	NA–NA		32.4	15.7–52.1		5.6	1.0–16.5	
Light chain type				0.086			0.112			0.13
Kappa	101	NA	NA–NA		31.1	24.5–43.2		1.0	0.1–4.9	
Lambda	89	NA	54.9–NA		24.3	17.3–30.2		4.5	1.5–10.3	
Presence of extramedullary disease at diagnosis				0.421			0.946			0.258
None	152	NA	NA–NA		24.8	21.7–32.6		3.3	1.2–7.1	
Present	38	NA	52.4–NA		26.6	15.7–44.8		0.0	0.0	
Lactate dehydrogenase at diagnosis (missing n = 8)				0.883			0.543			0.885
> Upper limit of normal	40	NA	58.2–NA		26.2	21.7–38.7		2.6	0.2–11.7	
Normal	142	NA	NA–NA		29.3	13.9–36.2		2.1	0.6–5.6	
β2-microglobulin at diagnosis, mg/L (missing n = 5)				0.002			<0.001			0.123
≥5.5	99	NA	NA–NA		39.2	30.1–52.1		1.0	0.1–5.0	
<5.5 and ≥3.5	44	NA	54.9–NA		17.3	14.5–30.2		2.3	0.2–10.5	
<3.5	42	NA	31.3–NA		16.4	11.2–24.0		7.1	1.8–17.6	

Supplementary Table 3. Continued

		Overall survival			Progression-free survival			Cumulative incidences of TRM		
Variables	Number	Median	95% CI	*P* value	Median	95% CI	*P* value	% at 4 years	95% CI	*P* value
Albumin at diagnosis, g/dL				0.047			0.122			0.06
≥3.5	113	NA	NA–NA		30.2	24.5–36.2		0.9	0.1–4.4	
<3.5	74	NA	58.2–NA		24	16.4–29.0		5.4	1.7–12.2	
Cytogenetic risk (missing n = 60)				0.732			0.394			0.371
Standard	93	NA	NA–NA		30.2	21.7–40.0		2.2	0.4–6.8	
High	37	NA	58.2–NA		29.2	16.6–38.7		0.0	0.0	
Time to ASCT from diagnosis, months							0.419			0.681
≥ Median (6.4 months)	96	NA	52.4–NA		27.8	18.6–36.2		3.1	0.8–8.1	
< Median (6.4 months)	94	NA	NA–NA		26	21.0–38.1		2.1	0.4–6.8	
Induction treatment				0.475			0.636			0.478
Bortezomib-thalidomide-dexamethasone	173	NA	NA–NA		26.6	12.5–76.5		2.9	1.1–6.2	
Others[2]	17	NA	54.9–NA		25.6	23.3–32.4		0.0	0.0	
Lactate dehydrogenase at time prior ASCT				0.241			0.206			0.033
> Upper limit of normal	66	NA	48.5–NA		24	16.8–32.9		6.1	1.9–13.6	
Normal	124	NA	NA–NA		29	24.3–40.0		0.8	0.1–4.0	
Response status at time prior ASCT				0.898			0.148			0.174
Complete response	77	NA	54.9–NA		30.1	21–51.8		0.0	0.0	
Very good partial response	92	NA	58.2–NA		26.6	18.8–32.6		4.4	1.4–10.0	
Partial response or stable disease	21	NA	NA–NA		17.3	11.7–NA		4.8	0.3–20.2	
Mobilization of peripheral blood mononuclear cell				0.055			0.794			0.469
G-CSF plus cyclophosphamide	67	NA	58.2–NA		26.8	21.0–38.1		1.5	0.1–7.1	
Others[3]	123	NA	NA–NA		25.6	17.3–32.6		3.3	1.1–7.6	
Absolute neutrophil count at time prior ASCT, /mm³				0.973			0.16			0.438
≥1.5	170	NA	NA–NA		26.2	21.0–31.4		2.9	1.1–6.3	
<1.5	20	NA	33.3–NA		52.1	12.1–NA		0.0	0.0	
Platelet count at time prior ASCT, /mm³				0.332			0.149			0.508
≥150	175	79.6	71.2–85.8		29	24–32.9		2.9	1.1–6.2	
<150	15	72.2	41.7–88.6		14.5	7.3–26.4		0.0	0.0	
Glomerular filtration rate at time prior ASCT, mL/min/1.73m²				0.119			0.191			<0.001
≥60	167	NA	NA–NA		29	24.0–32.9		1.2	0.2–3.9	
<60	23	NA	48.5–NA		18.6	14.5–33.0		13.0	3.1–30.2	
Conditioning regimen				0.145			0.336			0.653
High dose melphalan	122	77.6	65.3–86.0		24	18.6–29.2		3.3	1.1–7.6	
Melphalan plus busulfan	23	95.2	70.7–99.3		32.7	25.4–NA		0.0	0.0	
Others[4]	45	72.8	56.9–83.6		29	17.3–39.2		2.2	0.2–10.3	
Infused CD34+ cell, x10⁶/kg				0.697			0.541			0.174
≥ Median (5.45)	95	NA	58.2–NA		29.2	20.3–43.2		1.1	0.1–5.2	
< Median (5.45)	95	NA	NA–NA		25.6	18.8–32.6		4.2	1.4–9.7	
Maintenance therapy after ASCT				0.4			0.224			0.601
Yes	58	NA	58.2–NA		31.1	18.8–31.4		1.8	0.1–8.3	
No	132	NA	NA–NA		25.6	24.0–51.8		3.0	1.0–7.1	

[1]Cut-off for low muscle density was defined by sex-specific lowest quantile: 31.8 HU in male and 18.4 HU in female, respectively; [2]others include four of bortezomib-dexamethasone, four of thalidomide-dexamethasone, and nine of bortezomib-melphalan-prednisolone; [3]others include 36 of G-CSF only, 84 of G-CSF plus etoposide, and 3 of G-CSF plus plerixafor; [4]others include 32 of melphalan, busulfan plus thiotepa, 2 of busulfan plus thiotepa, and 11 of bortezomib, busulfan plus melphalan; NA, not available due to not-reached median survival outcome; CI, confidence interval; ASCT, autologous hematopoietic stem cell transplantation; Ig, immunoglobulin; LDCT, low-dose chest CT; G-CSF; granulocyte-colony stimulation factor; TRM, transplant-related mortality; HU, Hounsfield unit.

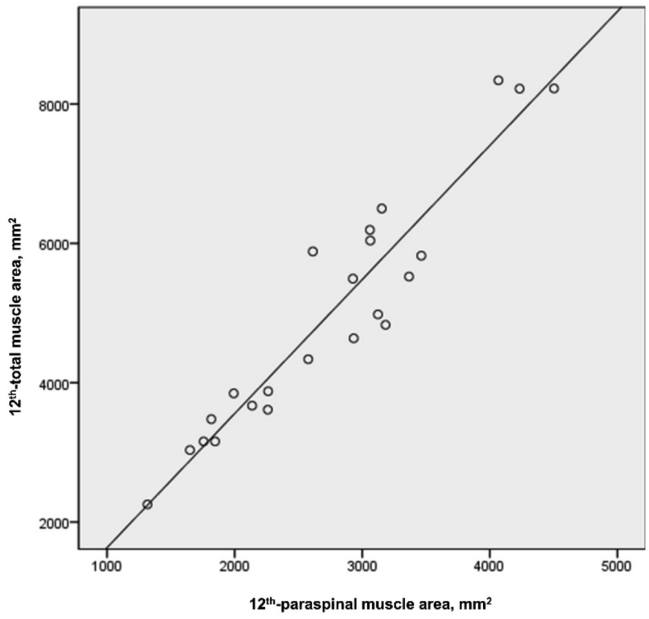

Supplementary Figure 1. A strong correlation between 12th-paraspinal muscle area and 12th-total muscle area. In pilot investigation (n = 23), paraspinal muscle area (PSMA) and total muscle area (TMA) including latissimus dorsi, intercostal, rectus abdominis, external oblique, internal oblique, and paraspinal muscles were measured from axial computed tomography image at the level of 12th thoracic vertebra. Pearson correlation analysis showed that 12th-PSMA had a strong correlation with 12th-TMA (Pearson's correlation coefficient, 0.949). Since measuring 12th-PSMA instead of 12th-TMA is a simpler and more convenient method, 12th-PSMA was finally selected as the criterion in current study.

Diagn Interv Radiol 2023; DOI: 10.4274/dir.2022.221317

INTERVENTIONAL RADIOLOGY

ORIGINAL ARTICLE

Copyright@Author(s) - Available online at dirjournal.org.
Content of this journal is licensed under a Creative Commons Attribution-NonCommercial 4.0 International License.

Thermal ablation of ultrasound and non-contrast computed tomography invisible primary and secondary liver tumors: targeting by selective intra-arterial lipiodol injection

Adrian Kobe
Lambros Tselikas
Frédéric Deschamps
Charles Roux
Alexandre Delpla
Eloi Varin
Antoine Hakime
Thierry de Baère

PURPOSE

To evaluate the technical feasibility and outcomes of thermal ablation following selective intra-arterial lipiodol injection (SIALI) for targeting primary and secondary liver tumors invisible on ultrasound (US) and non-contrast computed tomography (CT).

METHODS

This retrospective study included 18 patients with 20 tumors (67% male, mean age 60.8 ± 12.1 years). The 20 tumors included 15 liver metastases and 5 hepatocellular carcinomas. All patients underwent single-session SIALI and subsequent CT-guided thermal ablation. The primary outcome was a technical success, defined as visualization of the tumor after SIALI and successful thermal ablation. Secondary outcomes were local recurrence rate and procedure-related complications.

RESULTS

The median tumor size was 1.5 (1–2.5) cm. In addition, SIALI was performed with a median volume of 3 (1–10) mL of lipiodol resulting in intra-tumoral iodized oil accumulation in 19 tumors and negative imprint with iodized oil accumulation of the surrounding liver parenchyma in 1 tumor. The technical success rate was 100%. No local occurrence was observed at a mean follow-up time of 3 ± 2.5 years.

CONCLUSION

SIALI to tag liver tumors not visible with US and non-contrast CT before percutaneous ablation is highly feasible and has a high success rate for the treatment of both primary and secondary liver tumors.

KEYWORDS

HCC, invisible tumor, liver metastases, selective intra-arterial lipiodol injection, thermal ablation

Percutaneous thermal ablation of primary and secondary liver tumors is an accepted alternative to surgery for tumors measuring less than 3 cm.[1-3] Thermal ablation is typically guided by ultrasound (US) or non-contrast computed tomography (CT).[1] However, in some cases, the lesions are not visible on either imaging method. Different techniques, such as image fusion with pre-treatment magnetic resonance imaging (MRI) or pre-treatment perilesional coil placement, have been utilized to overcome this problem.[4,5] Another promising technique is CT-guided thermal ablation after selective intra-arterial lipiodol injection (SIALI) with accumulation in the target tumor, mostly used today for hepatocellular carcinomas (HCCs).[6,7] So far, no studies exist that evaluate the efficacy of SIALI and subsequent thermal ablation in secondary liver tumors.

Hence, this study aims to evaluate thermal ablation's feasibility and therapeutic outcomes following SIALI for targeting US- and non-contrast-CT-invisible, mostly secondary, liver tumors.

From the Department of Interventional Radiology, (A.K., ✉ adrian.kobe@gustaveroussy.fr, L.T., F.D., C.R., A.D., E.V., A.H., T.de B.), Gustave Roussy-Cancer Center, Villejuif, France.

Received 16 January 2022; revision requested 26 January 2022; last revision received 14 March 2022; accepted 04 April 2022.

Epub: 28.12.2022

Publication date: 21.07.2023

DOI: 10.4274/dir.2022.221317

You may cite this article as: Kobe A, Tselikas L, Deschamps F, et al. Thermal ablation of ultrasound and non-contrast computed tomography invisible primary and secondary liver tumors: targeting by selective intra-arterial lipiodol injection. *Diagn Interv Radiol.* 2023;29(4):609-613.

Methods

This retrospective study was approved by the institutional review board (protocol number 2022-111). Written informed consent was waived.

Patients

Between April 2003 and January 2021, 103 patients underwent a single-session combined treatment of SIALI (or lipiodol-based transarterial chemoembolization) and percutaneous thermal ablation in various organs (Figure 1). Among the 84 patients treated with SIALI in the liver, 66 were treated in combination with chemotherapy for liver tumors of 3–5 cm with the goal of improving local tumor control with ablation.[8] The final study cohort consisted of 18 patients with 20 liver lesions, smaller than 3 cm and invisible on US and non-contrast CT (66.7% male, mean age 60.8 ± 12.1 years), treated with SIALI for the purpose of tumor visualization and thermal ablation.

Baseline characteristics are reported in Table 1. All patients had MRI or multiphase CT scans (native, arterial, portal venous, and delayed phase) of the liver at baseline, with the liver lesions only visible on the arterial phases. Five lesions were HCCs (25%), whereas the other 15 lesions were liver metastases from various locations (75%) (Table 1).

Interventional techniques

All interventions took place under general anesthesia in a hybrid room made of an angiography system (angioCT alphenix 4D+, Canon Medical Systems, Otawara, Japan) and a multidetector CT (MDCT) (Acquillion one Genesis, Canon Medical Systems, Otawara, Japan; LightSpeed 16, GE Medical Systems, Milwaukee, WI, USA).

SIALI

After the puncture of the common right femoral artery, a 5F sheath was inserted,

Main points

- Treatment of small liver tumors by percutaneous thermal ablation that are invisible on ultrasound or non-contrast computed tomography is challenging.
- Primary and secondary liver tumors can be visualized by selective intra-arterial lipiodol injection (SIALI), enabling same-session percutaneous thermal ablation.
- SIALI proved feasible with excellent oncologic outcomes and allowed for the treatment of both primary and secondary liver tumors.

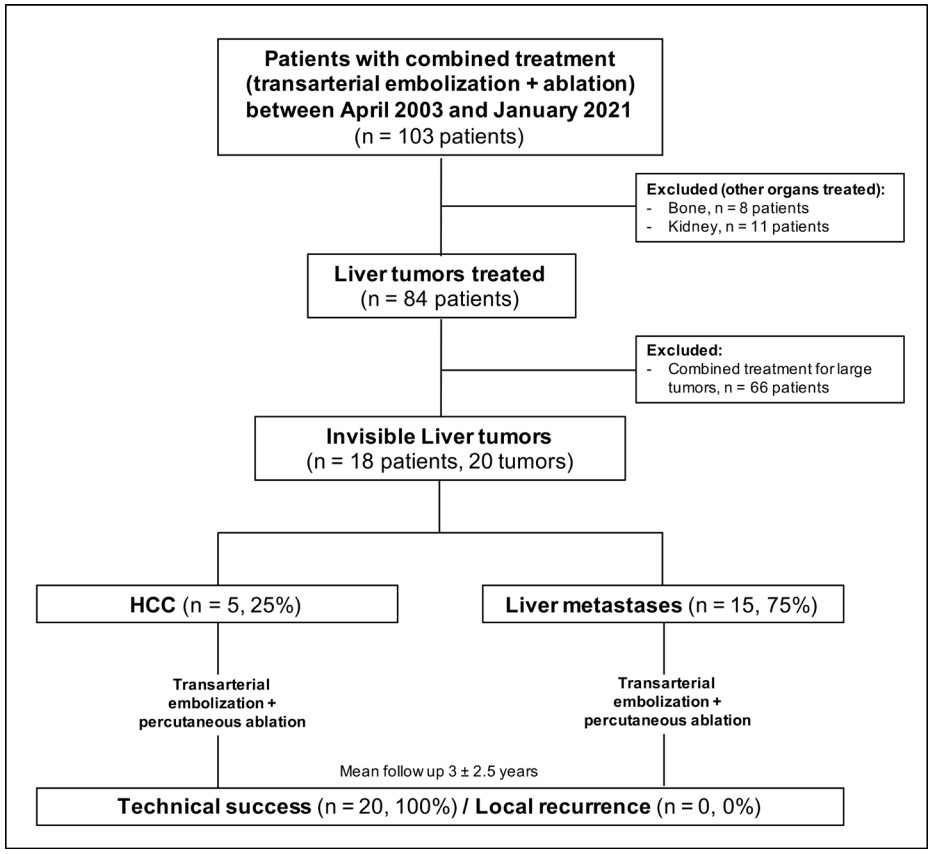

Figure 1. Patient inclusion and outcome flowchart. HCC, hepatocellular carcinoma.

Table 1. Baseline patient characteristics

	All
Total patients, n (%)	18 (100)
Age (years), mean ± SD	60.8 ± 12.1
Male, n (%)	12 (66.7)
Encountered histology	
Number of tumors treated, n (%)	20 (100)
HCC, n (%)	5 (25)
Metastases, n (%)	15 (75)
Neuroendocrine, n (%)	11 (73.3)
Adrenal carcinoma, n (%)	1 (6.7)
Thyroid carcinoma, n (%)	1 (6.7)
Paraganglioma, n (%)	1 (6.7)
GIST, n (%)	1 (6.7)
Tumor specifications	
Tumor size (cm), median (min–max)	1.5 (1–2.5)
Previous treatments	
No, n (%)	2 (11.1)
Surgery, n (%)	12 (66.7)
Radiotherapy, n (%)	1 (5.6)
IR, n (%)	8 (44.4)
Systemic chemotherapy, n (%)	8 (44.4)
Liver segment	
II	2 (10)
IV	3 (15)
V	1 (5)
VI	7 (35)
VII	2 (10)
VIII	5 (25)

GIST, gastrointestinal stromal tumor; HCC, hepatocellular carcinoma; IR, Interventional Radiology; SD, standard deviation.

and the common hepatic artery was catheterized. A digital subtraction angiography was performed to detect all tumor feeders. In case tumor feeders were not detected on digital subtraction angiography, a CT angiography was also carried out to locate the tumor-feeding arteries. Next, selective catheterization of the corresponding vessel was performed using a 2.4F microcatheter (PROGREAT®, Terumo, Tokyo, Japan). A CT angiography was conducted over the placed microcatheter to verify that the entirety of the tumor was covered. Iodized oil (Lipiodol Ultrafluid, Guerbet, Aulnay-Sons-Bois, France) emulsified with saline in a 3:1 ratio was injected into the corresponding artery. The SIALI endpoint was the visualization of the tumor on non-contrast CT.

Percutaneous ablation

Percutaneous ablation was performed immediately after SIALI once tumor tagging was confirmed on MDCT. A thermal ablation probe was inserted into the tumor under real-time MDCT guidance. The liver tumors were either treated by radiofrequency ablation (RFA), microwave ablation (MWA), or cryoablation (CRA) based on the preference of the treating interventional radiologist.

For RFA, either a deployable RFA needle (LeVeen, Boston Scientific, Natick, MA, USA) (Figure 2) or a triple cluster probe (Cool-tip™ RFA Cluster Electrode 2.5 cm active tip, Covidien, Mansfield, MA, USA) (Figure 3) was used. The standard ablation protocol consisted of 12 min with a target final temperature of 60°C or above for the triple cluster probe. For the deployable RFA needle, the ablation session was started at an energy of 30 W and increased by 10 W every 60 s until tissue impedance was raised and a roll-off was reached. In case the roll-off was reached before 12 min, an additional ablation session was performed.

The MWA was performed with microwave probes from different vendors. The time and power of ablation were adapted according to the tumor size, location, and comprehensive protocols supplied by the generator supplier.

The CRA was performed with a cryo-system (VISUAL ICE™, Boston Scientific, Natick, MA, USA) and multiple cryoprobes (IceSphere™ or IceRod™) to cover the entire lesion. A standard treatment cycle consisted of two freeze cycles over 10 min with an intermittent 10 min thawing cycle (9 min passive heating, 1 min active heating).

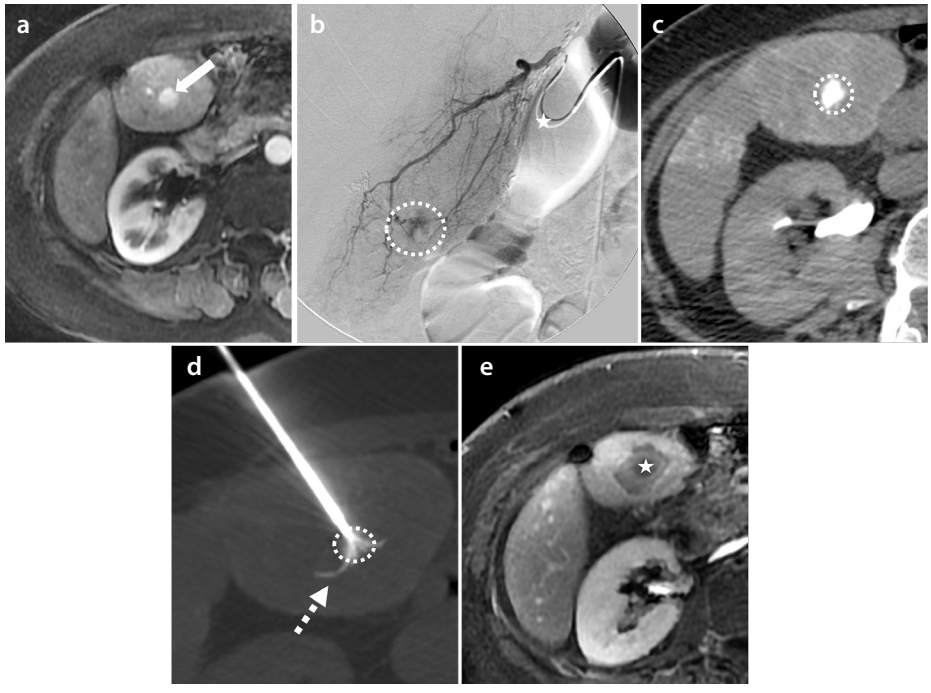

Figure 2. Tagging of a liver metastasis from a neuroendocrine tumor by selective intra-arterial iodized oil injection and subsequent radiofrequency ablation (RFA) in a 56-year-old female. Panel **(a)** shows an arterial phase of the pre-treatment magnetic resonance imaging (MRI) with a hypervascular tumor measuring 12 mm in segment IVb (white arrow). Panel **(b)** shows the selective angiography with a microcatheter (white star) placed in the segment IVa artery and a tumor blush (dotted circle). After injection of 2 mL of iodized oil, the tumor showed strong accumulation [dotted circle panel **(c)**]. Subsequently, an expandable RFA needle (LeVeen, Boston Scientific, Natick, MA, USA) (dotted white arrows) was placed under computed tomography guidance covering the entire tumor [panel **(d)**]. Panel **(e)** shows a contrast-enhanced MRI six months after treatment without evidence of tumor recurrence (white star).

A safety margin of 5 mm between the SIALI visualized tumor and the ablation zone, monitored with periprocedural CT, was considered sufficient for thermal ablation.

Follow-up treatment

Follow-up treatment consisted of clinical visits and imaging at 1, 2, 6, and 12 months, with subsequent annual visits. Technical success was defined as the visualization of the tumor after SIALI and successful thermal ablation. Local recurrence was defined as any contrast-enhancing nodular lesion in the treated area evaluated by multiphase CT or contrast-enhanced MRI. Complications were classified according to the Society of Interventional Radiology (SIR) standards of practice committee with a SIR adverse event (AE) severity scale of 1 to 5.[9] The primary outcome was a technical success. Secondary outcomes were local recurrence and procedure-related complications.

Statistical analysis

The Shapiro–Wilk test was used to test for the normal distribution of data. For descriptive data, mean values and standard deviations, as well as median (min–max) values, were provided as appropriate. Categorical variables were reported as frequencies and percentages. IBM SPSS software v25.0 was used for data analysis.

Results

Median tumor size was 1.5 (1–2.5) cm with 5 HCCs (25%) and 15 liver metastases (75%) treated. After SIALI with a median volume of 3 (1–10) mL of iodized oil, all but one tumor (95%) showed intra-tumoral iodized oil accumulation with enough conspicuity for ablation targeting. In one patient (5%), the tumor was visualized by a negative imprint with lipiodol accumulation of the surrounding liver parenchyma (Figure 4).

Thermal ablation was performed using a cluster probe RFA in seven cases (39%) with a mean ablation time of 11.6 ± 4 min and a mean end temperature of 79°C ± 6.4°C. A deployable RFA needle was used in four cases (22%), and MWA was used in six cases (33%) with a mean applicated power of 84 ± 22 W and a mean ablation time of 10 ± 3.5 min. CRA was used in one case (6%).

One complication (5.6%) was encountered (SIR AE severity scale 4) with cardiac arrest due to hormone discharge during ablation of a paraganglioma metastasis. In-hospital mortality was 0%. The first follow-up CT demonstrated ablation zones measuring 4 ±

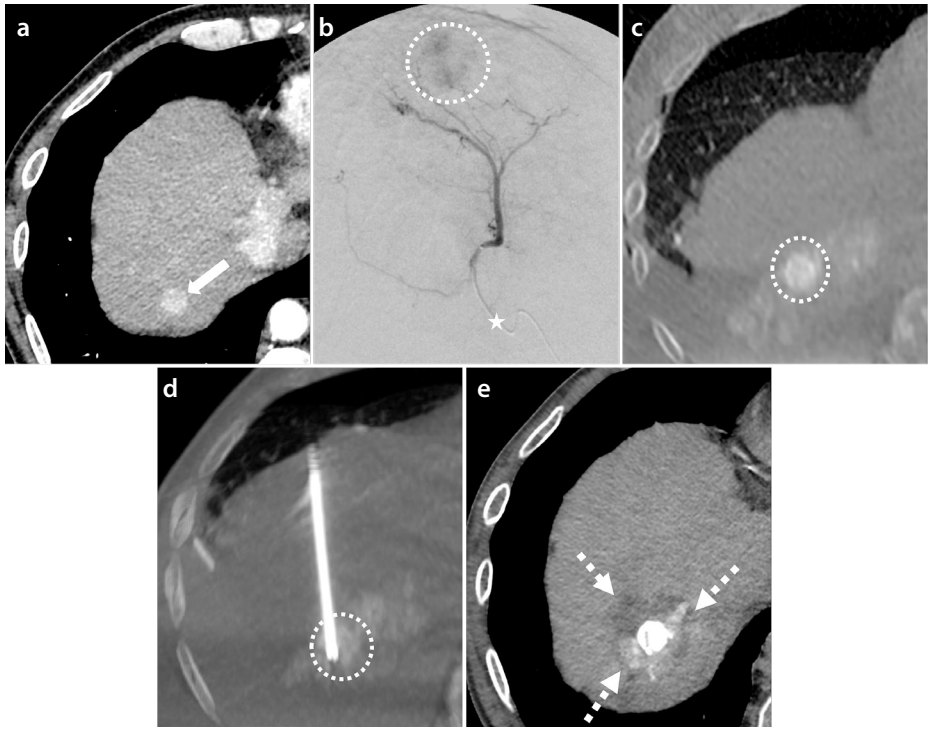

Figure 3. Tagging of a hepatocellular carcinoma by selective intra-arterial iodized oil injection and subsequent radiofrequency ablation (RFA) in a 54-year-old male. Panel **(a)** shows an arterial phase of the pre-treatment computed tomography (CT) with a hypervascular tumor measuring 14 mm in segment VIII (white arrow). Panel **(b)** shows the selective angiography with a microcatheter (white star) placed in the segment VIII artery and a tumor blush (dotted circle). After the injection of 3 mL of iodized oil, the tumor showed moderate accumulation [dotted circle panel **(c)**]. Subsequently, a triple cluster probe (Cool-tip™ RFA Cluster Electrode 2.5 cm active tip, Covidien, Mansfield, MA, USA) was placed under CT guidance [panel **(d)**]. The needle was placed transthoracically and diaphragmatically after creating an iatrogenic pneumothorax. Panel **(e)** shows a contrast-enhanced CT six months after treatment without evidence of tumor recurrence and the ablation zone (white dotted arrows) covering the entire tumor.

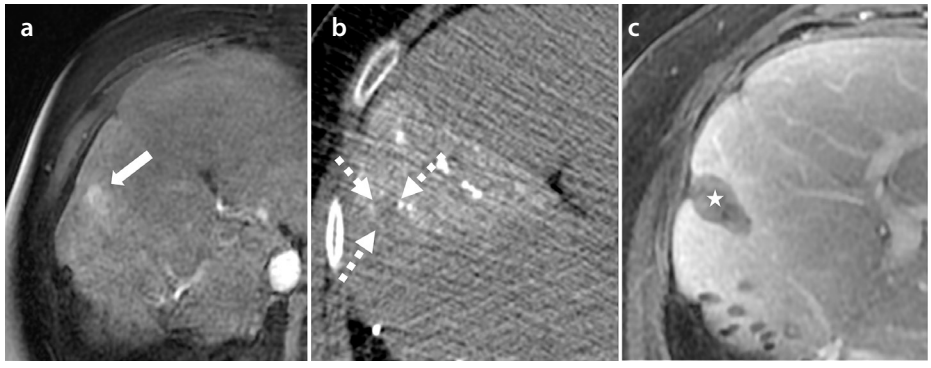

Figure 4. Tagging of a liver metastasis from a neuroendocrine tumor by selective intra-arterial iodized oil injection and subsequent microwave ablation in a 46-year-old male. Panel **(a)** shows an arterial phase of the pre-treatment magnetic resonance imaging (MRI) with a hypervascular tumor measuring 14 mm in segment IV (white arrow). The selective angiography of the segment IV artery did not reveal any tumoral blush. However, a total of 2 mL of iodized oil was injected with accumulation in the peritumoral liver parenchyma, enabling the detection of the tumor (white dotted arrows) on non-contrast intraprocedural computed tomography [panel **(b)**]. Subsequently, microwave ablation was performed without evidence of tumor recurrence (white star) on a follow-up MRI at six months [Panel **(c)**].

1.2 cm, which completely encompassed the targeted tumors with safety margins. The tumors were still visible at the time of follow-up due to iodized oil retention.

No local recurrence was observed during a mean follow-up period of 3 ± 2.5 years. Distant progression was observed in 11 patients (61.1%), with a mean time to systemic progression of 2.1 ± 1.5 years. Table 2 summarizes all intervention-related characteristics.

Discussion

The present study indicates that targeting invisible liver metastases by SIALI immediately before percutaneous ablation is highly feasible with a high local tumor control rate, as it is for primary liver tumors.

For percutaneous ablation, the visibility of the target lesion is of utmost importance, and US or non-contrast CT guidance is most commonly used. In tumors not depicted with US or non-contrast CT guidance, the technique to tag liver tumors by SIALI described in this study carries multiple advantages. First, it is a low-cost, ubiquitous technology with low additional intervention-related risks. Second, no additional software or hardware is needed. However, when MDCT and angiography are not located in the same room, either the puncture can be obtained under cone beam computed tomography (CBCT) guidance, or the patient has to be moved from the angiography suite to the MDCT after SIALI.[10,11] Even if there is a personal experience with CBCT-guided puncture after SIALI not reported here, the optimal solution is certainly an integrated angiography-CT suite, which is increasingly common in interventional oncology departments.[12]

An alternative technique for targeting US and CT non-visible lesions is image fusion with pre-treatment contrast-enhanced images, where the tumor is visualized.[13] However, image fusion has limitations due to different breathing phases and arm positioning between pre-treatment and per-treatment imaging, causing differences in liver configuration.[14] This problem might be overcome by non-rigid image registration, which is technically more demanding and likely unavailable today in routine practice.[15] Furthermore, due to diaphragm motion during breathing, tumors located in the hepatic dome are highly challenging. Especially in the case of special percutaneous access routes, such as a transthoracic/diaphragmatic probe placement after creating an artificial pneumothorax (Figure 3), image fusion is limited due to major hepatic deformations. Other emerging fields trying to solve the difficulties of invisible targets are stereotactic image-guided navigation and robotic navigation systems with trajectory planning on contrast-enhanced CT scans obtained before treatment.[13,16] However, these systems are associated with very high costs and low availability.

There are few studies in the literature examining the feasibility and long-term outcomes of SIALI or lipiodol-based transarterial chemoembolization for targeting small invisible HCCs, reporting excellent tumor visualization and local tumor control rates of 90%–100%.[6,7,17-20] While no published data exists for secondary liver tumors, the current cohort demonstrates successful tagging of

Table 2. Treatment and follow-up characteristics

	All
Intervention	
Type of ablation	
RFA cluster, n (%)	7 (38.9)
RFA expandable, n (%)	4 (22.2)
Ablation time (min), mean ± SD	11.6 ± 4
End temperature (°C), mean ± SD	79 ± 6.4
Microwave ablation, n (%)	6 (33.3)
Cryoablation, n (%)	1 (5.6)
Type of embolization	
Lipiodol	20 (100)
Lipiodol volume (mL), median (min–max)	3 (1–10)
Lipiodol retention, n (%)	19 (95)
Organ at risk in vicinity, n (%)	3 (16.7)
Technical success, n (%)	20 (100)
Ablation zone, mean ± SD	4 ± 1.2
In-hospital outcome	
Complications, n (%)	1 (5.6)
In-hospital mortality, n (%)	0 (0)
Hospital stay (days), median (min–max)	3 (1-8)
Follow-up (years), mean ± SD	3 ± 2.5
Local recurrence, n (%)	0 (0)
Systemic progression, n (%)	11 (61.1)
Time to systemic progression (years), mean ± SD	2.1 ± 1.5

RFA, Radiofrequency ablation; SD, Standard deviation.

all 15 secondary liver tumors from various primary origins, mostly with intratumoral lipiodol accumulation but also with negative staining due to iodized oil accumulation in the surrounding liver parenchyma (Figure 4). The 100% local tumor control rate after a mean follow-up period of 3 ± 2.5 years demonstrates the high effectiveness of SIALI, which is related to the precise needle positioning during percutaneous thermal ablation.

The main limitations of this study are the retrospective design and the limited number of patients.

In conclusion, utilizing SIALI to tag US- and non-contrast-CT-invisible liver tumors for percutaneous ablation is feasible with excellent outcomes and allows for the treatment of both primary and secondary liver tumors.

Conflict of interest disclosure

The authors declared no conflicts of interest.

References

1. Crocetti L, de Baére T, Pereira PL, Tarantino FP. CIRSE standards of practice on thermal ablation of liver tumours. Cardiovasc *Intervent Radiol*. 2020;43(7):951-962. [CrossRef]
2. Van Cutsem E, Cervantes A, Adam R, et al. ESMO consensus guidelines for the management of patients with metastatic colorectal cancer. *Ann Oncol*. 2016;27(8):1386-1422. [CrossRef]
3. Vogel A, Cervantes A, Chau I, et al. Hepatocellular carcinoma: ESMO Clinical Practice Guidelines for diagnosis, treatment and follow-up. *Ann Oncol*. 2018;29(Suppl 4):iv238-iv255. Erratum for: *Ann Oncol*. 2018 Oct 1;29(Suppl 4):iv238-iv255. [CrossRef]
4. Schullian P, Johnston E, Laimer G, et al. Thermal ablation of CT 'invisible' liver tumors using MRI fusion: a case control study. Int J Hyperther. 2020;37(1):564–572. [CrossRef]
5. Adam A, Hatzidakis A, Hamady M, Sabharwal T, Gangi A. Percutaneous coil placement prior to radiofrequency ablation of poorly visible hepatic tumors. Eur Radiol. 2004;14(9):1688-1691. [CrossRef]
6. Nakajima K, Yamanaka T, Nakatsuka A, et al. Clinical utility of radiofrequency ablation following transarterial injection of miriplatin-iodized oil suspension in small hepatocellular carcinoma. *Jpn J Radiol*. 2016;34(9):640–646. [CrossRef]
7. Takaki H, Yamakado K, Nakatsuka A, et al. Computed tomography fluoroscopy-guided radiofrequency ablation following intra-arterial iodized-oil injection for hepatocellular carcinomas invisible on ultrasonographic images. *Int J Clin Oncol*. 2013;18(1):46-53. [CrossRef]
8. Chu HH, Kim JH, Yoon HK, et al. Chemoembolization combined with radiofrequency ablation for medium-sized hepatocellular carcinoma: a propensity-score analysis. *J Vasc Interv Radiol*. 2019;30(10):1533-1543. [CrossRef]
9. Khalilzadeh O, Baerlocher MO, Shyn PB, et al. Proposal of a New Adverse Event Classification by the Society of Interventional Radiology Standards of Practice Committee. *J Vasc Interv Radiol*. 2017;28(10):1432-1437.e3. [CrossRef]
10. Lyu T, Wang J, Cao S, Song L, Tong X, Zou Y. Radiofrequency ablation guided by cone beam computed tomography for hepatocellular carcinoma: a comparative study of clinical results with the conventional spiral computed tomography-guided procedure. *J Int Med Res*. 2019;47(8):3699-3708. [CrossRef]
11. Bapst B, Lagadec M, Breguet R, Vilgrain V, Ronot M. Cone Beam Computed Tomography (CBCT) in the field of interventional oncology of the liver. *Cardiovasc Intervent Radiol*. 2016;39(1):8-20. Erratum in: *Cardiovasc Intervent Radiol*. 2015;38(5):1381. [CrossRef]
12. Erinjeri JP, Doustaly R, Avignon G, et al. Utilization of integrated angiography-CT interventional radiology suites at a tertiary cancer center. *Bmc Med Imaging*. 2020;20(1):114. [CrossRef]
13. Hui TC, Kwan J, Pua U. Advanced techniques in the percutaneous ablation of liver tumours. *Diagnostics (Basel)*. 2021;11(4):585. [CrossRef]
14. Kobe A, Kindler Y, Klotz E, et al. Fusion of preinterventional MR imaging with liver perfusion CT After RFA of hepatocellular carcinoma: early quantitative prediction of local recurrence. *Invest Radiol*. 2020;56(3):188-196. [CrossRef]
15. Park J, Lee J, Lee D, et al. Value of Nonrigid Registration of Pre-Procedure MR with Post-Procedure CT after radiofrequency ablation for hepatocellular carcinoma. *Cardiovasc Intervent Radiol*. 2017;40(6):873-883. [CrossRef]
16. Guiu B, De Baère T, Noel G, Ronot M. Feasibility, safety and accuracy of a CT-guided robotic assistance for percutaneous needle placement in a swine liver model. *Sci Rep*. 2021;11(1):5218. Erratum in: *Sci Rep*. 2021;11(1):8241. [CrossRef]
17. Gandhi S, Iannitti DA, Mayo-Smith WW, Dupuy DE. Technical report: lipiodol-guided computed tomography for radiofrequency ablation of hepatocellular carcinoma. *Clin Radiol*. 2006;61(10):888-891. [CrossRef]
18. Lee MW, Kim YJ, Park SW, et al. Percutaneous radiofrequency ablation of small hepatocellular carcinoma invisible on both ultrasonography and unenhanced CT: a preliminary study of combined treatment with transarterial chemoembolisation. *Br J Radiology*. 2009;82(983):908-915. [CrossRef]
19. Hyun D, Cho SK, Shin SW, Rhim H, Koh KC, Paik SW. Treatment of small hepatocellular carcinoma (≤2 cm) in the caudate lobe with sequential transcatheter arterial chemoembolization and radiofrequency ablation. *Cardiovasc Intervent Radiol*. 2016;39(7):1015-1022. [CrossRef]
20. Pan F, Do TD, Vollherbst DF, et al. Percutaneous irreversible electroporation for treatment of small hepatocellular carcinoma invisible on unenhanced CT: a novel combined strategy with prior transarterial tumor marking. *Cancers*. 2021;13(9):2021. [CrossRef]

Diagn Interv Radiol 2023; DOI: 10.4274/dir.2022.221288

INTERVENTIONAL RADIOLOGY

REVIEW

Copyright@Author(s) - Available online at dirjournal.org.
Content of this journal is licensed under a Creative Commons Attribution-NonCommercial 4.0 International License.

Review of genicular artery embolization, radiofrequency ablation, and cryoneurolysis in the management of osteoarthritis-related knee pain

Lynden Lee
Yan Epelboym

ABSTRACT

Osteoarthritis (OA) of the knee represents one of the most common diseases in the world, affecting an estimated 14 million people in the United States alone. Exercise therapy and oral pain medication are first-line treatments but have limited efficacy. Next-line treatments such as intra-articular injections are limited in durability. Moreover, total knee replacements, although effective, require surgical intervention, which has considerable variability in patient satisfaction. Novel minimally invasive image-guided interventions are becoming more widespread for treating OA-related knee pain. Recent studies of these interventions have revealed promising results, minor complications, and reasonable patient satisfaction. In this study, published manuscripts were reviewed in the field of minimally invasive, image-guided interventions for OA-related knee pain, with a focus on genicular artery embolization, radiofrequency ablation, and cryoneurolysis. Recent studies have demonstrated a significant decrease in pain-related symptoms following these interventions. Reported complications were mild in the reviewed studies. Image-guided interventions for OA-related knee pain exist as valuable options for patients who fail other therapies, may not be good surgical candidates, or wish to avoid surgical intervention. Further studies with randomization and an increased length of follow-up are needed to better characterize outcomes following these minimally invasive therapies.

KEYWORDS

Cryoneurolysis, genicular artery embolization, knee pain, osteoarthritis, radiofrequency ablation

Osteoarthritis (OA) is a major public health problem, with a growing prevalence and incidence.[1] OA of the knee, in particular, affects an estimated 14 million people in the United States alone.[2,3] Furthermore, knee OA is not simply a disease of the elderly, as one in eight individuals with symptomatic knee OA are under the age of 45, and nearly half the patients with OA are between 45 and 64 years.[4] Symptoms of knee OA include stiffness, leading to a reduction in the range of motion, tenderness, and swelling; however, the most common presenting symptom of knee OA is knee pain.

The pathophysiology of OA is complex, and a clear mechanism has not been confirmed. However, a variety of factors, including cartilage breakdown, synovial inflammation, angiogenesis, and recruitment of inflammatory markers, are thought to be the primary drivers of disease progression.[5-8] Risk factors, such as age, obesity, smoking, and mechanical stress, contribute to the degradation of articulating hyaline cartilage, periarticular tissues, and subchondral bone in joints throughout the body.[9] This process leads to a state of chronic inflammation, which is characterized by the release of inflammatory cytokines, including tumor necrosis factor alpha, interleukin (IL)-1β, and IL-6.[10] These cytokines trigger pro-inflammatory processes over time, leading to the release of vascular growth factors, neuropeptides, and β nerve growth factor.[6-8] These markers stimulate the growth of new blood vessels through a process of neovascularization. New vasculature grows into the local joint space of the knee and penetrates adjacent cartilage, synovium, and bone.[5] New blood vessels may also contribute to the growth and development of new sensory nerve fibers.[5] The common pain experienced by people with knee OA is likely a result of a combination of factors, including chronic inflammation, mechanical stress, and the development of unmyelinated nerve fibers along sites of neovascularity and chronic inflammation.

From the Albert Einstein College of Medicine (L.L. ✉ lslee@mednet.ucla.edu), The Bronx, United States; Department of Radiology (Y.E), Brigham and Women's Hospital, Harvard Medical School, Boston, United States.

Received 22 January 2022; revision requested 07 March 2022, accepted 10 April 2022.

Epub: 09.01.2023

Publication date: 21.07.2023

DOI: 10.4274/dir.2022.221288

You may cite this article as: Lee L, Epelboym Y. Review of genicular artery embolization, radiofrequency ablation, and cryoneurolysis in the management of osteoarthritis-related knee pain. *Diagn Interv Radiol.* 2023;29(4):614-620.

Current treatment options for symptomatic knee OA aim to limit pain symptoms. Exercise therapy is a first-line treatment for symptomatic OA because of its lack of adverse side effects, cost effectiveness, and reasonable efficacy.[11,12] The limitations of this therapy include poor adherence, observed in a majority of patients, as well as the inability to perform the exercises when pain levels become high.[13] Patients often progress to using over-the-counter pain medication, such as non-steroidal anti-inflammatories (NSAIDs), for the relief of symptoms. However, NSAIDs subject patients to the risks of gastrointestinal bleeding, kidney injury, and gastric ulcers.[14] Intra-articular steroid and hyaluronic acid injections may provide relief, but the benefits are not durable and have been shown in some studies to accelerate knee OA progression.[15-17] Total knee replacement (TKR) is reserved for patients with severe OA that is refractory to conservative therapy, and patients often suffer with OA-related knee pain symptoms for an average of 9 years prior to becoming surgical candidates.[18] More than 20% of patients receiving TKR experience persistent and unchanged pain after their surgery.[19-21]

In this context, novel minimally invasive interventions for OA-related knee pain may improve patient outcomes and satisfaction. Image-guided interventions for OA-related knee pain consist of varied minimally invasive procedures that include genicular artery embolization (GAE), radiofrequency ablation (RFA), and cryoablation. These interventions are becoming increasingly common given their safety profile and ability to be performed on an outpatient basis.[22] Recent studies of the modalities, which are discussed in this paper, have demonstrated promising results in the management of OA-related knee pain.

Main points

- Osteoarthritis (OA) is one of the most prevalent diseases in the world, with pain as the most common presenting symptom, necessitating the need for effective and safe treatment.
- Although current options for osteoarthritic knee pain relief exist, they are not without side effects and have varying levels of efficacy.
- Minimally invasive options such as genicular artery embolization, radiofrequency ablation, and cryoneurolysis have been demonstrated to produce significant pain relief in randomized controlled trials, and although further research is required to fully characterize their place in OA-related pain treatment, the use of these treatments should be considered.

Discussion

Genicular artery embolization

As previously discussed, neovascularity and its association with synovial inflammation may contribute to the progression of OA-related knee pain. Although other treatment options aim to specifically treat symptoms of pain through the disruption of pain signaling pathways, GAE aims to occlude synovial neovascularity in an effort to decrease the contribution of synovial inflammation to disease progression.[22]

The knee joint is classically supplied by six genicular arteries: a descending genicular artery, superior medial genicular artery, inferior medial genicular artery, superior lateral genicular artery, inferior lateral genicular artery, and anterior tibial recurrent artery (Figure 1). The descending genicular artery branches off from the distal superficial femoral artery. The medial and lateral genicular arteries originate from the popliteal artery, and as the names imply, superior genicular arteries course along the superior aspect of the knee, and inferior genicular arteries course along the inferior portion of the knee. GAE is performed by obtaining arterial access, commonly through the femoral artery, and guiding a microcatheter to the specific genicular arteries in the areas of reported pain. When the proper location is confirmed through fluoroscopy, an injection of embolization particles is administered if neovascularity and hyperemia are demonstrated.

Inflamed synovium neovascularity can be seen on angiography as a contrast-rich area reflecting synovial hyperemia (Figure 2a). The goal of GAE is to prune the neovascularity supplying the hyperemic region, thereby reducing the hyperemia and inflammation of the synovium (Figure 2b).[23] Embolization can be accomplished through the injection of permanent particles or temporary embolic agents into targeted vasculature.[23-26] Figure 3 presents a diagram of GAE.

Several studies have been conducted on the efficacy of GAE in treating OA-related knee pain. Okuno et al.[26] conducted a study in 2017 of 72 patients, defining the clinical success of GAE as a 50% reduction in the Western Ontario and McMaster Universities Arthritis Index (WOMAC) score versus baseline. The WOMAC score is used in the setting of hip and knee OA and ranges from 0 to 96.[27] It consists of a self-administered questionnaire, which has 24 items and is divided into three categories: pain, stiffness, and physical function. The results of the study reveal a clinical success rate of 86.3% and 79.8% at 6 months and 3 years, respectively.

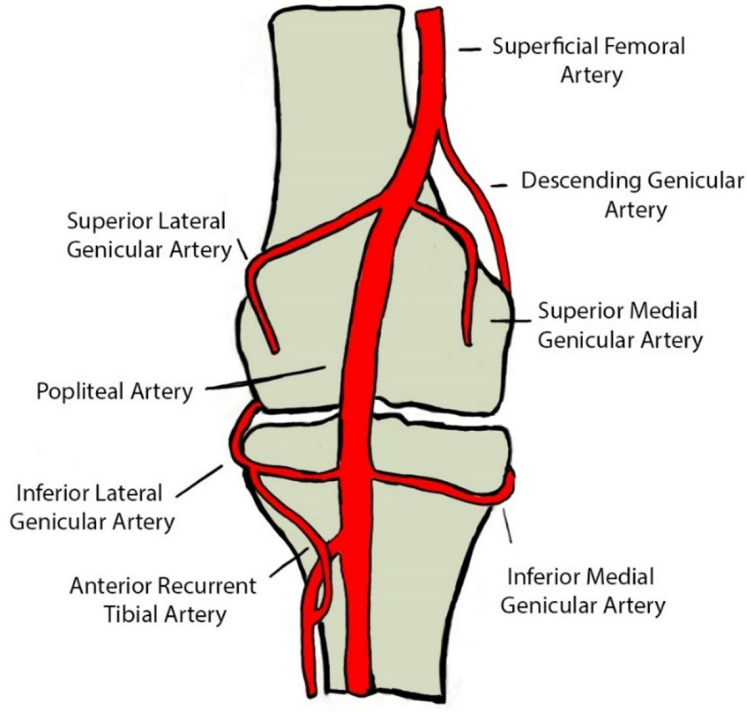

Figure 1. Vascular supply to the knee.

A study in 2020 by Landers et al.[25] included 10 patients at 1-, 6-, and 12-month postprocedure follow-up. Of these 10 patients, two withdrew from the study, with one undergoing a TKR with no reported benefit. This study reported an inferior treatment response compared with the findings of Okuno et al.[28], with a 60% response rate to intervention at 12 months. At 24 months, although the quality-of-life scores and 30-s chair stand test performance were substantially improved from baseline, pain and self-reported function returned to near baseline levels.

The GENESIS Trial, published in 2021, was a prospective trial including 38 patients [Kellgren–Lawrence (KL) grade 1–3] and a mean follow-up of 8 months.[23] Synovial hypervascularity was assessed through magnetic resonance imaging (MRI) to standardize the preprocedure and postprocedure imaging assessment. Significant reductions in pain were noted, measured using the knee injury and OA outcome score, at 6 weeks and 12 months. An MRI analysis revealed improvement in synovitis across all patients and an absence of postembolization cartilage loss.[28,29]

In 2022, Bagla et al.[30] conducted a randomized controlled trial consisting of GAE compared with a sham procedure in 21 patients over the course of 12 months. Patients randomized to the sham cohort had no significant reduction in pain at 1 month and were moved to the GAE cohort. At 12 months, patients receiving GAE exhibited a statistically significant mean reduction in both WOMAC pain scores (47) and Visual Analog Scale scores (54.6). Three patients withdrew from the trial because of increased pain from baseline following the GAE procedure. Similarly, the patients who moved to the treatment cohort exhibited statistically significant reductions in pain scores at all time points.

The potential complications of GAE include nerve injury, bone infarction, access site hematoma, skin erythema and ulceration, and non-target embolization.[28,31-33] To better predict a patient's response to GAE, studies have researched patient factors associated with inferior treatment outcomes.[31,33] Having a better understanding of these factors can potentially aid patient selection and improve the risk–benefit profile of the intervention. A study published in 2021 specifically focused on MRI findings in patients who underwent GAE.[33] The strongest predictor of diminished pain reduction after GAE, measured using the WOMAC score, was the presence of a full-thickness cartilage defect. Effusion synovitis, high-grade osteophytes, bone marrow lesions, and subregional cartilage lesions (all associated with a higher KL grade) were variables associated with decreased pain reduction. These findings suggest that MRI may be used to identify patients less likely to respond to GAE therapy.

Recent studies regarding GAE as a therapeutic option have demonstrated promising results. To further our understanding of GAE, additional randomized sham-controlled trials should be undertaken.

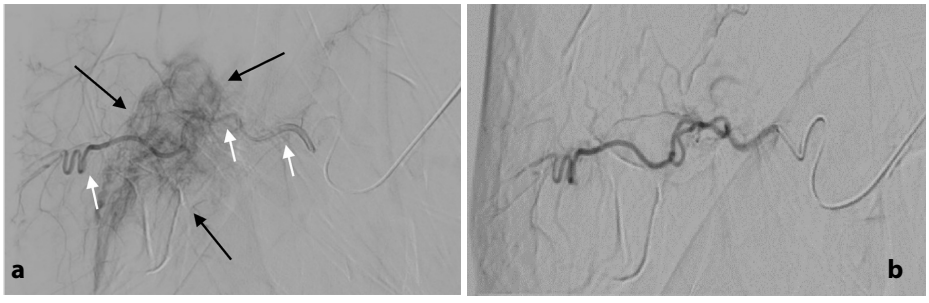

Figure 2. (a) Angiogram of the superior lateral genicular artery (white arrows) indicating hyperemia (black arrows) in the perfused territory. **(b)** Angiogram following genicular artery embolization showing the resolution of hyperemia in the perfused territory.

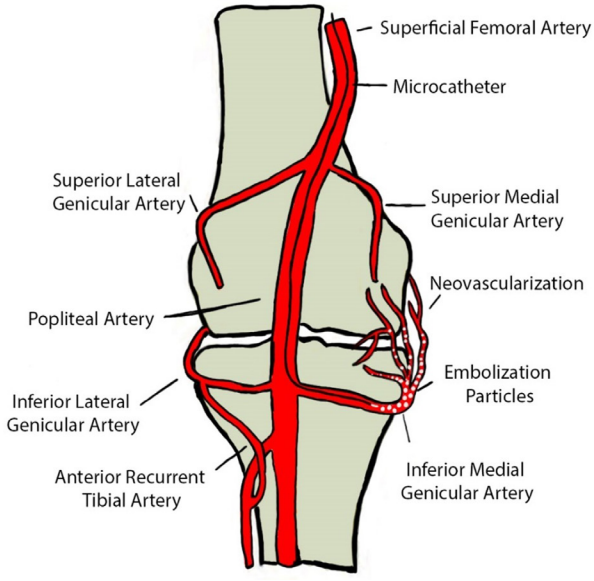

Figure 3. Genicular artery embolization procedure with embolization particles injected into the inferior medial genicular artery.

RFA

RFA was first described in 1891. It functions by creating an electromagnetic field around the tip of a device that transfers heat energy to adjacent structures.[34] This procedure has been used to treat conditions such as trigeminal neuralgia, lumbar spinal facet disease, and sacroiliac joint pain, as well as OA-related knee pain.[35-37] RFA ablation may be particularly useful for treating OA-related knee pain because of its targeted effect on neuropathic pain. The successful ablation of nerves prevents the transmission of pain signals sent as a result of chronic inflammation and direct bony contact in the context of OA.[38,39] Different options exist concerning the temperature range of the probe as well as the option of pulsed application.[40] Traditionally, the goal temperature ranges from 70 °C–90 °C, but recent studies have employed temperatures as low as 60 °C.[41]

Given that the genicular nerves supplying the knee consist of branches of the femoral, common peroneal, saphenous, tibial, and obturator nerves, multiple targets exist for ablation in an attempt to treat intra-articular nerve endings and inhibit the neurotransmission of nociceptive signals.[32,40,42] Commonly targeted nerves for OA-related knee pain include the superior lateral, superior medial, and inferior medial genicular nerves. Due to the role of the common peroneal nerve in motor control and the potential risk of motor nerve injury, the nearby inferior lateral genicular nerve is rarely targeted.[43] The

accurate placement of the RFA probe is made possible by using fluoroscopic guidance and ultrasound imaging.[22] Potential candidates undergo a diagnostic extra-articular injection with local anesthetic as a trial to assess whether the pain relief in the target area is adequate over a course of at least 24 hours. If significant pain relief is achieved, RFA may be scheduled. In this procedure, electrodes are placed using cannulas that are percutaneously stationed at the target area. Sensory and motor stimulation is performed prior to the ablation to ensure proper placement.[44] A diagram of the RFA procedure is shown in Figure 4.

Recent studies have focused on specific temperatures for RFA. A prospective randomized controlled study examined the use of cooled RFA (60 °C).[41] Cooler temperatures may change the shape of the ablation zone from ellipsoid to spherical, thereby affecting a greater area with less risk of thermal injury and complications.[41,45-48] Chen et al.[41] found that cooled RFA, when compared with hyaluronic acid injections, is effective at pain relief, reduction of stiffness, and improvement in physical function as well as global outcomes and quality of life at 12 months, shown as a 46.2% improvement in the WOMAC score.

Pulsed frequencies are often used instead of continuous radiofrequency in RFA. The use of a pulsed frequency has less potential for nerve injury.[49,50] Previous studies of RFA have indicated lower pain scores during follow-up when compared with placebo, with some studies demonstrating up to a >50% decrease in pain scores over a 6-month period.[35,49] A study by Masala et al.[42] in 2014 revealed a significant decrease in pain scores at 12-month follow-up and improved autonomy in daily life demonstrated by an improvement in the WOMAC score from a baseline of 67 to 21, 20, 23, and 30 at 1, 3, 6, and 12 months, respectively. A further study that combined pulsed RFA with viscosupplementations noted that knee pain, although lower than baseline, returned at the 12-month follow-up, suggesting a need for potential future reintervention in the case of pain recurrence.[51]

A recent meta-analysis of RFA completed by Zhang et al.[52] analyzed nine randomized controlled trials and included 802 patients. Their analysis revealed improvements in pain scores at 4, 12, and 24 weeks compared with placebo, with a statistically significant weighted mean difference between WOMAC scores at 12 and 24 weeks of 4.53 and 2.99, respectively. Another systematic review of 33 articles, including 13 randomized controlled trials, revealed a similar alleviation of OA pain symptoms, improvements in quality of life, and enhanced functionality for up to 3–12 months following intervention.[53] Six of these studies had clearly defined significant pain improvements with a >50% reduction from baseline, which was achieved by 65.5% of patients in the RFA group and only 19.3% in the control group. This analysis included studies using continuous RFA, pulsed RFA, and cooled RFA, with benefits seen in all three modalities.

The risks of RFA are mostly associated with injury to adjacent structures. Complications include pseudoaneurysm, arteriovenous fistula development, hemarthrosis, and osteonecrosis.[52,53] One study from the previously mentioned meta-analyses reported the development of pes anserine injury of the inferior medial genicular nerve following RFA.[54] Contraindications of RFA include uncontrolled diabetes, bleeding disorders, the presence of an implantable defibrillator or pacemaker, and knee infection.[17] The large number of studies demonstrating the success of RFA suggests that it is a valuable minimally invasive treatment option for symptomatic OA of the knee. Patients are generally satisfied with the procedure and note improvements in pain, functionality, and quality of life. Studies with larger populations and longer-term follow-up would be useful to evaluate the durability of the symptomatic benefits of RFA as well as the potential impact on the knee joint.

Cryoneurolysis

Similar to RFA, cryoneurolysis, or cryotherapy, aims to damage the nerve endings responsible for the pain experienced in knee OA.[22] As the name implies, this process is completed by using a cooling probe with temperatures ranging from −20 °C to −100 °C. The first reported use of cryoanalgesia was in 1963, when Irving S. Cooper used a hollow tube filled with liquid nitrogen.[55] Marked technological advancements have occurred since then to further develop the equipment and applications of this interventional treatment.[56] Cryoneurolysis leads to the Wallerian degeneration of nerves, which occurs when the distal portion of an injured nerve begins to progressively degenerate as both axon and myelin are broken down by macrophages.[57,58] This controlled, mild nerve damage allows for the complete regeneration and recovery of nerve function by preserving the structural elements of the nerve.[59-61] The cryoablation of these nerves leads to the decreased transmission of pain signals and disruption of the regulation of the IL-6 and IL-17 cytokine pathway observed in the chronic inflammatory state.[10] The infrapatellar branch of the saphenous nerve, which innervates the anterior and inferior part of the knee capsule and skin over the anteromedial knee, is often targeted for this procedure.[62] The specific location for innerva-

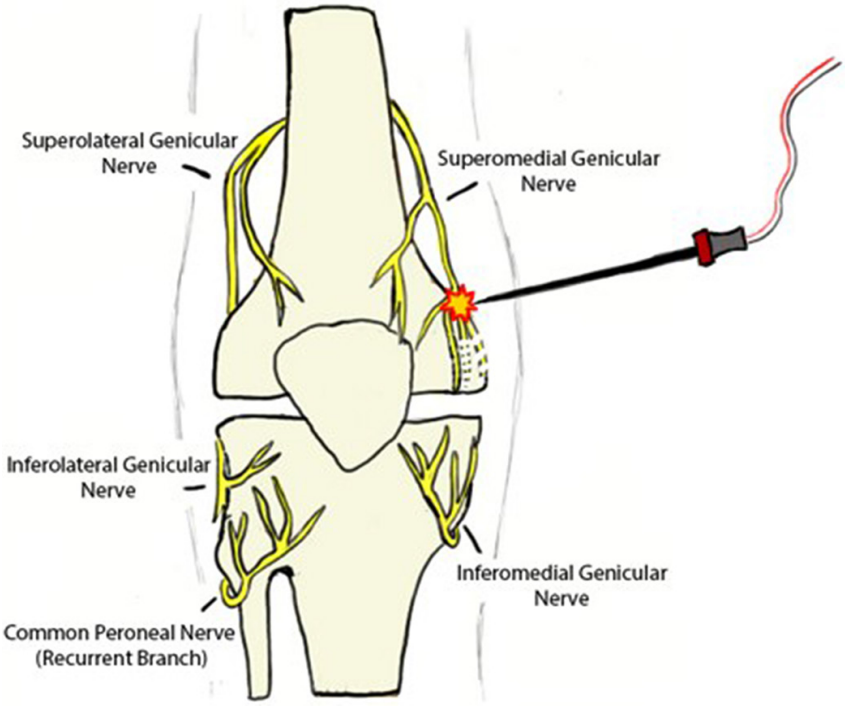

Figure 4. Radiofrequency ablation procedure with ablation to the superomedial genicular nerve.

tion is determined by transcutaneous nerve stimulation in the area of reported pain. The cooling probe can then be placed using ultrasound guidance prior to the cooling process.

Data on cryoneurolysis for OA-related knee pain is limited. A randomized controlled trial conducted by Radnovich et al.[57] included a total of 180 patients and compared cryoneurolysis to a sham procedure in the treatment of knee OA. During this trial period, patients discontinued all over-the-counter medications, herbal medications, and other treatments. An improvement in WOMAC score of 7.1 points at 1 month and 4.7 points at 2 months was identified when compared to the sham procedure.

The effectiveness of the procedure seems to depend on the proximity of the probe to the nerve, size of the probe, rate and duration of treatment, and temperature.[57,62,63] A major benefit of cryoneurolysis is its safety profile and the temporary effect on the treated nerve.[64,65] The risks of this intervention include damage to the skin, alopecia, depigmentation of the skin, and damage to surrounding structures.[66] Although cryoneurolysis has been used in many other applications, more studies are needed to assess efficacy, durability, and complications from this treatment in patients with knee OA.

In conclusion, the widespread prevalence of knee OA as a cause of daily pain and disability warrants an in-depth investigation into novel minimally invasive image-guided therapies. Although exercise, physical therapy, oral medications, joint injections, and joint replacement are mainstays of treatment, image-guided interventions have also entered the treatment landscape. This manuscript discusses minimally invasive image-guided interventions in the treatment of OA-related knee pain. Genicular artery embolization, RFA, and cryoablation have strong safety profiles, can be performed on an outpatient basis, and have been shown to significantly decrease pain scores. GAE recently exhibited promising results in decreasing pain scores and improving quality of life, but current studies have relatively small patient samples without randomization. RFA has been performed for decades, and recent modifications in temperature and pulsatility of frequency are being used to provide positive results. Cryoneurolysis for OA-related knee pain has limited data but has been shown to provide temporary pain relief with limited and minor complications. Although these results are certainly promising, further studies, specifically additional randomized controlled trials with placebo cohorts and extended durations of follow-up, are needed to advance our understanding of these minimally invasive treatments and establish where they fit in the algorithm of OA therapies.

Conflict of interest disclosure

The authors declared no conflicts of interest.

References

1. Safiri S, Kolahi AA, Smith E, et al. Global, regional and national burden of osteoarthritis 1990-2017: a systematic analysis of the Global Burden of Disease Study 2017. *Ann Rheum Dis.* 2020;79(6):819-828. [CrossRef]
2. Bhatia A, Peng P, Cohen SP. Radiofrequency procedures to relieve chronic knee pain: an evidence-based narrative review. *Reg Anesth Pain Med.* 2016;41(4):501-510. [CrossRef]
3. Lluch Girbés E, Nijs J, Torres-Cueco R, López Cubas C. Pain treatment for patients with osteoarthritis and central sensitization. *Phys Ther.* 2013;93(6):842-851. [CrossRef]
4. Deshpande BR, Katz JN, Solomon DH, et al. Number of persons with symptomatic knee osteoarthritis in the us: impact of race and ethnicity, age, sex, and obesity. *Arthritis Care Res (Hoboken).* 2016;68(12):1743-1750. [CrossRef]
5. Mapp PI, Walsh DA. Mechanisms and targets of angiogenesis and nerve growth in osteoarthritis. *Nat Rev Rheumatol.* 2012;8(7):390-398. [CrossRef]
6. Ashraf S, Mapp PI, Walsh DA. Contributions of angiogenesis to inflammation, joint damage, and pain in a rat model of osteoarthritis. *Arthritis Rheum.* 2011;63(9):2700-2710. [CrossRef]
7. Ashraf S, Wibberley H, Mapp PI, Hill R, Wilson D, Walsh DA. Increased vascular penetration and nerve growth in the meniscus: a potential source of pain in osteoarthritis. *Ann Rheum Dis.* 2011;70(3):523-529. [CrossRef]
8. Suri S, Gill SE, Massena de Camin S, Wilson D, McWilliams DF, Walsh DA. Neurovascular invasion at the osteochondral junction and in osteophytes in osteoarthritis. *Ann Rheum Dis.* 2007;66(11):1423-1428. [CrossRef]
9. Palazzo C, Nguyen C, Lefevre-Colau MM, Rannou F, Poiraudeau S. Risk factors and burden of osteoarthritis. *Ann Phys Rehabil Med.* 2016;59(3):134-138. [CrossRef]
10. Kapoor M, Martel-Pelletier J, Lajeunesse D, Pelletier JP, Fahmi H. Role of proinflammatory cytokines in the pathophysiology of osteoarthritis. *Nat Rev Rheumatol.* 2011;7(1):33-42. [CrossRef]
11. Lin KY, Yang CC, Hsu CJ, Yeh ML, Renn JH. Intra-articular injection of platelet-rich plasma is superior to hyaluronic acid or saline solution in the treatment of mild to moderate knee osteoarthritis: a randomized, double-blind, triple-parallel, placebo-controlled clinical trial. *Arthroscopy.* 2019;35(1):106-117. [CrossRef]
12. Walters SJ, Brazier JE. Comparison of the minimally important difference for two health state utility measures: EQ-5D and SF-6D. *Qual Life Res.* 2005;14(6):1523-1532. [CrossRef]
13. Angst F, Aeschlimann A, Michel BA, Stucki G. Minimal clinically important rehabilitation effects in patients with osteoarthritis of the lower extremities. *J Rheumatol.* 2002;29(1):131-138. [CrossRef]
14. Bacchi S, Palumbo P, Sponta A, Coppolino MF. Clinical pharmacology of non-steroidal anti-inflammatory drugs: a review. *Antiinflamm Antiallergy Agents Med Chem.* 2012;11(1):52-64. [CrossRef]
15. Kellgren JH, Lawrence JS. Radiological assessment of osteo-arthrosis. *Ann Rheum Dis.* 1957;16(4):494-502. [CrossRef]
16. Franco CD, Buvanendran A, Petersohn JD, Menzies RD, Menzies LP. Innervation of the anterior capsule of the human knee: implications for radiofrequency ablation. *Reg Anesth Pain Med.* 2015;40(4):363-368. [CrossRef]
17. Kidd VD, Strum SR, Strum DS, Shah J. Genicular nerve radiofrequency ablation for painful knee arthritis: the why and the how. *JBJS Essent Surg Tech.* 2019;9(1):e10. [CrossRef]
18. Canovas F, Dagneaux L. Quality of life after total knee arthroplasty. *Orthop Traumatol Surg Res.* 2018;104(1S):S41-S46. [CrossRef]
19. Filardo G, Di Matteo B, Di Martino A, et al. Platelet-rich plasma intra-articular knee injections show no superiority versus viscosupplementation: a randomized controlled trial. *Am J Sports Med.* 2015;43(7):1575-1582. [CrossRef]
20. Meheux CJ, McCulloch PC, Lintner DM, Varner KE, Harris JD. Efficacy of intra-articular platelet-rich plasma injections in knee osteoarthritis: a systematic review. *Arthroscopy.* 2016;32(3):495-505. [CrossRef]
21. Gato-Calvo L, Magalhaes J, Ruiz-Romero C, Blanco FJ, Burguera EF. Platelet-rich plasma in osteoarthritis treatment: review of current evidence. *Ther Adv Chronic Dis.* 2019;10:2040622319825567. [CrossRef]
22. Goldman DT, Piechowiak R, Nissman D, Bagla S, Isaacson A. Current concepts and future directions of minimally invasive treatment for knee pain. *Curr Rheumatol Rep.* 2018;20(9):54. [CrossRef]
23. Little MW, Gibson M, Briggs J, et al. Genicular artery embolization in patients with osteoarthritis of the knee (GENESIS) using permanent microspheres: interim analysis. *Cardiovasc In-*

tervent Radiol. 2021;44(6):931-940. Erratum in: *Cardiovasc Intervent Radiol.* 2021. [CrossRef]

24. Bagla S, Piechowiak R, Hartman T, Orlando J, Del Gaizo D, Isaacson A. Genicular artery embolization for the treatment of knee pain secondary to osteoarthritis. *J Vasc Interv Radiol.* 2020;31(7):1096-1102. [CrossRef]
25. Landers S, Hely R, Page R, et al. Genicular artery embolization to improve pain and function in early-stage knee osteoarthritis-24-month pilot study results. *J Vasc Interv Radiol.* 2020;31(9):1453-1458. [CrossRef]
26. Okuno Y, Korchi AM, Shinjo T, Kato S, Kaneko T. Midterm clinical outcomes and MR imaging changes after transcatheter arterial embolization as a treatment for mild to moderate radiographic knee osteoarthritis resistant to conservative treatment. *J Vasc Interv Radiol.* 2017;28(7):995-1002. [CrossRef]
27. Bellamy N, Buchanan WW, Goldsmith CH, Campbell J, Stitt LW. Validation study of WOMAC: a health status instrument for measuring clinically important patient relevant outcomes to antirheumatic drug therapy in patients with osteoarthritis of the hip or knee. *J Rheumatol.* 1988;15(12):1833-1840. [CrossRef]
28. Okuno Y, Korchi AM, Shinjo T, Kato S. Transcatheter arterial embolization as a treatment for medial knee pain in patients with mild to moderate osteoarthritis. *Cardiovasc Intervent Radiol.* 2015;38(2):336-343. [CrossRef]
29. Korchi AM, Cengarle-Samak A, Okuno Y, et al. Inflammation and hypervascularization in a large animal model of knee osteoarthritis: imaging with pathohistologic correlation. *J Vasc Interv Radiol.* 2019;30(7):1116-1127. [CrossRef]
30. Bagla S, Piechowiak R, Sajan A, Orlando J, Hartman T, Isaacson A. Multicenter randomized sham controlled study of genicular artery embolization for knee pain secondary to osteoarthritis. *J Vasc Interv Radiol.* 2022;33(1):2-10. [CrossRef]
31. Choi JW, Ro DH, Chae HD, et al. The value of preprocedural MR imaging in genicular artery embolization for patients with osteoarthritic knee pain. *J Vasc Interv Radiol.* 2020;31(12):2043-2050. [CrossRef]
32. Gulec E, Ozbek H, Pektas S, Isik G. Bipolar versus unipolar intraarticular pulsed radiofrequency thermocoagulation in chronic knee pain treatment: a prospective randomized trial. *Pain Physician.* 2017;20(3):197-206. [CrossRef]
33. van Zadelhoff TA, Okuno Y, Bos PK, et al. Association between baseline osteoarthritic features on MR imaging and clinical outcome after genicular artery embolization for knee osteoarthritis. *J Vasc Interv Radiol.* 2021;32(4):497-503. [CrossRef]
34. Lash D, Frantz E, Hurdle MF. Ultrasound-guided cooled radiofrequency ablation of the genicular nerves: a technique paper. *Pain Manag.* 2020;10(3):147-157. [CrossRef]
35. Kroll HR, Kim D, Danic MJ, Sankey SS, Gariwala M, Brown M. A randomized, double-blind, prospective study comparing the efficacy of continuous versus pulsed radiofrequency in the treatment of lumbar facet syndrome. *J Clin Anesth.* 2008;20(7):534-537. [CrossRef]
36. Patel N, Gross A, Brown L, Gekht G. A randomized, placebo-controlled study to assess the efficacy of lateral branch neurotomy for chronic sacroiliac joint pain. *Pain Med.* 2012;13(3):383-398. [CrossRef]
37. Tekin I, Mirzai H, Ok G, Erbuyun K, Vatansever D. A comparison of conventional and pulsed radiofrequency denervation in the treatment of chronic facet joint pain. *Clin J Pain.* 2007;23(6):524-529. [CrossRef]
38. Choi WJ, Hwang SJ, Song JG, et al. Radiofrequency treatment relieves chronic knee osteoarthritis pain: a double-blind randomized controlled trial. *Pain.* 2011;152(3):481-487. [CrossRef]
39. Davis T, Loudermilk E, DePalma M, et al. Twelve-month analgesia and rescue, by cooled radiofrequency ablation treatment of osteoarthritic knee pain: results from a prospective, multicenter, randomized, cross-over trial. *Reg Anesth Pain Med.* 2019:rapm-2018-100051. [CrossRef]
40. Chua NH, Vissers KC, Sluijter ME. Pulsed radiofrequency treatment in interventional pain management: mechanisms and potential indications-a review. *Acta Neurochir (Wien).* 2011;153(4):763-771. [CrossRef]
41. Chen AF, Khalouf F, Zora K, et al. Cooled radiofrequency ablation provides extended clinical utility in the management of knee osteoarthritis: 12-month results from a prospective, multi-center, randomized, cross-over trial comparing cooled radiofrequency ablation to a single hyaluronic acid injection. *BMC Musculoskelet Disord.* 2020;21(1):363. [CrossRef]
42. Masala S, Fiori R, Raguso M, Morini M, Calabria E, Simonetti G. Pulse-dose radiofrequency for knee osteoartrithis. *Cardiovasc Intervent Radiol.* 2014;37(2):482-487. [CrossRef]
43. Shahid KR, Dellon AL, Amrami KK, Spinner RJ. Sciatic and peroneal nerve injuries after endovascular ablation of lower extremity varicosities: case reports and review of the literature. *Ann Plast Surg.* 2015;74(1):64-68. [CrossRef]
44. Kidd VD, Strum SR, Strum DS, Shah J. Genicular nerve radiofrequency ablation for painful knee arthritis: the why and the how. *JBJS Essent Surg Tech.* 2019;9(1):e10. [CrossRef]
45. McCormick ZL, Korn M, Reddy R, et al. Cooled radiofrequency ablation of the genicular nerves for chronic pain due to knee osteoarthritis: six-month outcomes. *Pain Med.* 2017;18(9):1631-1641. [CrossRef]
46. Gupta A, Huettner DP, Dukewich M. Comparative effectiveness review of cooled versus pulsed radiofrequency ablation for the treatment of knee osteoarthritis: a systematic review. *Pain Physician.* 2017;20(3):155-171. [CrossRef]
47. Cedeno DL, Vallejo A, Kelley CA, Tilley DM, Kumar N. Comparisons of lesion volumes and shapes produced by a radiofrequency system with a cooled, a protruding, or a monopolar probe. *Pain Physician.* 2017;20(6):E915-e922. [CrossRef]
48. Menzies RD, Hawkins JK. Analgesia and improved performance in a patient treated by cooled radiofrequency for pain and dysfunction postbilateral total knee replacement. *Pain Pract.* 2015;15(6):E54-E58. [CrossRef]
49. Kvarstein G. Pulsed radiofrequency-time for a clinical pause and more science. *Scand J Pain.* 2012;3(3):124-126. [CrossRef]
50. Erdine S, Yucel A, Cimen A, Aydin S, Sav A, Bilir A. Effects of pulsed versus conventional radiofrequency current on rabbit dorsal root ganglion morphology. *Eur J Pain.* 2005;9(3):251-256. [CrossRef]
51. Filippiadis D, Velonakis G, Mazioti A, et al. Intra-articular application of pulsed radiofrequency combined with viscosupplementation for improvement of knee osteoarthritis symptoms: a single centre prospective study. *Int J Hyperthermia.* 2018;34(8):1265-1269. [CrossRef]
52. Zhang H, Wang B, He J, Du Z. Efficacy and safety of radiofrequency ablation for treatment of knee osteoarthritis: a meta-analysis of randomized controlled trials. *J Int Med Res.* 2021;49(4):3000605211006647. [CrossRef]
53. Ajrawat P, Radomski L, Bhatia A, Peng P, Nath N, Gandhi R. Radiofrequency procedures for the treatment of symptomatic knee osteoarthritis: a systematic review. *Pain Med.* 2020;21(2):333-348. [CrossRef]
54. Conger A, McCormick ZL, Henrie AM. Pes anserine tendon injury resulting from cooled radiofrequency ablation of the inferior medial genicular nerve. *PM R.* 2019;11(11):1244-1247. [CrossRef]
55. Copper IS. Cryogenic surgery: a new method of destruction or extirpation of benign or malignant tissues. *N Engl J Med.* 1963;268:743-749. [CrossRef]
56. Ilfeld BM, Preciado J, Trescot AM. Novel cryoneurolysis device for the treatment

of sensory and motor peripheral nerves. *Expert Rev Med Devices*. 2016;13(8):713-725. [CrossRef]

57. Radnovich R, Scott D, Patel AT, et al. Cryoneurolysis to treat the pain and symptoms of knee osteoarthritis: a multicenter, randomized, double-blind, sham-controlled trial. *Osteoarthritis Cartilage*. 2017;25(8):1247-1256. [CrossRef]
58. Chen P, Piao X, Bonaldo P. Role of macrophages in Wallerian degeneration and axonal regeneration after peripheral nerve injury. *Acta Neuropathol*. 2015;130(5):605-618. [CrossRef]
59. Zhou L, Shao Z, Ou S. Cryoanalgesia: electrophysiology at different temperatures. *Cryobiology*. 2003;46(1):26-32. [CrossRef]
60. Zhou L, Kambin P, Casey KF, et al. Mechanism research of cryoanalgesia. *Neurol Res*. 1995;17(4):307-311. [CrossRef]
61. Kerns JM, Braverman B, Mathew A, Lucchinetti C, Ivankovich AD. A comparison of cryoprobe and crush lesions in the rat sciatic nerve. *Pain*. 1991;47(1):31-39. [CrossRef]
62. Trescot AM. Cryoanalgesia in interventional pain management. *Pain Physician*. 2003;6(3):345-360. [CrossRef]
63. Hsu M, Stevenson FF. Wallerian degeneration and recovery of motor nerves after multiple focused cold therapies. *Muscle Nerve*. 2015;51(2):268-275. [CrossRef]
64. Carr AJ, Robertsson O, Graves S, et al. Knee replacement. *Lancet*. 2012;379(9823):1331-1340. [CrossRef]
65. Hawker GA, Mian S, Kendzerska T, French M. Measures of adult pain: visual analog scale for pain (VAS pain), numeric rating scale for pain (NRS pain), McGill pain questionnaire (MPQ), short-form McGill pain questionnaire (SF-MPQ), chronic pain grade scale (CPGS), short form-36 bodily pain scale (SF-36 BPS), and measure of intermittent and constant osteoarthritis pain (ICOAP). *Arthritis Care Res (Hoboken)*. 2011;63 Suppl 11:S240-S252. [CrossRef]
66. Ilfeld BM, Finneran JJ. Cryoneurolysis and percutaneous peripheral nerve stimulation to treat acute pain. *Anesthesiology*. 2020;133(5):1127-1149. [CrossRef]

Diagn Interv Radiol 2023; DOI: 10.4274/dir.2022.211144

INTERVENTIONAL RADIOLOGY

ORIGINAL ARTICLE

Copyright@Author(s) - Available online at dirjournal.org.
Content of this journal is licensed under a Creative Commons Attribution-NonCommercial 4.0 International License.

Liver regeneration after portal vein embolization: comparison between absolute ethanol and *N*-butyl-cyanoacrylate in an *in vivo* rat model

Mitsunari Maruyama
Haruyuki Takaki
Naoko Yamada
Yutaka Hirata
Koichiro Yamakado
Hajime Kitagaki

PURPOSE

To compare the effects of absolute ethanol (ethanol) and *N*-butyl-cyanoacrylate (NBCA) on non-embolized liver lobe regeneration in a rat model.

METHODS

Twenty-seven Sprague–Dawley rats underwent portal vein embolization (PVE) using ethanol:lipiodol, 1:1 (ethanol group, n = 11, 40.74%), NBCA:lipiodol, 1:1 (NBCA group, n = 11, 40.74%), or sham treatment (sham group, n = 5, 18.52%). The non-embolized and embolized lobe-to-whole liver weight ratios 14 days after PVE were compared among the groups (n = 5, 18.52%). The expressions of CD68 and Ki-67 and embolized-lobe necrotic area percentages one day after PVE were compared between the ethanol (n = 3, 11.11%) and NBCA (n = 3, 11.11%) groups.

RESULTS

The non-embolized lobe-to-whole liver weight ratio after PVE was significantly higher in the NBCA group (n = 5, 33.33%) than in the ethanol group (n = 5, 33.33%) (84.28% ± 1.53% vs. 76.88% ± 4.12%, $P = 0.029$). The embolized lobe-to-whole liver weight ratio after PVE was significantly lower in the NBCA group than in the ethanol group (15.72% ± 1.53% vs. 23.12% ± 4.12%, $P = 0.029$). The proportions of CD68- and Ki-67-positive cells in the non-embolized lobe after PVE were significantly higher in the NBCA group (n = 30, 50%) than in the ethanol group (n = 30, 50%) [60 (48–79) vs. 55 (37–70), $P = 0.003$; 1 (0–2) vs. 1 (0–2), $P = 0.004$]. The embolized-lobe necrotic area percentage after PVE was significantly larger in the NBCA group (n = 30, 50%) than in the ethanol group (n = 30, 50%) [29.46 (12.56–83.90%) vs. 16.34 (3.22–32.0%), $P < 0.001$].

CONCLUSION

PVE with NBCA induced a larger necrotic area in the embolized lobe and promoted greater non-embolized liver lobe regeneration compared with PVE with ethanol.

KEYWORDS

Absolute ethanol, *in vivo* rat model, liver regeneration, *N*-butyl-cyanoacrylate, portal vein embolization

From the Department of Radiology (M.M. ✉ maruyamamd@gmail.com, H.K.), Shimane University Faculty of Medicine Enya-cho Izumo, Japan; Department of Radiology (H.T., K.Y.), Hyogo College of Medicine, Hyogo, Japan; Department of Pathology (N.Y.), Hyogo College of Medicine, Hyogo, Japan; Division of Physiome, Department of Physiology (Y.H.), Hyogo College of Medicine, Hyogo, Japan.

Received 05 November 2021; revision requested 12 January 2022; last revision received 30 April 2022; accepted 25 May 2022.

Epub: 02.01.2023

Publication date: 21.07.2023

DOI: 10.4274/dir.2022.211144

Portal vein embolization (PVE) can be performed to induce compensatory hypertrophy of the remnant liver, thereby increasing the safety of major hepatectomy.[1,2]

Different embolic materials, including absolute ethanol, *N*-butyl-cyanoacrylate (NBCA), gelatin sponge, polyvinyl-alcohol particles, tris-acryl microspheres, vascular plugs, coils, fibrin glue, and polidocanol foam, have been used in PVE on the basis of previous studies.[3] A recent randomized controlled trial (RCT) revealed that NBCA plus iodized oil induced more rapid and robust hypertrophy of the future liver remnant than polyvinyl-alcohol particles plus coils.[4] Compared with the use of NBCA, the use of absolute ethanol by Japanese teams led to a larger future liver remnant after PVE.[5] Moreover, some systematic reviews have shown that absolute ethanol and NBCA induce greater hypertrophy of the future liver rem-

You may cite this article as: Maruyama M, Takaki H, Yamada N, Hirata Y, Yamakado K, Kitagaki H. Liver regeneration after portal vein embolization: comparison between absolute ethanol and *N*-butyl-cyanoacrylate in an *in vivo* rat model. *Diagn Interv Radiol.* 2023;29(4):621-627.

nant.[6-8] However, to date, a head-to-head comparison between NBCA and ethanol has not been made in an RCT model.

The current study aims to compare the effects of absolute ethanol and NBCA, the embolic materials used in PVE, on non-embolized lobe regeneration in a rat model.

Methods

Animal model

All applicable National Institutes of Health guidelines and/or institutional guidelines for the care and use of animals were followed. All procedures performed in studies involving animals were in accordance with the ethical standards of the institution or practice at which the studies were conducted (study number: 19-033). Moreover, the study was conducted according to the Fundamental Guidelines for Proper Conduct of Animal Experiments and Related Activities in Academic Research Institutions in Japan.

In total, 27 male Sprague–Dawley rats, weighing 400–450 g, (Oriental Yeast Co., Ltd., Tokyo, Japan) were included in this study. All rats were provided with unlimited access to food and water before and after the operative procedure. The rats were divided into the sham [5 (18.52%)], ethanol [5 (18.52%)], and NBCA [5 (18.52%)] groups. Then, changes in liver weight were evaluated. The remaining rats [12 (44.44%)] underwent histopathological analysis (the study flow is shown in Figure 1).

Portal vein embolization

The PVE process is demonstrated in Figure 2a. Rats were anesthetized via inhalation of isoflurane [Isoflurane Inhalation Solution (Pfizer)®, Mylan Inc., Tokyo, Japan). Then, an anesthetic mixture of 0.15 mg/kg body weight (BW) medetomidine (Domitor®, Nippon Zenyaku Kogyo Co., Ltd., Tokyo, Japan), 2.0 mg/kg BW midazolam (Dormicum®, Astellas Pharma Inc., Tokyo, Japan), and 2.5 mg/kg BW butorphanol (Vetorphale®, Meiji Seika Pharma Co., Ltd., Tokyo, Japan) was administered intraperitoneally.

After performing a midline laparotomy, the portal vein branch was exposed. A 22-gauge intravenous catheter (BD Insyte™ Autoguard™ BC®; Nippon Becton Dickinson Co., Ltd., Tokyo, Japan) was inserted from the portal vein branch (Figure 2a, left image, black arrow). Next, the catheter was advanced to the left-main portal branch under fluoroscopic guidance (Figure 2a, left image, black arrowhead). A 1:1 mixture of lipiodol (lipiodol 480 inj. 10 mL®; Guerbet Japan K.K., Tokyo, Japan) with either absolute ethanol (anhydrous absolute ethanol; Mylan Inc., Tokyo, Japan) [ethanol group, 5 (18.52%)] or NBCA (Histoacryl®, B. Braun Aesculap Japan Co., Ltd., Tokyo, Japan) [NBCA group, 5 (18.52%)] was used to embolize the left-main portal branch. The ethanol and NBCA groups received 0.10 mL of the embolic materials. In the ethanol group, to mimic the balloon occluded absolute ethanol injection, a vascular clip (cat. no. AS-1 KN353, Natsume Seisakusho, Tokyo, Japan) was used to clamp the left-main portal branch for 10 min during embolization (Figure 2a, middle image, curved black arrow). Moreover, to prevent non-targeted embolization, the right-main portal branch was clamped with a vascular clip during the administration of absolute ethanol and NBCA (Figure 2a, middle image, curved white arrow). In the sham group, the catheter was inserted into the left-main portal branches. However, PVE was not performed. At the end of PVE or the sham treatment, the vascular clips were removed, and a 4-0 nylon double-layer running suture was used to close the abdomen. The PVE was performed by an interventional radiologist with 11 years of experience.

Liver weight

The rats in the sham, ethanol, and NBCA groups were euthanized 14 days after the PVE or sham treatment (Figure 1). Then, the whole livers were harvested and divided into the non-embolized and embolized lobes (the left-lateral lobe and left portion of the medial lobe). Next, a laboratory microscale (AW120, SHIMADZU Co., Ltd., Kyoto, Japan) was used to weigh both lobes. In addition, the non-embolized or embolized lobe-to-whole liver weight ratios were calculated, as follows:

Non-embolized or embolized lobe-to-whole liver weight ratio (%) = non-embolized or embolized lobe (g) / whole liver weight (g) × 100.

Histological examination

The rats in the ethanol [3 (11.11%)] and NBCA [3 (11.11%)] groups were euthanized,

Main points

- This study compared the differences in non-embolized lobe regeneration after portal vein embolization (PVE) using absolute ethanol (ethanol) and *N*-butyl-cyanoacrylate (NBCA) in a rat model.
- The NBCA group [5 (33.33%)] had a significantly higher non-embolized lobe-to-whole liver weight ratio than the ethanol group [5 (33.33%)] (84.28% ± 1.53% vs. 76.88% ± 4.12%, $P = 0.029$). However, the NBCA group had a significantly lower embolized lobe-to-whole liver weight ratio than the ethanol group (15.72% ± 1.53% vs. 23.12% ± 4.12%, $P = 0.029$).
- NBCA for PVE induced a larger necrotic area in the embolized lobe and promoted greater non-embolized lobe regeneration compared with ethanol.

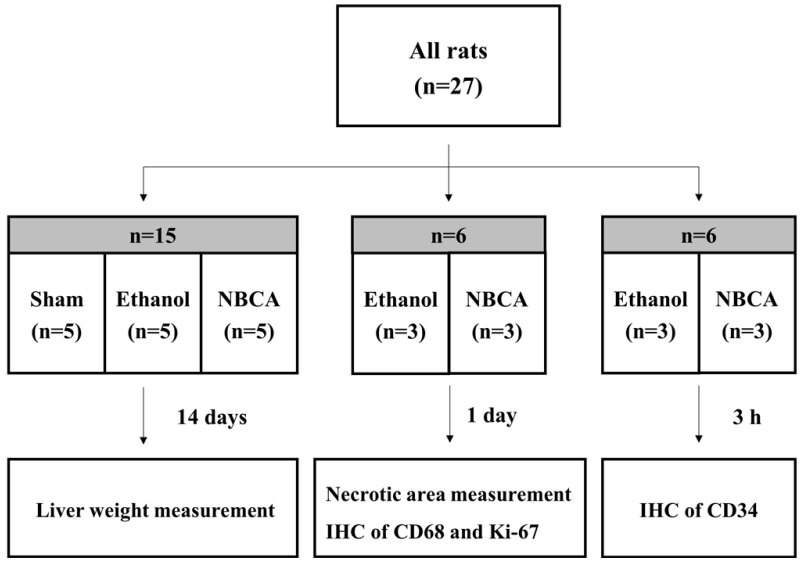

Figure 1. Summary of animal experiments. In total, 27 rats were included in this study. The rats received either sham treatment [5 (18.52%)] or PVE using absolute ethanol [5 (18.52%)] or NBCA [5 (18.52%)]. Then, 14 days after PVE, the liver weights were assessed. Six (22.22%) rats were used to analyze the necrotic area and IHC for CD68 and Ki-67 one day after PVE. The remaining six (22.22%) rats were used to evaluate portal endothelial injury 3 h after PVE via IHC for CD34. PVE, portal vein embolization; NBCA, *N*-butyl-2-cyanoacrylate; IHC, immunohistochemistry.

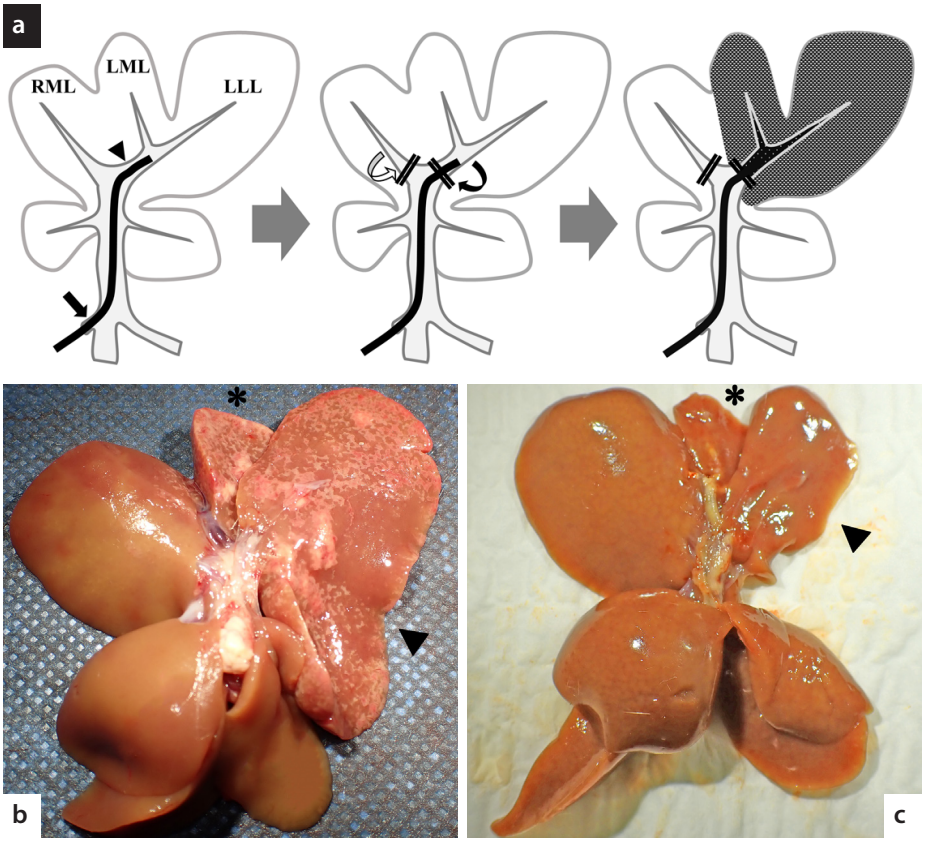

Figure 2. Portal vein embolization. (a) A 22-gauge intravenous catheter (thick black line) is inserted from the portal vein branch (left image, black arrow). Then, the catheter is advanced to the left-main portal branch under fluoroscopic guidance (left image, black arrowhead). The left-main portal branch is clamped with a vascular clip for 10 min during embolization in the ethanol group to mimic the balloon-occluded absolute ethanol injection (middle image, curved black arrow). The right-main portal branch is clamped with a vascular clip during the administration of absolute ethanol and NBCA to prevent the non-targeted embolization of the RML (middle image, curved white arrow). The PVE of the LLL and LML is performed (right image). (b) The liver was harvested one day after PVE using absolute ethanol. The black arrowhead shows the LLL, and the asterisk shows the LML. The color of the embolized lobes changed. (c) The livers were harvested 14 days after PVE. Atrophy of the embolized lobes (black arrowhead, LLL; asterisk, LML) is observed 14 days after PVE. PVE, portal vein embolization; RML, right portion of the medial lobe; NBCA, *N*-butyl-2-cyanoacrylate; LLL, left lateral lobe; LML, left portion of the medial lobe.

and lobe samples were harvested one day after each procedure (Figures 1 and 2b). The samples were used in the analysis of necrotic areas in the embolized lobe and the expression of molecular markers indicating non-embolized lobe regeneration (CD68 and Ki-67). In this study, CD68 and Ki-67 were used as markers for the proliferation of Kupffer and other cells, respectively. The rats in the ethanol [3 (11.11%)] and NBCA [3 (11.11%)] groups were euthanized 3 h after embolization (Figure 1) to evaluate portal endothelial damage via CD34 staining.

The harvested lobe samples were immersed and fixed in 4% formaldehyde and paraffin. A microtome was used to cut the embedded samples into 5-µm-thick sections, and contiguous sections were prepared. One section was stained with hematoxylin and eosin (H&E) to analyze the necrotic area in the embolized lobes. The other contiguous sections were used for immunohistochemical staining for Ki-67 (diluted at 1:100; ab 16667; abcam plc, Cambridge, UK), CD68 (diluted at 1:100; MCA341GA; Serotec Co., Ltd., Sapporo, Japan), and CD34 (diluted at 1:100; AF4117; R&D Systems, Inc., Minneapolis, MN, US).

Quantitative analysis of histopathological samples

OLYMPUS cellSens standard 1.17 (Olympus Corp., Tokyo, Japan) and ImageJ version 1.51 (National Institutes of Health, Bethesda, MD, US) were used to perform quantitative analyses of the histopathological samples. An H&E-stained maximum cut surface specimen obtained from the embolized lobes was used to quantify the necrotic areas in which the nucleus disappeared due to ischemia after PVE. The necrotic areas in the embolized lobes were measured manually in 10 visual fields (original magnification, 100×). Then, the percentage of the necrotic area was calculated.

The proportions of Ki-67- and CD68-positive cells in the non-embolized lobes were assessed in 10 random visual fields per rat at magnifications of 200× and 400×, respectively. The maximum cut surface of the non-embolized lobes was used to perform the evaluations. To evaluate cell count, ImageJ software was used.

Portal vein endothelial injury in the embolized lobe was evaluated 3 h after PVE. Ten CD34-stained specimens per rat were used. The specimens were evaluated at a 100× field of view. Then, the numbers and diameters of the portal veins were recorded. Desquamation of portal endothelial cells was defined as portal vein endothelial injury. The percentages of portal veins with endothelial injury were calculated. The analysis of the histopathological samples was performed by a pathologist with 23 years of experience.

Assessment

The embolized (or sham treatment) and non-embolized lobe-to-whole liver weight ratios 14 days after PVE among the sham, ethanol, and NBCA groups were compared. The percentage of necrotic area in the embolized lobes, expressions of CD68 and Ki-67 in the non-embolized lobes, and the presence of portal endothelium damage were compared between the ethanol and NBCA groups.

Statistical analysis

Descriptive statistics of the data are presented with n (%). Non-normalized variables are shown as the median (min–max), and normal distributions are shown as the mean ± standard deviation. The Shapiro–Wilk test was used to assess the normality of data distribution. If variables were not normally distributed, the Mann–Whitney U test was used. The independent samples t-test was used to analyze data with a normal distribution. The Welch's One-Way analysis of variance was used for three-group comparisons, and then the Games–Howell test was used for a post-hoc comparison if there was a statistical significance. Pearson's chi-squared test and Fisher's exact test were used to evaluate the percentages of portal veins with endothelial injury. All statistical analyses were performed in GraphPad Prism 9 (GraphPad Software Inc., San Diego, CA, US). A P value of <0.050 was considered to be indicative of statistical significance.

Table 1. Liver weight and weight ratios of non-embolized and embolized lobe-to-whole liver

	Sham	Ethanol	NBCA	*P* value			
n (%)	5 (33.33)	5 (33.33)	5 (33.33)	Welch's ANOVA	Games–Howell test		
Liver weight (g)					Sham - ethanol	Sham - NBCA	Ethanol - NBCA
Whole liver, mean ± SD	17.0 ± 1.4	15.6 ± 2.9	14.5 ± 1.0	0.046	0.607	0.031	0.720
Non-embolized lobe, mean ± SD	9.2 ± 0.8	12.0 ± 2.4	12.2 ± 0.8	0.002	0.119	0.001	0.979
Embolized lobe, mean ± SD	7.8 ± 0.9	3.6 ± 0.9	2.3 ± 0.3	<0.001	<0.001	<0.001	0.057
Weight ratio to whole liver (%)							
Non-embolized lobe, mean ± SD	54.03 ± 2.64	76.88 ± 4.12	84.28 ± 1.53	<0.001	<0.001	<0.001	0.029
Embolized lobe, mean ± SD	45.97 ± 2.64	23.12 ± 4.12	15.72 ± 1.53	<0.001	<0.001	<0.001	0.029

Ethanol = absolute ethanol; NBCA, *N*-butyl-2-cyanoacrylate; ANOVA = One-Way analysis of variance; SD, standard deviation.

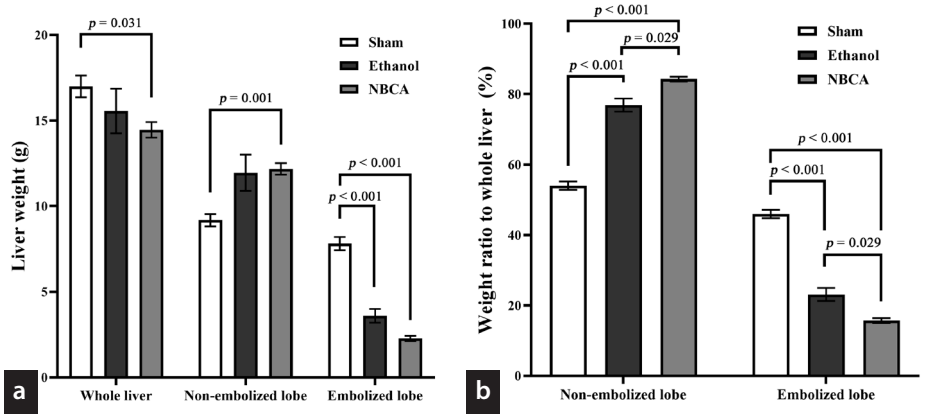

Figure 3. Liver weight and non-embolized and embolized lobe-to-whole liver weight ratio 14 days after PVE. **(a)** Liver weight 14 days after PVE. There are significant differences in all variables of the liver weight between the sham and NBCA groups, and there is a significant difference in the embolized lobe between the sham and ethanol groups (Table 1). The bars represent the SEM. **(b)** Non-embolized and embolized lobe-to-whole liver weight ratios. The non-embolized lobe-to-whole liver weight ratio is significantly higher in the NBCA group [5 (33.33%)] than in the ethanol group [5 (33.33%)] 14 days after PVE (84.28% ± 1.53% vs. 76.88% ± 4.12%, $P = 0.029$, Table 1). The embolized lobe-to-whole liver weight ratio is significantly lower in the NBCA group than in the ethanol group 14 days after PVE (15.72% ± 1.53% vs. 23.12% ± 4.12%, $P = 0.029$, Table 1). The bars represent the SEM. PVE, portal vein embolization; NBCA, *N*-butyl-2-cyanoacrylate; SEM, standard error of the mean.

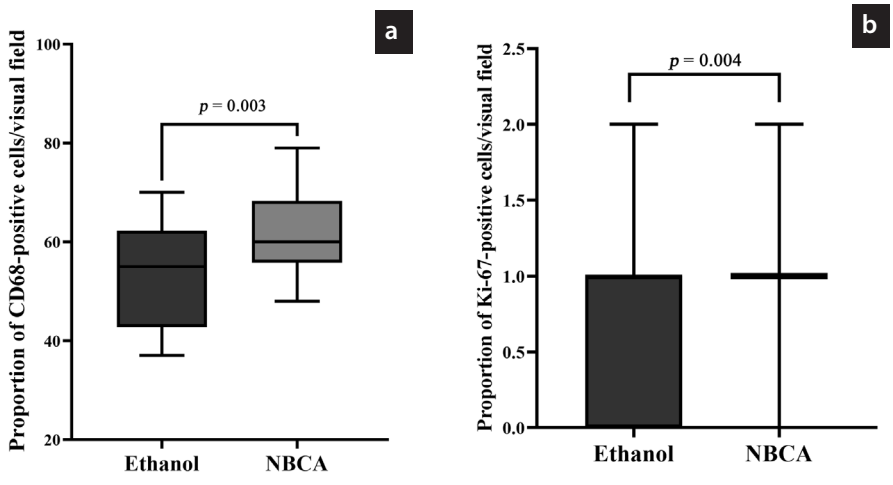

Figure 4. Proportions of CD68- and Ki-67-positive cells in the non-embolized lobe. **(a, b)** The proportions of CD68- and Ki-67-positive cells/visual field are significantly higher in the NBCA group [30 (50%)] than in the ethanol group [30 (50%)] [60 (48–79) vs. 55 (37–70), $P = 0.003$; 1 (0–2) vs. 1 (0–2), $P = 0.004$]. The proportions of CD68- and Ki-67-positive cells are determined in 10 random visual fields at magnifications of 400× and 200×, respectively. NBCA, *N*-butyl-2-cyanoacrylate.

Results

Non-embolized lobe and embolized lobe-to-whole liver weight ratios

The weights of the non-embolized and embolized lobes 14 days after PVE were 9.2 ± 0.8 and 7.8 ± 0.9 g in the sham group [5 (33.33%)], 12.0 ± 2.4 and 3.6 ± 0.9 g in the ethanol group [5 (33.33%)], and 12.2 ± 0.8 and 2.3 ± 0.3 g in the NBCA group [5 (33.33%)], respectively (Table 1, Figure 3a). The non-embolized lobe-to-whole liver weight ratio was significantly higher in the NBCA group than in the sham (84.28% ± 1.53% vs. 54.03% ± 2.64%, $P < 0.001$) and ethanol (84.28% ± 1.53% vs. 76.88% ± 4.12%, $P = 0.029$) groups (Table 1, Figure 3b). By contrast, the NBCA group had a significantly lower embolized lobe-to-whole liver weight ratio than the sham (15.72% ± 1.53% vs. 45.97% ± 2.64%, $P < 0.001$) and ethanol (15.72% ± 1.53% vs. 23.12% ± 4.12%, $P = 0.029$) groups (Table 1, Figure 3b).

CD68 and Ki-67 positive cells in the non-embolized lobe after PVE

The proportion of CD68-positive cells in the non-embolized lobe one day after PVE was significantly higher in the NBCA group [30 (50%)] than in the ethanol group [30 (50%)] [60 (48–79) vs. 55 (37–70), $P = 0.003$] (Table 2, Figure 4a). In addition, the proportions of Ki-67-positive cells in the non-embolized lobe were significantly higher in the NBCA group than in the ethanol group [1 (0–2) vs. 1 (0–2), $P = 0.004$] (Table 2, Figure 4b).

Percentage of necrotic area in the embolized lobe

The percentage of necrotic area in the embolized lobe one day after PVE was significantly larger in the NBCA group [30 (50%)] than in the ethanol group [30 (50%)] [29.46 (12.56–83.90%) vs. 16.34 (3.22–32.0%), $P < 0.001$] (Table 2, Figure 5c).

Table 2. Proportion of CD68- and Ki-67-positive cells, percentage of necrotic area (%)

	Ethanol	NBCA	*P* value
n (%)	30 (50)	30 (50)	
Proportion of CD68-positive cells/visual field, median (min–max)	55 (37–70)	60 (48–79)	0.003
Proportion of Ki-67-positive cells/visual field, median (min–max)	1 (0–2)	1 (0–2)	0.004
Percentage of necrotic area (%), median (min–max)	16.34 (3.22–32.0)	29.46 (12.56–83.90)	<0.001

Ethanol = absolute ethanol; NBCA, *N*-butyl-2-cyanoacrylate.

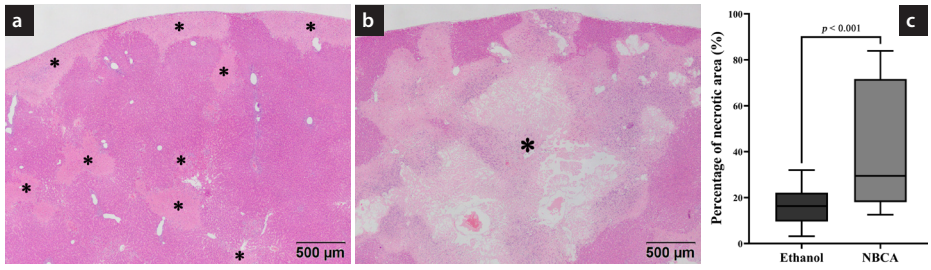

Figure 5. Necrosis in the embolized lobe. **(a, b)** Representative H&E staining of the necrotic area in the embolized lobe after PVE using **(a)** absolute ethanol and **(b)** NBCA (original magnification, 40×). Both groups show a patchy area of lobe necrosis (asterisk). **(c)** The percentage of the necrotic area in the embolized lobe one day after PVE is significantly larger in the NBCA group [30 (50%)] than in the ethanol group [30 (50%)] [29.46 (12.56–83.90%) vs. 16.34 (3.22–32.0%), $P < 0.001$]. The percentage of the necrotic area is evaluated by manually measuring the necrotic area in the embolized lobes in 10 random visual fields (original magnification, 100×). H&E, hematoxylin and eosin; PVE, portal vein embolization; NBCA, *N*-butyl-2-cyanoacrylate.

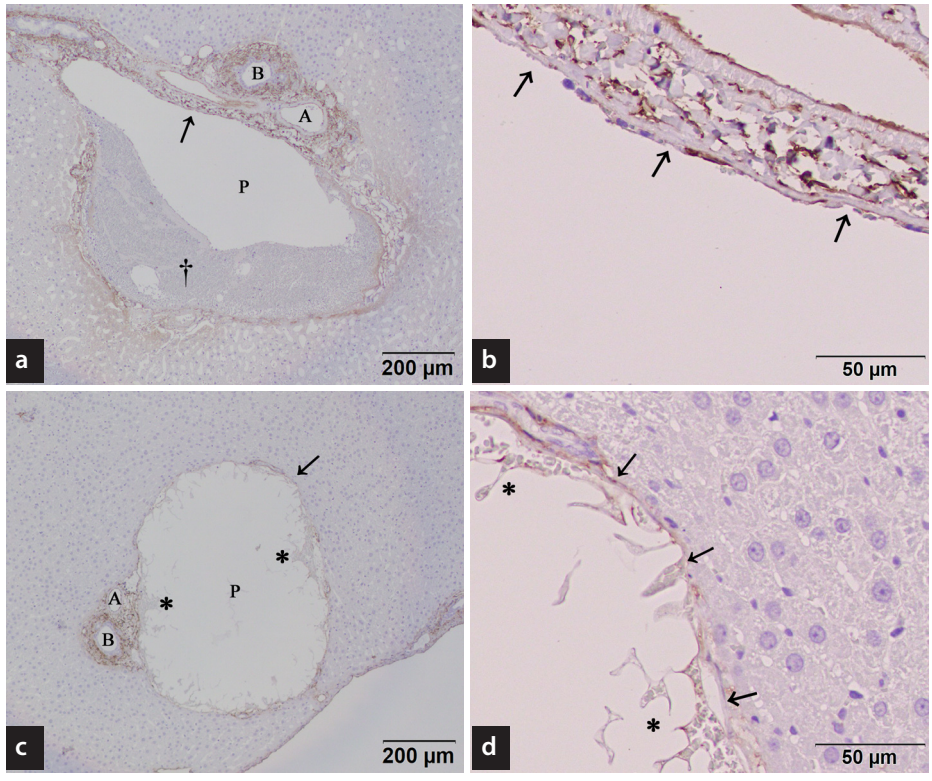

Figure 6. Immunohistochemistry for CD34 in the embolized lobe. **(a, b)** Embolized lobe after PVE using absolute ethanol (original magnification: 100×, 400×). **(c, d)** Embolized lobe after PVE using NBCA (original magnification: 100×, 400×). Injured endothelial cells embolized with absolute ethanol and NBCA after PVE are indicated (arrow). A thrombus is observed along the inner lumen of the portal vein (dagger). An NBCA cast adhesion is noted at the inner lumen of the portal vein (asterisk). PVE, portal vein embolization; NBCA, *N*-butyl-2-cyanoacrylate; P, portal vein; A, hepatic artery; B, bile duct.

Portal vein endothelial injury

Desquamation of portal endothelial cells was observed 3 h after embolization in the ethanol and NBCA groups (Figure 6). The percentage of portal veins with endothelial injury was significantly higher in the ethanol group [30 (32.26%)] than in the NBCA group [8 (6.84%)] ($P < 0.001$) if the portal vein diameter was ≤500 μm (Table 3). The percentages of portal veins with endothelial injury were similar between the ethanol and NBCA groups if the portal vein diameter was >500 μm (Table 3) ($P = 0.621$). In the NBCA group, a deposition of NBCA at the portal endothelium was observed in 9 (56.25%) of 16 portal veins with diameters >500 μm.

Discussion

The non-embolized lobe-to-whole liver weight ratio was significantly higher in the NBCA group than in the ethanol group 14 days after PVE, which showed that NBCA was more effective in promoting non-embolized lobe regeneration than absolute ethanol. The expressions of CD68- and Ki-67-positive cells in the non-embolized lobes were higher in the NBCA group than in the ethanol group. Kupffer cells and monocyte-derived macrophages, as well as CD68-positive cells, have important roles in liver regeneration by releasing growth factors, including hepatocyte growth factor.[9-11] The higher proportions of CD68- and Ki-67-positive cells in the NBCA group might explain the greater regenerative response to this embolic material than to absolute ethanol. However, the mechanisms by which NBCA for PVE promotes non-embolized lobe regeneration were not assessed in this study. One possible explanation is the difference in the degree of liver necrosis between the ethanol and NBCA groups. The percentage of necrotic area in the embolized lobe one day after PVE was larger in the NBCA group than in the ethanol group. Moreover, atrophy of the embolized lobe 14 days after PVE was more severe in the NBCA group than in the ethanol group. These differences might have led to the varying degrees of liver regeneration between the ethanol and NBCA groups. The weights of the non-embolized lobes 14 days after PVE were actually similar between the ethanol and NBCA groups (12.0 ± 2.4 vs. 12.2 ± 0.8 g), but the weights of the non-embolized lobes 14 days after PVE might have been affected by the *body* weights of the ethanol and NBCA groups 14 days after PVE (480 ± 40 vs. 464 ± 16 g).

de Baere et al.[3] showed that the rate of liver hypertrophy increased if necrosis-induced fibrosis in the embolized lobe was

Table 3. Percentage of portal veins with endothelial injury

Diameter of portal vein	Ethanol (n = 93)	NBCA (n = 117)	*P* value
All, n (%)	38 (40.86%)	20 (17.09%)	<0.001
≤500 μm, n (%)	30 (32.26%)	8 (6.84%)	<0.001
>500 μm, n (%)	8 (8.6%)	12 (10.26%)	0.621

The number of portal veins with endothelial injury in relation to the total number of portal veins in the visual field is enclosed in parentheses. Ethanol = absolute ethanol; NBCA, *N*-butyl-2-cyanoacrylate.

larger. Similarly, Furrer et al.[12] revealed that the rate of liver hypertrophy increased with a larger necrotic area in the embolized or ligated lobe. Another possible explanation is the difference in the degrees of foreign body reaction between ethanol and NBCA. In this study, a higher proportion of Kupffer cells was observed in the non-embolized lobe in the NBCA group. Therefore, a stronger foreign body reaction in the NBCA group might promote Kupffer cell recruitment in the non-embolized lobe, leading to greater liver regeneration.[13]

Notably, there was a higher incidence of endothelial injury after PVE using absolute ethanol, particularly in the small (≤500 μm) portal vein. However, the NBCA group had a larger percentage of necrotic areas in the embolized lobe. This discrepancy might be attributed to the different mechanisms of embolization between absolute ethanol and NBCA. Absolute ethanol causes tissue necrosis, and thrombus can form secondary to stagnant blood flow.[14] By contrast, NBCA polymerizes and forms a cast in the blood vessel.[15-18] This cast fills and adheres to the inner lumen of the blood vessel, thereby preventing blood flow and resulting in thrombus formation.[17] In this study, NBCA cast adhesion was observed in nine (56.25%) of the large (>500 μm) portal veins. Therefore, compared with ethanol, NBCA might induce thrombus formation in larger portal veins and a larger necrotic area.

This study had several limitations. First, this was a small-scale animal study. Therefore, the results cannot be immediately applied to humans, so further studies involving a large-scale animal model should be performed. Second, because of the lack of cross-sectional imaging modalities, such as computed tomography and magnetic resonance imaging, the actual lobe volume, including the non-embolized or embolized lobe before PVE, could not be evaluated in these small animals. Third, although various factors such as cytokine and micro-RNA levels can affect liver regeneration,[9,10] they were not investigated in this study. Fourth, the volume ratio of lipiodol and embolic materials was fixed at 1:1, and other ratios were not evaluated. Despite these limitations, this study's results provide useful information for determining the optimal embolic material for PVE that can efficiently promote liver regeneration.

In conclusion, compared with absolute ethanol, NBCA for PVE induced a larger necrotic area in the embolized lobe and promoted greater non-embolized lobe regeneration.

Acknowledgments

The authors thank Nahomi Yoshimura, Yumi Seshi, Naoya Kinota, Eisuke Ueshima, Hiroshi Kodama for the technical support. The part of this study was presented at the Annual Meeting of the Japanese Society of Interventional Radiology (JSIR) 2021: abstract no .O-054. PVE: *in vivo* comparison of absolute ethanol and NBCA in a rat model.

Funding

This work was supported by JSPS KAKENHI Grant Number 19K17199.

Conflict of interest disclosure

The authors declared no conflicts of interest.

References

1. Rahbari NN, Garden OJ, Padbury R, et al. Posthepatectomy liver failure: a definition and grading by the international study Group of Liver Surgery (ISGLS). *Surgery*. 2011;149(5):713-724. [CrossRef]
2. Huang SY, Aloia TA. Portal vein embolization: state-of-the art technique and options to improve liver hypertrohphy. *Visc Med*. 2017;33(6):419-425. [CrossRef]
3. de Baere T, Denys A, Paradis V. Comparison of four embolic materials for portal vein embolization: experimental study in pigs. *Eur Radiol*. 2009;19(6):1435-1442. [CrossRef]
4. Luz JHM, Veloso Gomes F, Costa NV, et al. BestFLR Trial: liver regeneration at ct before major hepatectomies for liver cancer-a randomized controlled trial comparing portal vein embolization with *N*-butyl-cyanoacrylate plus iodized oil versus polyvinyl alcohol particles plus coils. *Radiology*. 2021;299(3):715-724. [CrossRef]
5. Sugawara S, Arai Y, Sone M, et al. Retrospective comparative study of absolute ethanol with N-butyl-2-cyanoacrylate in percutaneous portal vein embolization. *J Vasc Interv Radiol*. 2019;30(8):1215-1222. [CrossRef]
6. van Lienden KP, van den Esschert JW, de Graaf W, et al. Portal vein embolization before resection: a systematic review. *Cardiovasc Intervent Radiol*. 2013;36(1):25-34. [CrossRef]
7. Wajswol E, Jazmati T, Contractor S, Kumar A. Portal vein embolization utilizing N-butyl cyanoacrylate for contralateral lobe hypertrophy prior to liver resection: a systematic review and meta-analysis. *Cardiovasc Intervent Radiol*. 2018;41(9):1302-1312. [CrossRef]
8. Luz JHM, Gomes FV, Coimbra E, Costa NV, Bilhim T. Preoperative portal vein embolization in hepatic surgery: a review about the embolic materials and their effects on liver regeneration and outcome. *Radiol Res Pract*. 2020;21:9295852. [CrossRef]
9. Hoffmann K, Nangel AJ, Tanabe K, et al. Markers of liver regeneration-the role of growth factors and cytokines: a systemic review. *BMC Surg*. 2020;20(1):31. [CrossRef]
10. Mao SA, Glorioso JM, Nyberg SL. Liver regeneration. *Trans Res*. 2014.163(4):352-362. [CrossRef]
11. Forbes SJ, Newsome PN. Liver regeneration - mechanisms and models to clinical application. *Nat Rev Gastroenterol Hepatol*. 2016;13(8):473-485. [CrossRef]
12. Furrer K, Tian Y, Pfammatter T, et al. Selective portal vein embolization and ligation trigger different regenerative responses in the rat liver. *Hepatology*. 2008;47(5):1615-1623. [CrossRef]
13. Sadato A, Wakhloo AK, Hopkins LN. Effects of a mixture of a low concentration of n-butylcyanoacrylate and ethiodol on tissue reactions and the permanence of arterial occlusion after embolization. *Neurosurgery*. 2000;47(5):1197-1203. [CrossRef]
14. Saguchi T, Arai Y, Kamei S, Komemushi A, Saito K. Guidelines for absolute ethanol for Use in Vascular Embolization, 2016 edition. *Interventional Radiology*. 2018;3(1):44-65. [CrossRef]
15. Tanaka T, Kawai N, Sato M, et al. Safety of bronchial arterial embolization with *n*-butyl cyanoacrylate in a swine model. *World J Radiol*. 2012;28(12):455-461. [CrossRef]
16. Kawai N, Sato M, Minamiguchi H, et al. Basic study of a mixture of *n*-butyl cyanoacrylate, absolute ethanol, and lipiodol as a new embolic material. *J Vasc Interv Radiol*. 2012;23(11):1516-1521. [CrossRef]
17. Takeuchi Y, Morishita H, Sato Y, et al. Guidelines for the use of NBCA in vascular embolization devised by the Committee of

Practice Guidelines of the Japanese Society of Interventional Radiology (CGJSIR), 2012 edition. *Jpns J Radiol*. 2014;32(8):500-517. [CrossRef]

18. Tanaka F, Kawai N, Sato M, et al. Effect of transcatheter arterial embolization with a mixture of n-butyl cyanoacrylate, lipiodol, and absolute ethanol on the vascular wall: macroscopic and microscopic studies. *Jpns J Radiol*. 2015;33(7):404-409. [CrossRef]

Diagn Interv Radiol 2023; DOI: 10.4274/dir.2022.221467

INTERVENTIONAL RADIOLOGY

TECHNICAL NOTE

Copyright@Author(s) - Available online at dirjournal.org.
Content of this journal is licensed under a Creative Commons Attribution-NonCommercial 4.0 International License.

The iceberg technique: an innovative approach for radiofrequency ablation of diving thyroid nodules

Antônio Rahal Junior
Erivelto Martinho Volpi
Bruno Pagnin Schmid
Priscila Mina Falsarella
Rodrigo Gobbo Garcia

ABSTRACT

Diving thyroid nodules are a limitation of radiofrequency ablation because the mediastinal component cannot be adequately identified by ultrasound (US). We aim to describe a new technique, the iceberg technique, to overcome this issue and explain our three-year experience of using this novel method. The iceberg technique consists of a two-stage treatment. First, the ablation of the cervical portion of the nodules (easily visualized during the initial US exam) using trans-isthmic access is performed using the moving-shot technique. After three to six months, there is a volumetric reduction of the treated portion, leading to retraction of the thyroid parenchyma. This brings the mediastinal component to the cervical region, thereby enabling a perfect visualization by US. Then, the second stage of treatment is carried out with complete nodule ablation, and the region that was treated first is looked at a second time. From April 2018 to April 2021, nine patients with nine benign nodules were submitted for the iceberg technique. No complications occurred during the entire follow-up period. The patients displayed normal hormonal levels after the procedures, and there was a significant volume reduction of the nodules until three months post-ablation. The iceberg technique is an effective and safe option for the radiofrequency treatment of diving goiters.

KEYWORDS

Ablation, goiter, interventional, nodule, thyroid

Thyroid nodules are highly prevalent across the world. Among thyroid nodules, the vast majority are benign nodules.[1] Among these benign nodules, a significant number may cause such symptoms as a volumetric increase, with or without a mediastinal diving component; autonomous nodules; esophageal and tracheal compression; and foreign body perception.[2] Before the advent of thyroid nodules ablation, surgery was the gold-standard treatment for symptomatic benign thyroid nodules and malignant nodules. However, this treatment is associated with complications, including hypothyroidism, nerve damage, and hypocalcemia.[3] Regarding this situation, radiofrequency thermal ablation (RFA) emerges as a valuable option, allowing minimally invasive treatment and preserving thyroid function in selected patients.[4] Since thyroid RFA is entirely guided by ultrasound (US), in diving thyroid nodules, just the cervical portion (the peak of the iceberg) is visible on the US, and the presence of a mediastinal immersion component that cannot be identified by the method may be a limitation to the safe treatment of these nodules. We describe a new technique, the iceberg technique, to overcome this issue and a three-year single-center experience using this approach.

Technique

This study was approved by the institutional review board and was in accordance with the Helsinki Declaration (ethics committee approval number: 24237019.0.0000.0071). All patients provided informed consent. From April 2018 to April 2021, 12 euthyroid consecutive patients were diagnosed with diving thyroid nodules presenting a mediastinal component. Among these, nine patients (six men, three women; mean age: 50.5 years) with nine benign

From the Department of Interventional Radiology (A.R.J., B.P.S. ✉ brunopschmid@gmail.com, P.F., R.G.G.), Hospital Israelita Albert Einstein, Sao Paulo, Brazil; Department of Head and Neck Surgery (E.M.V.), Hospital Alemão Oswaldo Cruz, Sao Paulo, Brazil.

Received 02 March 2022; revision requested 10 Apr 2022; last revision received 20 Apr 2022; accepted 10 May 2022.

Epub: 23.12.2022

Publication date: 21.07.2023

DOI: 10.4274/dir.2022.221467

You may cite this article as: Junior AR, Volpi EM, Schmid BP, Mina Falsarella P, Garcia RG. The iceberg technique: an innovative approach for radiofrequency ablation of diving thyroid nodules. *Diagn Interv Radiol.* 2023;29(4):628-631.

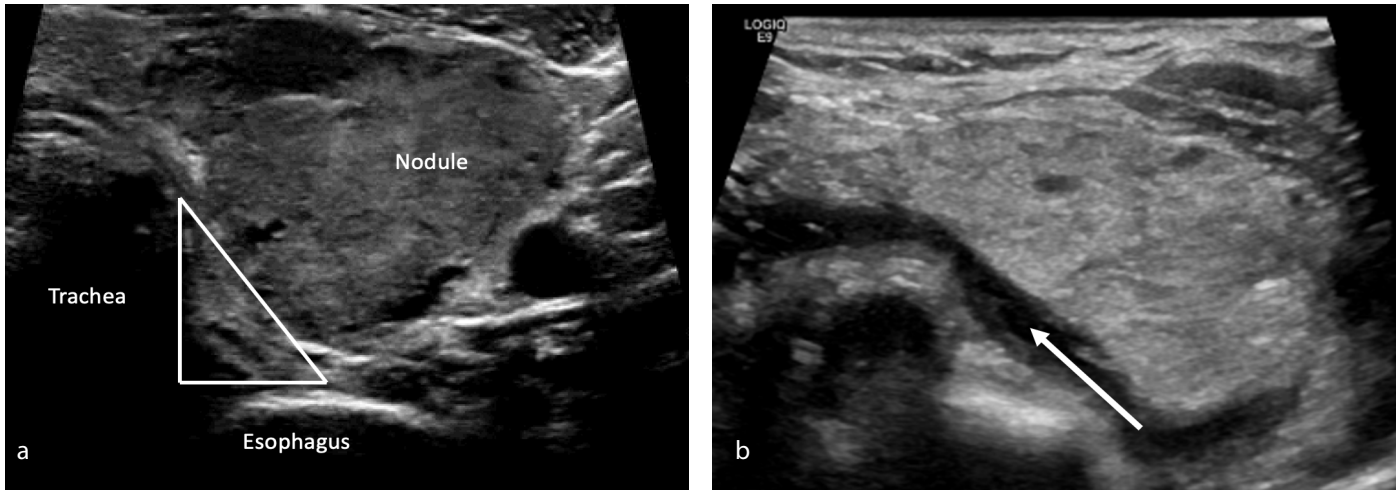

Figure 1. (a) Danger triangle zone: a space between thyroid parenchyma, trachea, and laryngeous recurrent nerve. This area must be protected from heat. Hydrodissection is an excellent option to protect these structures. **(b)** Pre-procedural hydrodissection with a 5% glucose solution. We got a protection layer of 0.7 cm (white arrow), allowing a larger area ablative zone with greater protection.

nodules refused surgical treatment and were submitted to RFA using the iceberg technique. A pre-procedural thyroid fine-needle aspiration biopsy was routinely performed to exclude malignancy. Procedures were performed in a tertiary care hospital under US guidance (Logic E9-General Electric Healthcare, Milwaukee, United States) with 12 and 9 MHz linear transducers. A generator and RFA device (Seoul, South Korea, RF Medical) and 1-cm active tips (power between 40 and 50 W) dedicated to the thyroid approach were used. All ablations were headed by a highly experienced interventional radiologist (>15 years in practice) and assisted by one interventional radiology fellow. All patients were submitted to ablative treatment in a supine position with neck extension and were placed under local anesthesia with programmed stop sedation.[4] The iceberg technique consisted of a two-stage treatment. Both began with the identification of the "danger triangle" zone, which included the recurrent laryngeal nerve and the esophagus.[5-7] A pre-procedural hydrodissection with a 5% glucose solution injection using a 22-gauge spinal anesthesia needle (BD Medical, New Jersey, United States) was performed in all treatments to provide minimal heat exposure to the danger zone (Figure 1).

Main points

- The iceberg technique is an effective and safe option for the radiofrequency treatment of diving goiters.
- Significant nodule volume reduction occurred until the third month.
- The main limitation of this technique was that it took a long time (at least three months).

During the first stage, the ablation of the cervical portion of the nodules (easily visualized during the initial US exam) using trans-isthmic access was performed using the moving-shot technique, from the posterior to the anterior portion, without incurring unnecessary risks, with good visualization of the area by real-time US (Figure 2). Approximately three to six months after the first stage, there was a volumetric reduction of the treated portion, leading to retraction of the thyroid parenchyma. This brought the mediastinal component (that was previously difficult to assess) to the cervical region, enabling a perfect visualization by the US. Then, second-stage treatment was carried out, with complete nodule ablation and a second look directed at the region that was first treated to obtain the optimal result. Ablation ended when all units of the nodule had changed to transient hyperechoic zones and the impedance values were high in the whole treated tissue (Figure 3). As per local protocol, the patients were discharged from the hospital 2 h following the procedure if no complications were noted. An ice pack was routinely applied to the puncture site at 15-minute intervals to prevent cervical edema and provide an anesthetic effect. Oral analgesics were prescribed only if the patient complained of pain. The follow-up protocol included regular clinical assessments and USs that were performed at 1, 3, 6, and 12 months after the procedure. All exams were evaluated by the same interventional radiology team that performed the ablations. No complications were observed during the procedure time or the entire follow-up period. Normal hormonal levels after the procedures were observed in all patients with normal thyroid function. The nodules' volumes were evaluated throughout different moments of US imaging. The mean and standard deviation were assessed and compared using the generalized estimation equations model, followed by the multiple comparison method of Bonferroni to assess each group and the moments when the differences occurred.

Statistical analysis

Statistical analyses were performed by a biomedical statistician using SPSS software version 22.0 (IBM, Armonk, NY, United States), and the statistical significance was assumed at the 5% level (Tables 1, 2).

Discussion

The iceberg technique was an effective and safe option for the radiofrequency treatment of diving goiters, especially those who were initially ineligible due to the voluminous mediastinal component. It showed no complications and enabled thyroid function preservation, even in anatomically challenging cases.

As in cases of ablation performed only in a single step, when the iceberg technique was selected for the approach of large goiters, we had early hospital discharge, which was approximately 2 h after the procedure, as well as an early return to usual activities, after the first session and the second and last sessions. Furthermore, it could be performed under sedation anesthesia in all cases, which is an important advantage compared with surgical resection that usually demands general anesthesia.

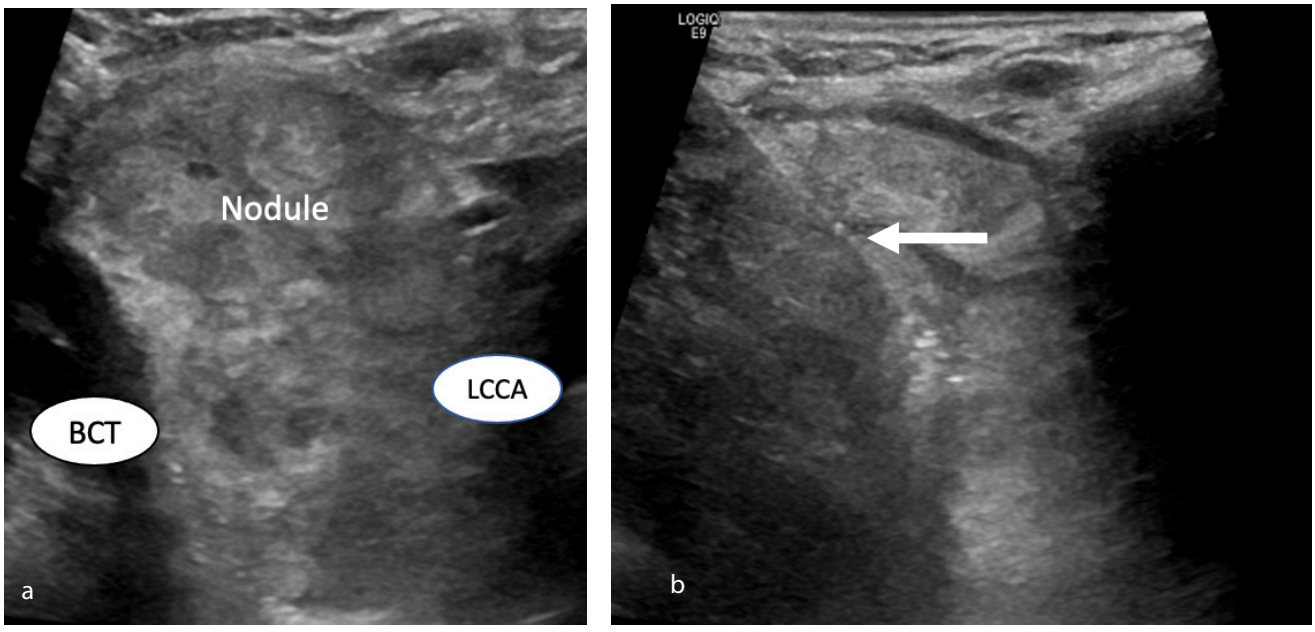

Figure 2. (a) Initial thyroid ultrasound assessment showing a diving thyroid nodule with its mediastinal component, the brachiocephalic trunk, and the left common carotid artery. **(b)** First stage ablation of the nodule's cervical portion. The white arrow shows the radiofrequency probe.

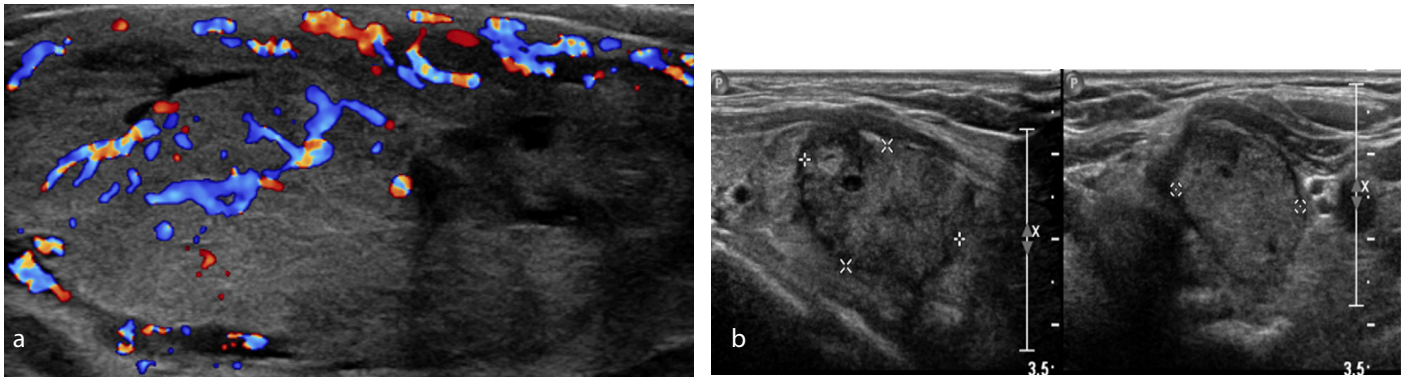

Figure 3. (a) Second thyroid color Doppler ultrasound assessment showing retraction of the mediastinal nodule's component (now well visualized) to the cervical region. Color Doppler US demonstrates the clear difference between the previously ablated zone (with no color flow and heterogeneous and hypoechogenic) and the residual portion (with color flow and isoechogenic). **(b)** Follow-up images demonstrate a 90% volume reduction after two ablative sessions.

Table 1. The nodules' volumes throughout different moments of ultrasound imaging

Time	Mean volume (cm^3)	SD	Median (range)	n	*P*
Pre-ablation	50.62	25.81	40 (21–92.5)	9	<0.001
1 month	33.23	17.92	30.25 (7.8–57)	6	
3 months	24.63	15.11	21.3 (4–41.3)	5	
6 months	19.95	12.25	17.2 (2.3–32.93)	5	
12 months	20.2	-	20.2 (20.2)	1	

n, number of nodules; SD, standard deviation.

Table 2. The nodules' volume reduction comparison between different moments of ultrasound imaging

Comparison	MD	SD	CI (95%)	*P*
Pre-ablation vs. 1 month	29.63	2.23	23.37–35.88	<0.001
1 month vs. 3 months	9.40	2.34	2.83–15.97	0.001
3 months vs. 6 months	4.11	2.59	-3.15–11.37	>0.999
6 months vs. 12 months	12.04	5.44	-3.22–27.30	0.268

SD, standard deviation; CI, confidence interval; MD, mean difference.

Our results also showed significant nodule volume reduction until the third month. This is especially important for the counseling of patients as they plan for the second ablation stage involved in the iceberg technique because this reduction is intimately associated with the migration of the mediastinal to the cervical region.

Therefore, we could infer that the ideal time to perform the second ablation was three months following the first procedure, aiming for the maximum retraction and, consequently, the best visualization during the US assessment and the optimal ablation zone.

The main limitation of this study was its small sample size (only nine patients). The main disadvantage of this technique is that it took a long time (at least three months). Despite this, we observed a significant improvement in symptoms, even after the first session. The second step was beneficial to obtain an optimal result, which was expected to be 90% after 12 months following the completed treatment.

Additionally, it required interventional radiologists with expertise in ablative methods and US imaging skills to avoid possible serious complications, such as recurrent laryngeal nerve damage, skin burn, esophagus perforation, or Claude Bernard Horner syndrome. It is also important to mention the hole of hydrodissection to prevent complications; in this study, all cases underwent previous hydrodissection.

Finally, this new technique should be considered as a valuable alternative for patients with thyroid nodules with a huge mediastinal component.

Acknowledgments

We are grateful to Rogério Ruscitto do Prado for statistical analysis.

Conflict of interest disclosure

The authors declared no conflicts of interest.

References

1. Junior AR, Falsarella PM, Rocha RD, et al. Correlation of thyroid imaging reporting and data system [TI-RADS] and fine needle aspiration: experience in 1,000 nodules. *Einstein (Sao Paulo)*. 2016;14(2):119-123. [CrossRef]
2. Haugen BR, Alexander EK, Bible KC, et al. 2015 American Thyroid Association Management Guidelines for Adult Patients with Thyroid Nodules and Differentiated Thyroid Cancer: The American Thyroid Association Guidelines Task Force on Thyroid Nodules and Differentiated Thyroid Cancer. *Thyroid*. 2016;26(1):1-133. [CrossRef]
3. Muhammad H, Santhanam P, Russell JO. Radiofrequency ablation and thyroid nodules: updated systematic review. *Endocrine*. 2021;72(3):619-632. [CrossRef]
4. Souza KP, Rahal A Jr, Volpi EM, et al. Hydrodissection and programmed stop sedation in 100 % of benign thyroid nodules treated with radiofrequency ablation. *Eur J Radiol*. 2020;133:109354. [CrossRef]
5. Sinclair CF, Téllez MJ, Peláez-Cruz R, Díaz-Baamonde A, Ulkatan S. Continuous neuromonitoring during radiofrequency ablation of benign thyroid nodules provides objective evidence of laryngeal nerve safety. *Am J Surg*. 2021;222(2):354-360. [CrossRef]
6. Baek JH, Lee JH, Valcavi R, Pacella CM, Rhim H, Na DG. Thermal ablation for benign thyroid nodules: radiofrequency and laser. *Korean J Radiol*. 2011;12(5):525-540. [CrossRef]
7. Zhao CK, Xu HX, Lu F, et al. Factors associated with initial incomplete ablation for benign thyroid nodules after radiofrequency ablation: first results of CEUS evaluation. *Clin Hemorheol Microcirc*. 2017;65(4):393-405. [CrossRef]

Diagn Interv Radiol 2023; DOI: 10.4274/dir.2022.221577

INTERVENTIONAL RADIOLOGY

TECHNICAL NOTE

Copyright@Author(s) - Available online at dirjournal.org.
Content of this journal is licensed under a Creative Commons Attribution-NonCommercial 4.0 International License.

Percutaneous thrombin injection under contrast-enhanced ultrasound guidance to control active extravasation not associated with pseudoaneurysm

Hippocrates Moschouris
Marina G. Papadaki
Nektarios Spanomanolis
Konstantinos Stamatiou
Katerina Malagari

ABSTRACT

The technique of percutaneous thrombin injection (PTI) under contrast-enhanced ultrasound (CEUS) guidance for control of acute hemorrhage-active extravasation not associated with pseudoaneurysm is demonstrated in three cases: 1) Massive spontaneous retroperitoneal hematoma in a patient with multiple comorbidities. Contrast-enhanced computed tomography (CT) showed extensive active extravasation, which was only partially controlled by transarterial embolization. CEUS was performed in the angiography suite. Contrary to unenhanced US and colour Doppler US (CDUS), CEUS confirmed persistent extravasation; CEUS-guided PTI was performed immediately thereafter. 2) Large rectus sheath hematoma in a patient on anticoagulant therapy. Contrast-enhanced CT and unenhanced US/CD could not definitely diagnose extravasation. CEUS clearly showed extravasation and was used for guidance of PTI. 3) Chest wall hematoma complicating central venous catheter placement in a patient with coronavirus on anticoagulant therapy. CDUS was inconclusive. CEUS was performed at the bedside, clearly showed active extravasation, and was used for guidance of PTI. In all three cases, post-PTI CEUS confirmed the absence of residual enhancement of the hematomas, and the hemodynamic status of the patients improved. PTI appears to be effective in selected cases of hematomas associated with active extravasation. In this context, CEUS may be the most suitable modality for guidance and for an immediate evaluation of the treatment effect.

KEYWORDS

Percutaneous thrombin injection, contrast-enhanced ultrasound, hematoma, active extravasation

Ultrasound (US)-guided percutaneous thrombin injection (PTI) has been used for the treatment of small aneurysms or pseudoaneurysms in several anatomical locations for more than 25 years;[1,2] however, application of PTI for the treatment of active extravasation not associated with pseudoaneurysm is very limited. Additionally, in these cases, localization of the source of bleeding with unenhanced US or colour Doppler US (CDUS) may often be impossible; this may be due to the relatively slow flow or unfavorable location, size, and morphology of extravasation. In this respect, contrast-enhanced US (CEUS) may be superior to the unenhanced US techniques[3] and could replace them as a guiding tool for selected cases of PTI.

CEUS exploits the properties of ultrasound contrast agents (UCAs), which are suspensions of microbubbles composed of an inert fluorinated gas core encapsulated by a phospholipid shell.[4] When insonated at low acoustic power (low mechanical index), microbubbles undergo non-linear oscillation and produce harmonic signals that can be selectively detected and separated from most background tissue signals. Thanks to the appropriate size of the microbubbles (1–5 µm), UCAs are true blood pool agents and do not diffuse in the extravascular space. With modern CEUS techniques, both intravascular circulation (lasting several minutes) and extravasation of the UCA (after vascular injury) can be detected in real time, with extremely high sensitivity.[3,4]

From the Department of Radiology (H.M. ✉ hipmosch@gmail.com, M.G.P., N.S.), Tzaneio Prefecture General Hospital of Piraeus, Piraeus, Greece; Department of Urology (K.S.), Tzaneio Prefecture General Hospital of Piraeus, Piraeus, Greece; Department of Radiology (K.M.), Attikon General University Hospital of Athens, Athens, Greece.

Received 10 April 2022; revision requested 05 May 2022; accepted 13 May 2022.

Epub: 24.02.2023

Publication date: 21.07.2023

DOI: 10.4274/dir.2022.221577

You may cite this article as: Moschouris H, Papadaki MG, Spanomanolis N, Stamatiou K, Malagari K. Percutaneous thrombin injection under contrast-enhanced ultrasound guidance to control active extravasation not associated with pseudoaneurysm. *Diagn Interv Radiol.* 2023;29(4):632-637.

This report demonstrates the technique of PTI under CEUS guidance for the control of acute hemorrhage associated with active extravasation in the absence of an aneurysm or pseudoaneurysm.

Technique

Case 1

A 70-year-old male, who was a patient in intensive care, developed sudden tachycardia and a drop in blood pressure. Contrast-enhanced computed tomography (CT) revealed a massive right retroperitoneal hematoma with multiple foci of active extravasation (Figure 1a).

The patient was transferred to the interventional radiology suite. Emergency digital subtraction angiography showed active extravasation from a right lumbar artery, which was successfully embolized with microspheres (Embozene 900, Varian) followed by gelfoam slurry. Unenhanced US and CDUS were performed on site, immediately post-embolization, with a portable US unit and a convex, 2–5 MHz probe (M8 Mindray, Shenzhen, China). These techniques failed to detect persistent extravasation. CEUS was then performed with the same equipment; the CEUS required a bolus intravenous injection of 1.5 mL of echo-enhancer (stabilized microbubbles of sulfur hexafluoride, "SonoVue"; Bracco, Milan, Italy) followed by 5 mL of normal saline. A contrast-specific, low MI (0.06–0.07) algorithm was applied. CEUS revealed two areas of persistent pooling of the echo-enhancer at the central part of the hematoma, fed by a single, T-shaped source of active extravasation (Figure 1b). Additional attempts were made to angiographically locate the source of bleeding, with catheterization of other arteries (right lumbar, iliolumbar, and ascending branches from the right superior gluteal artery), but they were fruitless. Additionally, this part of the intervention required a change of four angiographic catheters, 30 min of fluoroscopy time, 76 min of operation time, and 250 mL of intravenous iodine contrast agent. The patient showed no hemodynamic improvement. Taking into account the indicative CEUS findings and the projected safe route for a percutaneous approach, it was decided to attempt control of the hemorrhage with PTI under CEUS guidance.

Main points

- Percutaneous thrombin injection (PTI) can be an effective treatment for selected cases of active extravasation not associated with aneurysms or pseudoaneurysms.
- Contrast-enhanced ultrasound (CEUS) is a valuable guiding tool for PTI, when the source of hemorrhage cannot be identified with unenhanced US/colour Doppler US.
- With appropriate portable equipment, CEUS-guided PTI can be performed at the bedside and in the angiography suite, in combination with endovascular procedures.
- Availability of CEUS in the angiography suite and familiarization with this technique could improve the outcome of complex emergency interventional radiology procedures.

The patient remained on the angiography table. His right flank was prepared and draped in sterile fashion, and a sterile cover was placed on the convex US probe. CEUS was repeated (using the same protocol as before). A transverse section through the hematoma (clearly showing the most prominent part of the persistent extravasation) was selected. An entry point, just above the upper border of the probe, to facilitate an in-plane needle approach, was identified. A 20 cm long, 22 gauge Chiba needle was percutaneously advanced under continuous US/CEUS imaging ("dual screen" display mode) into the deepest part of the presumed source of the extravasation. Despite the deep location of the target (10 cm from the skin with an 11.5 cm-long trajectory of the needle), it could be reached with the first attempt. A total of 1,500 international units (IU) of human thrombin (approximately 3/4 of the content of the thrombin vial included in the "Surgiflo" kit; Ethicon Inc., Somerville, New Jersey, USA) were injected during slow withdrawal of the needle for 1.5 cm (Figure 1c, Supplementary Video 1). Immediate cessation of extravasation was noticed on CEUS. The needle was left in place for 2 min; it was then carefully removed, with slow injection into the hematoma of an additional 500 IU of thrombin during needle withdrawal.

Case 2

A 75-year-old man on oral anticoagulants presented with a large painful swelling of the right upper abdominal quadrant (after moderate physical effort) and severely deregulated blood coagulation (international normalized ratio: 7.2). Contrast-enhanced CT revealed a large right rectus sheath hematoma but could not definitely diagnose extravasation (Figure 2a). Unenhanced US and CDUS also failed to accurately locate the source of bleeding. However, CEUS (using the same protocol and equipment as in case 1) clearly showed two areas of pooling of the echo enhancer in the superficial part of the hematoma. After an unsuccessful attempt to control the hemorrhage by direct pressure with the transducer, PTI was performed under CEUS guidance. The larger area was triangular, with contrast emerging from its most proximal (superficial) edge and extending deeper. The proximal edge was targeted and PTI was performed (1,000 IU) with immediate cessation of hemorrhage (Figure 2b, c). The smaller area was a round spot, which was targeted at its center and treated successfully with a smaller thrombin dose (500 IU).

Case 3

A 76-year-old female patient with a history of atrial fibrillation on oral anticoagulants

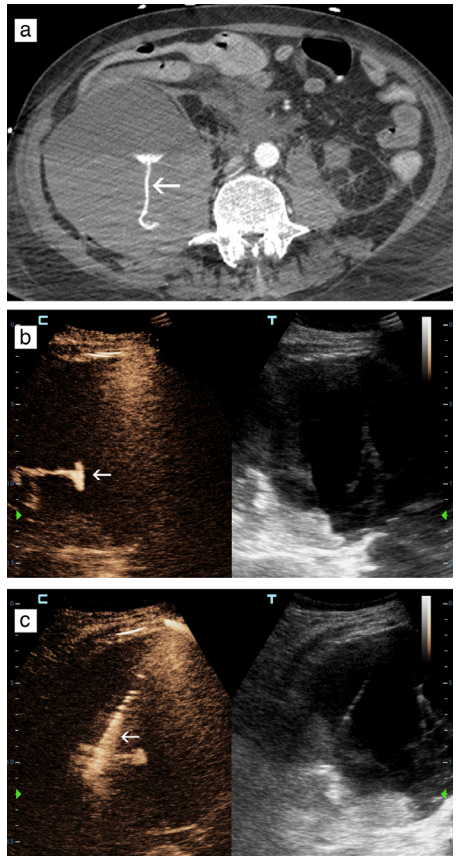

Figure 1. (a-c) Case 1. Axial section of contrast-enhanced CT (arterial phase) pre-intervention: **(a)** shows the large right retroperitoneal hematoma and one of the sites of extravasation (arrow). Sonographic "dual screen" image (unenhanced, reference, gray-scale image on the right; CEUS image on the left) immediately post-transarterial embolization; **(b)** shows a persistent jet of active extravasation (arrow); a close correlation with the CT image is noted. Sonographic image (same configuration as previous image) during PTI; **(c)** shows the Chiba needle, which has reached the proximal part of extravasation, and thrombin injection as linear and punctate echogenicities (arrow). CT, computed tomography; CEUS, contrast-enhanced ultrasound; PTI, percutaneous thrombin injection.

and with coronavirus involving the lungs had a large right chest wall hematoma, which complicated central venous catheter placement. Standard US was performed at the bedside and confirmed the lesion, but CDUS failed to definitely diagnose extravasation. CEUS (also performed at the bedside, using the same protocol and equipment as in the previous cases) clearly showed an ovoid spot of active extravasation. After an unsuccessful attempt to control the hemorrhage by direct pressure with the transducer, PTI (1,000 IU) was performed under CEUS guidance, targeting the center of the lesion.

In all three cases, the hemodynamic status and hematocrit levels of the patients improved after PTI, and follow-up with CEUS one to two days post PTI showed no recurrence of the extravasation. No complications related to PTI were encountered. The patient from Case 1 succumbed to multi-organ failure three days post-PTI, while the other two patients had uneventful recoveries. Additional data for the presented cases are provided in Table 1 and in the Supplementary File.

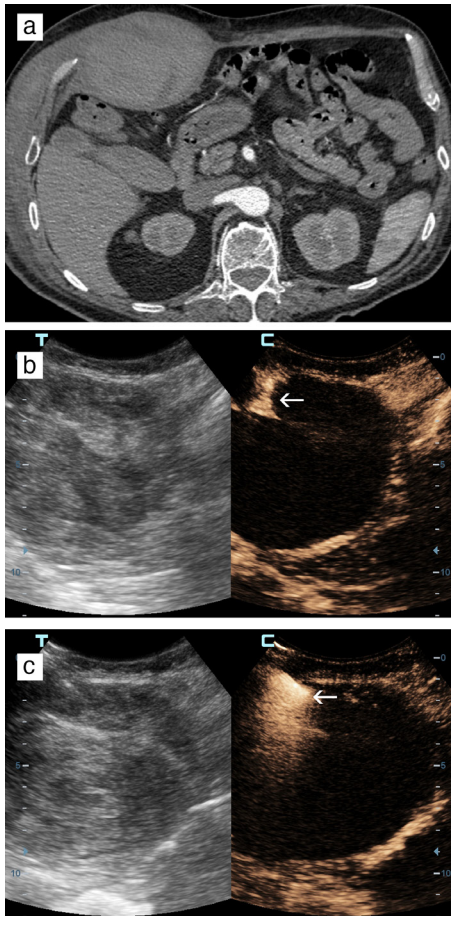

Figure 2. (a-c) Case 2. Axial section of contrast-enhanced CT (arterial phase) pre-intervention: **(a)** shows the right rectus sheath hematoma. No signs of active extravasation. Sonographic "dual screen" image (unenhanced, reference, gray-scale image on the right; CEUS image on the left) pre-intervention; **(b)** shows clearly a triangular-shaped extravasation (arrow). Sonographic image (same configuration as previous image) during PTI; **(c)** shows the Chiba needle, which has reached the proximal part of extravasation, and thrombin injection as linear and punctate echogenicities (arrow). CT, computed tomography; CEUS, contrast-enhanced ultrasound; PTI, percutaneous thrombin injection.

Discussion

As is shown in this report, management of active extravasation with PTI may be more challenging than PTI of pseudoaneurysms, since the former may not be detectable with unenhanced US/CDUS techniques. This emphasizes the role of CEUS, which often is the only sonographic modality that can accurately locate active extravasation and subsequently guide PTI. In an earlier work on CEUS for active abdominal bleeding,[5] two main patterns of leakage of the echo-enhancer were distinguished: the first was a round or oval spot of pooling of the echo-enhancer, and the second a fountain-like hyperechoic jet. The latter was associated with more severe hemorrhage and is very similar to the pattern that prevailed in the first two cases presented in this study. To control this type of extravasation, it was empirically decided to target the most proximal part of the detectable leakage to block the source of extravasation more effectively. This is at variance with a previously reported application of PTI for extravasation post-renal biopsy, where the injection was performed with the needle tip placed 2 mm superficial to the origin of the arterial jet.[6] Nevertheless, the maneuver presented herein proved effective, with complete and immediate cessation of UCA leakage and with no need to cover the entire area of extravasation. In addition, there were no complications. We speculate that, even if this approach to the source of extravasation eventually resulted in intravascular injection of thrombin, it would only occlude minor muscular branches with no clinical consequences. Contrary to the first two cases, the ovoid area of extravasation in the third case resembled the first of the aforementioned patterns ("pooling" instead of "fountain") and was associated with less dramatic hemorrhage. A proximal, narrow source of extravasation could not be clearly identified in this case. It was therefore preferred to target the center of the "pool" and fill it with thrombin.

The availability and portability of CEUS greatly facilitates application of PTI in the emergency setting and in combined interventional radiology (IR) procedures. If CEUS had not been available during the intervention for case 1 and after the inconclusive angiograms, the search for persistent hemorrhage would have required the application of cone-beam CT (CBCT) after bolus intravenous (and perhaps even intra-arterial) iodine contrast injection. Compared to CEUS, CBCT is much more cumbersome, time consuming, and difficult to perform in critically ill patients who are connected to tubes, vascular lines, and monitoring equipment. In case 3, CEUS enabled the operator to control the hemorrhage at the bedside, immediately after diagnosis and with no patient transfer. An additional advantage of US/CEUS as guiding tools for PTI is that they are free from metal artifacts, which appear on CT/CBCT during needle placement. These artifacts may obscure contrast extravasation and interfere with targeting.

In the first case in this report, the deep location of extravasation represented an additional challenge. It should be recognized that

Table 1. Additional data for the presented cases (n = 3)

Case	Hematoma size (mm)	Comorbidities/ predisposing factors	Ht prior to PTI	Shape of dominant extravasation	Additional treatments	Ht 2 days post PTI
1	158 × 88 × 201	Sepsis possible vasculitis (investigation incomplete)	15	T-shaped/ fountain-like	Embolization blood transfusions	22.5
2	114 × 89 × 204	Cardiac surgery acenocoumarol	12.3	Triangular/ fountain-like	Blood transfusions FFP transfusions direct pressure	22.3
3	92 × 43 × 47	Atrial fibrillation rivaroxaban	18.4	Teardrop-/ pool-shaped	Direct pressure blood transfusions	23.4

Ht, hematocrit; PTI, percutaneous thrombin injection; FFP, fresh frozen plasma.

CEUS guidance is more complex than unenhanced US guidance. Good coordination with the injection of the echo-enhancer and some degree of expertise are therefore required to perform CEUS-guided PTI of deeply seated extravasations. It should also be emphasized that CEUS-guided PTI for control of active extravasation has not been tested in large-scale, prospective studies and that its long-term efficacy is not known. Therefore, the approach presented herein should be considered as a rescue technique that should be performed only if embolization (a well-established endovascular treatment for control of hemorrhage) is not feasible.

In conclusion, CEUS-guided PTI appears to be a promising alternative to more complex procedures for the treatment of selected cases of active extravasation, even when this extravasation is not associated with pseudoaneurysms and is undetectable with unenhanced sonographic techniques.

Conflict of interest disclosure

The authors declared no conflicts of interest.

Acknowledgements

The authors are grateful to Mrs Elena Prokaki for her valuable assistance in preparation of this manuscript.

References

1. Liau CS, Ho FM, Chen MF, Lee YT. Treatment of iatrogenic femoral artery pseudoaneurysm with percutaneous thrombin injection. *J Vasc Surg.* 1997;26(1):18-23. [CrossRef]
2. Gorsi U, Agarwal V, Yaser M, et al. Utility of percutaneous thrombin injection for treating visceral pseudoaneurysms. *Minim Invasive Ther Allied Technol.* 2021;30(3):174-178. [CrossRef]
3. Clevert DA, Weckbach S, Kopp R, et al. Imaging of aortic lesions with color coded duplex sonography and contrast-enhanced ultrasound versus multislice computed tomography (MS-CT) angiography. *Clin Hemorheol Microcirc.* 2008;40(4):267-279. [CrossRef]
4. Malone CD, Fetzer DT, Monsky WL, et al. Contrast-enhanced US for the interventional radiologist: current and emerging applications. *Radiographics.* 2020;40(2):562-588. [CrossRef]
5. Catalano O, Cusati B, Nunziata A, Siani A. Active abdominal bleeding: contrast-enhanced sonography. *Abdom Imaging.* 2006;31(1):9-16. [CrossRef]
6. Mafeld S, McNeill M, Haslam P. Percutaneous perirenal thrombin injection for the treatment of acute hemorrhage after renal biopsy. *Diagn Interv Radiol.* 2016;22(2):190-192. [CrossRef]

Supplementary Video 1: https://youtu.be/LblHGXn_MTg

Supplementary images for case 1

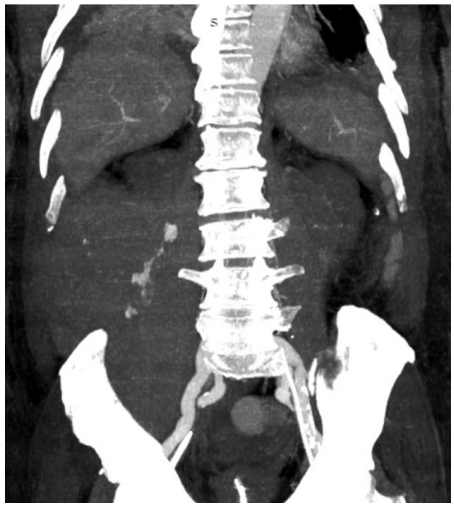

Coronal maximum intensity projection of contrast-enhanced computed tomography pre-intervention, shows the large right retroperitoneal hematoma and multiple foci of extravasation.

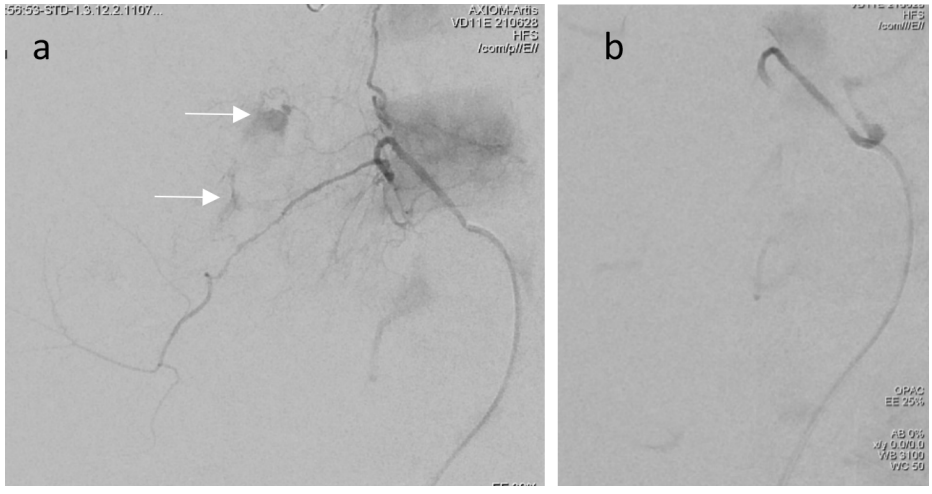

(a) Digital subtraction angiography (DSA) at baseline shows active extravasation from a right superior lumbar artery. **(b)** DSA post embolization shows complete occlusion of this artery.

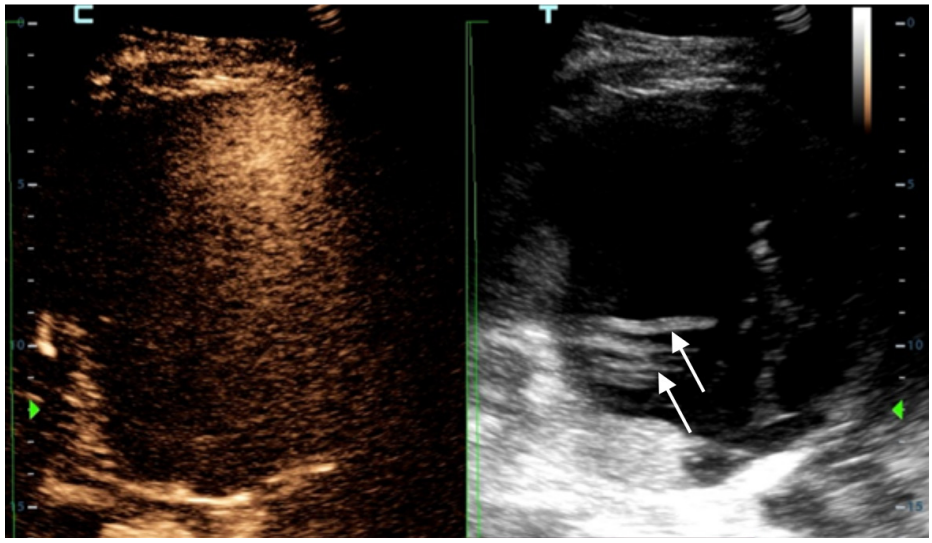

Sonographic image (unenhanced, reference gray-scale image on the right, CEUS image on the left) immediately post percutaneous thrombin injection shows no enhancement of the hematoma and newly appearing echogenic thrombotic material (arrows).

Supplementary images for case 3

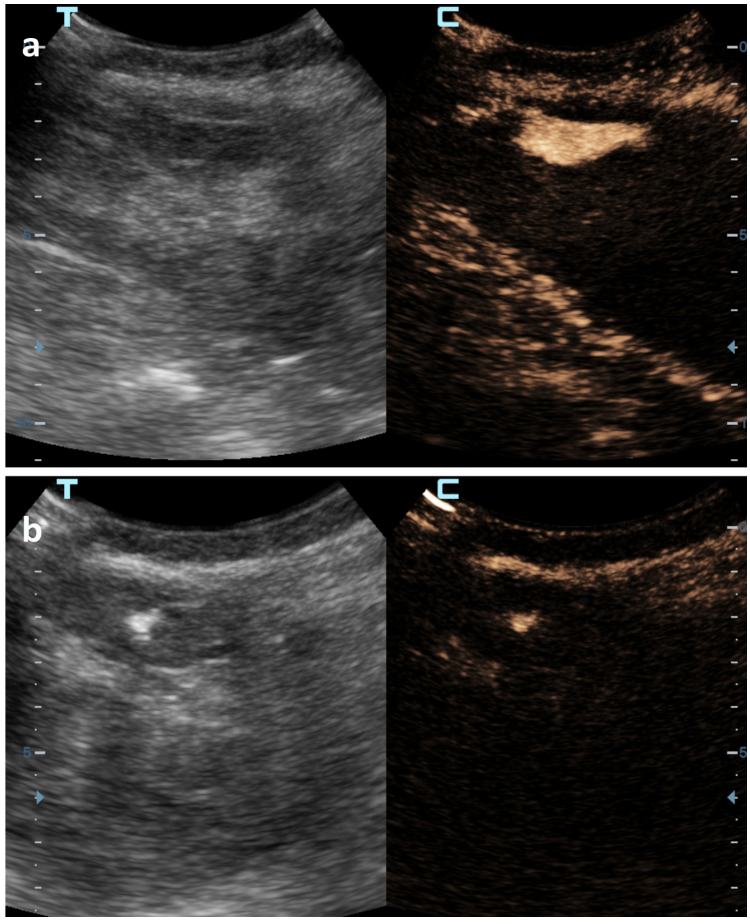

Sonographic images (unenhanced, reference gray-scale image on the right, contrast-enhanced ultrasound image on the left) before **(a)** and immediately post PTI **(b)**.

Diagn Interv Radiol 2023; DOI: 10.4274/dir.2022.221551

INTERVENTIONAL RADIOLOGY

TECHNICAL NOTE

Copyright@Author(s) - Available online at dirjournal.org.
Content of this journal is licensed under a Creative Commons Attribution-NonCommercial 4.0 International License.

Direct superior vena cava puncture for inferior vena cava filter retrieval

Ashwin Deshmukh
Gaurav Parmar
Juan Carlos Perez Lozada
Joshua Cornman-Homonoff

ABSTRACT

Most inferior vena cava (IVC) filters are designed for retrieval from a superior approach. Retrieval becomes technically challenging when the central veins in the chest are occluded. In a patient with thrombosis of the bilateral brachiocephalic veins, the authors describe direct puncture of the superior vena cava (SVC) under fluoroscopy, followed by the successful retrieval of a fractured IVC filter using forceps. A snare inserted into the SVC via the common femoral vein was used as a radiopaque target for direct SVC puncture from the lower neck. Cone beam computed tomography and pullback tractography were used to confirm a safe access trajectory. Thus, direct SVC access may be used for filter retrieval in similar clinical scenarios.

KEYWORDS

Advanced filter retrieval, deep vein thrombosis, filter, inferior vena cava, inferior vena cava filter, IVC filter retrieval, superior vena cava

An inferior vena cava (IVC) filter is typically retrieved via internal jugular (IJ) venous access. Subclavian venous access can be used when the IJ veins are occluded. Filter retrieval becomes technically challenging when both the IJ and subclavian veins are occluded. The authors describe direct superior vena cava (SVC) puncture to obtain access for IVC filter retrieval. Institutional review board approval is not required for case reports at the author's institution.

A 38-year-old woman with systemic lupus erythematosus-induced renal failure who had undergone a kidney transplant was admitted with coronavirus disease-induced respiratory failure and found to have an IVC filter (Recovery G2, Bard, New Providence, USA), which had been placed approximately 20 years prior. The filter, positioned within the hepatic IVC, had tilted and fractured (Figure 1a). It was decided to retrieve the IVC filter, given the concern about its migration into the heart. Of note, the patient had bilateral brachiocephalic vein occlusions and a persistent left SVC.

Technique

Intravascular ultrasound was performed via right common femoral venous (CFV) access, confirming the wide patency of the IVC and SVC to the level of the azygous inflow. Attempts to traverse the occluded upper extremity veins were unsuccessful. Similarly, the SVC could not be accessed via the collateral veins in the neck. Consequently, a 10-mm gooseneck snare (Medtronic, Dublin, Ireland) was deployed from the CFV access into the cranial-most aspect of the SVC. A 21-Gauge, 15-cm Chiba needle was inserted from a supraclavicular approach into the right neck under fluoroscopic guidance, targeting this snare, and the needle was successfully advanced through the snare loop. A 0.018 inch angled Glidewire (Terumo, Somerset, USA) was inserted through this Chiba needle, snared, and pulled through the femoral access (Figure 1b). Cone beam computed tomography (CBCT) was then performed, showing the initial puncture to be trans-pleural; this process was then repeated via a more medial approach (Figure 1c, d). Pullback tractography was also performed, ensuring the absence of arterial transgression. The cervical access site was then upsized using a 3–5 Fr transitional dilator, and a 16-Fr, 30-cm sheath was introduced. Through this, the filter and fractured fragment were retrieved using rigid endobronchial forceps (Figure 2a). Post-retrieval digital subtraction

From the Department of Radiology (A.D., G.P.), Yale New Haven Health Bridgeport Hospital, Bridgeport, USA; Department of Radiology and Biomedical Imaging (J.C.P.L., J.C.-H. ✉ joshua.cornman-homonoff@yale.edu), Yale University, New Haven, USA.

Received 01 April 2022; revision requested 05 May 2022; accepted 08 June 2022.

Epub: 28.12.2022

Publication date: 21.07.2023

DOI: 10.4274/dir.2022.221551

You may cite this article as: Deshmukh A, Parmar G, Perez Lozada JC, Cornman-Homonoff J. Direct superior vena cava puncture for inferior vena cava filter retrieval. *Diagn Interv Radiol.* 2023;29(4):638-639.

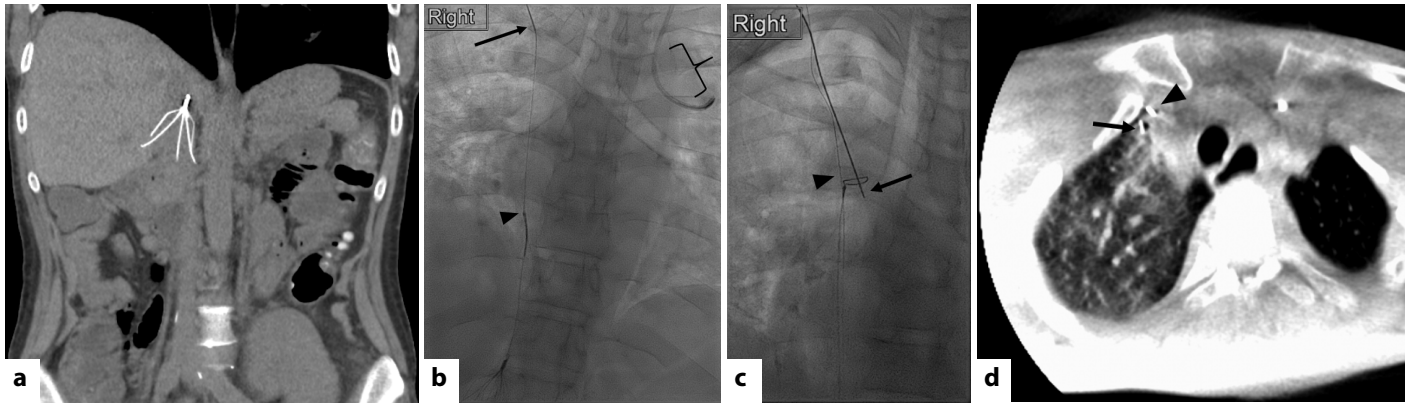

Figure 1. (a) Coronal non-contrast computed tomography showing the filter position within the hepatic inferior vena cava. **(b)** Fluoroscopic image demonstrating the initial needle pass (arrow) and snared wire (arrowhead). The left internal jugular central line (brace) is incidentally seen. **(c)** Fluoroscopic image showing the second, more medial approach (arrow). The wire from the initial puncture remains in place (arrowhead). **(d)** Axial cone beam computed tomography demonstrating the positions of the first (arrow) and second (arrowhead) passes.

venography demonstrated no abnormality (Figure 2b), so the sheath was removed, and hemostasis was obtained with manual compression.

Discussion

Most retrievable IVC filters are designed to be retrieved via a superior approach. Occlusion of the neck and/or the central veins in the chest makes IVC filter retrieval technically challenging. A recent study described external jugular venous access as a feasible alternative to IJ venous access.[1] However, since this patient had occluded brachiocephalic veins, it was not surprising that SVC could not be accessed via the smaller neck veins, including the collateral veins in the neck. Two cases have been reported in which percutaneous transhepatic access was obtained, and the IVC was accessed via the hepatic veins.[2,3] This approach may pose a higher bleeding risk and risk of injury to the liver. Advanced maneuvers for filter retrieval, such as the loop-snare technique, could be more challenging given the acute angulation in such cases. Similarly, retrieval via rigid forceps would be impossible. Hence, transhepatic access was not a suitable option in this case, as the filter had been placed 20 years ago and was fractured, necessitating its removal via forceps. Filter retrieval via femoral venous access would have necessitated inverting the filter. This was considered unsafe, as the filter was fractured and likely to be fragile, thus posing a high risk of filter fragment migration to the heart while attempting this maneuver. Snaring the guidewires out through the femoral access may have eased the process of tract dilation. The potential risks of direct SVC puncture include transgression of the pleura and/or lungs with associated complications, inadvertent puncture of the arteries within the thorax with the potential difficulty in achieving hemostasis, and transgression of a high pericardial insertion. These risks were mitigated with a thinner 21 Gauge needle for the initial access, CBCT to provide direct visualization of the needle trajectory, and pullback tractography. Thus, direct SVC access may be safely used for filter retrieval in similar clinical scenarios.

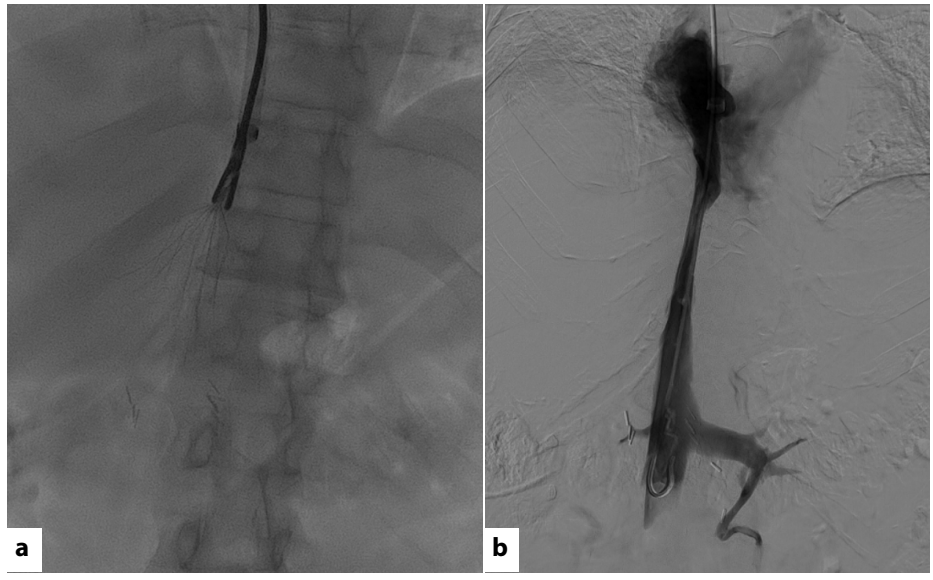

Figure 2. (a) Fluoroscopic image demonstrating filter retrieval. **(b)** Post-retrieval digital subtraction venogram confirming the absence of complication.

Main points

- Most inferior vena cava (IVC) filters are designed to be retrieved via a superior approach.
- Retrieval becomes technically challenging when bilateral jugular and subclavian or bilateral brachiocephalic veins are occluded.
- In this technical modification, the authors describe direct puncture of the superior vena cava to obtain central venous access and successfully retrieve a longstanding, fractured IVC filter.

Conflict of interest disclosure

The authors declared no conflicts of interest.

References

1. Zeng X, Zeng X, Zeng Q, et al. The external jugular vein is a feasible and safe alternative access for retrieval of inferior vena cava filter. *J Vasc Access*. 2022:11297298211064467. [CrossRef]
2. Hughes JA, Lynch FC. Transhepatic removal of an inferior vena cava filter. *J Vasc Interv Radiol*. 2012;23(7):983-985. [CrossRef]
3. Dionisio RG, Shin DS, Ingraham CR, Vaidya SS. Transhepatic inferior vena cava filter retrieval due to chronic occlusion of jugular and subclavian veins. *Radiol Case Reports*. 2019;14(11):1385-1388. [CrossRef]

Diagn Interv Radiol 2023; DOI: 10.4274/dir.2023.222045

INTERVENTIONAL RADIOLOGY

ORIGINAL ARTICLE

Copyright@Author(s) - Available online at dirjournal.org.
Content of this journal is licensed under a Creative Commons Attribution-NonCommercial 4.0 International License.

Can expiratory or inspiratory contrast-enhanced computed tomography be more efficient for fast-track cannulation of the right adrenal vein in adrenal venous sampling?

Yoshinori Tsukahara
Keisuke Todoroki
Takeshi Suzuki
Akira Yamada
Masahiro Kurozumi
Yasunari Fujinaga

PURPOSE

This study compares the usefulness of expiratory arterial phase (EAP)–contrast-enhanced computed tomography (CT) (CECT) with that of inspiratory arterial phase (IAP)–CECT in adrenal venous sampling (AVS).

METHODS

Sixty-four patients who underwent AVS and CECT at the authors' hospital between April 2013 and June 2019 were included in this study. The patients were classified into the following two groups: EAP (32 patients) and IAP (32 patients) groups. The single arterial phase images were obtained at 40 seconds in the IAP group. The double arterial phase images were obtained at 40 seconds in the early arterial phase and 55 seconds in the late arterial phase in the EAP group. The authors then compared the right adrenal vein (RAV) visualization rate on the CECT, the difference between the CECT images and adrenal venograms in the localization of the RAV orifice, the cannulation time to the RAV, and the volume of contrast agent administered intraoperatively between the two groups.

RESULTS

The rates of the RAV visualization in the EAP group were 84.4% in the early arterial phase, 93.8% in the late arterial phase, and 100% in the combined early and late arterial phases. The rate of the RAV visualization in the IAP group was 96.9%. There was no significant difference between the two groups in terms of the rate of the RAV visualization. However, there was a small difference in the location of the RAV orifice between the CECT images and adrenal venograms in the EAP group as compared with the IAP group ($P < 0.001$). The median time to the RAV catheterization was significantly shorter in the EAP group (27.5 minutes) than in the IAP group (35.5 minutes; $P = 0.035$). The rates of the RAV visualization in the EAP group were not significant between the early arterial phase, late arterial phase, and combined early and late arterial phases ($P = 0.066$). However, the mean volume CT dose index in the combined early and late arterial phases was significantly higher than in the early and late arterial phases ($P < 0.001$).

CONCLUSION

The EAP–CECT is more useful for increasing the speed of the RAV cannulation due to the small difference in the localization of the RAV orifice compared to IAP–CECT. However, since EAP–CECT has double contrast arterial phases and increased radiation exposure compared to IAP–CECT, only the late arterial phase may be acceptable to reduce radiation exposure.

KEYWORDS

Adrenal, aldosteronism, contrast, CT, venography

From the Department of Radiology (Y.T. ✉ tsukahara@shinshu-u.ac.jp, K.T., A.Y., M.K., Y.F.), Shinshu University School of Medicine, Matsumoto, Japan; Department of Radiology (T.S.), Nagano Municipal Hospital, Nagano, Japan.

Received 08 December 2022; revision requested 26 January 2023; last revision received 15 March 2023; accepted 18 April 2023

Epub: 16.05.2023

Publication date: 21.07.2023

DOI: 10.4274/dir.2023.222045

You may cite this article as: Tsukahara Y, Todoroki K, Suzuki T, Yamada A, Kurozumi M, Fujinaga Y. Can expiratory or inspiratory contrast-enhanced computed tomography be more efficient for fast-track cannulation of the right adrenal vein in adrenal venous sampling? *Diagn Interv Radiol.* 2023;29(4):640-646.

The characteristic features of primary aldosteronism (PA) are hypertension and hypokalemia.[1,2] PA is diagnosed in between 5% and 20% of patients with refractory hypertension.[2-4] Compared with essential hypertension, PA significantly increases the risk of cardiovascular complications, cerebrovascular disorders, and renal damage.[4,5] The treatment for PA is laparoscopic adrenalectomy for patients with unilateral disease, whereas patients with bilateral disease are treated medically with mineralocorticoid receptor antagonists.[6] Therefore, the identification of PA lateralization is required to determine the treatment strategy. Adrenal venous sampling (AVS) is recommended for distinguishing unilateral from bilateral PA.[7] In a large multicenter AVS registry study conducted recently,[8] bilateral cannulation was successful in 80.1% of the procedures. AVS is a relatively difficult procedure, and it is especially difficult to cannulate the right adrenal vein (RAV) due to its small size, variable anatomy, and the effects of the patient's respiratory motion during cannulation. Dynamic contrast-enhanced computed tomography (CT) (CECT) before AVS is useful for increasing the success rate of AVS.[9] Dynamic CECT has long been used to differentiate adrenal tumors.[10] Matsuura et al.[11] reported that the RAV visualization rate was 76% using CECT. However, recent studies have reported improvements in the visualization rate of the RAV, which is challenging to cannulate, on multiple-phase dynamic CECT (>90%).[12-15] Many of those reports obtained CECT images with the patient in the expiratory position.[9,12,15] However, several reports have also focused on the inspiratory position,[11,16,17] and little is known about the optimal breath-holding position during dynamic CECT in AVS. Therefore, the purpose of this study is to evaluate the advantage of the expiratory arterial phase (EAP)–CECT (at 40 and 55 seconds, respectively, after contrast media injection) compared with the inspiratory arterial phase (IAP)–CECT (at 40 seconds after contrast media injection) in AVS.

Main points

- The right adrenal vein (RAV) was well visualized on the arterial phase contrast-enhanced computed tomography (CT) (CECT) scan.
- The RAV had a minimal difference between the expiratory CT scan images and the adrenal venograms.
- The expiratory arterial phase–CECT scan was useful for the fast-track cannulation of the RAV.

Methods

Patients

The Shinshu University Certified Review Board of Clinical Research approved this retrospective study, and informed consent was waived (Internal Review Board approval number: 5087).

The authors reviewed the medical records at the authors' hospital and selected 95 consecutive patients diagnosed with PA who underwent AVS between April 2013 and June 2019. Patients who did not undergo CECT at the hospital (n = 11), those who used contrast agents other than those containing 370 mgI/MI (n = 19) of Iopamiron, and those who had inferior left vena cava visualization (n = 1) were excluded from the study. Of the 19 patients who had contrast agents other than those containing 370 mgI/mL of iopamiron, 13 were included in the IAP group and 6 in the EAP group. There are no reports comparing different iodine concentrations of contrast agents in the visualization of the RAV on CECT. However, if contrast injection conditions are constant, vascular CT values are proportional to the iodine concentration.[18] As the authors thought this would affect the visualization of the RAV, we only analyzed patients imaged with 370 mgI/mL of contrast agent, which was the majority of cases. Thus, 64 patients were included in the study.

Computed tomography examinations

All abdominal dynamic CECT examinations were performed before AVS. The median interval between CECT and AVS was 28 days (range: 1–189 days). Images were obtained using any of the following CT scanners: a 64-row detector CT scanner (LightSpeed VCT; GE Healthcare, Milwaukee, WI, USA). Scan parameters were as follows: tube voltage, 120 kVp; reconstruction thickness, 1.25 mm; beam collimation, 40 mm; rotation time, 0.4 seconds; and helical pitch, 0.984. CECT was performed using 100 mL of contrast agent containing 370 mgI/mL of iopamidol (Iopamiron 370; Bayer Healthcare, Berlin, Germany) at an injection rate of 3 mL/s. Dual-phase contrast-enhanced dynamic scans during breath-hold inspiration or three-phase contrast-enhanced dynamic scans during breath-hold expiration were performed. In the dual-phase contrast-enhanced dynamic scans, arterial phase images were obtained at 40 seconds (in the IAP group), and delayed phase images were obtained at 130 seconds after the start of the contrast agent injection. In triple-phase contrast-enhanced dynamic scans, the double arterial phase images were obtained at 40 and 55 seconds (in the EAP group), and the delayed phase image was obtained at 130 seconds after the start of the contrast agent injection. We defined the 40-second phase after the start of the contrast agent injection as the early arterial phase and the 55-second phase after the start of the contrast agent injection as the late arterial phase. The late arterial phase in the EAP group was added to prolong the peak contrast effect because expiration decreases cardiac output and venous circular flow.[19] The EAP was performed on patients with AVS, as indicated in the request details, during CECT. Alternatively, the IAP was performed as a routine abdominal CECT.

Adrenal venous sampling procedure

During the study period, the main operator who performed AVS was among the 11 radiologists [with 5–16 years of experience in interventional radiology (IVR)] involved in this study. AVS was performed using one of the following angiography systems: Infinix Celeve Active (Canon Medical Systems, Otawara, Japan) or Artis zee BA Twin (Siemens Healthineers, Bayern, Germany). All operators performed AVS according to the following procedure: operators inserted 5-Fr introducer sheaths via the right and left common femoral veins. A 4-Fr catheter with a two-dimensional shape (shepherd's hook catheter; Meditkit Co., Ltd., Tokyo, Japan), a 5-Fr catheter designed for the RAV (Hanaco Medical, Saitama, Japan), or a 5-Fr catheter with a three-dimensional shape designed to accommodate five RAV patterns (Adselect Series; Hanaco Medical)[20] were inserted into the RAV (Figure 1). A 5-Fr catheter designed for the left adrenal vein (LAV) (Hanaco Medical) was inserted into the LAV. Depending on the operator, the catheter was first inserted into the LAV and then into the RAV. After the operator performed a venography and confirmed the cannulation into the RAV and LAV (Figure 2), venous blood samples of at least 3 mL were obtained, respectively. Blood samples of the RAV were collected once or twice from each patient. Blood samples were also subsequently obtained from the inferior vena cava (IVC) above the confluence of the RAV and under the confluence of the left renal vein. The authors did not always assess the patient selectivity index (i.e., adrenal vein cortisol concentration/IVC cortisol concentration ratio) intraoperatively if the RAV was clearly observed on venography. Fifteen minutes after administration of the adreno-

corticotropic hormone (ACTH), venous blood samples were obtained again from the RAV, LAV, and IVC in the same manner. The cannulation time of the RAV, incident dose of the entire procedure, fluoroscopy time of the entire procedure, and volume of contrast agent were recorded. The cannulation time of the RAV was defined as the time from inserting the sheath to performing the RAV venography or from performing the LAV venography to performing the RAV venography (Figure 3). The insertion time of the sheath was extracted from the intraoperative record written by the operating nurse. The venography time of each adrenal vein was recorded from the image of each adrenal vein attached to the operative report. The criterion for successful cannulation of the RAV was a selectivity index after ACTH stimulation of ≥5.[21]

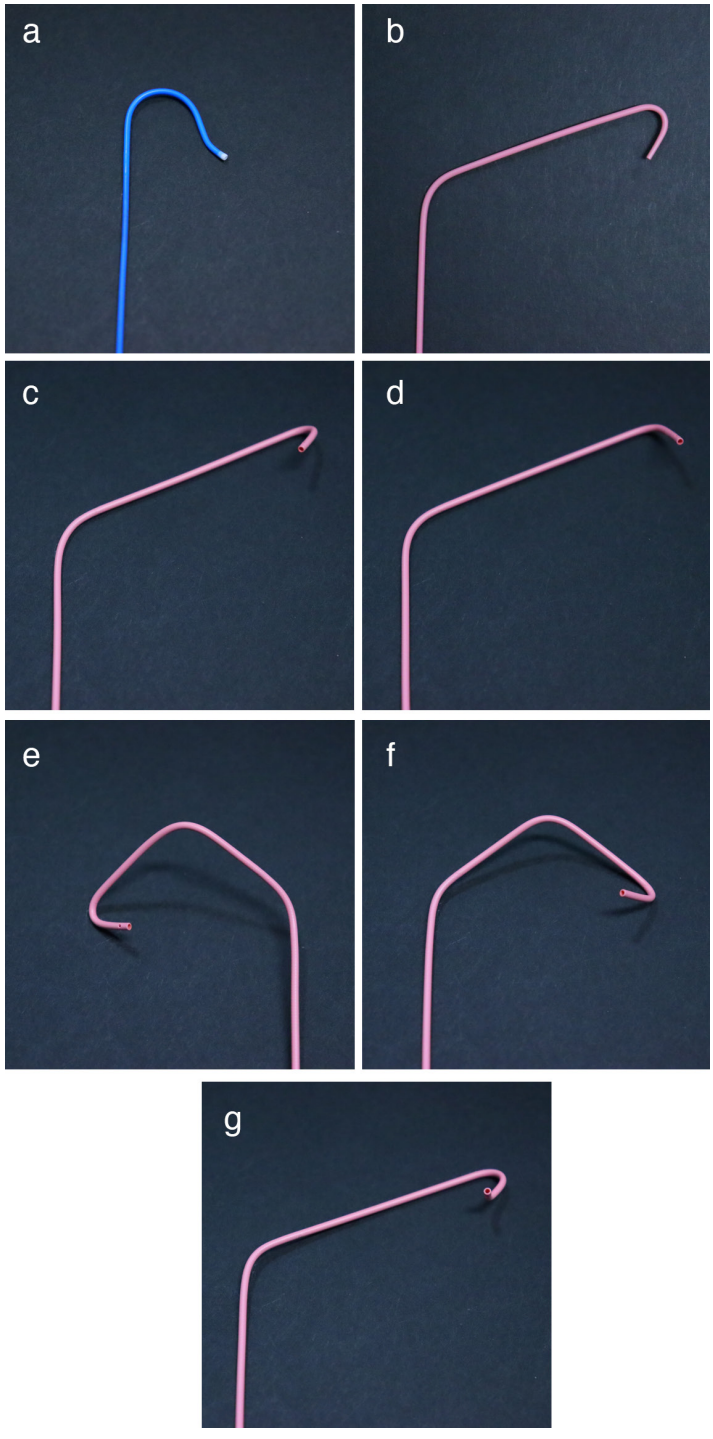

Figure 1. (a-g) The catheters used for cannulation of the right adrenal vein (RAV). The authors selected the appropriate catheter based on the shape of the RAV. **(a)** A 4-Fr shepherd's hook–type catheter with a two-dimensional shape. **(b)** A 5-Fr catheter, designed for the RAV with a two-dimensional shape. **(c-g)** A 5-Fr catheter with a three-dimensional shape designed to accommodate five RAV patterns.

Image analysis

Two radiologists (readers A and B, with 7 and 6 years of experience in IVR, respectively) who had not performed AVS as operators independently evaluated the CECT images using a commercial software package (EV Insite; PSP Corporation, Tokyo, Japan). The RAV was defined as an enhanced tubular or linear structure from the right adrenal gland, as observed on the CT images, which eventually entered the IVC either directly or indirectly.[21] The degree of visualization was recorded using a 4-point scale from a previous report:[12] 4, the RAV runs between the IVC and the right adrenal gland; 3, the RAV is unequivocally detectable, although the contrast of the RAV to the surrounding structures is not so strong; 2, equivocal detection of the RAV, with minimal contrast to surrounding structures; 1, the RAV is not visualized (Figure 4). A grade of 3 or 4 was regarded as RAV visualization. In cases of discrepancies between the visualization grades of 3–4 and 1–2 in readers A and B, reader C (who had 15 years of experience in IVR) evaluated the CT images to obtain a consensus. With reference to a previous report,[22] the localization of the RAV orifice was divided and numbered into 24 parts from the 10th thoracic vertebra to the second lumbar vertebra from the cranial side to the caudal side (Figure 5). Each vertebral body was subdivided into four equal levels from the cranial side to the caudal side and one additional section representing the vertebral disk. Reader C recorded the localization numbers of the RAV orifice on the CECT image and the adrenal venography image, respectively. The localization of the RAV on the CECT was determined by the level of the CECT-scout image corresponding to the axial CECT image visualizing the RAV. The localization of the RAV on the venogram was determined by the level of the catheter tip with the right adrenal venogram.

Statistical analysis

We performed statistical analyses using Bell Curve in Excel (Social Survey Research Information Co. Ltd., Tokyo, Japan). We used the Student's t-test to compare the patient's age, body mass index (BMI), height, and body weight. The chi-squared test was used to compare the patient's sex, the visualization rate, and the catheter cannulation success rate in the RAV.

The Mann–Whitney U test was used to compare the time for cannulating the RAV, the fluoroscopy time of the entire procedure, the whole entrance dose of the entire

procedure, the volume of contrast media, years of experience in IVR, and the difference between CECT images and adrenal venograms in localization of the RAV orifice. The Friedman test was used to compare the mean volume CT dose index adjusted for body size and the visualization rates of the RAV between the arterial phase, late arterial phase, and combined arterial and late arterial phases in the EAP group. If a significant difference was indicated, multiple intergroup comparisons were performed using the Scheffé post-hoc test. The inter-reader agreement was assessed using Cohen's weighted kappa analysis. A kappa value of ≤0.20 indicated poor agreement; 0.21–0.40, fair agreement; 0.41–0.60, moderate agreement; 0.61–0.80, good agreement; and 0.81–1.00, excellent agreement. A *P* value of <0.05 was considered statistically significant.

Results

Patient characteristics

Table 1 shows the patient characteristics, including age, sex, height, body weight, BMI, and years of IVR experience. Of 64 patients, 32 patients were classified into the EAP group and 32 in the IAP group. There were no significant differences between the two groups with regard to age, sex, height, body weight, BMI, and years of IVR experience.

Evaluation of right adrenal vein visualization and radiation exposure on contrast-enhanced computed tomography

Table 2 shows the degree of the RAV visualization. On the early arterial phase image, although the IAP group had a better visualization rate than the EAP group, the visualization rates were not significantly different between the two groups. In the EAP group, visualization rates for the late arterial phase were improved compared with the early arterial phase. In the combined early and late arterial phase images of the EAP groups, the visualization rates were 100%, which were not significantly different from those of the IAP group. Furthermore, the EAP group showed no significant difference in the RAV visualization rate between the early arterial phase, late arterial phase, and combined early and late arterial phases ($P = 0.066$).

In the EAP group, the weighted kappa values for the RAV visualization score on the early and late arterial phase images were 0.71 and 0.54, respectively, which indicated good inter-reader agreements. Furthermore, in the IAP group, the weighted kappa value for the RAV visualization score on the early phase image was 0.35, which indicated a fair inter-reader agreement.

The mean volume CT dose indexes of the EAP group were 18.74 ± 3.16 mGy in the early arterial phase, 18.54 ± 3.06 mGy in the late arterial phase, and 37.27 ± 6.21 mGy in the combined early and late arterial phases. No significant differences were noted in the mean volume CT dose indexes between the early and late arterial phases ($P = 0.75$). However, the mean volume CT dose indexes in the combined early and late arterial phases were significantly higher than those in the early and late arterial phases ($P < 0.001$). The mean volume CT dose index of the IAP group was 19.06 ± 3.35 mGy in the early arterial phase.

Difference between the contrast-enhanced computed tomography images and adrenal venograms in the localization of the right adrenal vein orifice

In the EAP group, the CECT image showed that the RAV orifice was located between level 6 and level 16 (median: 11), whereas on the adrenal venogram, the RAV orifice was located between level 5 and level 18 (median: 10.5; Figure 5a). On the other hand, the RAV orifice on the CECT image in the IAP group was located between level 9 and level 23 (median: 14), whereas on the adrenal venogram, it was located between level 4 and level 19 (median: 12; Figure 5b). The EAP group had a smaller location difference in the RAV orifice between the CECT images and adrenal venograms than the IAP group ($P < 0.001$; Figure 6).

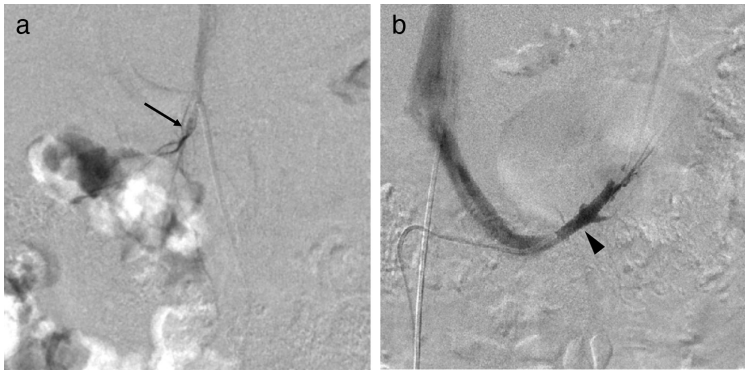

Figure 2. (a, b) A case of adrenal venous sampling in a 52-year-old man with primary aldosteronism. **(a)** A 5-Fr catheter with a three-dimensional shape designed for the right adrenal vein (RAV) is successfully cannulated in the RAV (arrow). **(b)** A 5-Fr catheter designed for the left adrenal vein (LAV) is successfully cannulated in the common trunk of the LAV (arrowhead).

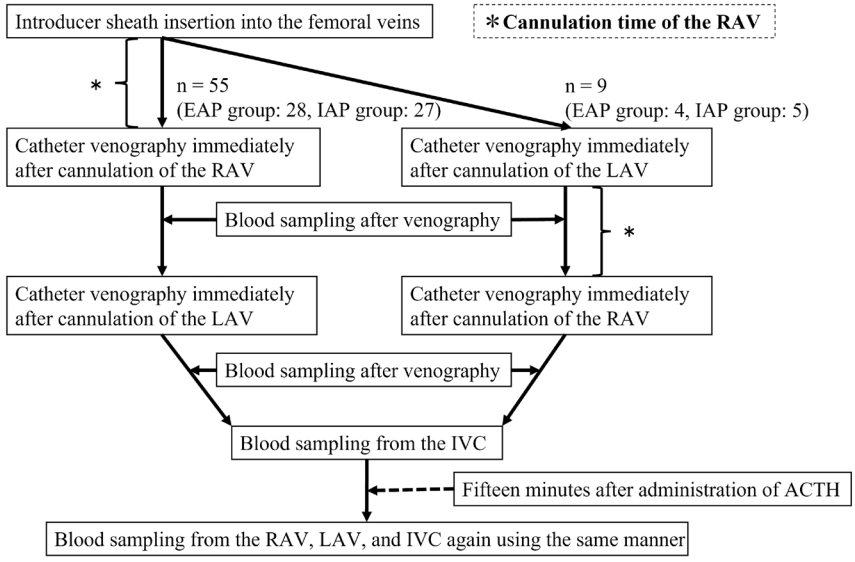

Figure 3. A flowchart of the adrenal venous sampling procedure. The cannulation time of the right adrenal vein is marked with asterisks. RAV, right adrenal vein; EAP, expiratory arterial phase; IAP, inspiratory arterial phase; LAV, left adrenal vein; IVC, inferior vena cava; ACTH, adrenocorticotropic hormone.

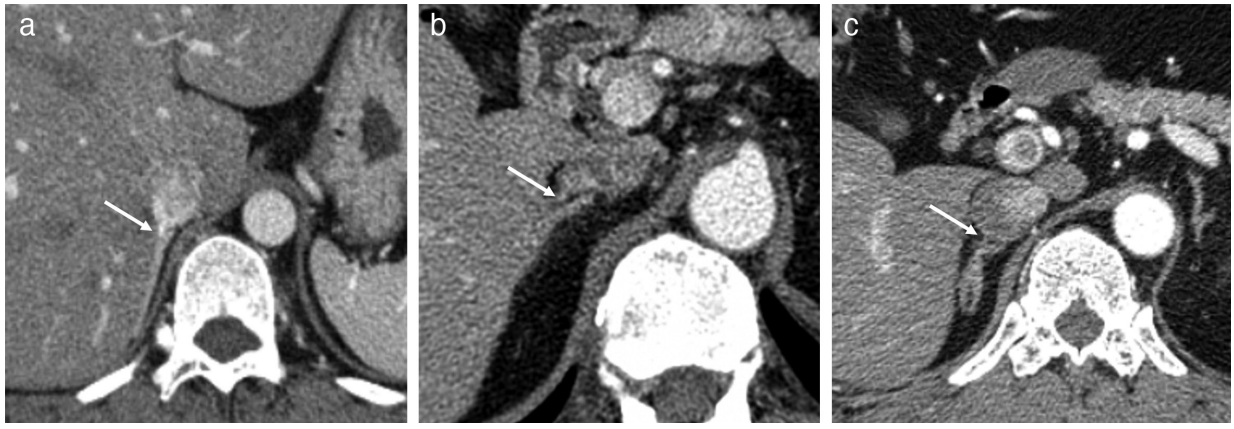

Figure 4. (a-c) The scores of the right adrenal vein (RAV) visualization on computed tomography images. Examples of score 4 **(a)**, score 3 **(b)**, and score 2 **(c)**. The RAV is marked with arrows.

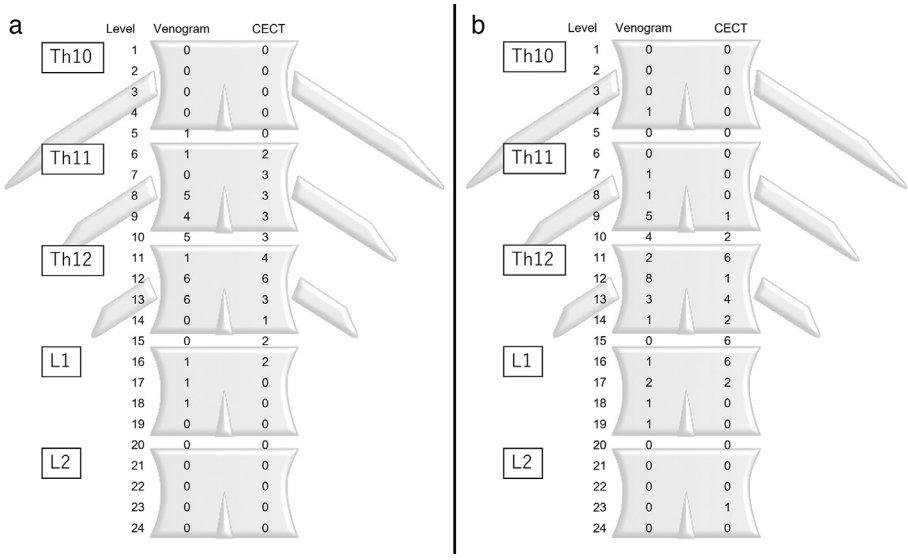

Figure 5. (a, b) Localization of the right adrenal vein (RAV) orifice. The location of the RAV orifice was determined and numbered from cranial to caudal in 24 anatomical levels from the top of the 10th thoracic vertebra to the bottom of the second lumbar vertebra. **(a)** The number of the RAV orifice on contrast-enhanced computed tomography (CECT) images and venograms in the expiratory arterial phase–CECT group. **(b)** The number of the RAV orifice on CECT images and venograms in the inspiratory arterial phase–CECT group.

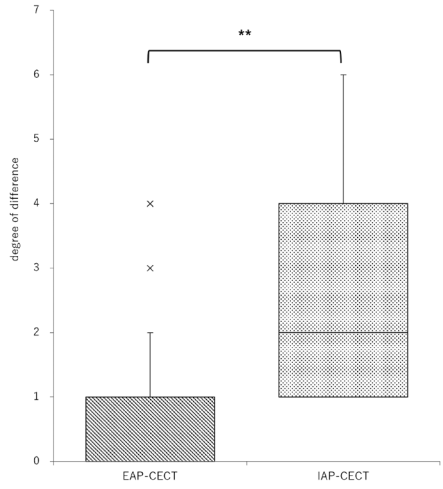

Figure 6. The positional difference between contrast-enhanced computed tomography and venography at the localization of the right adrenal vein orifice. ***P* < 0.001; CECT, contrast-enhanced computed tomography; EAP, expiratory arterial phase; IAP, inspiratory arterial phase.

Table 1. Characteristics of the patients

	EAP group (n = 32)	IAP group (n = 32)	*P* value
Age (years) Mean ± SD	48.34 ± 11.82	50.91 ± 11.03	*P* = 0.70
Sex (M/F)	19/13	14/18	*P* = 0.32
Height (m) Mean ± SD	1.66 ± 0.088	1.63 ± 0.079	*P* = 0.52
Weight (kg) Mean ± SD	71.08 ± 13.82	69.97 ± 15.03	*P* = 0.64
BMI (kg/m^2) Mean ± SD	25.65 ± 4.35	26.40 ± 5.20	*P* = 0.32
Experience in IVR (years) Median (range)	7 (5–16)	8 (6–16)	*P* = 0.051

EAP, expiratory arterial phase; IAP, inspiratory arterial phase; SD, standard deviation; BMI, body mass index; IVR, interventional radiology; M, male; F, female.

Comparison of adrenal venous sampling between the expiratory arterial phase–contrast-enhanced computed tomography group and the inspiratory arterial phase–contrast-enhanced computed tomography group

Table 3 shows the comparison of AVS between the EAP–CECT group and the IAP–CECT group. The median time to RAV cannulation was significantly shorter in the EAP–CECT group (27.5 minutes) than in the IAP–CECT group (35.5 minutes; *P* = 0.035). No significant intergroup differences were noted in terms of exposure dose, fluoroscopy time during the entire procedure, and volume of contrast agent.

Table 2. Visualization rates of the right adrenal vein

	EAP group (n = 32)	IAP group (n = 32)	*P* value
Early arterial phase	27/32 (84.4%)	31/32 (96.9%)	*P* = 0.20
Late arterial phase	30/32 (93.8%)		†*P* = 1.00
Early and late arterial phase	32/32 (100%)		††*P* = 1.00

†Comparison between the late arterial phase (EAP group) and the early arterial phase (IAP group); ††Comparison between the arterial and late arterial phases (EAP group) and the arterial phase (IAP group). EAP, expiratory arterial phase; IAP, inspiratory arterial phase.

Table 3. Adrenal venous sampling between the expiratory arterial phase and inspiratory arterial phase groups

	EAP group (n = 32)	IAP group (n = 32)	*P* value
Success rate of RAV cannulation	100% (32 of 32)	97% (31 of 32)	*P* = 1.00
Time to RAV cannulation (min) Median (range)	27.5 (5–154)	35.5 (7–174)	*P* = 0.035*
Exposure dose (mGy) Median (range)	429.20 (94–1548.16)	497.84 (93.2–1824)	*P* = 0.40
Fluoroscopy time (min) Median (range)	45.25 (13.8–92.6)	45.95 (17.2–130.1)	*P* = 0.51
Volume of contrast agent (mL) Median (range)	76.5 (25–260)	100 (20–280)	*P* = 0.11

*Statistically significant. EAP, expiratory arterial phase; IAP, inspiratory arterial phase; RAV, right adrenal vein.

Discussion

To the authors' knowledge, there are no reports mentioning the cannulation time of the RAV and the amount of contrast media in AVS as a result of different CECT imaging methods used before AVS. This study's results showed no significant between-group differences in the RAV visualization and the cannulation success rate. However, the cannulation time of the RAV was significantly shorter in the EAP group than in the IAP group.

The RAV visualization rate of the IAP group was 96.9% in the early arterial phase. The RAV visualization rates of the EAP group were 84.4% in the early arterial phase and 93.8% in the late arterial phase. The RAV visualization rate of the EAP group in the combined early and late arterial phases was 100%. Hence, there was no significant difference in the RAV visualization rates between the IAP and EAP groups. In the EAP group, there was an improvement in the RAV visualization rate in the late arterial phase compared with that in the early arterial phase. This finding may be attributed to changes in venous circular flow caused by respiration. In the expiratory position, intrathoracic pressure decreases, causing a decrease in venous circular flow, and cardiac output is correspondingly decreased. Therefore, the peak of the contrast-enhanced effect on the RAV was considered to be prolonged.[19] Some reports have evaluated the RAV visualization rates of CECT in the expiratory position.[9,12,15,22] Morita et al.[15] reported the usefulness of the dual adrenal venous phase images obtained at 45 and 55 seconds using the constant injection time technique of contrast media (iodine of 600 mgI/kg body weight) in the expiratory position. They found combined rates of the RAV visualization of the first and the second adrenal venous phase of 98%. In this study, the contrast media injection technique was constant regarding both injection time and injection rate. However, the rate of the RAV visualization in the combined early and late arterial phases was satisfactory at 100% in the EAP group. Nevertheless, there was no significant difference in the RAV visualization rate between the combined early and late arterial phases and early and late arterial phases. In contrast, the mean volume CT dose index in the combined early and late arterial phases was significantly higher than in the early and late arterial phases. From the viewpoint of exposure dose reduction, only the late arterial phase in the EAP group may be acceptable.

The authors found a smaller location difference in the RAV orifice between the CECT images and the adrenal venograms in the EAP group than in the IAP group. This result suggests that the CECT images in the expiratory position were closer to the location of the RAV orifice than those in the inspiratory position. In addition, because the adrenal venogram was usually obtained during natural breath holding to keep the catheter stable, the RAV orifice on AVS was closer to that on the CECT images in the expiratory position. The authors, therefore, believe that preoperative simulation using the CECT images in the expiratory position has the advantage of reducing the procedure time required for the RAV catheterization. Some studies have compared the CECT images in the expiratory position and the images on AVS for the location of the RAV orifice. Onozawa et al.[9] compared the cannulated position of the RAV orifice with the RAV orifice on dynamic CECT in the expiratory position and interventional CT (a system that combines angiographic and CT equipment with a single fluoroscopy table). According to their report, the median difference of the RAV between the dynamic CECT and the interventional CT was only half a vertebra. Degenhart et al.[22] compared the location of the RAV orifice between a CECT image obtained in the expiratory position and a venogram. The location of the RAV orifice on the CECT image and the venogram was highly consistent between the two readers (70% and 88%, respectively). Their results support those in this study.

As mentioned above, the authors speculated that the RAV cannulation time was shorter in the EAP group due to the smaller difference of the RAV orifice on the CECT. This preoperative simulation reduces the stress on the patient and the operator. Furthermore, this could lead to a reduction of radiation exposure on AVS. Based on the authors' findings, the authors believe that the EAP is a useful imaging method for selecting the RAV on AVS. Although the EAP group had a lower dose of radiation exposure and shorter fluoroscopy time throughout the entire procedure as compared with the IAP–CECT group in this study, there was no significant difference.

The authors must also mention the limitations of this study. First, this was a retrospective study, and the sample size was small because the authors excluded many samples due to the different types of contrast media used in the CECT procedure. Moreover, the AVS procedure was performed by several operators. Second, because interventional CT of the RAV was not performed at AVS, the authors could not confirm whether the RAV on the abdominal dynamic CECT was the same as the blood vessel visualized by the adrenal venography.

In conclusion, EAP–CECT is useful for increasing the speed of the RAV cannulation due to the small difference in the localization

of the RAV orifice compared to IAP–CECT. However, since EAP–CECT has double contrast arterial phases and increases radiation exposure compared to IAP–CECT, only the late arterial phase may be acceptable to reduce radiation exposure.

Acknowledgments

The authors would like to thank all the staff at the Division of Diabetes, Endocrinology, and Metabolism of the Department of Internal Medicine, Shinshu University School of Medicine. This work was supported by a Grant-in-Aid for Scientific Research (no: 22K07689) from the Japan Society for the Promotion of Science. Additionally, the authors would like to thank Enago (www.enago.jp) for the English language review.

References

1. Yang Y, Reincke M, Williams TA. Prevalence, diagnosis and outcomes of treatment for primary aldosteronism. *Best Pract Res Clin Endocrinol Metab*. 2020;34(2):101365. [CrossRef]
2. Chao CT, Wu VC, Kuo CC, et al. Diagnosis and management of primary aldosteronism: an updated review. *Ann Med*. 2013;45(4):375-383. [CrossRef]
3. Wolley M, Thuzar M, Stowasser M. Controversies and advances in adrenal venous sampling in the diagnostic workup of primary aldosteronism. *Best Pract Res Clin Endocrinol Metab*. 2020;34(3):101400. [CrossRef]
4. Ohno Y, Sone M, Inagaki N, et al. Prevalence of cardiovascular disease and its risk factors in primary aldosteronism: a multicenter study in Japan. *Hypertension*. 2018;71(3):530-537. [CrossRef]
5. Mulatero P, Monticone S, Bertello C, et al. Long-term cardio- and cerebrovascular events in patients with primary aldosteronism. *J Clin Endocrinol Metab*. 2013;98(12):4826-4833. [CrossRef]
6. Catena C, Colussi G, Sechi LA. Treatment of primary aldosteronism and organ protection. *Int J Endocrinol*. 2015;2015:597247. [CrossRef]
7. Rossi GP, Auchus RJ, Brown M, et al. An expert consensus statement on use of adrenal vein sampling for the subtyping of primary aldosteronism. *Hypertension*. 2014;63(1):151-160. [CrossRef]
8. Rossi GP, Rossitto G, Amar L, et al. Clinical outcomes of 1625 patients with primary aldosteronism subtyped with adrenal vein sampling. *Hypertension*. 2019;74(4):800-808. [CrossRef]
9. Onozawa S, Murata S, Yamaguchi H, et al. Can an enhanced thin-slice computed tomography delineate the right adrenal vein and improve the success rate? *Jpn J Radiol*. 2016;34(9):611-619. [CrossRef]
10. Foti G, Faccioli N, Mantovani W, Malleo G, Manfredi R, Mucelli RP. Incidental adrenal lesions: accuracy of quadriphasic contrast enhanced computed tomography in distinguishing adenomas from nonadenomas. *Eur J Radiol*. 2012;81(8):1742-1750. [CrossRef]
11. Matsuura T, Takase K, Ota H, et al. Radiologic anatomy of the right adrenal vein: preliminary experience with MDCT. *Am J Roentgenol*. 2008;191(2):402-408. [CrossRef]
12. Noda Y, Goshima S, Nagata S, et al. Visualization of right adrenal vein: comparison with three phase dynamic contrast-enhanced CT. *Eur J Radiol*. 2017;96:104-108. [CrossRef]
13. Omura K, Ota H, Takahashi Y, et al. Anatomical variations of the right adrenal vein: concordance between multidetector computed tomography and catheter venography. *Hypertension*. 2017;69(3):428-434. [CrossRef]
14. Ota H, Seiji K, Kawabata M, et al. Dynamic multidetector CT and non-contrast-enhanced MR for right adrenal vein imaging: comparison with catheter venography in adrenal venous sampling. *Eur Radiol*. 2016;26(3):622-630. [CrossRef]
15. Morita S, Nishina Y, Yamazaki H, Sonoyama Y, Ichihara A, Sakai S. Dual adrenal venous phase contrast-enhanced MDCT for visualization of right adrenal veins in patients with primary aldosteronism. *Eur Radiol*. 2016;26(7):2073-2077. [CrossRef]
16. Tannai H, Makita K, Matsui S, Koike Y, Tsurutani Y, Saito J. Radiological characteristics and diagnostic impact of duplicated right adrenal veins on adrenal venous sampling in primary aldosteronism. *Diagn Interv Radiol*. 2021;27(6):754-761. [CrossRef]
17. Tannai H, Makita K, Koike Y, et al. Usefulness and accuracy of segmental adrenal venous sampling on localisation and functional diagnosis of various adrenal lesions in primary aldosteronism. *Clin Radiol*. 2022;77(8):652-659. [CrossRef]
18. Bae KT, Heiken JP, Brink JA. Aortic and hepatic contrast medium enhancement at CT. Part I. Prediction with a computer model. *Radiology*. 1998;207:647-655. [CrossRef]
19. Bae KT, Heiken JP, Brink JA. Aortic and hepatic contrast medium enhancement at CT. Part II. Effect of reduced cardiac output in a porcine model. *Radiology*. 1998;207:657-662. [CrossRef]
20. Satani N, Ota H, Seiji K, et al. Intra-adrenal aldosterone secretion: segmental adrenal venous sampling for localization. *Radiology*. 2016;278(1):265-274. [CrossRef]
21. Funder JW, Carey RM, Mantero F, et al. The management of primary aldosteronism: case detection, diagnosis, and treatment: An Endocrine Society Clinical Practice Guideline. *J Clin Endocrinol Metab*. 2016;101(5):1889-1916. [CrossRef]
22. Degenhart C, Strube H, Betz MJ, et al. CT mapping of the vertebral level of right adrenal vein. *Diagn Interv Radiol*. 2015;21(1):60-66. [CrossRef]